Pressure estimation using time-lapse seismic in compacting reservoirs

Margarita Maria Corzo Mojica

Submitted for the Degree of Doctor of Philosophy.

Heriot-Watt University, Heriot-Watt Institute of Petroleum Engineering

October, 2009

Abstract

Pressure estimation using time-lapse seismic in compacting reservoirs

Margarita Maria Corzo Mojica

Institute of Petroleum Engineering, Heriot-Watt University

PhD. 2009

This thesis focuses on developing a new approach to estimate pressure changes from 4D amplitude attributes in compacting reservoirs. The time-lapse seismic signal in these types of reservoirs results from the combination of pressure depletion, rock compaction and stress redistribution within the reservoir and throughout the surrounding rocks. Simulations using iterative coupling are performed to understand the link between geomechanics, fluid flow and the seismic response. The analysis of synthetic data defines a power law equation (eq.1) which relates pressure changes (ΔP) to 4D amplitude attributes (ΔA). The coefficients (C_1 and C_2) are a function of initial porosity. The pressure predictions show an agreement with the output from the reservoir modelling. However the results indicate that the rock compaction has considerable effect on the normal average stress, and the 4D seismic response shows a stronger correlation with effective stress than with pore pressure.

$$\Delta A = C_1 * (\Delta P^{C_2}) \tag{1}$$

The technique is applied to the south east flank of the Valhall Field, Norwegian North Sea. The areas where the initial porosities are above 38 % show a good correlation between the pressure changes predicted from 4D amplitude and the pressure changes from the reservoir model. However, major differences between both outputs occur in areas where no 4D signal is observed; these areas are correlated with low porosity zones where the porosity reduction has not been significant enough to enhance the 4D signal. Furthermore, the pressure predictions from the 4D seismic identify areas where the reservoir has not been properly drained.

The impact of geological structure and gas saturation on the technique is assessed. Strong thickness variations within the reservoir interval increase the errors on the pressure prediction. This is mitigated if relative values instead of absolute values are used to estimate pressure changes, i.e. equation 1 becomes equation 2. Furthermore, the presence of gas on the reservoir requires a modification of the

equation 1 in order to accurately predict the pressure changes and account for the presence of free gas on the reservoir (eq. 3).

$$\frac{\Delta A}{A_1} = C_1 * (\frac{\Delta P}{P_1})^{C_2} \tag{2}$$

$$\Delta A = (C_3 * \Delta P) + C_4 \tag{3}$$

Finally, sensitivity analysis suggests that uncertainties in the elastic properties of the overburden (rarely measured with accuracy) have little impact on the reservoir 4D amplitude response. Synthetic models show that variations between 10 % to 15 % in the Poisson's ratio and Young's modulus of the layer immediately above the reservoir causes negligible changes (less than 4 %) in the 4D amplitude response.

Acknowledgements

Doing a PhD has been once in a live experience and there are many people that in one way or in another helped me.

Firstly, I must give huge thanks to my main supervisor Colin MacBeth for giving me the opportunity to be part of the Edinburgh Time Lapse Project (ETLP). Colin's offers of support, his ideas and overall helpful attitude over the last four years are greatly appreciated.

Thanks also to Olav Barkved from BP-Norway. Olav gave me access to the Valhall data and the chance to spend a very productive time in sunny Stavanger. Also, he was always happy to provide me with fresh ideas either during his visit in Edinburgh or at conferences.

This thesis could not be accomplished without the financial support of the sponsors of the Edinburgh Time-Lapse Seismic Project (ETLP): BG Group, BP, Chevron, ConocoPhillips, ExxonMobil, Fairfield, Landmark, Maersk, Norsk-Hydro, Shell, Statoil and Total.

I'd like also to thank Dale Walters for his enormous help with GEOSIM especially resolving all the bugs with the software.

I have great memories of my time at Heriot-Watt in Edinburgh. I was very lucky to have the opportunity to meet and share great moments with really nice and smart people during that time. Neil, Christophe, Fabian, Jesus, Hansel, Said, Mariano, Oscar, Susana, Isabel, Ludovic, Mateo are great friends and have been a source of much of fun!

Mama, Papa y hermano "muchas gracias" for giving me a lot of encouragement and have always been there for me during the whole time - I know you three will be happy to hear that "Por fin ya acabe"

Finally, many many thanks to my Richard for his love, patience..you are the best!

Contents

Abstract i

Acknowledgements iii

Table of Contents iv

List of Figures xi

List of Tables xx

List of Symbols xxii

1 Introduction **1**

1.1 Overview of rock mechanics 2

1.1.1 Stress 2

1.1.2 Strain 4

1.1.3 Elastic moduli: Young's modulus, Poisson's ratio and bulk modulus 6

1.2 Reservoir compaction induced by hydrocarbon production 7

1.2.1 The compaction mechanism: Origin and quantification of compaction 7

1.3 Global examples of subsidence above compacting reservoirs 14

1.3.1 Examples of subsidence in hydrocarbon reservoirs (1910 and 1984) 14

1.3.2 Examples of compacting hydrocarbon reservoirs (1986 to date) 17

1.4 Tools to monitor compaction and subsidence 19

1.4.1 Tiltmeter monitoring . . . 19
1.4.2 Monument surveys . . . 19
1.4.3 Borehole depth surveys . . . 20
1.4.4 Seafloor pressure measurements . . . 20
1.4.5 Synthetic Aperture Radar (SAR) . . . 20
1.4.6 Time-lapse seismic . . . 21
1.5 Challenges for time-lapse seismic analysis of compacting reservoirs . . . 24
1.6 Focus of this thesis . . . 28
1.6.1 Summary of aims and objectives . . . 28
1.6.2 Synopsis . . . 28

2 Time-lapse seismic studies, geomechanical modelling and a methodology to estimate the time-lapse response of compacting reservoirs 30

2.1 Time-lapse seismic studies in non-compacting reservoirs . . . 31
2.1.1 Rock physics based methods . . . 32
2.1.2 The engineering approach for pressure and saturation separation (EPASS) . . . 35
2.2 Time-lapse seismic studies in compacting reservoirs . . . 40
2.2.1 Time-lapse studies focused on monitoring dynamic reservoir properties in compacting reservoirs . . . 45
2.3 Geomechanical modelling of compacting reservoirs . . . 46
2.3.1 Coupling types used in geomechanical models . . . 47
2.3.2 Description of GEOSIM . . . 50
2.3.3 Derivation of the porosity equation . . . 50
2.3.4 Iteration process for coupled modelling . . . 54

2.4 Methodology used to model the time-lapse seismic response of compacting reservoirs . 55

2.5 Summary 58

3 Analysis of simulated data **60**

3.1 Model Description 61

3.1.1 Geomechanical data 61

3.1.2 Reservoir data 65

3.1.3 Description of producing wells 67

3.1.4 Reservoir simulation results 68

3.2 From the simulator to the seismic data: the workflow 78

3.2.1 Estimation and analysis of the reservoir acoustic properties 78

3.2.2 Estimating the acoustic properties for the overburden and underburden rocks . 85

3.3 The final synthetic seismic response 87

3.3.1 Reflectivity response at the reservoir level at initial conditions 87

3.3.2 Reflectivity response at the reservoir level trough time 87

3.4 Time-lapse attributes observed on the synthetic example 91

3.4.1 The Largest Positive Value attribute 91

3.4.2 The speed-up attribute 93

3.5 Factors that influence the largest positive amplitude 96

3.5.1 Reservoir thickness and tuning effects 97

3.5.2 Reservoir fluids 98

3.5.3 Seismic properties in the layer immediately above the reservoir 98

3.6 Analysis of the cross-plots of the largest positive amplitude attribute and pressure changes 99

3.7 Pressure changes inverted from the largest positive amplitude attribute 103

3.8 Causes for the errors on the pressure predictions from the largest positive amplitude attribute 107

3.8.1 The effective stress changes 107

3.8.2 Acoustic impedance changes in Layer 9 108

3.9 Correlation between speed-up attribute and the pore-pressure and effective stress changes 117

3.10 Summary 119

4 Pressure estimation in the south east flank of the Valhall Field 121

4.1 Geological description of the Valhall Field 122

4.2 Compaction of the Valhall Field 127

4.3 Description of the Life of Field Seismic (LoFS) 129

4.3.1 Installation 130

4.3.2 Acquisition and processing to optimize 4D repeatability 130

4.4 Time-lapse seismic responses due to pressure depletion, compaction and water injection observed in the LoFS data in the Valhall Field 133

4.5 Development and production history in the south east flank of the Valhall Field 138

4.6 Time-lapse seismic attributes due to pressure depletion in the south east flank 144

4.6.1 The Largest Positive Value: the time-lapse amplitude attribute used to predict pressure changes in the south east flank of the Valhall Field 144

4.6.2 The speed-up attribute: the time-shift attribute used to predict pressure changes in the south east flank of the Valhall Field 145

4.6.3 Impact of the horizon seismic interpretation on the quality of the 4D seismic attributes extraction 147

4.7 A methodology to map reservoir pressure change from the time-lapse amplitude attribute 153

4.7.1 Steps 1 and 2: Definition of polygons around the producer wells and extraction of average porosity, pressure and 4D amplitude 154

4.7.2 Step 3: Correlating 4D amplitude against pressure changes and defining the equation 155

4.7.3 Step 4: Estimation of the final pressure changes map from 4D seismic amplitude 157

4.8 Analysis of the discrepancies between the pressure changes estimated from the 4D amplitude attribute and the pressure outputs from the reservoir model 163

4.8.1 Initial porosity map 164

4.8.2 Low porosity effect 166

4.8.3 Normal stress changes and overburden velocity changes 174

4.9 Summary 181

5 Effect of structure and the presence of gas on the pore pressure predictions from time-lapse amplitude attributes 183

5.1 Effect of structure and thickness on pore pressure estimations from time-lapse amplitude attributes 184

5.1.1 Description of the synthetic models: Model I (constant thickness) and model II (variable thickness) 184

5.1.2 Influence of the structure and thickness in the stress and strain distribution during hydrocarbon production 187

5.1.3 Variation of the elastic properties during production due to the structure . . . 196

5.1.4 Accuracy of the methodology of predicting pressure changes from 4D amplitude attributes when the structure and thickness vary across the reservoir 204

5.2 Pressure changes predicted from time-lapse amplitudes on a three phase reservoir . . . 212

5.2.1 Description of the synthetic model 212

5.2.2 Analysis of pore pressure and fluid saturation during production 213

5.2.3 Analysis of the stresses and strain distribution during production 214

5.2.4 Calculation and analysis of the acoustic property changes for a three phase reservoir 214

5.2.5 Estimation of pressure changes from 4D amplitude attributes in a three phase reservoir 220

5.3 Summary 231

6 Investigating the impact of the overburden elastic parameters on the 4D seismic signal 233

6.1 Description of elastic parameters of the overburden in the different models 234

6.2 Effect of the overburden elastic parameters on the reservoir pore-pressure, average normal stress and effective stress 239

6.3 Variations in vertical strain due to changes in Young's modulus of the layer immediately above of the reservoir 242

6.4 Variations in the vertical strain due to changes in Poisson's ratio of the layer immediately above of the reservoir 245

6.5 4D seismic amplitudes and variations in the overburden elastic parameters 248

6.5.1 Generation of the synthetic seismic for each of the models 248

6.5.2 Comparison of the 4D amplitude response between the models 251

6.5.3 Effect of the R-factor on the 4D amplitude response 252

6.6 Effect of the overburden elastic parameters on the time-shift attribute 256

6.7 Summary 262

7 Conclusions and recommendations for future work 264

7.1 Conclusions 264

7.2 Recommendations for future work 267

7.2.1 Separation of pressure and gas saturation 267

7.2.2 Investigation of the effect of water injection on the 4D seismic for compacting reservoirs 268

7.2.3 Strain from 4D amplitude maps 269

7.2.4 Use of geomechanical models to calibrate the results from 4D seismic analysis . 269

7.2.5 Impact of the 4D noise 270

References **271**

A Derivation of the compaction equation **278**

B Biot's equations for deformation in a 3D porous media and Darcy's flow equations 279

List of Figures

1.1 Components of a force acting on a cross-section 3

1.2 Stress tensor notation for a single plane in three dimensions 3

1.3 Components of the displacement 5

1.4 Illustration of the effective stress principle 8

1.5 Illustration of uniaxial strain conditions 10

1.6 Illustration of the movement of a free surface due to a nucleus of strain 12

1.7 Subsidence map for the Valhall Field 13

1.8 Compaction profiles for the Valhall Field 13

1.9 Location of the fields that have reported compaction due to hydrocarbon production . 16

1.10 Photos illustrating the sea floor subsidence in Ekofisk Field 18

1.11 Subsidence map acquired by SAR in Belridge and Lost Hill oil fields 21

1.12 Time component warp shift for the Valhall Field 22

1.13 Time component of the warp shift for the south east flank of the Valhall Field 23

1.14 Results of the fluid substitution and rock physics modelling for scenarios A and B . . 26

1.15 P-wave to P-wave reflectivity versus incidence angle plot for scenarios A and B 27

2.1 Time-lapse seismic in the Gullfaks Field 32

2.2 Inverted fluid saturation and pore-pressure maps from time-lapse seismic using Landrø's approach . . . 33

2.3 Gas saturation and pore-pressure maps from time-lapse seismic in the Schiehallion Field 34

2.4 EPASS-1 results: P50 maps of oil saturation and pore-pressure for a Jurassic reservoir in the UK North Sea . . . 37

2.5 Pressure and fluid saturation estimated for the Schiehallion Field, applying EPASS-2 approach . . . 39

2.6 Illustration of the principal parameters used in Landrø's method 1 to quantify compaction and velocity changes . . . 41

2.7 Compaction maps at the top of the reservoir inverted from time-lapse seismic for the Ekofisk Field . . . 43

2.8 Changes in one-way travel time in twin wells . . . 44

2.9 Results from the technique to determine pore pressure from overburden strain in the Genesis Field . . . 46

2.10 Illustration of the interaction between Geomechanics and fluid flow . . . 47

2.11 Comparison of reservoir pressure from fully coupled and standard reservoir simulation 48

2.12 Flow chart for iterative coupling . . . 55

2.13 Methodology to estimate the time-lapse response due to changes in pressure, saturation and deformation in compacting reservoirs . . . 57

3.1 Synthetic model geometry . . . 62

3.2 Pressure-strain curves for different porosities in the Valhall Field . . . 64

3.3 Initial porosity map . . . 66

3.4 Distribution of porosities for the most porous zone in the south flank of the Valhall Field 66

3.5 Porosity reduction seen on the model . . . 69

3.6 Reservoir pressure outputs from year 1 up to year 12 . . . 70

3.7 Reservoir porosity outputs from year 1 up to year 12 71

3.8 Pressure depletion and porosity loss at well 3 72

3.9 Profile E-W across the model to illustrate of the normal and effective stresses variation 74

3.10 Development of the vertical displacement through time for a E-W cross-section 75

3.11 E-W cross-sections across the maximum displacement in the reservoir 76

3.12 Normalized compressional and shear wave velocities for dry chalk from the Ekofisk Field 80

3.13 Parameters used for equations 3.2 and 3.3 against initial porosity 81

3.14 Curves for the elastic moduli versus effective stress for different initial porosities . . . 82

3.15 Compressional wave velocity vs porosity 83

3.16 Changes in the acoustic reservoir properties vs effective stress and pore pressure changes 84

3.17 Computed P-wave acoustic impedance log for a well in the south flank of the Valhall Field 86

3.18 Seismic traces for different porosities at pre-production conditions 88

3.19 Changes in acoustic impedance logs and seismic traces for a rock of 42% porosity during 10 years of production 89

3.20 Changes in acoustic impedance logs and seismic traces for a rock of 35% porosity during 10 years of production 90

3.21 Diagram illustrating the approach taken to aligned the monitor volumes to the baseline 92

3.22 Procedure to extract the difference volumes 92

3.23 Time-lapse seismic response for a 41% porosity rock 94

3.24 Approach taken to extract the maximum positive amplitude attribute 95

3.25 Cumulative time-shifts between time 10 and pre-production stage 96

3.26 Amplitude spectrum from the baseline survey 98

3.27 Pressure and porosity changes, together with the corresponding largest amplitude value attribute maps . . . 100

3.28 Cross plot between the time-lapse amplitude and the pressure changes . . . 101

3.29 Coefficients (C_1 and C_2) against Initial porosity . . . 103

3.30 Pressure change map from time-lapse seismic volumes . . . 104

3.31 Error between pressure estimated from seismic and the outputs from the simulator using equations 3.9 and 3.12 . . . 105

3.32 Largest positive value attribute vs pressure changes . . . 106

3.33 Cross-plots between dynamic reservoir properties and time-lapse amplitude for all the initial porosities used on the model . . . 109

3.34 Comparison between time-lapse amplitude, effective stress changes and porosity reduction for a initial porosity of 42% . . . 110

3.35 Cross-plots between dynamic reservoir properties and time-lapse amplitude for all the initial porosities used on the model II . . . 111

3.36 Comparison between the pressure change maps estimated for scenarios I and II . . . 112

3.37 Error distribution for scenarios I and II . . . 113

3.38 Effect of the vertical strain in the time-lapse amplitude response . . . 116

3.39 Cross-plot between vertical strain at layer 9 and the parameter DIF . . . 117

3.40 Reservoir properties changes (effective stress and fluid pressure) against the speed-up attribute in the synthetic example . . . 118

4.1 The Valhall Field location . . . 123

4.2 The Valhall Field geological settings . . . 125

4.3 Late Cretaceous and Paleocene stratigraphy for Valhall-Hod area . . . 126

4.4 Comparison between two Scanning Electro Microscope images from a North Sea Chalk and a sandstone rock . . . 127

4.5 Design of the geophone array for the LoFS project 131

4.6 Error distribution for the shot position on survey 3 132

4.7 Workflow implemented to assist the LoFS interpretation 133

4.8 Time-lapse response in the north area of the Valhall Field 135

4.9 Seismic section along the injector well, I_2, showing the acoustic impedance decrease at the reservoir due to pressure increase 136

4.10 Comparison between the time-lapse attributes from BP and PGS processing approaches 137

4.11 Structural cross-section along the south east flank of the Valhall Field 139

4.12 4D RMS amplitude attribute due to pressure depletion at P_1 140

4.13 LoFS acquisition schedule and accumulative production for the wells in the south east flank of the Valhall Field 142

4.14 Reservoir pressure map for the south east flank of the Valhall Field 143

4.15 Largest positive value (amplitude attribute) for the time-lapse volumes I 146

4.16 Largest positive value (amplitude attribute) for the time-lapse volumes II 147

4.17 Comparison between the Largest Positive Value for LoFS6minLoFS1 and the reservoir properties (porosity and thickness) 148

4.18 Extraction of the maximum and minimum time-shift attribute 149

4.19 Speed-up and amplitude attributes for the time-lapse volumes I 150

4.20 Speed-up and amplitude attributes for the time-lapse volumes II 151

4.21 Seismic sections from the south east flank of the Valhall Field 152

4.22 Cross-plot between pressure changes and time-lapse seismic amplitude for the south east flank of the Valhall Field 158

4.23 Linear approximations for pressure depletion vs 4D amplitude 159

4.24 Distribution of threshold amplitude values and coefficients (D_1 and D_2) 160

4.25 Pressure changes estimated from 4D seismic amplitude for the period of time between LoFS4 and LoSF1 . . . 161

4.26 Pressure changes estimated from 4D seismic amplitude for the period of time between LoFS4 and LoSF1 . . . 162

4.27 4D seismic amplitude map for LoFS2minLoFS1 . . . 164

4.28 P_3 well analysis . . . 165

4.29 P_3 well analysis . . . 167

4.30 Initial porosity map for layer 5 . . . 168

4.31 Porosity distribution for the perforations in well P_3 . . . 169

4.32 Comparison between a 4D amplitude anomaly caused by two different initial porosity families . . . 171

4.33 Comparison between a 4D amplitude anomaly caused by two different initial porosity families . . . 172

4.34 Evolution of 4D amplitude anomaly in the toe of well P_2 . . . 173

4.35 Porosity distribution for the perforations in well P_5 . . . 175

4.36 Determining the trend equation for predicting pressure depletion from the speed-up attribute . . . 176

4.37 Comparison between the pressure predicted from the speed-up attribute and the 4D amplitude attribute . . . 178

4.38 Time-Shift between LoFS1 and LoFS2 around P_2 and P_5 . . . 179

4.39 Cross-plot between P-wave velocity and initial porosity . . . 179

5.1 Layers distribution for models I and II . . . 185

5.2 Geometry of models I and II . . . 186

5.3 Initial pressure profiles for models I and II . . . 189

5.4 Pressure and effective stress profiles along models I and II 191

5.5 Vertical strain in the reservoir for models I and II 192

5.6 Vertical strain in the overburden for models I and II 193

5.7 Pore pressure change along profile B-B′ for models I and II 194

5.8 Vertical strain along profile B-B′ for models I and II 195

5.9 Effect of the reservoir thickness in the initial acoustic properties 197

5.10 Acoustic impedance against effective stress cross-plot 198

5.11 Acoustic impedance changes against effective stress changes for models I and II 199

5.12 Acoustic impedance changes against effective stress changes for model I. 200

5.13 4D amplitude attribute vs fluid pressure and effective stress 202

5.14 4D amplitude response extracted at the top of reservoir for model II 205

5.15 4D amplitude attributes against pressure and effective stress changes 206

5.16 4D amplitude attribute vs pore pressure cross-plot 207

5.17 Pressure depletion maps estimated from 4D amplitude 208

5.18 Absolute error of pressure changes estimated from 4D amplitude using equations 5.3 and 5.5 209

5.19 Error distribution of pressure changes predictions for model II 211

5.20 Production data at the well location from the reservoir simulator 215

5.21 Fluid saturations at the well location 216

5.22 Variation in the total stress due to pressure depletion 217

5.23 Elastic properties changes against pore pressure. 219

5.24 Seismic traces extracted around the well location 221

5.25 Initial porosity map 222

5.26 Cross-plot 4D amplitude vs pressure changes for dead and live oil model 223

5.27 Cross-plot 4D amplitude vs pressure changes for the live oil model 224

5.28 Coefficients (C_1, C_2) against initial porosity for a live oil scenario 225

5.29 Cross-plot 4D amplitude vs pressure changes for data below BBP 227

5.30 Coefficients (C_3, C_4) against initial porosity for a live oil scenario 228

5.31 Pressure changes, gas saturation changes and 4D amplitude map at 20 years of production for a live oil case 229

5.32 Pressure changes predicted from 4D amplitude for a live oil case 230

5.33 Histogram of the absolute error for the pressure prediction 231

6.1 Layers distribution for the seven models 235

6.2 Thickness of layers 7, 8 and 9 237

6.3 Initial reservoir porosity 238

6.4 Young's modulus for layer 9 in model 6 238

6.5 Variation of the pore-pressure, stress and strain after 18 years of production 241

6.6 The effect of the Young's modulus in the vertical strain 243

6.7 Vertical strain changes in the models relative to the vertical strain in model 1 for layer 9 245

6.8 The effect of the Poisson's ratio in the vertical strain for layer 9 247

6.9 Vertical strain changes in the models 5 and 6 relative to the vertical strain in model 1 for layer 9 248

6.10 P-wave velocity changes in the reservoir and the layer immediately above the reservoir 250

6.11 Example of the time-lapse response observed in the models 251

6.12 4D amplitude response at the top of the reservoir 253

6.13 4D amplitude changes in the models relative to the 4D amplitude in model 1 254

6.14 4D amplitude response due to different R-factors 255

6.15 The time-shift attribute for the seven models 258

6.16 Location of the data points used in table 6.3 259

6.17 4D attributes using different R-factors for model 5 260

6.18 Percentage change in time-lapse attributes due to two different R-factors (5 and 15) . 261

List of Tables

1.1 Parameters used to determine the sea floor subsidence in the Valhall Field using the nucleus strain concept 14

1.2 Input properties to estimate the P-wave velocity changes for scenarios A and B 25

1.3 Summary table of the reflectivity results for scenarios A and B 28

2.1 Reported R-factor for North Sea fields 45

3.1 Geomechanical parameters for the non-reservoir layers of the model 63

3.2 Fluid reservoir properties used in the simulation 67

3.3 Production for the wells in the model 67

3.4 Porosity error from the iterative coupled simulation 77

3.5 Initial seismic properties for the non reservoir rocks 85

3.6 Tuning thickness as a function of P-wave velocity 97

3.7 Coefficients C_1 and C_2 for equation 3.9 102

3.8 Coefficients C_1 and C_2 for equation 3.9, when the overburden velocity changes are not considered 114

4.1 Calculated stresses for some North Sea fields 129

4.2 LoFS surveys that were acquired between 2003 and 2005 130

4.3 Reservoir model zonation for the south east flank of the Valhall Field 141

4.4 Average initial porosity for each polygon 156

4.5 C_1 as a function of initial porosity 156

4.6 Pore fluid pressure for the wells in the South East Flank 180

5.1 Linear elastic parameters 187

5.2 Coefficients C_1 and C_2 for equation 5.3 205

5.3 Coefficients C_1 and C_2 for equation 5.5 212

5.4 Fluid and reservoir properties for the live oil model 213

5.5 Coefficients C_1, C_2 for equation 5.9 224

5.6 Coefficients C_3, C_4 for equation 5.13 226

6.1 Linear elastic parameters for the upper 6 layers and the underburden used in the seven models 236

6.2 Linear elastic parameters for the models 239

6.3 Summary of the changes in 4D signal (amplitude and time-shift) for the different models relative to model 1 257

List of Symbols

α	Biot's constant
$\bar{\sigma}$	Mean normal stress
ΔA	4D amplitude
ΔAI	Changes in acoustic impedance
ΔD	Change in elevation
ΔH	rock compaction
ΔP	Pore pressure depletion
ΔS	Oil saturation change
Δt	Time-shift
$\Delta \rho$	Changes in density
ΔV_p	Changes in P-wave velocity
κ	Bulk Modulus
κ	Bulk modulus of the saturated rock
κ_{fl}	Bulk modulus of the fluid
κ_{fr}	Bulk modulus of the framework
κ_{fr}	Bulk modulus of the rock frame

κ_m	Bulk modulus of the matrix rock
κ_s	Bulk modulus of the mineral grains
λ	The Lamè constant
μ	Shear modulus
μ	Shear modulus
ν	Poisson's ratio
$\overline{A}$	The average amplitude attribute at baseline survey
$\overline{P}_i$	Average initial pressure
$\overline{S}_i$	Average initial oil saturation
ϕ	Porosity
ϕ^*	New porosity in GEOSIM
ϕ_i	Initial porosity
ρ	Density
ρ_{brn}	Density of the brine
ρ_f	Density of the fluid
ρ_m	Density of the matrix
ρ_o	Density of the oil
σ	Normal stress
σ_h	Hydrostatic stress
σ_{ij}	Stress normal to axis "i" and parallel to axis "j"
ε	Strain
ε_{ij}	Stress normal to axis "i" and parallel to axis "j"

ε_v	Volumetric strain
A	Area of a surface
AI	Acoustic impedance
Bo	Oil formation volume factor
C_b	Bulk compressibility
C_m	Uniaxial compressibility
C_p	Dimensionless coefficients
C_s	Dimensionless coefficients
C_1	Coefficient of the trend equation
C_2	Coefficient of the trend equation
E	Young's modulus
F	Force
K_{fl}	The bulk modulus of the fluid
K_{fr}	The bulk modulus of the frame
K_g	The bulk modulus of the grain
K_{sat}	The bulk modulus of the saturated rock
L	Sample length
P_f	Final pressure
P_f	Pore fluid pressure
P_i	Initial pressure
P_o	Oil pressure
P_w	Water pressure

P_{cwo} Oil water capillary pressure

$P_{o-datum}$ Oil pressure at known datum

Rs Oil gas ratio

S_w Water saturation

t Time

V_p P-wave velocity

Vol_b Current pore volume in GEOSIM

Vol_b^0 Initial pore volume in GEOSIM

$\sigma^{'}$ Effective stress

σ_T Normal total stress

H Thickness

U Displacement

Chapter 1

Introduction

Time-lapse seismic has gained acceptability as a tool to monitor and estimate dynamic reservoir changes over mature and developed fields. Deciphering the time-lapse seismic signature as both pressure and fluid saturations change in compacting reservoirs represents a new and additional challenge in reservoir geophysics. Geomechanically active reservoirs are excellent candidates for 4D analysis because the pressure depletion gives a number of expected effects, including reduced pore and reservoir volume, physical movement of the reflectors, bulk density and velocity changes. The combination of all of these effects generates a strong, stable and measurable time-lapse signal.

Reservoir compaction develops due to porosity reduction when fluids are extracted from a weak or over-pressured reservoir. The effective stress changes cause the pore structure to collapse, and there is an associated thickness reduction. The magnitude of this compaction effect depends on the overall mechanical stiffness of the rock. The time-lapse signal is relatively easy to observe, since changes in the elastic properties of the rocks are not just restricted to the reservoir zone but also occur in the overburden and underburden rocks as they undergo strain deformation. However the rock compaction makes predicting pressure and saturation from 4D seismic more challenging.

In most 4D studies, the integration of geophysics, reservoir engineering and geology is required. However, for compacting reservoirs, geomechanics is an additional and essential discipline necessary to understand the time-lapse response. In the following sections I first provide a brief introduction of geomechanical principles. After this, I present some field examples to outline the geological environments that are prone to reservoir compaction and its associated sea floor/ground subsidence.

Next, I describe available tools to monitor and predict those geomechanical phenomena and show a 1D synthetic example to understand how the reservoir compaction affects the time-lapse seismic. Finally, I summarize the aims of this thesis, and provide a synopsis of the subsequent chapters.

1.1 Overview of rock mechanics

In this section, I give an introduction in rock mechanics - several of its concepts are used in this thesis. The models used throughout this thesis assume that the rocks behave with linear elasticity. Elasticity is the ability of a material to resist and recover from deformations produced by a force. One type of response is where there is a linear relationship between external force and the corresponding deformation. Elasticity is based on two concepts stress and strain.

1.1.1 Stress

Stress (σ) is defined by a force (F) and a surface area (A) (eq. 1.1) and is commonly measured in Pascal (Pa) or psi. Depending on the orientation of the surface relative to the force, the stress can be referred as a normal or shear stress. Figure 1.1 shows a force applied to a cross-section. This force is not normal to the cross-section. Therefore, it is resolved into two components. F_n that is the normal force to the cross-section and F_p that is parallel to the cross-section. Subsequently, two types of stresses can be defined, the normal stress (σ) and the shear stress (τ) (equations 1.2 and 1.3). The magnitude of each stress depends on the orientation of the surface.

$$\sigma = \frac{F}{A}. \tag{1.1}$$

$$\sigma = \frac{F_n}{A}. \tag{1.2}$$

$$\tau = \frac{F_p}{A}. \tag{1.3}$$

The stress tensor is used to give a complete description of the stress state at a certain point within a sample. Figure 1.2 describes the stress tensor in three dimensions. The notation is as follows: (a) Both types of stresses (normal and shear) are denoted σ_{ij}. (b) The subscripts i and j are any of the

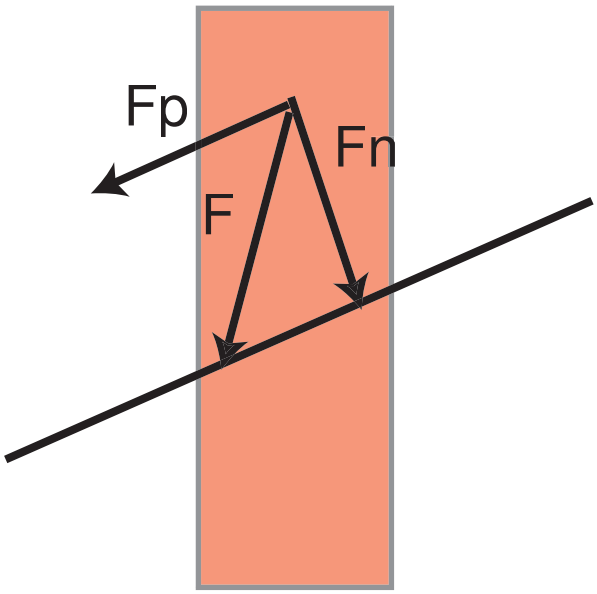

Figure 1.1: Components of a force acting on a cross-section.

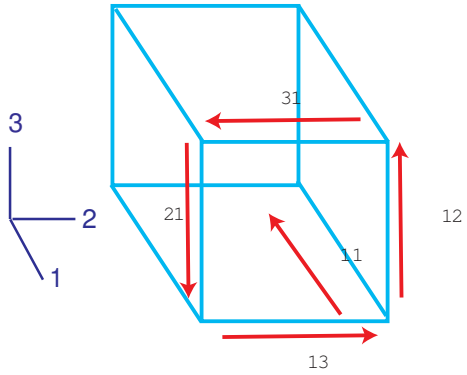

Figure 1.2: Stress tensor notation for a single plane in three dimensions.

numbers 1, 2 and 3 which represent three mutually perpendicular directions. The first subscript (i) is the normal axis to the plane where the force is acting on and the second subscript (j) is the direction of the force. In figure 1.2, σ_{11} is equal to the normal stress on the axis 1 while σ_{13} is the shear stress on the same direction and they are caused by a force in the vertical direction (axis 3). In total there are nine stresses related to a certain point. Equation 1.4 is a matrix that describes the stress tensor; the average of the normal stresses (i.e. stresses in the principal diagonal of the matrix) is known as mean normal stress (eq. 1.5).

$$\begin{pmatrix} \sigma_{11} & \sigma_{12} & \sigma_{13} \\ \sigma_{21} & \sigma_{22} & \sigma_{23} \\ \sigma_{31} & \sigma_{32} & \sigma_{33} \end{pmatrix} \tag{1.4}$$

$$\bar{\sigma} = \frac{(\sigma_{11} + \sigma_{22} + \sigma_{33})}{3}. \tag{1.5}$$

1.1.2 Strain

Strain is the change in shape and/or size of a body caused by stress induced by a external force. Figure 1.3 illustrates the two forms of the displacement of a continuous body: translation and strain. If after displacement of the body the relative displacement between particles in the current configuration is zero i.e. the distance between particles remains unchanged, then there is no strain and a translation of the rigid-body has occurred (figure 1.3A). Contrarily, if after a displacement of the body there is a relative displacement between particles, then strain has occurred. (figure 1.3B). In this case the body is said to be strained and the quantity is called elongation and defined by equation 1.6. Similar to the stress, there are two types of strain. Given a surface within a material, Shear strain is the strain parallel to the surface whereas normal strain is perpendicular to the surface. Furthermore, the strains can be organized in a strain tensor (eq. 1.7). The sum of the element in principal diagonal of the strain tensor represent the volumetric strain (ε_v), which is the relative change in volume (eq. 1.8) and is independent of the co-ordinate axes.

$$\varepsilon = \frac{L - L'}{L}. \tag{1.6}$$

$$\begin{pmatrix} \varepsilon_{11} & \varepsilon_{12} & \varepsilon_{13} \\ \varepsilon_{21} & \varepsilon_{22} & \varepsilon_{23} \\ \varepsilon_{31} & \varepsilon_{32} & \varepsilon_{33} \end{pmatrix} \tag{1.7}$$

$$\varepsilon_v = \varepsilon_{11} + \varepsilon_{22} + \varepsilon_{33} \tag{1.8}$$

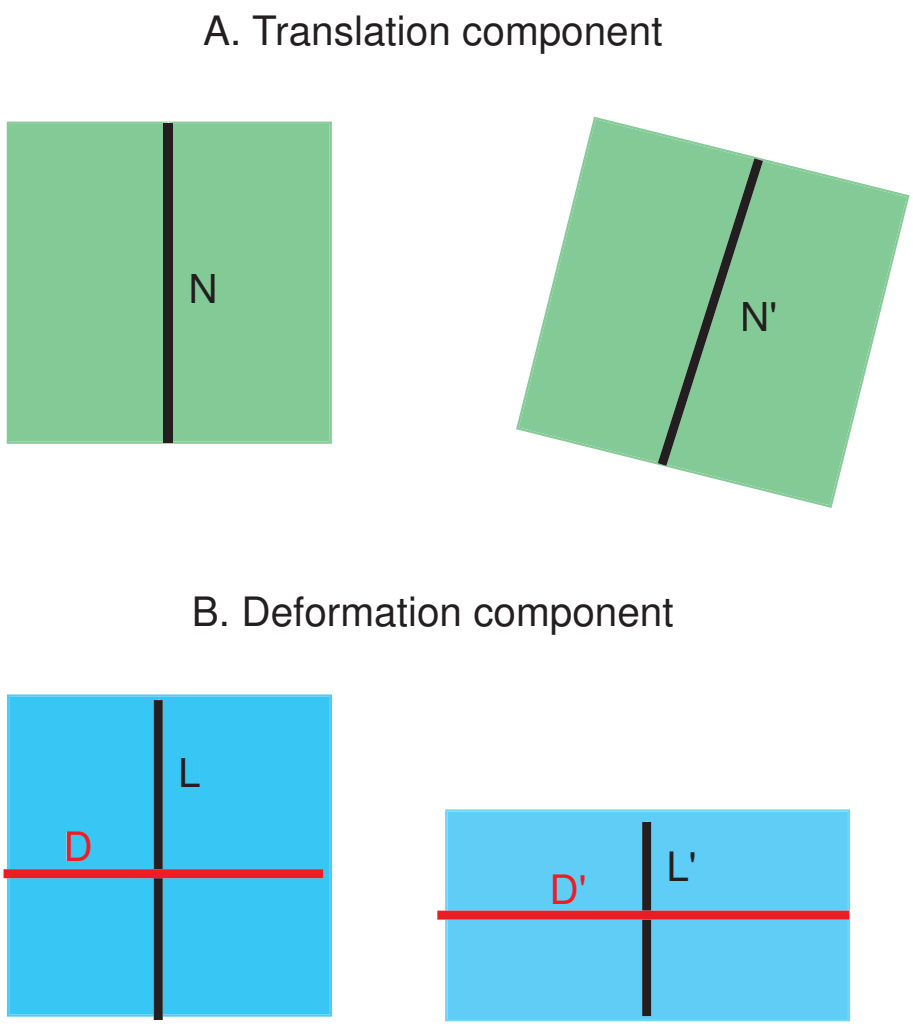

Figure 1.3: Components of the displacement. A. Translation component: If the displacement is the same for every particle within the sample, then the displacement is simply a translation of a rigid body (i.e. N is equal to $N^{'}$) B. Strain component: A sample is strained when the relative position of the particles within the sample are changed (i.e. L is not equal to $L^{'}$).

1.1.3 Elastic moduli: Young's modulus, Poisson's ratio and bulk modulus

Linear elasticity means that there are linear relationships between applied stress and resulting strain. Figure 1.3B shows a sample of length L and cross sectional area A. When a force is applied on the top and bottom of the sample, the length of the sample is reduced to $L^{'}$. The applied stress σ_x is equal to $\frac{F}{A}$ and the corresponding strain ε_x is equal to $\frac{L-L^{'}}{L}$. If the sample behaves linearly there is a linear relationship between σ_x and ε_x and is described by equation 1.9. This equation is known as Hooke's law. The coefficient E is called the Young's modulus and it is a measure of the stiffness of the sample.

$$\varepsilon_x = \frac{1}{E} * \sigma_x \tag{1.9}$$

The applied stress σ_x (figure 1.3B) also causes an increase in the width D of the sample. The lateral elongation is ε_y=$\frac{D-D^{'}}{D}$. If $D^{'}$ is > D, then ε_y is negative. The ratio defined in equation 1.10 is known as Poisson's ratio (ν) and it is a measure of the lateral expansion relative to the longitudinal contraction.

$$\nu = -\frac{\varepsilon_y}{\varepsilon_x} \tag{1.10}$$

Another important elastic modulus is the bulk modulus (κ). κ is defined as the ratio of hydrostatic (σ_h) stress relative to the volumetric strain (ε_v) as shown by equation 1.11 and its inverse is known as bulk compressibility ($C_b = \frac{1}{\kappa}$). The hydrostatic stress is defined when the principal stresses are equal (σ_1=σ_2= σ_3).

$$\kappa = \frac{\sigma_h}{\varepsilon_v} \tag{1.11}$$

Isotropic materials are materials whose response is independent of the orientation of the applied stresses. Furthermore, the principal axes of stress and the principal axes of strain always coincide in isotropic materials. For isotropic and linear elastic materials, the general relations between stress and strain can be written as shown in equations 1.12, 1.13 and 1.14.

$$E\varepsilon_x = \sigma_x - \nu(\sigma_y + \sigma_z) \tag{1.12}$$

$$E\varepsilon_y = \sigma_y - \nu(\sigma_x + \sigma_z) \tag{1.13}$$

$$E\varepsilon_z = \sigma_z - \nu(\sigma_x + \sigma_y) \tag{1.14}$$

1.2 Reservoir compaction induced by hydrocarbon production

This section introduces the compaction and its related subsidence. Compaction associated with hydrocarbon production is not a recent phenomenon and has been investigated many times. Some worldwide examples of the compaction phenomenon are also described in this section.

1.2.1 The compaction mechanism: Origin and quantification of compaction

Effective stress concept

Reservoir compaction is common in unconsolidated sediments and high porosity chalks. The main parameter that controls the reservoir deformation is the effective stress. The reduction in effective stress due to pore pressure depletion leads to the reduction in porosity and thickness. Consider a reservoir rock made up of a solid framework and the fluid that fills the pore spaces. The total stress (σ_T) acting on the rock has two components: the pore fluid pressure (P_f) and the effective stress ($\sigma^{'}$). Physically this means that the solid framework carries part of the total stress (the effective stress) while the remaining part is carried by the fluid. All the deformation of the rock occurs in response to the changes in the effective stress as a result of a variation in either the total stress or the pore pressure (figure 1.4). The effective stress concept (eq. 1.15) was introduced by Terzaghi (1936) and is the basic concept to understand the mechanical behavior of porous materials.

$$\sigma^{'} = \sigma_T - P_f. \tag{1.15}$$

This equation neglects the variations in porosity or intergranular contact areas on the magnitude of the effective stress. However, the ratio of the bulk modulus of the framework (κ_{fr}) to the bulk modulus of the mineral grains (κ_s) has an effect on the magnitude of the effective stress (Skempton, 1960). This observation leads to a revised equation (eq. 1.16).

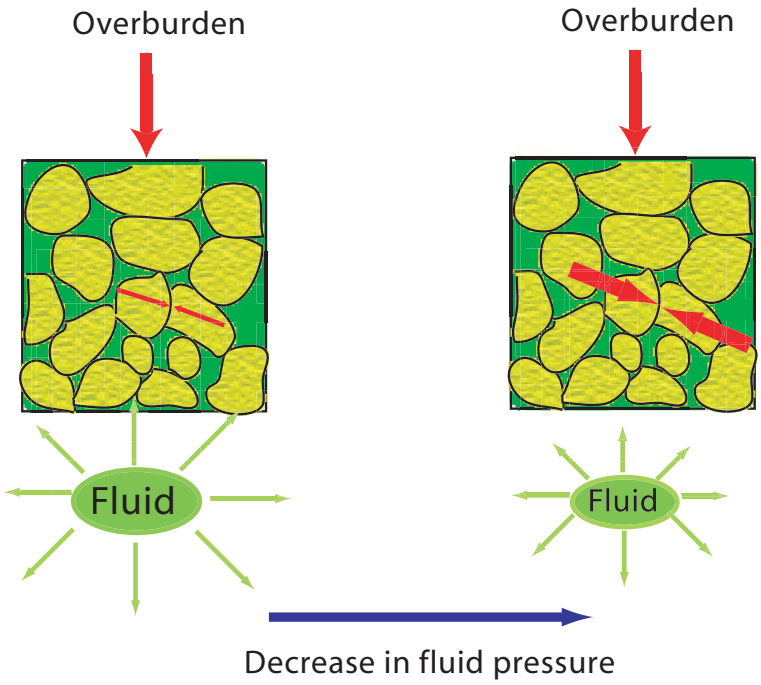

Figure 1.4: Illustration of the effective stress principle: The effective stress acting between the grains influences the bulk rock stiffness and is equal to the difference between the overburden pressure and the fluid pressure (the overburden "pushes" the grains together whereas the fluid acts to separate the grains). Thus a decrease in fluid pressure results in an increase in effective stress and an associated increase in bulk rock stiffness.

$$\sigma^{'} = \sigma_T - \alpha * P_f. \tag{1.16}$$

The parameter α is called the Biot's constant.

$$\alpha = 1 - \frac{\kappa_{fr}}{\kappa_s}; \tag{1.17}$$

K_{fr} is always smaller than K_s, and thus α is generally smaller than one, theoretically, the upper limit of K_{fr} is (1-ϕ)*K_s and the lower limit is zero. Thus, α is restricted to the region $\phi < \alpha \leq 1$. In unconsolidated or weak rocks, α is close to 1.

The relationship of compaction to effective stress is illustrated as follows: assume that a reservoir rock is supporting a total normal stress (σ_T) of 50 MPa, the fluid pressure (P_f) is 45 MPa, therefore the effective stress ($\sigma^{'}$) is 5 MPa. If this reservoir is then put on production, the fluid pressure reduces and more of the external load is carried by the framework and this leads to a deformation of the rock represented by a thickness reduction due to porosity decrease.

Subsidence of the ground surface may not occur, depending on whether the rocks deposited between the reservoir and ground surface have certain geomechanical properties and geometry to transfer a proportion of the strain into the ground as a vertical displacement. Investigating how the reservoir and the surrounding rocks respond to the changes in effective stress due to depletion is the major objective of compaction/subsidence studies.

Estimating compaction/subsidence

The basic model for describing the compaction phenomenon is the uniaxial strain condition. This assumption considers the lateral dimensions of a reservoir to be significantly large compared with its vertical thickness, therefore the deformation will be predominately in the vertical plane, i.e. the reservoirs compact in the vertical direction and the vertical stress remains constant. Following this assumption, compaction in a reservoir of thickness H can be expressed as the vertical strain (eq. 1.18) in a reservoir of thickness H (figure 1.5)

$$\varepsilon_z = \frac{\Delta H}{H} \tag{1.18}$$

where ε_z is the vertical stress, ΔH is the compaction.

If Hooke's law is applied (eq. 1.9), and hence linear elastic behavior is assumed, the compaction formula can be written in response to the applied stress (see Appendix A for a complete derivation).

$$\frac{\Delta H}{H} = \frac{1-\nu-2*\nu^2}{(1-\nu)*E} * \Delta P \tag{1.19}$$

where ν and E are the Poisson's ratio and the Young's modulus of the reservoir respectively and ΔP is the pore pressure depletion. Equation 1.19 can be re-written as follows,

$$\frac{\Delta H}{H} = C_m * \Delta P \tag{1.20}$$

where C_m is the uniaxial compressibility.

Equation. 1.19 is a general definition valid also for non-elastic deformation, but within the elastic regime, the uniaxial compaction coefficient (C_m) is related to the bulk compressibility (C_b) by

$$C_m = \frac{1+\nu}{1-\nu} * \frac{C_b}{3} \tag{1.21}$$

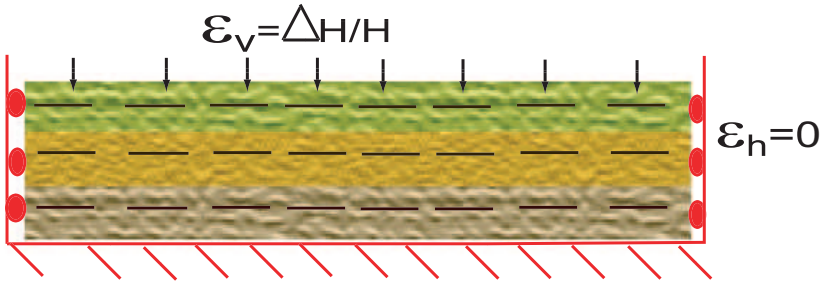

Figure 1.5: Illustration of uniaxial strain conditions: Idealized representation of the reservoir compaction, where the reservoir is deformed in the vertical direction, therefore horizontal strain is equal to zero.

Several limitations have been pointed out by Fjær et al (1992) in applying these formulae to real reservoirs. For example, it is assumed that the reservoir will support the full overburden load. This approximation may be true for the central part of the reservoir, but at the flanks the surrounding rocks will take part of the load. Also, assuming that lateral deformation is null may not be the case since the reservoir walls are not rigid and some horizontal deformation may be expected even when the reservoir height is considerably less than its lateral dimensions. An additional problem in using the equations 1.19 and 1.21 to estimate reservoir compaction is to determine a reasonable set of values for the parameters involved (ν, C_m, E, C_b and ΔP). Neither the pressure depletion nor the elastic properties are homogenous across a field and therefore if the maximum compaction in the most depleted area of a field needs to be estimated, a better approach is to use typical values for that area instead of using average values of the field.

Geertsma (1973) proposed the first analytical method for coupled compaction and subsidence. This approach is still used today and offers a good approximation to describe the compaction/subsidence effect. Geertsma (1973) used the nucleus-of-strain concept in the half space (figure 1.6) to show that subsidence is the result of reservoir compaction which in turn depends on the reservoir depletion, the thickness of the reservoir and rock compressibility.

The perpendicular displacement of the free surface due to a nucleus of strain of small but finite volume (ΔV) under the influence of a pore-pressure reduction, ΔP, is equal to

$$U_z(r,0) = -\frac{1}{\pi} * C_m(1-\nu) * \frac{D}{(r^2+D^2)^{3/2}} \Delta P \Delta V \tag{1.22}$$

Similarly, the horizontal surface movement is given by

$$U_r(r,0) = +\frac{1}{\pi} * C_m(1-\nu) * \frac{r}{(r^2+D^2)^{3/2}} \Delta P \Delta V \tag{1.23}$$

Using equations 1.22 and 1.23, the ratio of the horizontal and the vertical surface displacements above the nucleus-strain is given by $\frac{-r}{D}$.

Analyzing the deformation pattern around a disk-shaped reservoir of thickness H, radius r, at depth D (figure 1.6), for an uniform reservoir pressure reduction ΔP throughout the reservoir, the movement of the free surface can be approximated to:

$$U_z(r,0) = -2C_m(1-\nu)\Delta P * H * R * \int_0^{\inf} e^{-D\alpha} J_0(\alpha R) J_1(\alpha r) d\alpha \tag{1.24}$$

$$U_r(r,0) = +2C_m(1-\nu)\Delta P * H * R * \int_0^{\inf} e^{-D\alpha} J_1(\alpha R) J_1(\alpha r) d\alpha \tag{1.25}$$

where J_1 and J_0 are Bessel functions of zero and first order, respectively and the integrals are known as "Hankel-Lipschitz" integrals. Numerical approximation of the integrals have been presented by Eason et al. (1955). They tabulated their solutions as a function of the ratios $\varphi = \frac{r}{R}$ and $\eta = \frac{D}{R}$. Therefore equations 1.24 and 1.25 are re-written in a simpler form.

$$U_z(r,0) = -2C_m(1-\nu)\Delta P * H * A(\varphi,\eta) \tag{1.26}$$

$$U_z(r,0) = -2C_m(1-\nu)\Delta P * H * B(\varphi,\eta) \tag{1.27}$$

To use equations 1.26 and 1.27 it is necessary to treat the reservoir and surrounding rocks as isotropic - in other words C_m and ν are assumed to be constant throughout the entire half-space. For r=0, the maximum subsidence (A) is expressed as follows

$$A(0,\eta) = 1 - \frac{\eta}{\sqrt{1+\eta^2}} \tag{1.28}$$

therefore U_z is given by

$$U_z(0,0) = -2C_m(1-\nu)\Delta P * H * (1 - \frac{\eta}{\sqrt{1+\eta^2}}) \tag{1.29}$$

Using equation 1.20 to recover the reservoir compaction (ΔH) one can write

$$\frac{Subsidence}{Reservoircompaction} = -2 * (1-\nu) * A \tag{1.30}$$

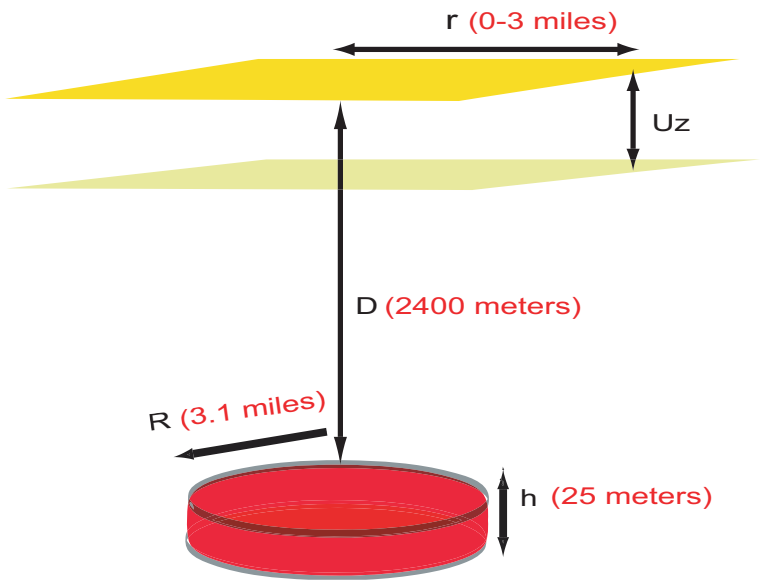

Figure 1.6: Illustration of the movements (perpendicular and horizontal) of a free surface due to a nucleus of strain: definition of the variables introduced by Geertsma (1973) in equations 1.22 and 1.23.

It can be concluded that the ratio between the maximum subsidence and reservoir compaction is governed by the ratio η between depth of burial and lateral extent of the reservoir. For instance small, deeply buried reservoirs are incapable of producing significant subsidence, even if the reservoir compaction can not be neglected. Conversely, large deep reservoirs may be potential candidates for subsidence (Geertsma, 1973)

To illustrate the deformation pattern of a compacting reservoir, I estimated the sea floor subsidence for a reservoir along a 6 km profile (figures 1.7 and 1.8). Table 3.1 summarizes the properties of the reservoir. These properties are the average properties for the Valhall Field (North Sea Norway), I use seismic and production data from this field during this thesis. The sea floor subsidence profile was compared with the bathymetric data for the Valhall Field. There is a fairly good match between the maximum compaction in the middle of the subsidence bowl predicted by the Geertsma method and the one from the bathymetric data. However, there are significant differences in the width of the profile. These discrepancies are due to the simplifications implicit within equations 1.26 and 1.27 that the reservoir and overburden are isotropic and that there is a uniform pressure depletion.

A more rigorous approach can be taken by using a coupled solution of the fluid flow and the rock deformation, which will give a more realistic description of the re-distribution of the stress/strain in

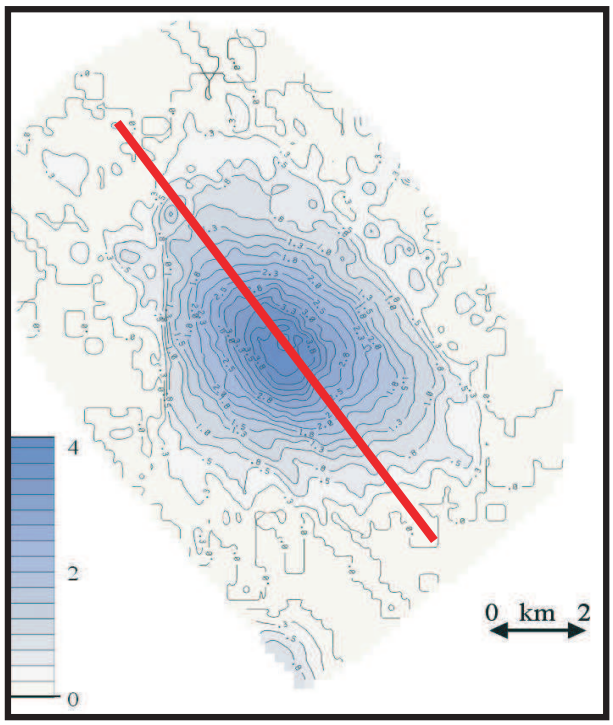

Figure 1.7: Subsidence map for the Valhall Field using bathymetric data between 1978-2001, the red line indicates the profile in figure 1.8. After Hall et al (2005).

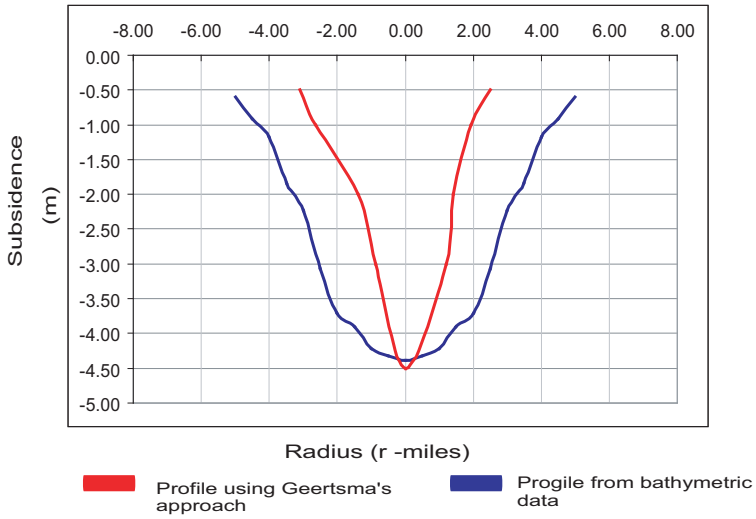

Figure 1.8: Compaction profiles for the Valhall Field: The red profile was estimated by applying Geertsma's approach and the blue profile was calculated from the bathymetric map in figure 1.7.

Parameter	Units	Value
Thickness (H)	meters	25
Depth	meters	2400
Uniaxial Compressibility (C_m)	psi-1	5000000
Poisson's ratio (ν)		0.3
Pressure depletion (ΔP_f)	psi	31

Table 1.1: Parameters used to determining the sea floor subsidence in the Valhall Field using the nucleus strain concept. They were taken from Barkved et al., 2003 and represent average values for the crest of the field

the reservoir and overburden/underburden rocks. The different coupled algorithms available for this current research are discussed in chapter 2.

1.3 Global examples of subsidence above compacting reservoirs

1.3.1 Examples of subsidence in hydrocarbon reservoirs (1910 and 1984)

Recognition of reservoir compaction due to hydrocarbon extraction is not new. Figure 1.9 shows the location of the most known cases around the world.

Cases of reservoir compaction from 1910 to 1984 are summarized by Jones et al (1987). The first example is the Buena Vista Oil Field in California situated in an anticline at the southern end of the Great Valley and to the north-east of the San Andreas Fault. Oil production started in 1910 from a Tertiary sandstone reservoir. In 1932, local casing failures began to occur between 23 m and 242 m below the surface. The subsidence rate of the ground surface above the reservoir was estimated around of 8 cm/year. The geodetic surveys acquired between the 1930's and 1960's indicated the original subsidence rate of 8 cm/year had reduced 2 cm/year. By 1970 the total displacement had reached 76 cm.

The Goose Greek Oil Field in Texas was discovered in 1908 and it was the first offshore drilling for oil in Texas. The reservoir consists of a series of Pliocene and Miocene deltaic sand lenses within clays and shales at depths of between 213 m and 1371 m. The field is a salt dome with overlying beds slightly arched. The peninsula where the oil field is situated was known to be 60 cm above sea level before the production started. By 1918 it became obvious that the surface was subsiding, so much so that the roadways and the base of the derrick had to be raised. During 1924, the annual

rate of subsidence was 6 cm.

The Inglewood Oil Field (California) is an anticline of Tertiary and Quaternary sediments, which overlie the Newport-Inglewood transcurrent fault zone. The reservoir rocks are poorly consolidated Pliocene sands. Production began in 1924, after 6 years a 100 cm subsidence was produced by a 4 MPa pressure drop, but between 1930 and 1962 the pore pressure decreased by 1 MPa, accompanied by an increased subsidence rate. Survey studies showed that substantial horizontal movements were occurring (12 cm between 1950 and 1963) towards the centre of the subsidence bowl which has an area almost twice as large as that of the oil field. Since 1957 cracks up to 800 m in length had developed around the south-eastern edge of the subsidence bowl, which coincide with the known position of existing faults. These cracks have developed as active normal faults that have damaged the oil wells and produced small earthquakes. Continued movements in 1963 caused the collapse of the Baldwin Hill reservoir dam, killing 5 people and damaging 277 houses.

The Niigata gas deposits (Japan) consist of sediments of Miocene to recent age that were deposited in both marine and lagoon environments. The rocks have high porosity and permeability and consist of alternation of relatively unconsolidated gravels, sands, and clays. The first significant reserves of gas were discovered in 1926. Natural gas production began in 1947 and increased rapidly in the 1950's. Surface subsidence was initiated by this extraction, which achieved a maximum rate in the city of Niigata of the order of 50 cm/year after 1956. By 1958 much of the harbor, which was originally 200 cm above sea level, was being damaged by wave action. Several investigations were carried out between 1957 and 1959. The main conclusion was that the gas production was leading to reservoir compaction in sediments between 380 m and 610 m below surface. Consequently, since 1960, there has been a limit on the gas production.

The Lagunillas Field, Venezuela, was the first oil field to be developed on the eastern coastline of Lake Maracaibo. The reservoir consists of thick unconsolidated sands and thinner clays which pinch out towards the north-east. The production started in 1923 from the reservoirs at depths between 300 m and 1200 m below the surface. After 3 years of production, the coastline of the lake showed signs of subsidence when one of the camps involved with the oil activity was flooded after a dyke had been breached. Part of the shoreline had become permanently flooded. A leveling survey showed that the subsidence rate was 20 cm/year. The subsidence had reached 410 cm by 1976 (Eason *et al.*, 1976). Protection walls have been raised to counteract the subsidence. However the majority of subsidence

Figure 1.9: Location of the fields that have reported compaction due to hydrocarbon production: The compaction phenomenon generally occurs in unconsolidated sand, chalks, turbidities deposit and high pressure/high temperature reservoirs.

studies have focused on knowing where and by how much the walls needed to be raised and do not concentrate on the geological aspects of the problem.

Wilmington Oil Field, California, is an asymmetric anticline about 30 km long, containing approximately 300 m of Miocene to recent sands, shales and silts. The production activity intensified around 1936 and by 1942, when there were over 1000 wells, producing from seven different zones between 762 m to 1830 m below the surface (Poland & Davis, 1969). The subsurface subsidence in this field not only led to destruction of the well casings and oil facilities, but affected the Long Beach Naval Dockyard which is located over the center of the subsidence bowl. The subsidence started in 1937; by 1946 it had amounted to 180 cm. In 1949, the subsidence had increased to up to 490 cm. Horizontal movements of 190 cm towards the center of the subsidence bowl, periods of small uplifts and subsidence pulses were all reported in 1954. It was observed that well casing in the overburden was being split. The subsidence rate was estimated at 60 cm/year in 1992. The maximum rate of subsidence (71 cm/year) occurred 1952 which was nine months after the maximum rate of oil production.

1.3.2 Examples of compacting hydrocarbon reservoirs (1986 to date)

In former years, measurements to deal with compaction and its secondary effects such as subsidence, casing damages were taken after the consequences were observed. Nowadays, potential cases of compaction are studied carefully in order to mitigate the damages and prolong the life of the wells. The new discoveries of deep-water and high pressure/high temperature (HPHT) reservoirs also raise the need to understand this phenomenon.

The North Sea region has several HPHT fields, which include the Jurassic reservoirs of Elgin, Franklin and Shearwater fields. Shearwater is a gas reservoir, the reservoir pressure is 100 MPa and the temperature 180°C. The porosity in areas can be higher than 30%. Uniaxial compaction experiments suggest that these porosities can undergo pore-collapse and considerable creep at the pressure ranges expected during the depletion of the field. Some of the early geomechanical models predicted a reservoir compaction in the order of 4.2% around some well locations (Kenter *et al.*, 1998). Even though actual reservoir compaction has not been reported, 4D seismic has recorded time-shift in the overburden and in the reservoir due to stress and strain redistribution caused by the compaction (Stables *et al.*, 2007).

Franklin and Elgin (North Sea) were discovered in 1986 and 1991 respectively and the initial pore pressure was 110 MPa and temperature around 190°C. The production started in 2001 and one of the major challenges for infill drilling was to minimize the wellbore hole stability problems caused by the compaction since both reservoirs depleted by 50 MPa (Hawkins *et al.*, 2007).

The Genesis Field is another recent example of compaction induced by pore pressure depletion. The field is located in the Gulf of Mexico and is characterized by stacked Plio-Pleistocene sandstone turbidities lying on the flank of a buried salt ridge. The field was discovered in 1988, however the first production occurred in 1999. During the first 4 years of production, the major impact of the compaction has been in the well productivity as the wells have suffered considerable reduction in permeability. An important lesson learned is that the compaction values calculated from early core studies underestimated the actual reservoir compaction (Pourciau *et al.*, 2004). Early results suggested that the reservoir compressibility varied from 20 to 25x10^{-6} psi^{-1}, however analysis of the permeability changes and history matched reservoir simulations indicate that the actual reservoir compressibility is between 40 to 45x10^{-6} psi^{-1}.

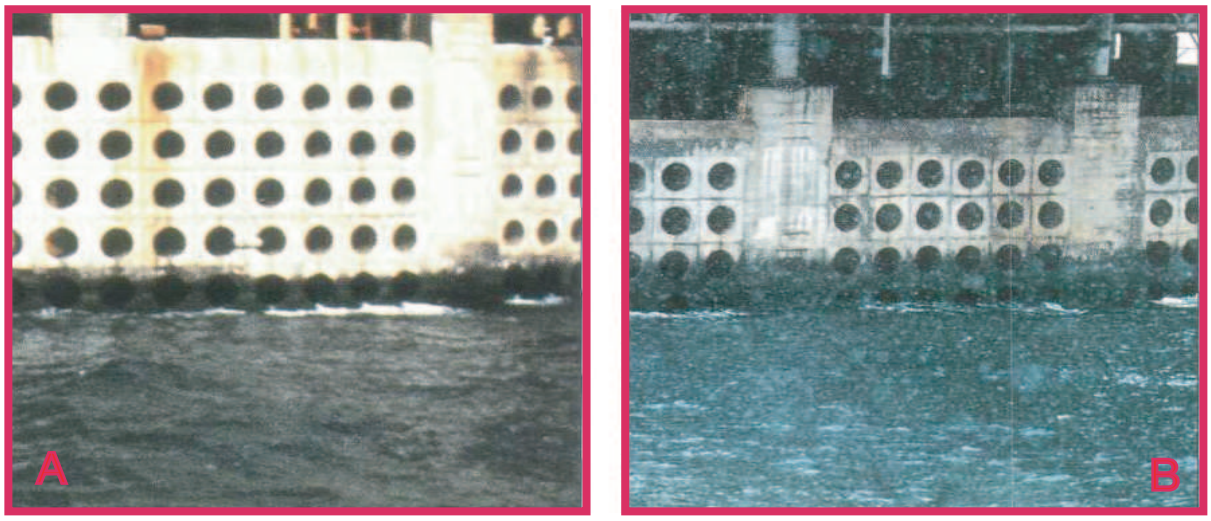

Figure 1.10: The two photos of Ekofisk tank, from 1975 (A) and 1986 (B), show that some rings were missing due to the sea floor subsidence.

The first evidence of subsidence problems in the chalk fields was observed in Ekofisk Field (offshore Norway) about 13 years after production start (Wiborg & Jewhurst, 1986). A rumor about Ekofisk sinking started in the early 1980's, when the people working on the field noticed that a boat-landing on the east side of the Ekofisk tank was partially under water while it used to be visible in 1973. A comparison between pictures of the storage tank taken at the mid seventies and more recent ones shows that indeed some rings at the base of the tank were under water (figure 1.10)

In 1985, the news was released to the public and sea floor subsidence under the platform of the Ekofisk Field was confirmed. The explanation was simple; some reservoir rocks are soft material such as chalks and unconsolidated sands and the hydrocarbon extraction can lead to compaction. This effect can propagate upward to the seabed depending on the strength of the overburden. If this happens, the ocean floor will subside.

The Valhall Field (offshore Norway) is another chalk field that undergoes compaction. It was discovered in 1982 and the first evidences of sea floor subsidence were seen after 5 years of production. The seismic data sets used during working this thesis are from the Valhall Field, - a more detailed description of the compaction process in this field is given in chapter 4.

1.4 Tools to monitor compaction and subsidence

Reservoir deformation and the corresponding subsidence cause several problems such as casing collapse, chalk/sand production, damage of offshore platforms and porosity and permeability reduction, all of which can reduce the productivity of a field. Therefore, the installation of tools to monitor compaction and subsidence is now common practice in geomechanically active reservoirs. There are at least five ways summarized below to monitor deformation caused by hydrocarbon withdrawal (Davis *et al.*, 2000)

1.4.1 Tiltmeter monitoring

The aim is to detect the direction of the gravity field by the use of sensitive tiltmeters placed near to the earth's surface. This technique has been applied in Cymric/Mckittrick Field and the South Belridge Field (Davis *et al.*, 2000), both are diatomite reservoirs in the San Juaquin Basin (North America). Downhole tiltmeters can be installed in order to know exactly where the compaction is taking place. This technique can be impractical and expensive to use offshore for large fields because the tiltmeters requires shallow boreholes (5 to 12 m deep) for stability and a dense array for integration (Stenvold *et al.*, 2006)

1.4.2 Monument surveys

Monument surveys are the most common method used to monitor subsidence in oil and gas fields. GPS or optical techniques are used to periodically detect the depth of fixed surface monuments spread across the area of interest. Similarly using bathymetric data, seafloor subsidence can be reconstructed. This technique is commonly applied to monitoring sea floor subsidence in Ekofisk (Nagel, 1998a) and Valhall Fields (Barkved *et al.*, 2003). The most recent published map for Valhall, was built using data from 1978 and 2001 and it suggests that the greatest subsidence at the sea floor is 4.5 m and it is located on crestal part where there is maximum well activity (figure 1.7).

1.4.3 Borehole depth surveys

This technique is also known as the Radioactive Marker Technique (RMT). It was originally developed for the Groningen Gas Field in the Netherlands and has recently been implemented in the North Sea, Gulf of Mexico and the Northern Adriatic (Ferronato *et al.*, 2006). The technique is based on the regular monitoring of the distances between a number of low-emission radioactive bullets (markers), which are shot at fixed intervals along the wells. The distance between two adjacent markers are dictated by the tool geometry (approximately 10 m). The marker position is detected by a specific gamma ray logging tool. The RMT records allow the calculation of the uniaxial vertical compressibility, which is a essential parameter for geomechanical modelling.

1.4.4 Seafloor pressure measurements

This technique has been implemented in the Troll Field Norwegian North Sea (Stenvold *et al.*, 2006). An instrument is placed on the sea floor for 20-30 minutes to record pressure and gravity information and then, moved to another location. After the pressure is corrected for ocean tides, wind setup and air pressure, it is converted to depths by using an average density profile of the measured depth interval for the survey period. In order to obtain the sea floor subsidence maps, several surveys are acquired over a long period of time. In the case of the Troll Field, 4 surveys were acquired over a 7 year period. The average subsidence for a period between 2002 and 2005 was 4 cm/year.

1.4.5 Synthetic Aperture Radar (SAR)

This relatively new technique uses satellite radar to periodically measure the distance between the satellite and the ground. A microwave sensor passes a spot on the ground and takes an image of it, then after certain period of time another image is taken of the same place. Comparing the two shots with a reference elevation map, provides a detailed surface deformation map for the period between the two passes (Xu & Nur, 2001). Efforts are focused to resolve problems related to signal decorrelation (due to rainfall and vegetation) and spatial resolution. Figure 1.11 shows a subsidence map generated for the Lost Hill oil filed using SAR data.

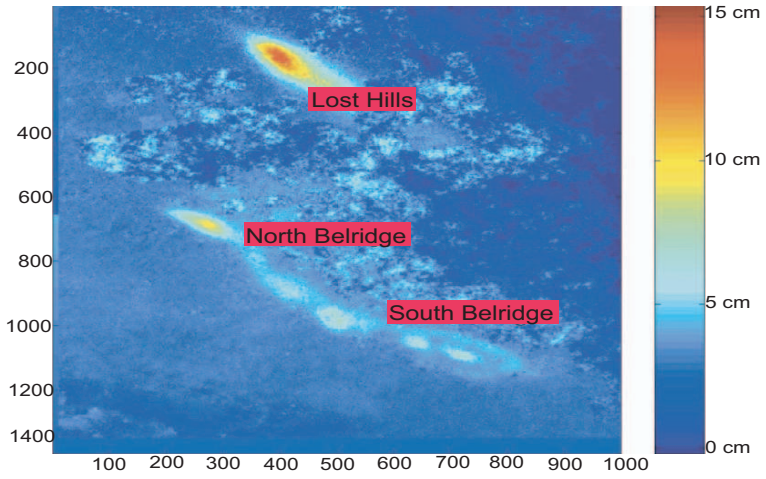

Figure 1.11: Subsidence map acquired by SAR in Belridge and Lost Hill oil fields over 105 days in 1995-96. Scale is in centimeters. The maximum subsidence was 15 cm in the center of Lost Hills (After Xu, N and Nur, A.,2001).

1.4.6 Time-lapse seismic

The tools described above directly measure the compaction/subsidence effect. However, during recent years, time-lapse seismic has also started to be used as a technique to monitor reservoir compaction. For example, Hall et al (2005) used 3D interpreted warping as a time-lapse attribute to assess subsidence and compaction caused by production in the Valhall Field. The data sets considered in that study were 3D streamer and 3D OBC data and despite the acquisition difference, the results were very encouraging (figure 1.12). The warp maps show the down-shift in the center of the field. This zone is the main area of production where the major compaction is occurring. The maximum time component of the warp shift is seen at the Top Hard Chalk just below the reservoir level, with decreasing values for shallower horizons.

The warp derivation procedure is based on the cross-correlation of small data volumes from the two data sets, at nodes positioned on picked horizons but distributed evenly in x and y space. At each node, a small reference volume in the reference data set is extracted and cross correlated with an equivalent sized volume in the second data set. This is done for all possible such volumes within a search volume defined around the reference volume.

I applied this technique to the 1992 and 2002 streamer data acquired in Valhall and the results agreed with Hall's previous work. The seismic interpretation used for the warping needs to be interpolated in the crestal area, since this zone was not interpreted due to bad data quality. For this reason the

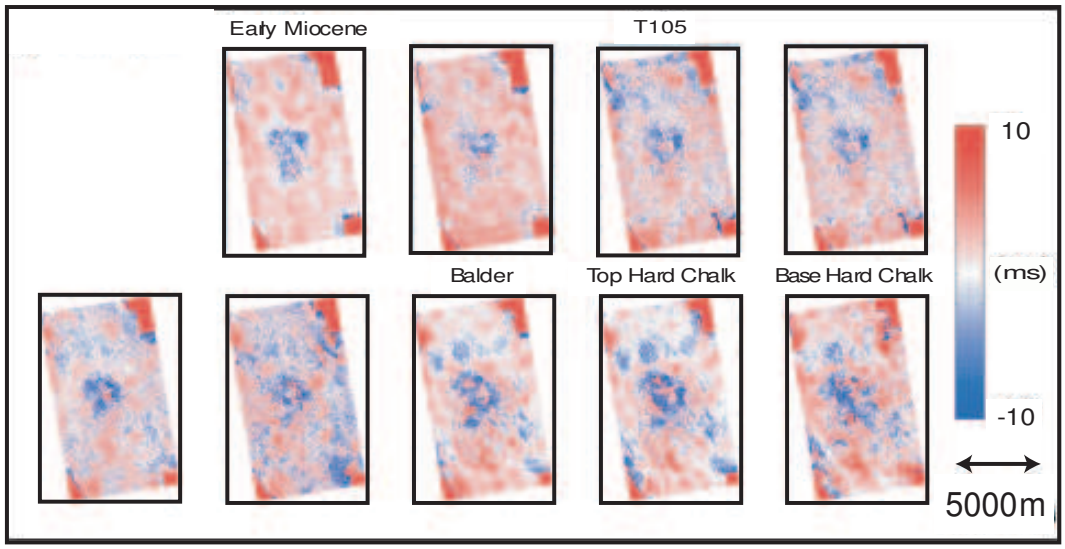

Figure 1.12: Time component warp shift for the Valhall Field. The results for different reflectors are shown, the time-shift is decreasing for shallower horizons. The maximum values are observed at The top of the Hard Chalk, just below the reservoir level. The highest vales are located on the crestal part of the field, where the major compaction is occurring (Hall *et al.*, 2005).

warping results in this area are not reliable. Three horizons were used to do the warping; T105 and Balder which are overburden formations and the top Hard Chalk which is immediately underneath the reservoir zone.

The warping time component maps indicate that the largest shifts are located in the center of the field, as described by Hall et al (2005). However, part of this zone is affected by the presence of gas and this causes the seismic quality to decrease. Figure 1.13 presents the results of the final streamer-streamer warping analysis for a depleted area on the south east flank (outside the gas cloud). The 4D signal on the flank is caused by Well A, which was put on production 2 years after the first survey was acquired. The warping results indicate that the compaction propagates outside the reservoir zone. The warping time component is observed in T105 formation (shallower than the reservoir). However the time-shift decreases towards the sea floor. Sea floor subsidence has not been reported in this part of the field. Immediately above and below the reservoir the time warping has its highest values (Balder and Hard Chalk formations), indicating that the reservoir is compacting and its deformation is having an impact on the surrounding rocks.

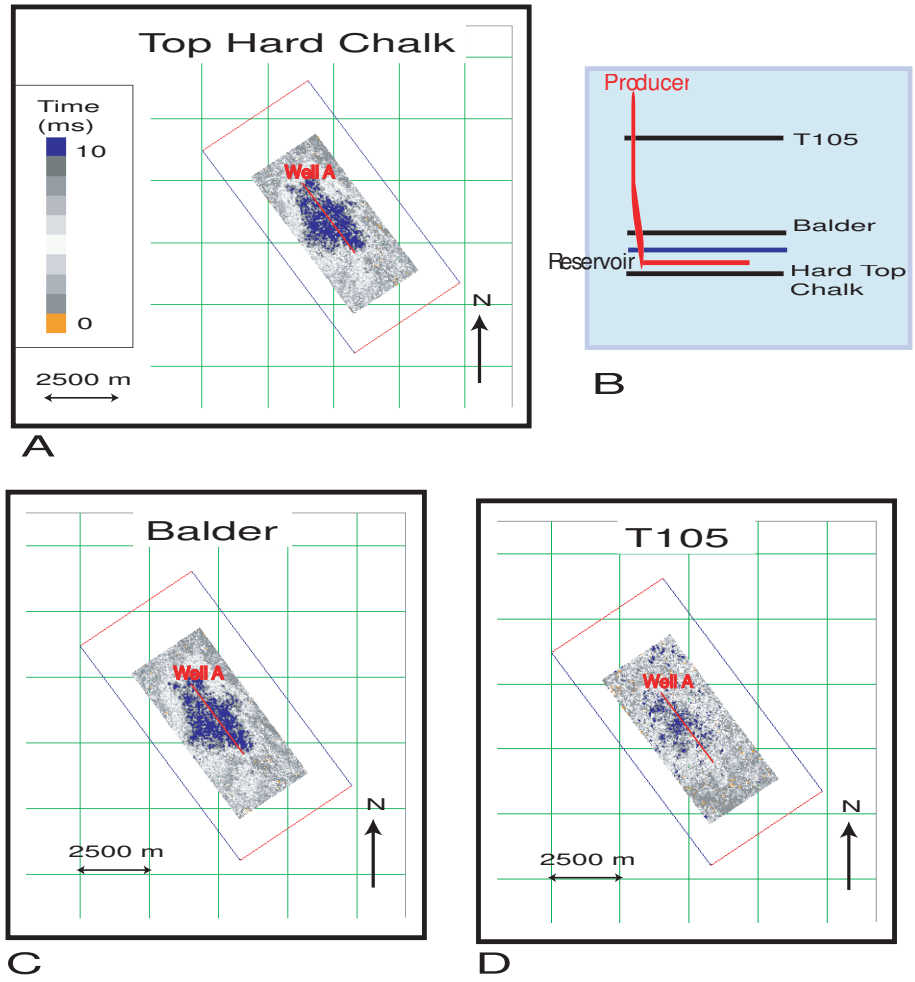

Figure 1.13: Time component warp shift for the south east flank of the Valhall Field: A. Time component warping for Top Hard Chalk. B. Vertical section to illustrate the location the horizons with reference to the well A and the reservoir. C. Time component warping for the Balder. D. The time component warping for T105. The time-shift decreases for shallower horizons, and maximum values are observed at the top of the Hard Chalk, just below the reservoir level.

1.5 Challenges for time-lapse seismic analysis of compacting reservoirs

Time-lapse seismic is growing as a technique to monitor dynamic changes within reservoirs as the spatial sampling offers an excellent opportunity to collect information away from the well penetrations. Reservoir dynamic changes (pressure drops or fluid saturation changes) affect the bulk elastic properties (figure 1.14C). When a reservoir starts to produce, the pressure decrease (effective stress increase) causes an increase in P-wave velocity. In a water injection scenario, the effect of water replacing oil, increases the P-wave velocity. The decrease in P-wave velocity due to de-pressurization of the reservoir is very difficult to detect. For a compacting reservoir in addition to pressure and fluid changes, the porosity reduction needs to be included to estimate the elastic properties. A 1D model was created in order to assess what differences in acoustic properties can be expected between a compacting reservoir and a non compacting reservoir. Scenario A is a conventional reservoir, where porosity is kept constant through time and there are no velocity changes in the overburden. In the second scenario B, the reservoir compacts but the porosity decreases as shown in figure 1.14A. Both scenarios are given the same reservoir and fluid properties based on Valhall Field (table 1.2).

Figure 1.14C shows a comparison of the P-wave velocity changes for the two cases. At very low effective stress (<13MPa) the curves are almost identical; however, the curves start to separate as the effective stress increases. This can be explained by looking into the rock physics equations. The P-wave velocity (V_p) is a function of the bulk modulus (κ) and the density (ρ) of the saturated rock and the shear modulus (μ) as shown in equation 1.31. The Gassmann equation (Gassmann, 1951) calculates κ using the known bulk moduli of the solid matrix (κ_m), the frame (κ_{fr}), and the pore fluid (κ_{fl}) as shown in equation 1.32. Equation 1.33 is used to calculate the density of the saturated rock which depends on the porosity (ϕ) and the fluid density (ρ_{fl}). Therefore, the P-wave velocities are lower in the compaction scenario than the ones from the non-compacting scenario because (a) κ decreases as porosity decreases (eq. 1.32). (b) ρ increases when the porosity reduces (eq. 1.33). The effect of the compaction on the density of the saturated rock is shown in figure 1.14B. The density curves as a function of effective stress are estimated for a constant water saturation of 10 %. It is observed that the density for the compacting reservoir case (magenta line) is higher than the density

for the no-compacting reservoir (blue line)

$$V_p = \sqrt{\frac{1}{\rho} * (\kappa + \frac{4 * \mu}{3})} \tag{1.31}$$

$$\kappa = \kappa_{fr} + \frac{1 - \frac{\kappa_{fr}}{\kappa_m^2}}{\frac{\phi}{\kappa_{fl}} + \frac{1-\phi}{\kappa_m} - \frac{\kappa_{fr}}{\kappa_m^2}} \tag{1.32}$$

$$\rho = (1 - \phi)\rho_m + \phi\rho_{fl} \tag{1.33}$$

Property	Value
Overburden Stress (MPa)	50.00
Pore Pressure (Reservoir Pressure) (MPa)	45.16
Effective pressure (MPa)	4.83
Bubble point pressure (MPa)	28 - 32
GOR (scf/stb)	800
Initial Porosity	0.4
Temperature	90
API	36
Water Saturation	0.1 -0.5
Salinity (1/106)	100000
FVF	1.615
Gg	0.766
Density of the matrix (gr/cm3)	2.71
Bulk Modulus for calcite	65*1e9

Table 1.2: Input properties to estimate the P-wave velocity changes for scenarios A and B

In compacting reservoirs a re-distribution of stress in the overburden and underburden is expected as production from the reservoir proceeds. Immediately above and below of the depletion area, the stress field becomes less compressive. However, outside the pressure depletion area, an increase in the stress field occurs in the overburden and underburden. These stress variations will have an effect on the seismic velocities. For example, a 4D check-shot in the Valhall Field shows that the velocities in the overburden reduced by around 1 - 2 % due to 11 years of production/subsidence (Barkved & Kristiansen, 2003). This means that the time-lapse response is not confined to the reservoir zone but also occurs in the overburden and underburden. Several authors have used time-lapse seismic to estimate the changes in the elastic properties of the overburden due to reservoir compaction. Their approach and results will be discussed later (chapter 2).

To understand how the porosity reduction and velocity decrease of the overburden influence the 4D seismic response I calculate the P to P reflectivity for the two scenarios described previously (figure

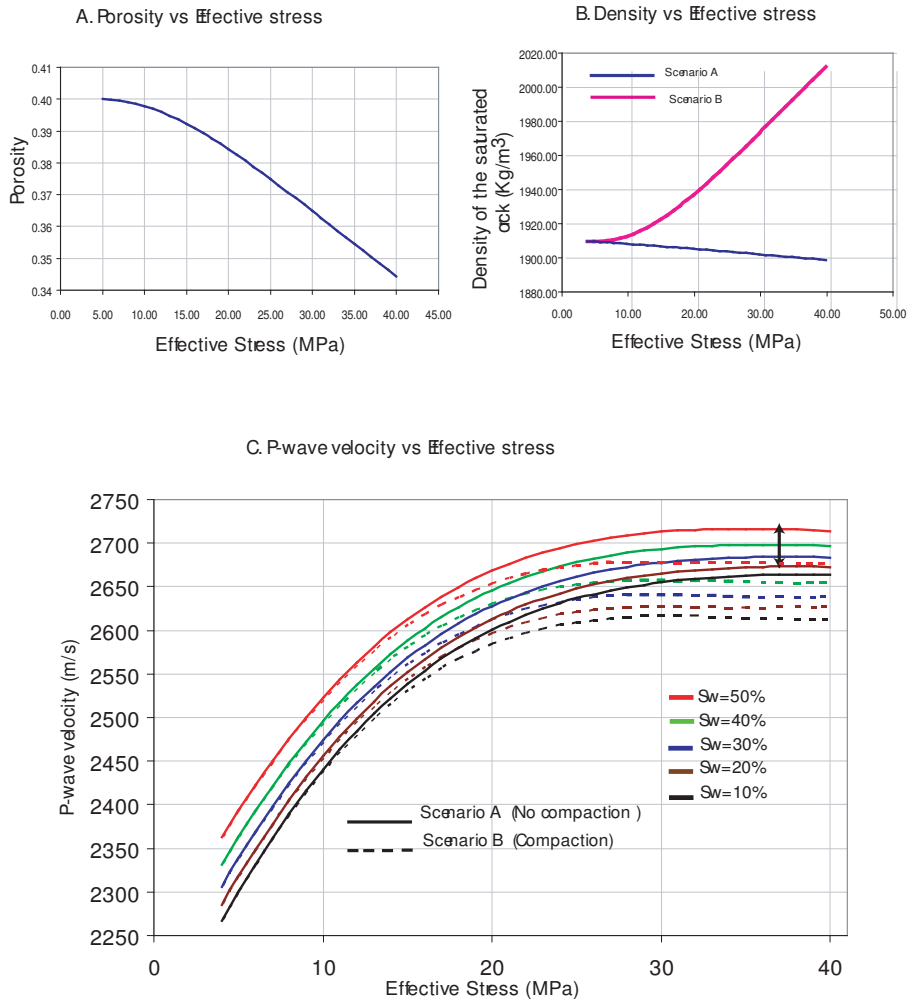

Figure 1.14: Results of the fluid substitution and rock physics modelling for scenarios A and B. A. Porosity versus effective stress plot used to estimate the elastic properties in the compaction case. B. Density of the saturated rock versus effective stress for both scenarios. The density changes for scenario A (blue line) are due to merely pressure changes while the density increase for the compaction changes is due to the combined effect of pressure changes and porosity reduction (magenta line) C. P-wave velocity response. The initial effective stress is equal to 5 MPa (red arrow). The black arrow indicates the shift in P-wave velocity due to the changes in porosity; for higher effective stress, this difference tends to increase.

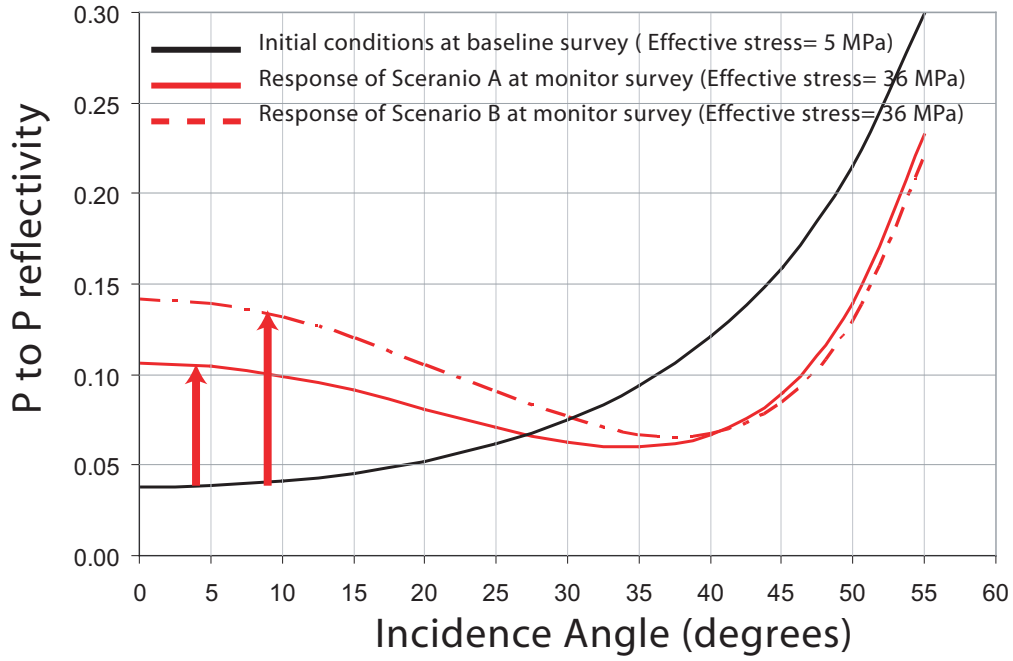

Figure 1.15: The P-to-P reflectivity vs incidence angle plot. The black curve represents the initial conditions for both scenarios. The continuous red line is the reflectivity for Scenario A and the broken red line is for Scenario B. In the compaction case, the changes in P-to-P reflectivity are intensified by the increase of overburden velocities and the porosity reduction.

1.15). I assumed that the baseline and monitor surveys were acquired when the effective stress was 5 MPa and 36 MPa respectively. For Scenario B, the overburden velocities have decreased by 4%. The results for the two cases are shown in figure 1.15 and table 1.3. They suggest that scenario B (compacting reservoir) will produce a stronger 4D seismic response than Scenario A, and indicate that the time-lapse signal in compacting reservoirs should be easy to recognize. This is because any conventional 4D signal is enhanced by the effect of compaction/subsidence.

This simple exercise demonstrates that to understand the time-lapse anomalies in compacting reservoirs, inclusion of the overburden and underburden elastic properties into the analysis is required. Therefore a good knowledge of the geomechanical properties (e.g. how porosities change with reservoir pressure and the stress variation in the overburden and underburden rocks) is needed. The strong link between pressure depletion and the rock deformation, which in turn has an effect on the seismic velocities justifies the coupling of both effects in order to understand the 4D seismic signature.

$\Delta\sigma'$ =30 MPa			
Near offset		Far Offset	
Scenario A	Scenario B	Scenario A	Scenario B
200%	140%	38%	40%
$\Delta\sigma'$ =12 MPa			
Near offset		Far Offset	
Scenario A	Scenario B	Scenario A	Scenario B
17%	4%	17%	18%

Table 1.3: Summary table of the reflectivity results for scenarios A and B

1.6 Focus of this thesis

1.6.1 Summary of aims and objectives

Time-lapse seismic analysis has evolved from a tool used to identify un-swept areas and fluid contact movements towards a quantitative technique that may be implemented by a multidisciplinary team in order to improve the overall reservoir management. Under this premise, the interest of this thesis is to determine if 4D seismic attributes in compacting reservoirs can be used directly in combination with reservoir engineering data to estimate the expected pressure depletion. Within this aim, the specific objectives include:

- Determine the link between time-lapse seismic, pore pressure changes and rock deformation
- Model the seismic response in compacting reservoirs; this involves the use of an iterative coupling approach to integrate fluid flow and the stress/strain relationships
- Develop a technique to invert for pressure changes in compacting reservoirs using 4D amplitude attributes and reservoir engineering data
- Test out the new approach on a 4D seismic dataset from the Valhall Field
- Sensitivity analysis

1.6.2 Synopsis

Following on this introductory chapter, in **chapter 2**, I discuss published 4D studies carried out to quantify reservoir changes. Special emphasis is placed on the time-lapse work in compacting

reservoirs. For these type of fields the efforts have been focused on the correlation of the time-shifts attributes with the rock deformation and relatively few attempts have been made to use 4D amplitude attributes as a tool to estimate reservoir dynamic changes. In addition, I review the approaches used to integrate fluid flow and stress/strain relationships, placing emphasis on the iterative coupling algorithm.

In **chapter 3**, a synthetic model is created to understand the impact that rock compaction has on the time-lapse seismic and to develop a methodology to estimate pressure changes from 4D amplitude attributes. The first step of the approach involves cross plotting 4D amplitudes against pore pressure changes; the second step is to define a trend equation that captures the changes in amplitude as a function of pressure and initial porosity. The final step is to use the equation to estimate the pressure changes for generating pressure maps from 4D amplitude attributes. For the model the pressure estimations from a 4D amplitude attribute gave maximum errors of 15%. These errors are mainly due to two factors. First, the 4D amplitude attribute correlates better with effective stress changes than with pressure. Secondly, errors arise from the changes in the elastic properties of the layers immediately above the reservoir.

The methodology outlined in chapter 3 is applied to a real scenario in **chapter 4**. The case study comes from the south east flank of the Valhall Field. The final product is a pressure depletion map from a 4D amplitude attribute. This map is compared with the pressure map from the reservoir simulator in order to evaluate its reliability.

The following two chapters focus on understanding the influence that other factors can have on the proposed approach to predict pressure changes from 4D attributes. **Chapter 5** investigates the effect that structure and presence of gas have on the robustness of the approach and **chapter 6** attempts to quantify the effect of varying the elastic parameters of the layer immediately above the reservoir, has on the 4D amplitude response. All of this analysis is done by creating different synthetic models that capture each one of these factors.

Finally, **chapter 7** summarizes the main findings of this research and proposed further work in order to validate more the technique.

Chapter 2

Time-lapse seismic studies, geomechanical modelling and a methodology to estimate the time-lapse response of compacting reservoirs

The first part of this chapter is dedicated to reviewing and discussing studies that have been focused on using the time-lapse seismic as a technique for surveillance reservoir dynamic changes. There is a special emphasis on the engineering approaches (EPASS-I and EPASS-II) since I intend to modify these techniques to make them applicable for compacting reservoirs. This chapter also covers the previously published work in compacting reservoirs; the main observation from these studies is that including the impact of stress and strain changes during field life can improve the 4D interpretation. The chapter concludes by outlining the coupled fluid flow-deformation strategy employed in this thesis and the methodology used to estimate the time-lapse response of compacting reservoirs.

2.1 Time-lapse seismic studies in non-compacting reservoirs

The standard methodology for interpreting time-lapse anomalies usually starts by comparing the time-lapse seismic data with other time-lapse reservoir data (e.g. reservoir simulator outputs, well production and surveillance data). Normally, this step involves modelling the expected seismic response using the available reservoir data, and synthetic models guide the interpreter to decide if the 4D anomalies observed in the real data are a result of the production/injection activity rather than artifacts of acquisition or processing. After defining the 4D anomalies that are related to production, a qualitative interpretation can be carried out. At this stage, areas where the reservoir conditions (pressure or saturation) have varied are identified. However, the interpretation can be very difficult if there are several reservoir properties that are varying at the same time. For instance, in a water injection case, the water saturation increases but the effective stress decreases or in compacting reservoirs, the pressure drops and the porosity decreases (changes in the rock compressibility). To reduce interpretational uncertainties, it is more appropriate to use a quantitative approach. This involves inverting for the dynamic reservoir properties using time-lapse seismic data.

Qualitative time-lapse interpretations have given valuable inputs to identify unswept areas and locate infill drilling options. In the Gullfaks Field (Norwegian North Sea), the 4D qualitative interpretation contributed towards successfully drilling 14 infill targets with estimated volumes corresponding to 56 mbbls (Stronen & Digranes, 2000). In some areas, the time-lapse data indicate that water is replacing oil. This effect is observed on the 4D seismic as a strong decrease in the amplitudes at the reservoir top (figure 2.1).

Gouveia et al. (2004) presented a 4D study of the Jotun Field (North Sea). They combined the time-lapse interpretation with PLT data to delineate areas with remaining oil and three infill wells were drilled using the findings from the 4D seismic. The actual oil water contact (OWC) was found 2 m shallower than the one estimated from the 4D seismic. This depth difference is associated in the uncertainty with the time-lapse interpretation. As illustrated by these two examples the time-lapse seismic has proven to be an excellent reservoir surveillance tool, however recently efforts have been orientated to transform the 4D anomalies directly into pressure and saturation maps. This quantitative approach falls into two categories, the rock-physics-based methods and the engineering-based methods. In the first category, the expressions for estimating pressure or saturation changes are based on a rock physic models calibrated with well log data and core data. On the contrary, the

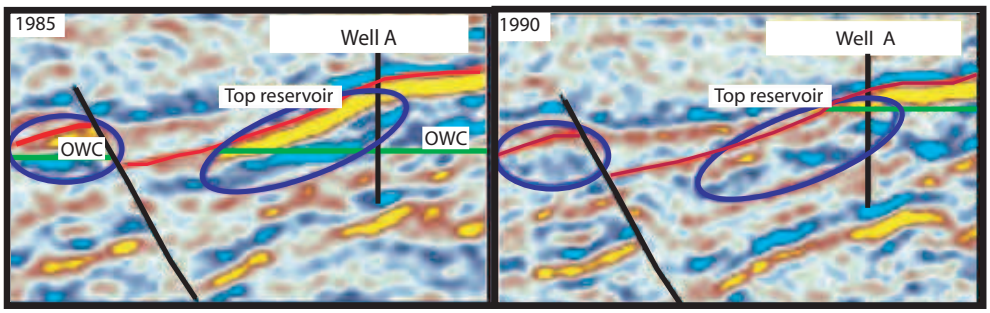

Figure 2.1: Time-lapse seismic in the Gullfaks Field. Amplitude differences between surveys 1985 and 1996 can be used to map the movement of the oil-water contact (OWC). A series of repeated water saturation logs from well A show the increase of water in the area. Therefore using combined well data and time-lapse seismic data the new oil water contact was defined. After Stronen and Digranes (2000).

engineering based approach calibrates the 4D seismic to the dynamic changes, using the engineering data from wells or the reservoir simulator.

2.1.1 Rock physics based methods

Landrø (1999, 2001) used Amplitude Versus Offset analysis (AVO) and formulated the dynamic changes in pressure and saturation as a function of the changes in the AVO intercept and gradient. The expressions for estimating changes in the elastic properties due to reservoir dynamic properties are based on a rock physics model calibrated with well log data and ultrasonic measurements in cores. This method was applied to the Gullfaks Field where attributes cubes of pressure and saturation change were generated (figure 2.2).

Cole et al. (2005) used forward modelling of the fluid and rock physics to estimate pressure and saturation changes in the Schiehallion Field, North Sea. The method consists of building a 3D cube, where each bin contains the possible responses in terms of P-wave and S-wave impedance for a certain combination of reservoir and fluid properties. To perform the inversion, one must select the possible combination of pressure-saturation contained in each bin of the cube. The solution was chosen whose input porosity value is close to the average porosity of the reservoir model. Then, P and S impedance change maps are extracted from the real seismic. For each location in the attribute maps, the corresponding P and S impedance are found in the 3D forward model, the pressure-saturation

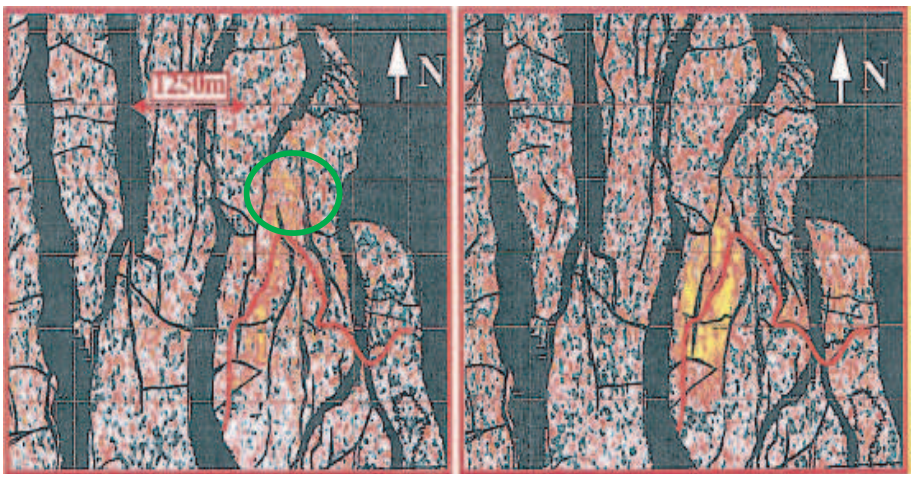

Figure 2.2: Inverted fluid saturation and pore-pressure maps from time-lapse seismic using Landrø's approach. Map view of the fluid saturation (left) and pressure (right) changes estimated from time-lapse seismic, the original oil water contact (OOWC) is displayed on both maps (red line). The distribution of the pressure is controlled by the faults while the saturation anomaly appears to follows the OOWC. The high amplitude values at the north of the OOWC on the fluid saturation map (green circle) are not real and it is due to a leak between the pressure and saturation cubes. After Landrø (2001).

combination that produce these changes are estimated and placed at the appropriate location in the observed seismic signal.

A different approach by Lumley et al. (2005) was carried out with the same data set. Their technique is based on cross-plotting two time-lapse attributes against each other, and then pressure and saturation axes are identified in the cross-plot domain. These are the axes along which pressure-changes-only and saturation-change-only points plot. These data points can be determined by a) cross-plotting production data or simulation data at the wells or b) rock physics forward modelling or (c) identifying pressure and saturation patterns interpreted in the data. Finally, a coordinate transformation is applied to the cross-plot attributes to obtain pressure and saturation estimates. The pressure and gas saturation maps from both techniques are very similar and highlight the major changes occurring in the Schiehallion Field (figure 2.3).

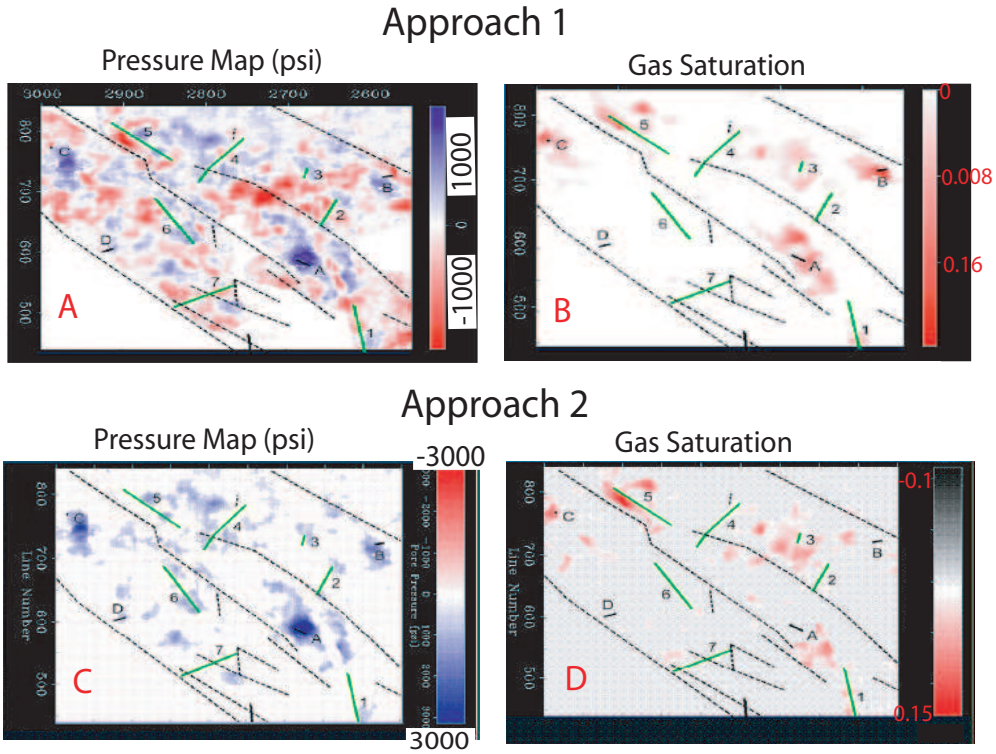

Figure 2.3: Gas saturation and pore-pressure maps from time-lapse seismic in the Schiehallion Field. Map view of the saturation and pressure changes estimated from time-lapse seismic. Figures A and B are results from Cole et al. (2005) (Approach 1). Figures C and D are results from Lumley et al. (2005) (Approach 2). Black lines denote injector wells and green lines denote producer wells. Both methods identify the pressure increase around the injectors, however Lumley's approach estimates higher pressure changes. The two works seem to diagnose the presence of gas around the injector A which is very unlikely.

2.1.2 The engineering approach for pressure and saturation separation (EPASS)

The pressure and saturation techniques EPASS-1 and EPASS-2 determine the pressure and fluid saturation changes from time-lapse seismic data. The techniques are based on an equation that relates the seismic attribute changes to the dynamic reservoir changes. This equation needs to be built based on the expected rock physics for the reservoir; however the advantage is that it does not require an exact formulation of the rock and fluid physics equations.

EPASS-1: MacBeth et al. (2004) gave equation 2.1, where the statistical mean of the 4D signal ($\frac{\Delta A}{\overline{A}_i}$) is equal to the mean relative change of the reservoir pressure ($\frac{\Delta P}{\overline{P}_i}$) plus the mean relative change in the oil saturation ($\frac{\Delta S}{\overline{S}_i}$).

$$\frac{\Delta A}{\overline{A}_i} = C_p \frac{\Delta P}{\overline{P}_i} + C_s \frac{\Delta S}{\overline{S}_i} \tag{2.1}$$

ΔA = 4D amplitude signature (any seismic attribute difference)

$\overline{A}$ = The average amplitude attribute at baseline survey

ΔP = Pore Pressure change

$\overline{P}_i$ = Average initial pressure

ΔS = Oil saturation change

$\overline{S}_i$ = Average initial oil saturation

C_p and C_s = Dimensionless coefficients

This equation is valid for a non-compacting siliciclastic reservoir in which only two phases, oil and water, are present and where there is no reservoir compaction (i.e. porosity and thickness are not varying with time) and the dynamic changes are not unreasonably large. The authors suggested that in order to calculate the C_s and C_p coefficients, one could use the benefits of a baseline survey, 1, and two further repeated surveys, 2 and 3. Hence, the two equations with the time-lapse differences A12 and A13 are:

$$\frac{\Delta A_{12}}{\overline{A}_1} = C_p \frac{\Delta P_{12}}{\overline{P}_1} + C_s \frac{\Delta S_{12}}{\overline{S}_1} \tag{2.2}$$

$$\frac{\Delta A_{13}}{\overline{A}_1} = C_p \frac{\Delta P_{13}}{\overline{P}_1} + C_s \frac{\Delta S_{13}}{\overline{S}_1} \tag{2.3}$$

From which the coefficients C_s and C_p can be estimated. However some well activity (production/injection) is required between each of the surveys. This inversion was tested on a synthetic

example (MacBeth *et al.*, 2004) and was applied to a United Kingdom Continental Shelf (UKCS) Jurassic turbidite reservoir (Floricich *et al.*, 2005). The maps for pressure and oil saturation for this field between 1995 and 2002 at a 50% confidence level (P50) are shown in figure 2.4. The pressure changes map shows an increase of pressure around the injector wells and high values in the north that can be explained by sealing faults building up the pressure. The map of oil saturation changes was validated by the water cutoff in the producers; the wells A, B and C had a higher water cutoff whereas the water production at well D was very low.

EPASS-2: Floricich et al. (2005) proposed a multi attribute approach for estimation of Cs and Cp that requires just one repeat survey and a calibration with pressure and saturation data at the well locations. The equation 2.2 can be defined for any seismic attribute that is considered sensitive to reservoir pressure and saturation. In fact, if two or more set of attributes can be found with different coefficients, such that they are observed to have different response to changes in pore pressure or oil saturation, then inverting for pressure and saturation changes is possible.

The methodology involves firstly selecting the most appropriate attributes. This is accomplished by testing different attribute combinations and then inverting the results at several wells where pressure and saturations are known.

EPASS-2 has been extended for three phase reservoirs and was used to invert for pressure and saturation changes in the Schiehallion Field (figure 2.5). The equation to predict the 4D seismic response to pressure and saturation changes (gas, oil and water) is expressed as follows (Floricich *et al.*, 2006b):

$$\Delta A = a(e^{b*\Delta S_g} - 1) + c * \Delta S_w + d * \Delta P^2 + f * \Delta P \tag{2.4}$$

where a, b, c, d, f are constants to be determined by calibration to the engineering data. The calibration requires the availability of reservoir information from permanent down hole gauge measurements, simulator predictions and well production logs to produce reliable estimation of the pressure and fluid saturation changes.

After the selection of the attribute, a cross-validation technique is used to choose the best attribute combination for the pressure and saturation inversion. In this technique, a well sample is set aside as a testing sample and the remaining wells are used as training samples. The coefficients (a, b, c, d and f) are calculated using the training samples. Then, the pressure and saturation are predicted for the test

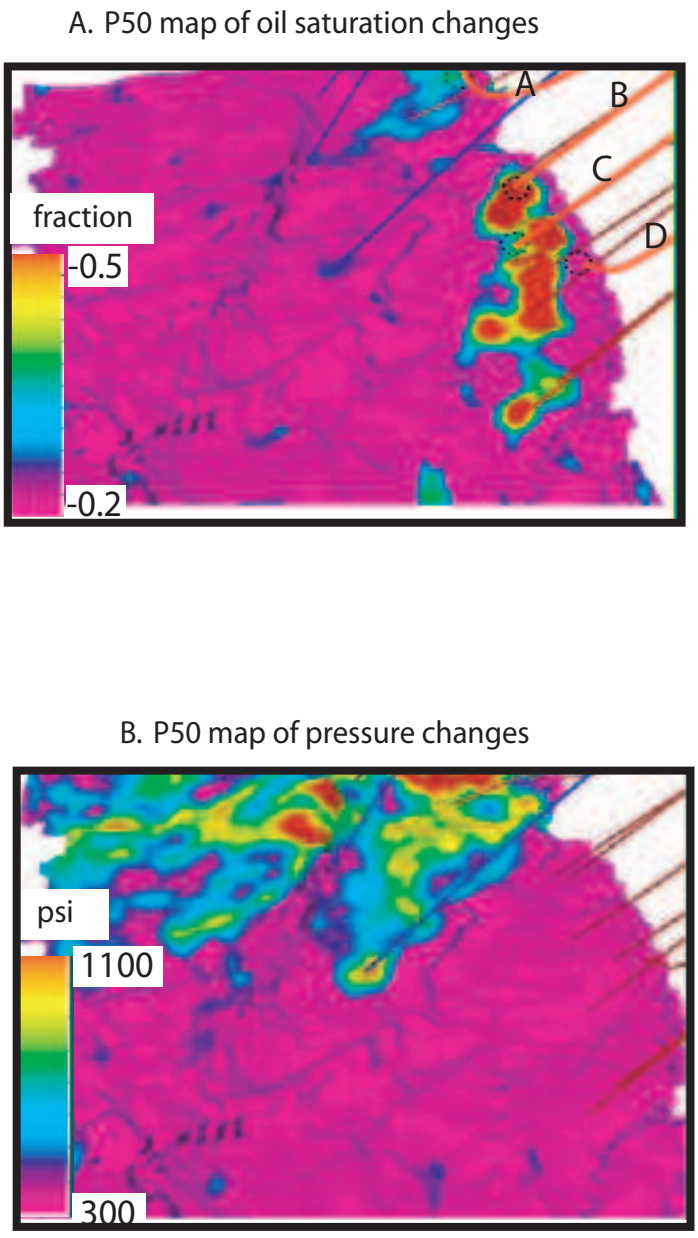

Figure 2.4: EPASS-1 results. A. P50 map of oil saturation. B. P50 map of pressure. Injector wells are in blue and producers in red. The water has displaced the oil at the producers A, B and C but not at well D. After Floricich et al. (2005).

sample and the predicted error is calculated. This process is repeated for all possible combinations. The parameters with the smallest prediction error is chosen. Finally, a Bayesian inversion for pressure and fluid saturation is carried out. Bayes theorem is used to generate probability maps or volumes for the pressure and saturation change predictions.

These engineering approaches have been tested in siliciclastic reservoirs but the compaction phenomena has yet to be addressed.

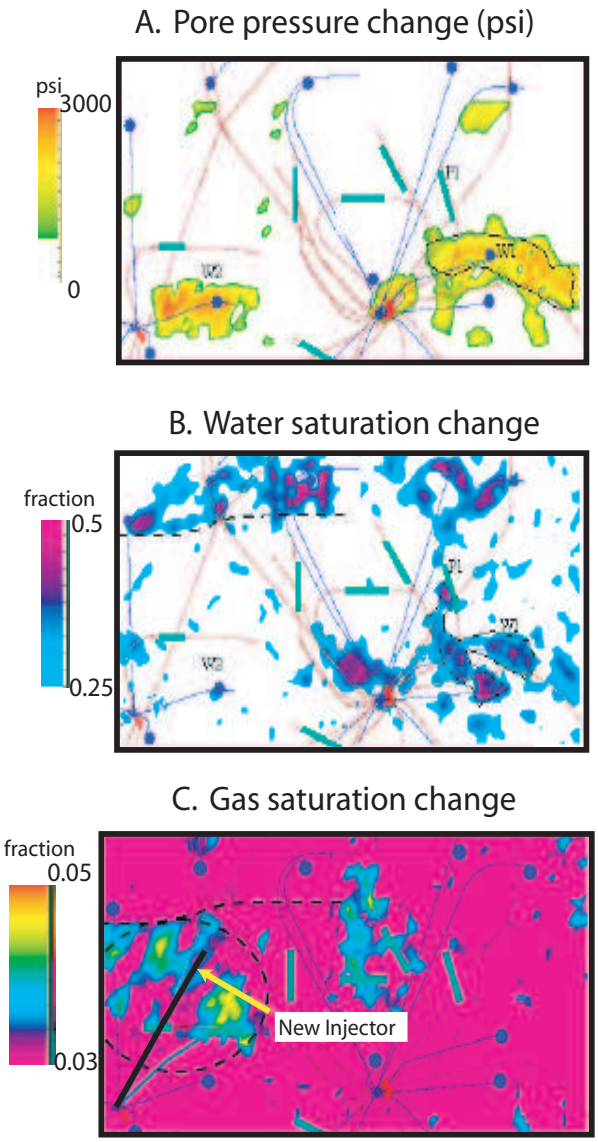

Figure 2.5: Pressure and fluid saturation estimated for the Schiehallion Field, applying EPASS-2 approach A. Reservoir pressure change . B. Water saturation change. C. Gas saturation change. The water saturation maps suggest a possible sealing fault in the northwest. Furthermore, the observed increase gas saturation justifies a new injector in the area. After Floricich et al. (2006a).

2.2 Time-lapse seismic studies in compacting reservoirs

So far the examples discussed have been concentrated on non-compacting reservoirs. Quantifying dynamic properties in compacting reservoirs is a relatively new demand for time-lapse seismic. The reason is that reservoir properties that were commonly considered static, such as porosity and thickness, vary with time in compacting reservoirs, thereby adding more complications to the problem. This obliges us not only to combine the knowledge of geophysics, geology and reservoir simulation but also to include geomechanics in order to understand what occurs in the reservoir.

The majority of studies to date have focused on estimating the overburden strain due to reservoir compaction by using time-shifts. Little effort has been concentrated on inverting for pressure and saturation changes.

The first attempts to try to estimate compaction from 4D seismic were made by Landrø and Stammeijer (2004). They introduced two methods, one based on the measured seismic pre-stack travel time and the other based on the post-stack travel time and amplitude changes.

Landrø and Stammeijer method 1-Using near and far offset travel time-shifts: Assuming that the 4D time-shifts capture the combined effect of velocity and thickness changes within a layer, the normalized time-shifts of a single layer that is undergoing compaction (figure 2.6), can be expressed as follows:

$$\frac{\Delta t}{t} \approx \frac{\Delta z}{z} - \frac{\Delta V_p}{V_p} \tag{2.5}$$

where z is the layer thickness and V_p is the P-wave velocity. Also, Landrø and Stammeijer (2004) approximate the relative changes in layer thickness and layer velocity in terms of near (Δt_N) and far (Δt_F) offset times and the angle of incidence of the far (θ_F) and near (θ_N) offsets

$$\frac{\Delta z}{z} = \frac{(1 + tan^2\theta_F) * \frac{\Delta t_N}{t} - (1 + tan^2\theta_N) * \frac{\Delta t_F}{t}}{(tan^2\theta_F - tan^2\theta_N)} \tag{2.6}$$

$$\frac{\Delta V_p}{V_p} = \frac{\frac{\Delta t_N}{t} - \frac{\Delta t_F}{t}}{(tan^2\theta_F - tan^2\theta_N)} \tag{2.7}$$

To apply equations 2.6 and 2.7 the top and base of the layer need to be interpreted with high confidence on pre-stack gathers. Other assumptions are that production-induced velocity changes in one layer have negligible effect on the overall seismic ray path and the vertical and horizontal P-wave velocities change equally and lateral velocity variations are neglected.

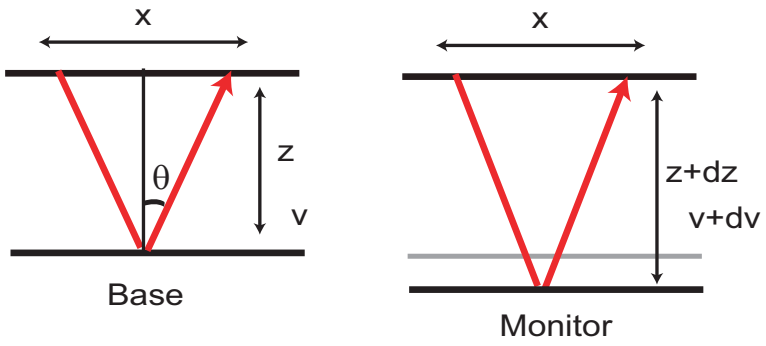

Figure 2.6: Illustration of the principle parameters used in Landrø's method 1 to quantify compaction and velocity changes based on near and far offset travel time-shifts. The offset array before (left) and after (right) compaction. x is offset, z is thickness, θ is incidence angle and v is velocity. After Landrø and Stammeijer (2004).

Landrø and Stammeijer method 2-Using impedance changes and travel times: For this method conventional stacked data can be used, however it requires reservoir property information. The idea is that 4D travel time and acoustic impedance (AI) changes show different sensitivities to velocity (V_p) changes and compaction. For AI changes, the first order approximation is:

$$\frac{\Delta AI}{AI} \approx \frac{\Delta \rho}{\rho} - \frac{\Delta V_p}{V_p} \tag{2.8}$$

By combining this equation with equation 2.5, the relationship between density (ρ) changes and thickness changes can be written as:

$$\frac{\Delta \rho}{\rho} = -a_0 * \frac{\Delta z}{z} - a_1 \tag{2.9}$$

Now, expressions for compaction and velocity changes can be determined:

$$\frac{\Delta z}{z} = \frac{\frac{\Delta t}{t} + \frac{\Delta AI}{AI} + a_1}{1 - a_0} \tag{2.10}$$

$$\frac{\Delta V_p}{V_p} = \frac{a_0 * \frac{\Delta t}{t} + \frac{\Delta AI}{AI} + a_1}{1 - a_0} \tag{2.11}$$

where the coefficients a_0 and a_1 depend on the reservoir parameters porosity (ϕ), fluid (ρ_f) and matrix (ρ_m) densities. For a water flood scenario, these coefficients can be written as follows:

$$a_0 = \frac{\rho_m - \rho_f}{\rho} * (1 - \phi) \tag{2.12}$$

$$a_1 = -(\alpha - 1) * \phi * \frac{\rho_f}{\rho} \tag{2.13}$$

For water replacing oil α is described as a function of brine (ρ_{brn}), oil (ρ_o) and fluid densities.

$$\alpha = -1 + \Delta S_w * \frac{\rho_{brn} - \rho_o}{\rho_f} \tag{2.14}$$

Landrø and Stammeijer (2004) applied both methods to a synthetic example based on the Ekofisk Field. The uncertainties calculated for the example demonstrated that the reliability of these methodologies depends on the repeatability of the time-lapse seismic and the uncertainty in the ray angle estimates.

Guilbot and Smith (2002) presented the idea of 4D constrained tomography to estimate a depth model at the time the monitor survey was acquired. The required input data are time-lapse measurements (time-shifts), sea bed subsidence and a depth model for the baseline survey. The technique accounts for the changes in velocity due to reservoir compaction and overburden stretch. The method is based on three main assumptions: a) uniaxial strain, b) constant depth at the base reservoir and c) a linear velocity-porosity relation for the reservoir and overburden rocks. This methodology was tested at the Ekofisk Field to produce a seismic-derived compaction map at the top reservoir (figure 2.7). An important outcome from this work is that if the overburden velocity changes had been neglected the magnitude of reservoir compaction would have been overestimated by a factor ranging from 1 to 10.

Changes in the elastic properties of the overburden/underburden rocks need to be considered if 4D amplitude attributes or time-shift at the reservoir level are used to estimate pressure and saturation changes. It is known that velocity in the overburden can vary due to pressure drop in chalk reservoirs (Barkved & Kristiansen, 2003). Figure 2.8 compares two time-lapse check-shots acquired during a 10 year period in the Valhall Field. The velocities in the rocks above the reservoirs had reduced by approximately 1 to 2 %. Isolating the changes in the overburden is a very complicated task and time corrections are commonly applied to align the monitor survey to the baseline. However the amplitude changes due to the changes in the elastic properties of the overburden still remain on the time-lapse data.

Many 4D studies aim to understand the relation between reservoir compaction and strain and stress changes in the overburden (Hatchell *et al.*, 2005a; Hatchell & Bourne, 2005; Stables *et al.*, 2007; Hawkins *et al.*, 2007). The geomechanical changes in the overburden and underburden rocks depend on the amount of reservoir compaction, but furthermore on their own mechanical properties. Recent

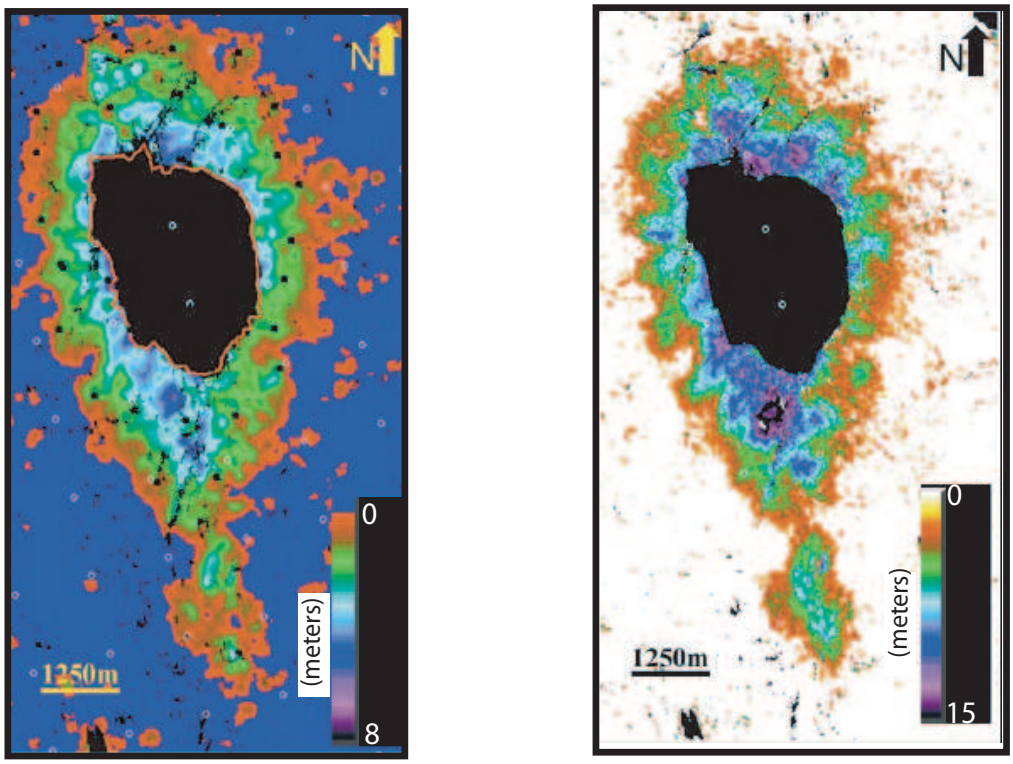

Figure 2.7: Compaction maps at the top of the reservoir inverted from time-lapse seismic for the Ekofisk Field. Left:Compaction map from seismic including the overburden effect. Right: Reservoir compaction map if the overburden velocities are neglected. After Gilbot and Smith (2002).

work focused on using an empirical equation to relate time-shifts to changes in the overall strain and velocity changes. Hatchell et al. (2005a) create a model incorporating geomechanical predictions of the stress and strain field changes due to reservoir compaction to explain the time-shifts that occur on real seismic. Hatchell and Bourne (2005) introduce a formula that relates the fractional changes in velocity (V_p) with the vertical strain (ε_z) and a dimensionless parameter R,

$$\frac{\Delta V_p}{V_p} = -R * \varepsilon_z \tag{2.15}$$

assuming that positive strain is extensional and tend to decrease the velocity. Using equations 2.15 and 2.5, the fractional change in travel time becomes

$$\frac{\Delta t}{t} = (1 + R) * \varepsilon_z \tag{2.16}$$

In compacting reservoirs, the reservoir velocity increases and therefore $R < 0$. In the overburden, the seismic velocities decrease due to relaxation of the rocks and $R > 0$. The R-factor has been

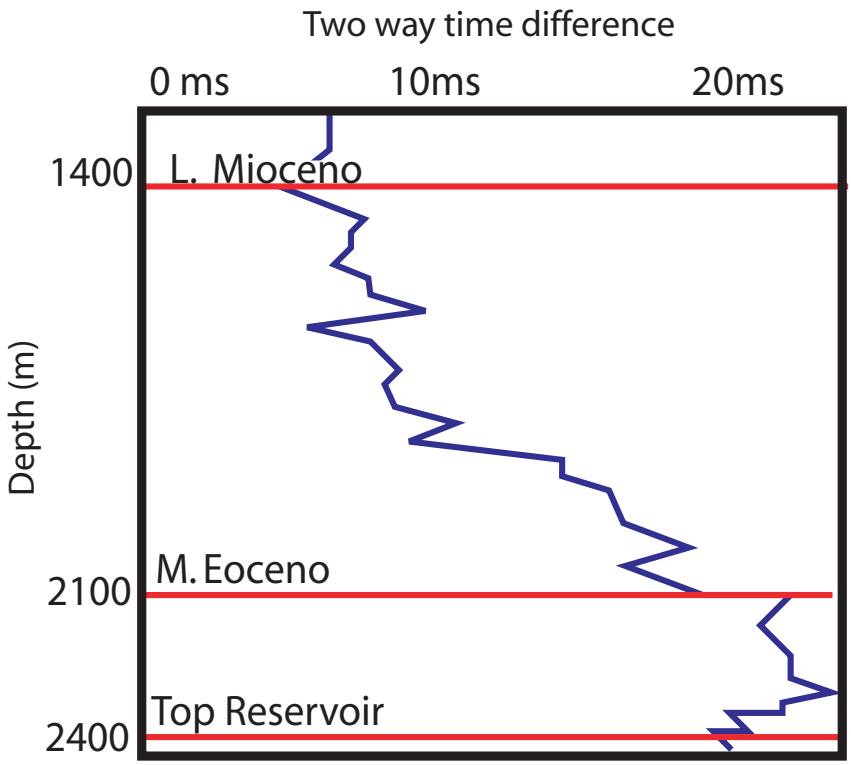

Figure 2.8: Changes in one-way travel time in twin wells. The check-shots were acquired within a time window of 10 years. The logs come from two wells that were separated less than 80m. The velocity overburden decreased between 1 to 2 % during that period. After Barkved and Kristiansen (2003).

estimated for different fields. Stables et al. (2007) predicted an R-factor of between 5 and 10 for the reservoir in the Shearwater Field, while Hawkins et al. (2007) requires on R-factor of 7 in the Elgin and Franklin fields. For the overburden layers in the North Sea, the R-factor has been estimated by several authors, their findings are listed in table 2.1. For the Shearwater Oil Field, the best match between the strain and time-shift cubes was obtained by using different R-factors across the field (Stables *et al.*, 2007). Hatchell and Bourne (2005) suggest, based on a number of cases, that the R-factor is approximately 5 for rocks that undergo elongation strain (unloading) and smaller for rocks undergoing contraction (loading). Furthermore, in the Ekofisk Field, there are inconsistences between the R-factors for the overburden (Janssen *et al.*, 2006). R-factors of between 4 to 6 were measured from the time-lapse time-shifts. Whereas R-factors between 1 to 3 were obtained from rock properties trends. Furthermore, core analysis from the Ekofisk reservoir shows much larger stress sensitivity (R-factors=10-30) that the predictions for the overburden using time-lapse time-shifts and rock properties trends. The influence that the overburden velocity sensitivity to strain has on

estimating pressure from time-lapse seismic is investigated in chapter 6

Field	R-factor	Reference
Ekofisk Field	6-7	Byerley et al. (2006)
Ekofisk Field	4-6 (From rock properties trends)	Janssen et al. (2006)
Ekofisk Field	1-3 (From time-lapse time-shifts)	Janssen et al. (2006)
Valhall Field	4-8	Hatchell and Bourne,
Valhall Field	5	Hatchell et al. (2005)
Shearwater Field	6-10	Stables et al. (2007)
Elgin and Franklin fields	4-6	Hawkins et al. (2007)

Table 2.1: Reported R-factor for North Sea fields

2.2.1 Time-lapse studies focused on monitoring dynamic reservoir properties in compacting reservoirs

There are few studies regarding estimation of the dynamic reservoir properties from time-lapse seismic in compacting reservoirs. Hodgson et al. (2007) extended the concept of time strain to invert for reservoir pressure changes. The time strain refers to the fractional change in travel time and it is estimated by taking the first derivative of the time-shift volume (Rickett *et al.*, 2007). The approach assumes the time strain observed at certain point in the overburden is related to a Green's function multiplied by the pore pressure changes at the reservoir. The Green's function is the solution for the nucleus of strain approach given by Geertsma (1973).

The technique was applied to the Genesis Field and it showed encouraging results (figure 2.9). However, simplifying the mechanical response of the overburden by assuming that the geomechanical properties of the cap rock are the same as the reservoir ones and considering that the overburden strain only depends on the pressure depletion can magnify the error in the inversion. For instance, as will be further discussed in chapter 4, there have been some indications that the overburden shale in the Valhall Field can be a contributor to the sea floor subsidence due to the large pressure differential across the cap rock/reservoir interface (Kristiansen, 1998).

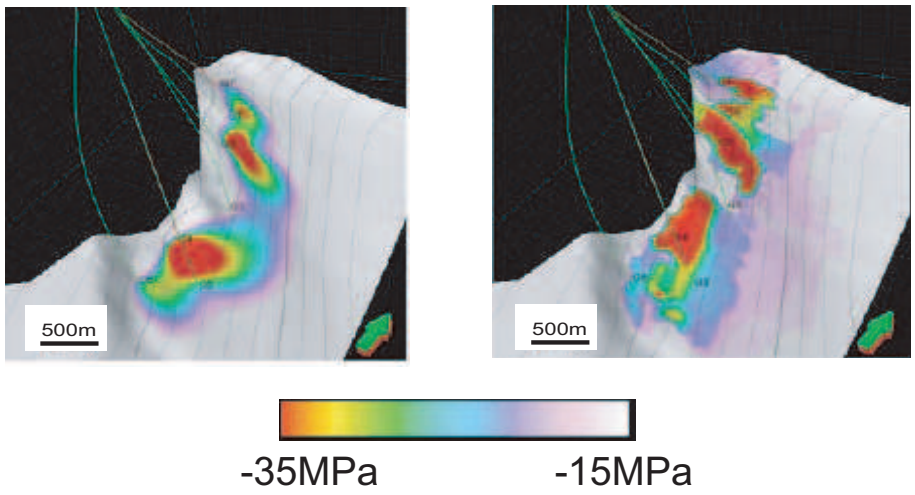

Figure 2.9: Pressure inverted from 4D seismic using overburden strain (left) compared with the reservoir simulator predictions (right) in the Genesis Field. After Hodgson et al. (2007).

2.3 Geomechanical modelling of compacting reservoirs

An introduction to different approaches for coupled geomechanics and fluid flow simulation are discussed in this section. This is followed by a detailed description of the iterative coupled algorithm used in this thesis.

In the last two decades, there has been a growing interest for the importance of geomechanics in reservoir simulation, especially in cases of heavy oil reservoirs, water injection in fractured and heterogenous reservoirs and compacting fields. Figure 2.10 illustrates the interconnection between rock deformation and fluid flow in a deformable reservoir. Fluid pressure carries part of the load of the external rocks transmitted to the reservoir. A decrease in the fluid pressure changes the effective stress following Terzaghi's principle (section 1.2) and induces the rock deformation and re-distribution of the in-situ stress (Gutierrez *et al.*, 2001). In general, two types of fluid flow and rock deformation coupling exist: a) stress-permeability coupling is used when the change in pore structure due to rock deformation affect the permeability and fluid flow, and b) deformation-fluid pressure coupling (volume coupling) is used when the rock deformation affects fluid pressure and vice versa. The volumetric coupling is important in the simulation of problems where the effects of shear or plastic deformation cause large changes in porosity; this is the case for soft compacting reservoirs such as North Sea Chalks (Tran *et al.*, 2004).

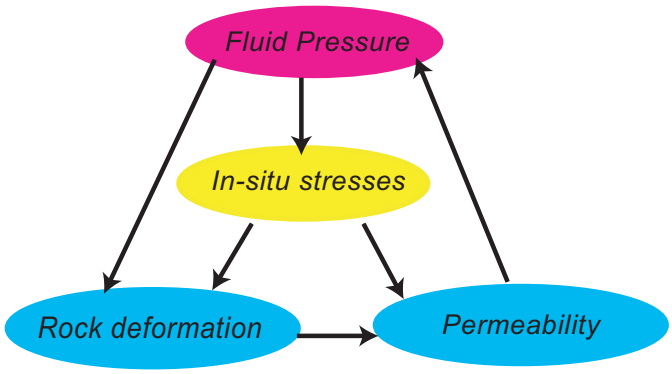

Figure 2.10: Diagram of the interconnection between rock deformation and fluid flow in a deformable reservoir. After Gutierrez et al. (2001).

2.3.1 Coupling types used in geomechanical models

When fluid flow and geomechanics are coupled, the equations that are required to be solved are Biot's equations for deformation in a 3D porous media and Darcy's fluid flow equations (Appendix B). The methods for resolving these functions fall into the four categories as outlined below (Tran *et al.*, 2004).

Fully coupled

In this type of coupling, fluid-flow and Biot's equations are solved simultaneously to calculate the unknown variables, pressure, temperature and displacements. This method is sometimes recognized as implicit coupling because the whole system is captured on a single grid and solved simultaneously. This method needs to be run on parallel computers and a full-field model can take several weeks to run. The Finite Element Method (FEM) is employed to solve the equations in the fully coupled case, however more development is needed to bring their flow-model capabilities to a comparable level with the commercial flow (finite difference) simulators (Settari & Walters, 1999). The finite element implementation of the fully coupled equations are presented by Gutierrez et al. (2001) together with the results of applying this approach to an idealized North Sea reservoir. The main outcome from their study is that using conventional reservoir simulation in compacting reservoirs, where the only mechanical parameter is rock compressibility, can lead to the incorrect prediction of pressure depletion distribution because standard simulators neglect or simplify the effect rock deformation has

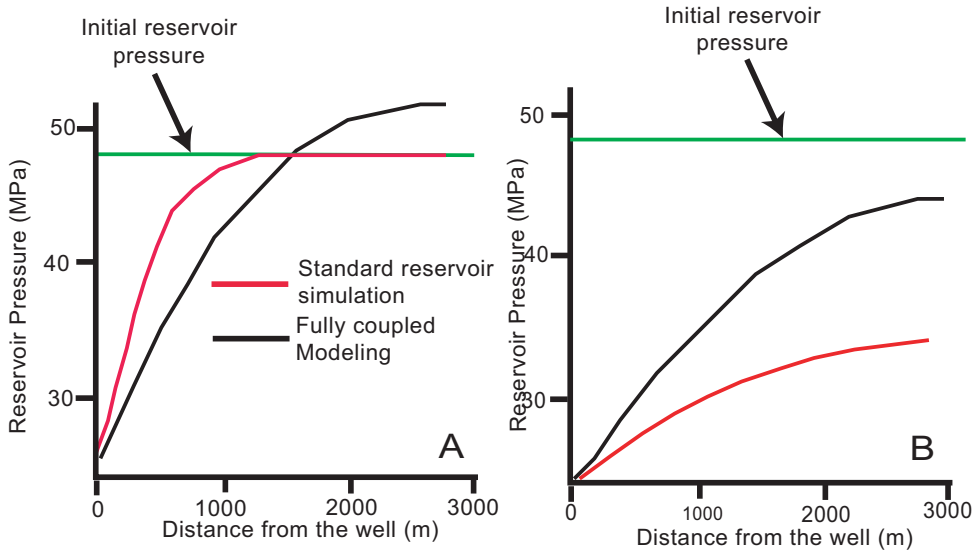

Figure 2.11: Comparison of reservoir pressure from fully coupled and standard reservoir simulation for two scenarios. A. Scenario A: soft reservoir (Young's modulus=0.05 GPa). B. Scenario B: Stiff reservoir (Young's modulus=0.85 GPa). A coupled simulation predicts higher pressures (black lines) than the ones from a standard reservoir simulator (red lines). Furthermore, varying the stiffness of the reservoir rock and maintaining the other input data (including production rate) constant gives different pressure outputs. The pressure drop is confined around the well when the reservoir is weak (steep gradient on the left figure). For a strong reservoir, the pressure changes are more gradual (a gentle slope on the right figure). After Gutierrez et al. (2001).

on the reservoir productivity.

Figures 2.11A and 2.11B show the final results for two scenarios from the Gutierrez et al. (2001) study. Scenario A assumes a weak reservoir and scenario B assumes a hard reservoir. For both scenarios coupled solution and standard simulations were used (black and red profiles in figures 2.11A and 2.11B). According to this study, the coupled simulation predicts higher pressures than the one from a standard reservoir simulator. Furthermore, varying the stiffness of the reservoir rock and maintaining the other input data constant (including production rate) gives different pressure outputs, demonstrating that the rock stiffness influences the reservoir pressure. Also when the coupled solution is used, pressures higher than the initial reservoir pressure are observed far from the well (black profile in figure 2.11A). For scenario B, the pressure changes are more gradual (a gentle slope in figure 2.11B).

Explicit coupling or one-way coupling method

This coupling provides the weakest link between reservoir flow and geomechanical deformation. The information is transferred one way from the simulator to the geomechanics module. This means changes in the pore pressure field induce changes in stresses and strain, but changes in the stress and strain fields do not affect the pore pressure. Normally, this approach is taken to carry out full-field subsidence studies, where forecast and history matched pressure changes at different times are extracted from the reservoir simulator and they represent the loading of the reservoir rock causing compaction/subsidence. The most common rock deformation softwares are ISAMGEO, ABAQUS, VISAGE and MARK II.

Pseudo-coupling

In this coupling a conventional reservoir simulator itself can calculate some of the geomechanics responses such as compaction and horizontal stress changes through simple relationships between porosity and stress. The empirical model can be entered into the simulator as tables of porosity/permeability versus pressure. In the Eclipse software (commercial reservoir simulator), this option can be implemented by using the module GEOMECH.

Iterative Coupling

GEOSIM, the software package used during this research, is based on this method. The iterative coupling method divides the coupled system of equations into two subsystems: the stress and flow equations. It solves the coupled system by exchanging shared variables values between the reservoir simulator and the geomechanics model. The fluid simulator passes pressure and temperature data to the geomechanics module, while the geomechanics module sends a porosity function to the fluid simulator. The transfer of information between a reservoir simulator and a geomechanics module is normally performed through a coupling module (driver) that also monitors the convergence of the coupling iteration. (Tran *et al.*, 2004; Chin *et al.*, 2002). Also, a different numerical method can be implemented for the reservoir simulator and the geomechanics module when iterative coupling is used. For instance, the reservoir simulator can use finite difference while the geomechanics module uses finite element. The main difference between pseudo and iterative coupling is that the pseudo coupling

transfers only information from the reservoir module to the geomechanical model, while the iterative passes information back and forward from one module to the other one. The iterative coupling has some advantages over the fully coupled method. First, fully coupled models for a full-field model are normally more computationally expensive than iterative coupled models. Second, the iterative coupling method can be implemented with existing reservoir simulators and existing geomechanics modules by introducing a coupling module. On the contrary, it takes a lot of effort to develop and implement a fully coupled method, since it requires to bring all the reservoir and geomechanical data into a single software to run the simulations.

2.3.2 Description of GEOSIM

GEOSIM software is used for modelling coupled geomechanical and reservoir flow problems using the iterative approach. GEOSIM comprises TERASIM, FEM3D and GEOINT. TERASIM is a black oil reservoir simulator which models the flow of oil, gas and water. The term "black oil" means that the PVT properties for both oil and gas are functions only of pressure and not of composition. FEM3D is the geomechanical module. The stress model is set up to solve the displacement, stresses and strains with the pressure and temperature fields computed externally. FEM3D is a general three-dimensional finite element program that is designed for the analysis of coupled poro- and thermo-elasticity and GEOINT is the driver or the "bridge" that links TERASIM and FEM3D. Any data manipulation which is required to ensure correct input data for any of the two modules is done in GEOINT.

2.3.3 Derivation of the porosity equation

The information that FEM3D sends to TERASIM is a porosity function. In this section, I describe the formulation of the porosity equation developed by Settari and Mourits (1998). The aim is to derive mathematical expressions that represent the pore volume (PV) changes in the reservoir model through the solution of the stress model. In standard reservoir engineering, the new porosity ϕ^* after depletion has occurred is represented by a simple function of pressure if isothermal conditions are assumed.

$$\phi^* - \phi_i = \phi_i * [c_R(P_f - P_i)] \tag{2.17}$$

where ϕ_i and P_i are the initial porosity and pressure, c_R is referred to as the rock compressibility and is assumed to be constant and P_f represents the final pressure.

In GEOSIM, because a standard reservoir simulator (TERASIM) is going to be used for coupling with a geomechanics module (FEM3D), the bulk volume and the pore volume have to obey two conditions:

- Bulk volumes of the reservoir blocks are constant throughout the simulation, i.e. the reservoir grids do not deform.
- Reservoir pore volume must be equal to the true pore volumes computed by the geomechanics module.

To satisfy the second condition, the reservoir porosity (ϕ^*) and the true porosity (ϕ) are defined according to the following expressions:

$$\phi^* = \frac{Vol_p}{Vol_b^0} \tag{2.18}$$

$$\phi = \frac{Vol_p}{Vol_b} \tag{2.19}$$

where Vol_p is the current pore volume, Vol_b is the current bulk volume and Vol_b^0 is the initial bulk volume. When a porous material is filled with fluid, the linear elastic equations 1.12, 1.13 and 1.14 (section 1.1) become:

$$E * \varepsilon_x = \sigma_x - \nu * (\sigma_y + \sigma_z) - \Delta P * \frac{E}{3S} \tag{2.20}$$

$$E * \varepsilon_y = \sigma_y - \nu * (\sigma_x + \sigma_z) - \Delta P * \frac{E}{3S} \tag{2.21}$$

$$E * \varepsilon_z = \sigma_z - \nu * (\sigma_x + \sigma_y) - \Delta P * \frac{E}{3S} \tag{2.22}$$

Equations 2.20, 2.21, 2.22 are known as the poroelasticity equations for strain. ν and E are the Poisson's ratio and the Young's modulus of the reservoir respectively. ΔP is the pore pressure depletion, ε is the strain. In terms of stress these equations become,

$$\sigma_x = \lambda * \varepsilon_v + 2\mu * \varepsilon_x + \alpha * \Delta P \tag{2.23}$$

$$\sigma_y = \lambda * \varepsilon_v + 2\mu * \varepsilon_y + \alpha * \Delta P \tag{2.24}$$

$$\sigma_z = \lambda * \varepsilon_v + 2\mu * \varepsilon_z + \alpha * \Delta P \tag{2.25}$$

where σ_x, σ_y and σ_z are the normal stresses in x, y and z directions, λ and μ are the Lamè constant and shear modulus respectively and α is Biot's constant of poroelasticity.

Adding equations 2.20, 2.21 and 2.22, the volumetric strain (ε_v) is equal to:

$$\varepsilon_v = \frac{3 * (1 - 2 * \nu)}{E} * (\overline{\sigma} - \overline{\sigma_0}) - \frac{1}{S} * (P - P_0) \tag{2.26}$$

where $\overline{\sigma}$ is the mean normal stress defined as

$$\overline{\sigma} = \frac{\sigma_x + \sigma_y + \sigma_z}{3} \tag{2.27}$$

and, S is given by:

$$S = \frac{1}{C_b - C_s} \tag{2.28}$$

where C_s and C_b are known as the grain and bulk compressibilities respectively. The latter one can be expressed as a function of E and ν,

$$C_b = \frac{3 * (1 - 2 * \nu)}{E} \tag{2.29}$$

Using the definition of volumetric strain ($\varepsilon_v = -\delta V_b / V_b$) and equation 2.26, the bulk volume can be expressed as follows:

$$V_b = V_b^0 * (1 - \varepsilon_v) = V_b^0 * [1 - C_b * (\overline{\sigma}_f - \overline{\sigma_0}) + (C_b - C_s) * (P - P_0)] \tag{2.30}$$

Equation 2.30 is the basis for estimating pore volume changes in all stress models.

The next step is to estimate the coefficient c_R used in equation 2.17. The porosity ϕ^* can be written as

$$\phi^* = \frac{V_p}{V_b} * \frac{V_b}{V_b^0} = \phi * (1 - \varepsilon_v) \tag{2.31}$$

According to Biot's poroelasticity theory (Geertsma, 1957), the true porosity ϕ is expressed in an incremental form by:

$$\phi = \phi_0 + [C_b(1 - \phi_0) - C_s] * (\Delta P - \Delta\overline{\sigma}) \tag{2.32}$$

The initial porosity is ϕ_0 in equation 2.32. According to equations 2.31 and 2.32, the reservoir and true porosities (ϕ^* and ϕ) are a function of the volumetric strain. The volumetric strain is a function of stress and pressure as shown by equation 2.26. Therefore, the reservoir porosity can be written in a general form,

$$\phi^* = \phi(\Delta P, \Delta\overline{\sigma}) * [1 - \varepsilon_v(\Delta P, \Delta\overline{\sigma})] \tag{2.33}$$

This indicates that equation 2.17, which is the equation used to estimate porosity changes in a standard reservoir simulator, does not capture all the effects that are causing the porosity changes. In other words, equation 2.17 does not account for the changes in the mean normal stress ($\Delta\overline{\sigma}$). Normally, the mean normal stress is assumed to be constant in the reservoir using a conventional reservoir simulator. However, there are many cases where equation 2.17 can not be used to accurately quantify the pore volume change.

Settari and Mourits (1998) derived another formula for estimating reservoir porosity:

$$\phi^* - \phi_0 = \phi_0 * [C_p(P - P_0)] + \Delta\phi_I \tag{2.34}$$

The coefficients in equation 2.34 can be estimated by comparing this expression with equation 2.31 and replacing ε_v using equation 2.26.

$$C_p = \frac{C_b - (1+\phi) * C_s}{\phi_0} \tag{2.35}$$

$$\Delta\phi_I = -[C_b - C_s] * \Delta\overline{\sigma} \tag{2.36}$$

One can compare the results of uncoupled and coupled simulations by correlating the rock compressibility (C_R) and the coefficients C_P and $\Delta\phi_I$. Consider free deformation in all directions, such that no incremental average normal stress $\Delta\overline{\sigma} = 0$ is generated as a result of pressure changes. In this case the rock compressibility calculated using equation 2.34 is equal to C_p and it is denoted by C_R^I.

$$C_R^I = C_p = \frac{[C_b - (1+\phi) * C_s]}{\phi_0} \tag{2.37}$$

Now, assuming a second case where the system is constrained laterally and free to move vertical (isotropic uniaxial strain conditions), the mean stress changes can be denoted by

$$\Delta\overline{\sigma} = E * \frac{2(C_b - C_s)}{3 * (1-\nu)} * \Delta P \tag{2.38}$$

and a second rock compressibility (C_R^{II}) can be written as

$$C_R^{II} = \frac{(C_b - (1+\phi)C_s)}{\phi_0} - \frac{2 * (C_b - C_s)^2 * (1 - 2 * \nu)}{3 * C_b * \phi_0 * (1-\nu)} = C_R^I - \Delta C \tag{2.39}$$

Therefore, the compressibility C_R^{II} is smaller by ΔC compared to the unconfined case. This discrepancy shows that the rock compressibility used in reservoir engineering can be inaccurate because this

value depends on the degree of the containment. To compare results from uncoupled and coupled simulations, the appropriate C_R for standard reservoir simulations is the one that the best approximates the boundary conditions imposed on the stress solution in the coupled case.

2.3.4 Iteration process for coupled modelling

FEM3D runs simultaneously with TERASIM and TERASIM is the main driving program. The fluid flow solution from TERASIM and the stress solution from FEM3D are iterated during each time increment. The iteration is known as the "geomechanical iteration". Each iteration is computationally equivalent to solving a time step of the reservoir model and a load step of the stress model.

Figure 2.12 illustrates the iterative coupling process. At time=0, both TERASIM and FEM3D are set at the initial conditions. Based on the initial fluid pressure distribution, FEM3D establishes the initial stress state of the model. At this stage, the initialization phase is completed and the reservoir model is ready to start the first time-step calculation. In the solution phase, within any given time increment (i.e. $\Delta t = t_n - t_{n+1}$, n=1, 2, 3, etc), TERASIM and FEM3D solve their system of equations separately and each of them provides the needed variables through a coupled iteration loop with an iteration number counter g (g=1, 2, 3, etc) (i.e. TERASIM passes pressure and FEM3D sends the coefficients (C_p and $\Delta\phi_I$) from equations 2.35 and 2.36). For the first couple iteration (g=1) of the geomechanics model, the pressure is treated as an external loads and estimates the displacements. Then, strains are determined through the strain/displacement relationships and stress is estimated using the strain/stress constitutive relationships. Once the geomechanics solution is achieved, the true porosity ϕ is calculated using equation 2.32. Subsequently the a new set of coefficients ${C_p}^{(g+1)}$ and ${\Delta\phi_I}^{(g+1)}$ are estimating. A new porosity function is computed by using these coefficients in equation 2.34. Then, the reservoir simulator estimates a new pressure based on the new porosity. This process is repeated until the convergence is reached (i.e. the norm of pressure changes between two consecutive coupling iterations is below a given tolerance value). The tolerance value for convergence is defined by the user. After the solution is updated, a new time increment starts and the couple iteration counter is reset to 1.

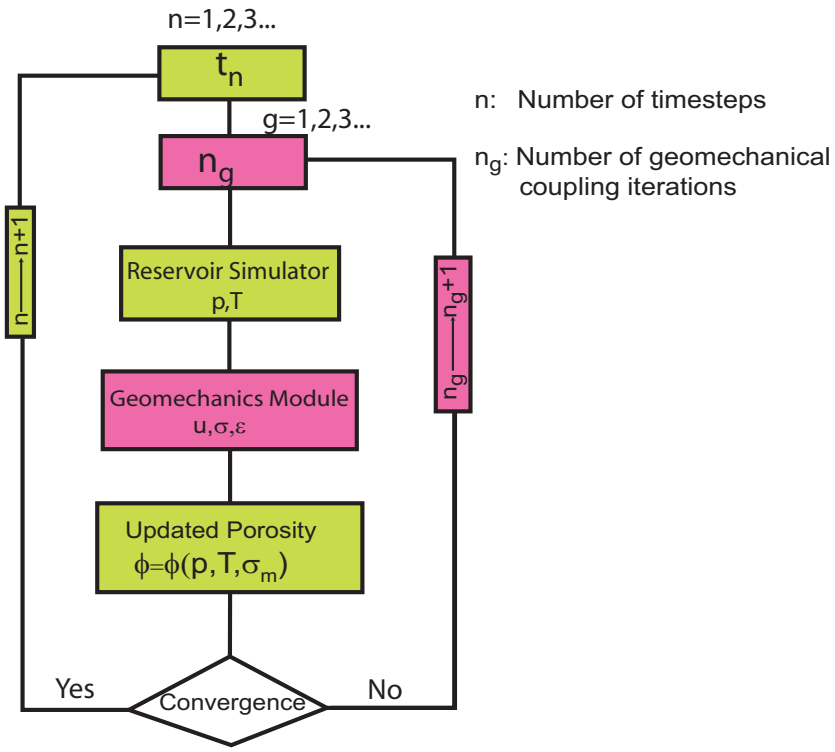

Figure 2.12: Flow chart for iterative coupling. The codes names used during the present study are highlighted in blue. After Tran et al. (2004).

2.4 Methodology used to model the time-lapse seismic response of compacting reservoirs

Section 1.5 has emphasized that in order to fully understand time-lapse response in compacting reservoirs, it is required to integrate the rock deformation with fluid flow modelling. Even though an analytical solution (Geerstma's method) can give a reasonable description of the compaction problem, numerical solutions provide a hint of how the stress and strain re-distribute in the whole earth due to the reservoir deformation, and therefore how the compaction will influence the time-lapse seismic.

Some authors have employed the results from geomechanics models to estimate the strain and stress changes and then to calculate the seismic velocities with the aim of obtaining a more realistic seismic response in compacting reservoirs. For example, Minkoff et al. (2004) described the results of a loosely coupled simulation. They present two numerical examples based on data from the Belridge Field. The materials are considered linear elastic and the model has three fluid phases. Gassmann's

equations are used to estimate changes in acoustic properties. The porosity values used during the fluid and rock physics calculation vary with time. Their synthetic examples are focused on the velocity variations at the reservoir level. Reflectivity changes or time-shifts due to compaction are not discussed in the paper. Vidal et al. (2002) used a single-phase gas flow, one-way coupled with a geomechanics simulator to study the Cere-la-Ronde underground gas storage reservoir in the Paris basin. Their rock physics modelling is based on Hertz-Mindlin theory, which assumes that the velocity varies with the effective stress. A 1-D convolutional synthetic model is used to obtain the synthetic traces for different time-steps. The results have been interpreted in term of P wave velocities and time-shift attributes at the reservoir layers.

The methodology that I use to model the time-lapse response in this study is summarized in figure 2.13. The first step involves a run with an iterative coupled geomechanics and fluid flow simulation to predict the strain/stress response of the rocks due to a certain pressure depletion in the reservoir. The outputs from the simulator are divided into two types: reservoir and geomechanical data. The first set of data comprises properties such as fluid pressure, fluid saturations, temperature, oil formation volume factor (Bo), oil and water viscosity and oil gas ratio (Rs). The geomechanical data include normal stresses, effective stress, displacements, vertical strain and porosity changes.

The second step is to estimate seismic acoustic properties for pre-production and produced cases. The resultant pressures, saturations and reservoir model properties are used to calculate the acoustic impedances by conventional fluid substitution using the combination of the Gassmann equation (Gassmann, 1951) and fluid property correlations proposed by Batzle and Wang (1992). However after the rock deformation occurs, the geomechanical results need to be taken into account if the synthetic seismic are to be used as guidelines for interpreting the observed data. The effective stress and the porosity change outputs are used to estimate the rock-frame elastic moduli (bulk and shear), which are needed for the reservoir elastic model. Also, the vertical strain is used to estimate the overburden velocities using equation 2.15.

In the third step, the synthetic seismograms are generated using convolutional modelling. For this step the data needed are the acoustic impedance calculated earlier and the deformed grid from the geomechanical model.

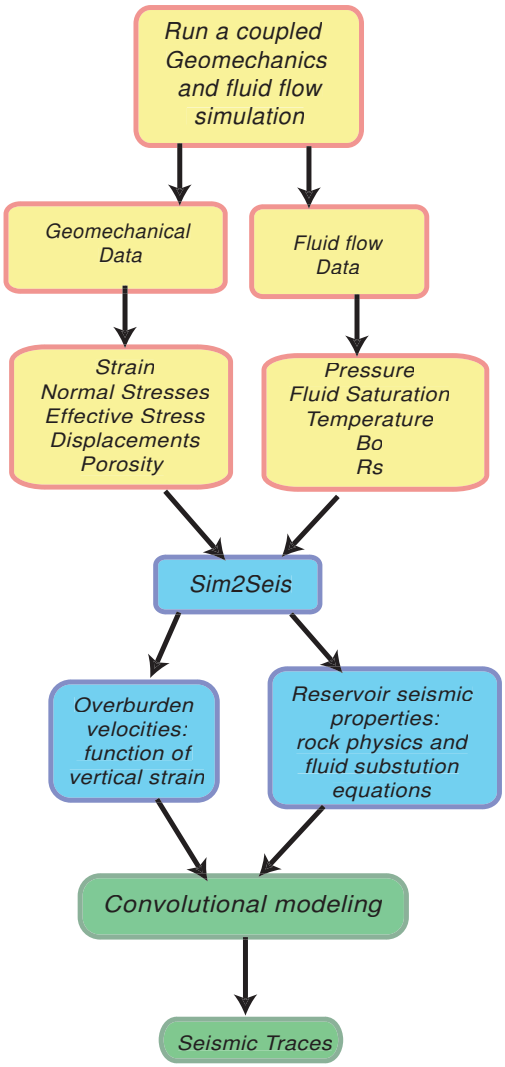

Figure 2.13: Methodology to estimate the time-lapse response due to changes in pressure, saturation and deformation in compacting reservoirs. The 4D synthetic seismic is generated through petro-elastic transformation of the simulation outputs followed by a seismic modelling.

2.5 Summary

This chapter has presented an overview of time-lapse seismic studies in non- and compacting reservoirs. In general, there has been an increasing number of published examples that transform the 4D anomalies directly into pressure and saturation maps. In order to do this, some authors use rock physics models while others use more reservoir engineering data on their analysis. Landrø (1999, 2001) and Cole et al. (2005) used rock physics and forward modelling to estimate pressure and saturation changes in the Gullfaks and Schiehallion fields. The engineering based approaches comprises EPASS-1 and EPASS-2. MacBeth et al. (2004) proposed an equation (eq. 2.1), where the 4D signal is equal to the weighted combination of the oil saturation and the relative change in the reservoir pressure (EPASS-1). Floricich et al. (2005) developed a multi-attribute approach for the estimation of the coefficients in this relation that requires just one repeat survey and a calibration with pressure and saturation data at the well locations (EPASS-2). The engineering approach has been tested in siliciclastic reservoir and extended to systems with three fluid phases.

Quantifying dynamic properties in a compacting reservoir is a relatively new demand for time-lapse seismic. Analyzing the 4D signal in compacting reservoirs requires not only the combined knowledge of geophysics, geology and reservoir simulation but includes geomechanics in order to understand what occurs in the reservoir. At present, the time-lapse studies in compacting reservoirs have been focused on a) determining the time-shift in the overburden and how this might be used to provide information about dynamic reservoir properties (Landrø & Stammeijer, 2004) b) estimate the reservoir compaction (Guilbot & Smith, 2002) and c) use an empirical equation to relate time-shifts to changes in the overall strain and velocity changes (Hatchell *et al.*, 2005a). However, few efforts have been concentrated on inverting for pressure and saturation changes using directly 4D amplitude attributes.

In section 2.3.2, I explained the iterative coupled geomechanics and fluid flow simulation method. This type of coupling will be used to predict the rock deformation due to hydrocarbon production in the synthetic example presented in chapter 3. In compacting reservoirs, the rock compaction occurs when the porosity decreases due to reservoir pore pressure depletion. The importance of coupling rock mechanics and fluid flow is shown by equation 2.32. The porosity changes as a function of stress depending on the deformation of the reservoir caused by changes in pressure. In the case of no coupling between a reservoir simulator and a geomechanics module, the mean total stress is considered to be constant in the reservoir; the porosity, thus is a function of pressure as indicated by

equation 2.17.

Finally, section 2.4 introduced the methodology that I used to create the synthetic seismograms discussed in the thesis. The 4D synthetic seismic is generated through petro-elastic transformation of the simulation output followed by seismic modelling. The methodology is summarized as follows:

- Step 1: Run a iterative coupled geomechanics and fluid flow simulation in order to predict the strain/stress response of the rocks due to particular pressure depletion at the reservoir. The outputs from the simulator are divided into two types: reservoir and geomechanical data. The reservoir data comprise properties such as pressure, fluid saturations, temperature, Bo and Rs. The geomechanical data include normal stresses, effective stress, displacements, vertical strain and porosity changes.

- Step 2: Estimate seismic elastic properties for pre-production and produced cases. The resultant pressures, saturations and reservoir model properties are used to calculate the acoustic impedances by a conventional fluid substitution using the combination of Gassmann equation and fluid property correlations proposed by Batzle and Wang (1991) . However after the rock deformation occurs, the geomechanical results need to be taken into account if the synthetic seismic are to be used as guidelines for interpreting the observed data. The effective stress and the porosity changes output are used to estimate the rock-frame elastic moduli (bulk and shear). These parameters are needed for the reservoir's petro-elastic model. Also, the vertical strain is used to estimate the overburden velocities, using equation 2.15.

- Step 3: Generate the synthetic seismograms using the convolutional modelling. For this step the data needed are the P wave impedance calculated earlier and the deformed grid from the geomechanical model (except for the pre-production case).

Chapter 3

Analysis of simulated data

In this chapter I present the results of time-lapse analysis carried out on a numerically simulated data set. The reservoir model is based on the southeast part of the Valhall Field (chapter 4). This analysis allows me to understand and validate several relationships between the geomechanics parameters, dynamic reservoir properties and time-lapse seismic attributes.

As discussed in chapter 2, rock deformation and fluid simulation need to be linked to accurately estimate the reservoir and the overburden/underburden changes due to pressure depletion. Furthermore, modelling the time-lapse seismic response from geomechanically active reservoirs requires stress and strain information from both the reservoir and overburden; however these data are not always available in practice. The data here are simulated with GEOSIM which uses the iterative coupling approach explained in section 2.3. GEOSIM not only provides the input data for creating the synthetic seismic but helps to understand the rock compaction in order to improve the understanding of the time-lapse signal when this phenomenon is present.

Section 3.1 describes the model and parameters used for the simulation. Section 3.2 explains the work flow from taking the outputs from the simulator to convert them into synthetic seismograms. Subsequently section 3.4 discusses the relationships between time-lapse seismic attributes and the dynamic properties in the reservoir (pressure, porosity and effective stress). This analysis will lead to an equation which can be used to generate pressure maps from time-lapse amplitude attributes. Finally, in section 3.7 the equation is tested and the results are compared with the pressure output from the simulator.

3.1 Model Description

An iterative coupling simulation requires two types of information. Firstly, the simulation requires geomechanical data, which comprise the parameters needed to calculate the stress and strain states. The second type of information required is the reservoir data which is used to solve the fluid flow equations such as porosity, fluid properties, matrix permeability.

3.1.1 Geomechanical data

Full grid geometry

The finite element stress grid represents the full earth model (overburden, side-burden, reservoir and underburden) and it is considerably larger than the reservoir grid. The present model has 60 grid cells in the x and y directions and 14 layers in z dimension (60x60x14). The total number of grid cells is 50400. The x and y dimensions of each grid block decrease towards the reservoir area. The reservoir grid is a subset of the finite element stress grid and its size is 50x50x1. The horizontal dimensions of each reservoir grid cell is 50x50 m. At the initial condition the grid represents a horizontal layered model and after the wells start to produce the grid deforms (figure 3.1)

Geomechanics parameters

The constitutive equations determine which parameters are required to model the geomechanical response of the rock material. The overburden and underburden consist of 10 materials, which are constrained to follow linear elastic theory. The input parameters for each material are listed in table 3.1.

The geomechanical parameters for the overburden are based on the results of several studies carried out in the Valhall and Ekofisk fields (Kristiansen, 1998; Nagel, 1998b; Herwanger & Horne, 2005). The elastic properties are derived mainly from log velocities, because there is very little core data for the overburden. Based on the available geological information, it was decided that the most optimal way to represent the overburden in the Valhall Field is by dividing it into 9 layers. From top to base, the first four layers correspond to the Nordland group, the next two layers are the Hordaland group and the Rogaland group (Balder, Sele and Lista) is represented by the last three layers. The

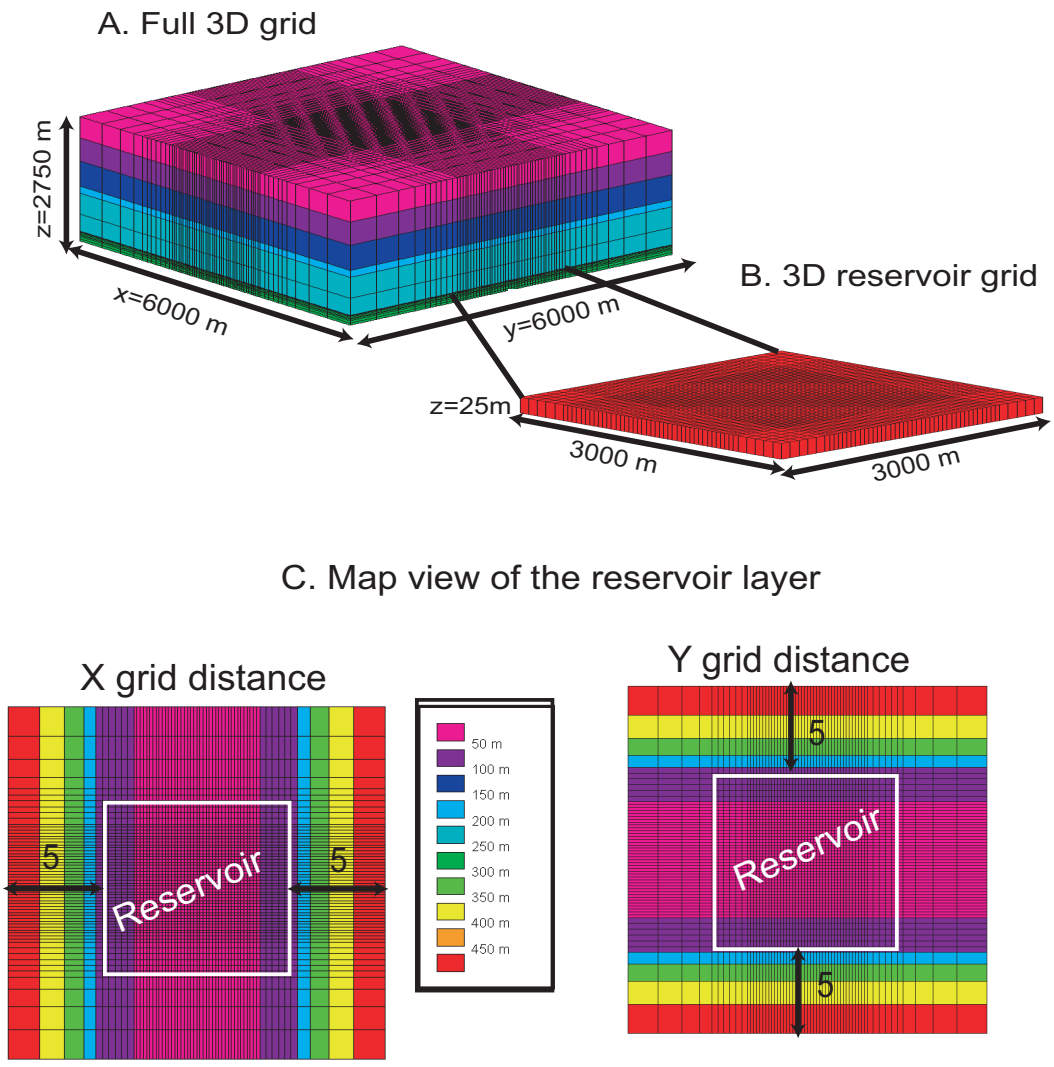

Figure 3.1: Synthetic model geometry. A. 3D view of the full model. B. 3D view of the reservoir grid. C. Map views of the top of layer 10 from the full model. Layer 10 contains the reservoir. The maps are color coded by x and y distances. The reservoir is the white rectangle on the maps.

Layer	Young modulus (E) (MPa)	Poisson's ratio (ν)
Overburden		
Layer 1	800	0.4
Layer 2	800	0.4
Layer 3	800	0.4
Layer 4	600	0.4
Layer 5	920	0.43
Layer 6	600	0.4
Layer 7	810	0.46
Layer 8	810	0.46
Layer 9	810	0.46
Under-burden		
Layer 11	600	0.18
Layer 12	600	0.18
Layer 13	2000	0.3
Layer 14	2000	0.3

Table 3.1: Geomechanical parameters for the non-reservoir layers of the model

overburden is mainly characterized by sand (quartz) and clays, and therefore the bulk modulus and density for the mineral matrix was set equal to that for quartz 37.5 GPa and 2.65 kg/m respectively.

Assuming linear elastic behavior in the overburden is the most common approach to take when geomechanical modelling is carried out on field scale. Also Kristiansen (1998), observed that considering plasticity on the overburden did not have an impact on the sea-floor subsidence prediction for the Valhall Field.

For the reservoir materials a slightly different approach was taken in order to capture the compaction phenomena. A series of compaction curves for different porosity families are used to extrapolate a two slope elastic behavior. These curves are derived from history matched geomechanical models, radio active markers and gravimetry data from the Valhall Field and they can be plotted on a stress versus strain diagram (figure 3.2). Two different elastic behaviors are identified. The gentle slope, before to the knee point of the curve indicates that the rock is stronger than the rock after this point. When the fluid reaches a certain critical pore pressure (knee point in the curve), the compaction accelerates and the rock behaves as a softer rock (steep slope). In order to duplicate the curves, GEOSIM allows input tables for each porosity family that consist of pairs of mean effective stress and Young's modulus.

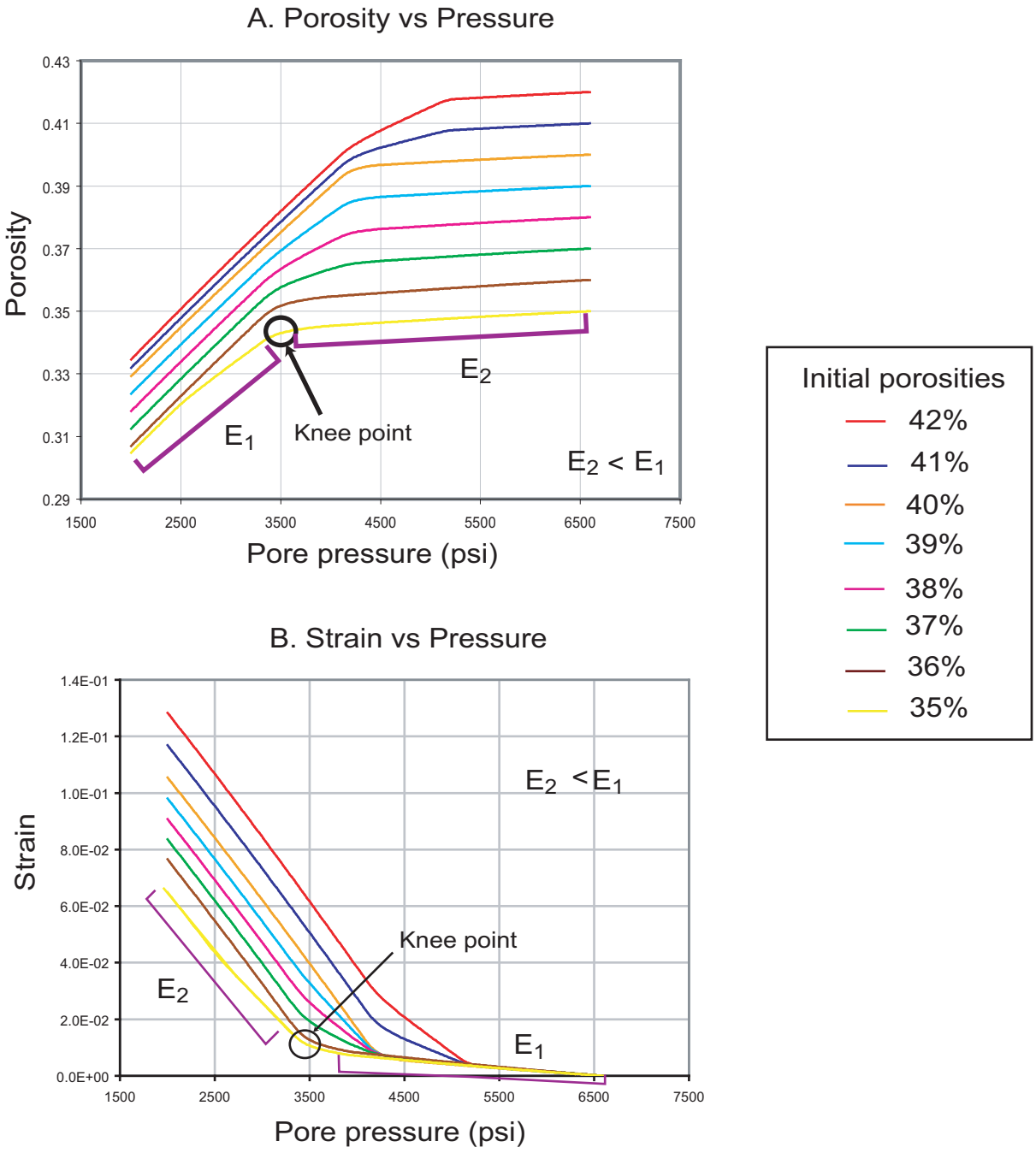

Figure 3.2: Pressure-strain curves for different porosities in the Valhall Field. The compaction curves indicates that the porosity reduction is not uniform and it will depends on the initial porosity. These synthetic curves are derived from history matched geomechanical models, radio active markers and gravimetry data from the Valhall Field.

Stress initialization and boundary conditions

The boundary conditions for the model are set up to assume uniaxial strain deformation, which means that the vertical strain is the only deformation occurring at the boundaries of the model. Regarding the modeled stress state before production, the maximum and minimum principal stresses are equal to the total vertical stress (σ_v) and the horizontal stresses (σ_H and σ_h), respectively. The initial in situ stresses were obtained from a previous BP internal geomechanical study in the south-east flank of the Valhall Field. The vertical gradient and horizontal gradient are 20.5 KPa/m and 19.1 KPa/m. The stress initialization was done using these gradients and a reference depth of 0 m. The model is initialized as horizontally isotropic, σ_H and σ_h are equal to 53.3 MPa and σ_v is 49.6 MPa.

3.1.2 Reservoir data

Reservoir Properties

The reservoir depth is 2600 m and its thickness is 30 m. This represents the average thickness for the producing unit in the south east flank (Tor Formation). The initial porosity values were chosen based on the porosity maps for the Valhall Field. Figure 3.4 shows the reservoir porosity distribution for the south east flank of the Valhall Field. The most common porosities ranges from 35% up to 42%. Therefore, I use those initial porosity values in the model (figure 3.3).

The Valhall Field is characterized for having low matrix permeability. At the crest of the field, the permeability is highly influenced by the fractures but that is not the case for the flanks, where there is a low fracture density. Therefore, the matrix permeability was considered to be isotropic (5 mD) and it was kept constant through the simulation time.

Fluid Properties

The fluid properties such as oil density, and relative permeabilities, used in the model are similar to those reported for the Valhall Field (Barkved *et al.*, 2003). Table 3.2 lists the fluid properties used in the model. The example is a dead oil model (i.e. the only two fluid phases are oil and water). The reservoir is fully oil saturated with connate saturation water of 5%.

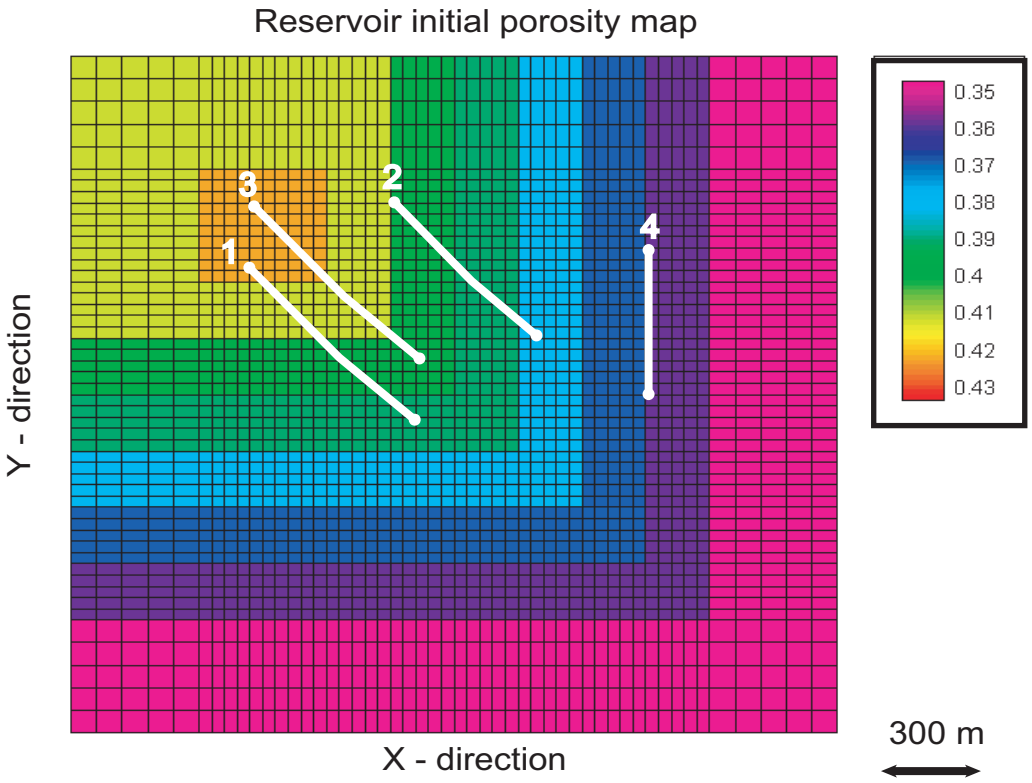

Figure 3.3: Initial porosity map. These porosity values represent the most frequent porosities found in the south flank of the Valhall Field. The lines indicate the 4 horizontal wells used in the model.

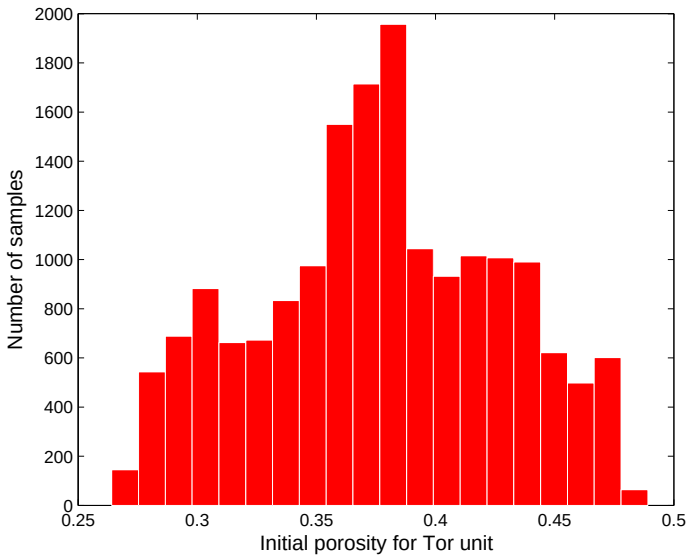

Figure 3.4: Distribution of porosities for the most porous zone in the south flank of the Valhall Field. The information is extracted from the porosity maps used on the Valhall reservoir model.

Property	**Description / Value**
Type of oil	Dead
System	oil-water
Oil viscosity (cp)	2.05
Oil gravity (API)	36
Thickness (m)	30
Reservoir depth (m)	2600
Initial pressure (MPa)	45.5
Temperature	90
Vertical and Horizontal permeability	5
Connate water (%)	5

Table 3.2: Fluid reservoir properties used in the simulation.

3.1.3 Description of producing wells

The location of the wells and their production record are decided carefully in order to investigate the relationship between pressure depletion, porosity reduction and time-lapse response. For instance, do areas with similar pressure depletion but producing from different porosities give a different time-lapse seismic response? Or will a low porosity but highly depleted area generate a larger time-lapse anomaly than a high porosity zone but less depleted? In order to answer these questions, I used 4 horizontal wells producing from the reservoir zone. Well 1 and Well 3 produce from the highest porosities, followed by well 2 that produced from intermediate porosities and well 4 producing from a single porosity of 36%.

Well 1 commences production from year 1 and the remaining wells are put on production after 3 years. The initial daily production for each well is listed in table 3.3. Well 4 is producing from the same porosity while the rest of the wells are situated along different porosity cells (figure 3.3). The maximum horizontal separation between wells is 600 m and the length of the producers is approximately 800 m.

Well	Horizontal length (m)	Initial Production (bpd)
1	950	3100
2	650	1000
3	750	2500
4	700	1000

Table 3.3: Production for the wells in the model.

Iteration parameters

The number of iterations used for the geomechanical simulator (FEM3D) to converge were 6. The pressure tolerance for convergence was 25 kPa but the majority of the time steps gave a pressure solution difference less than 2 kPa. The CPU time was 3 hours for each run, and approximately 100 runs were needed to match the porosity decrease in the model with the synthetic curves from the Valhall Field. The matching procedure involves extracting the porosity versus the pore pressure through time at one grid cell and compared with the synthetic porosity curves from Valhall Field (figure 3.5).

3.1.4 Reservoir simulation results

Comparison of porosity curves from the model and the Valhall Field

To validate the results, a synthetic porosity/pressure curve for each initial porosity was extracted from the model and compared with its equivalent from the Valhall data (figure 3.5). The porosity profiles from the model resemble the ones generated for the Valhall Field. The absolute errors were calculated using equation 3.1 and they are very low (less than 2%) giving the confidence that the numerical example results represent and capture the compaction phenomena in the Valhall Field (table 3.4).

$$error = \frac{(\phi_{syntheticcurves} - \phi_{iterativemodel}) * 100}{\phi_{syntheticcurves}} \tag{3.1}$$

Reservoir simulation results

The model was run for 11 years of production and I generated synthetic seismic every two years. The reservoir outputs shown in the next figures correspond to years 1, 2, 4, 6, 8 and 10. The pressure and porosity changes through time are displayed in figures 3.6 and 3.7 respectively. Time 1 represents the pre-production stage. During time 2, the major pressure depletion is located around well 1. After time 4, the other 3 wells begin to produce accelerating the pressure depletion. At time 10, the maximum pressure depletion is located around well 1 and 3. These two wells have the highest oil rate and produce from the most porous areas of the reservoir and consequently the greatest porosity

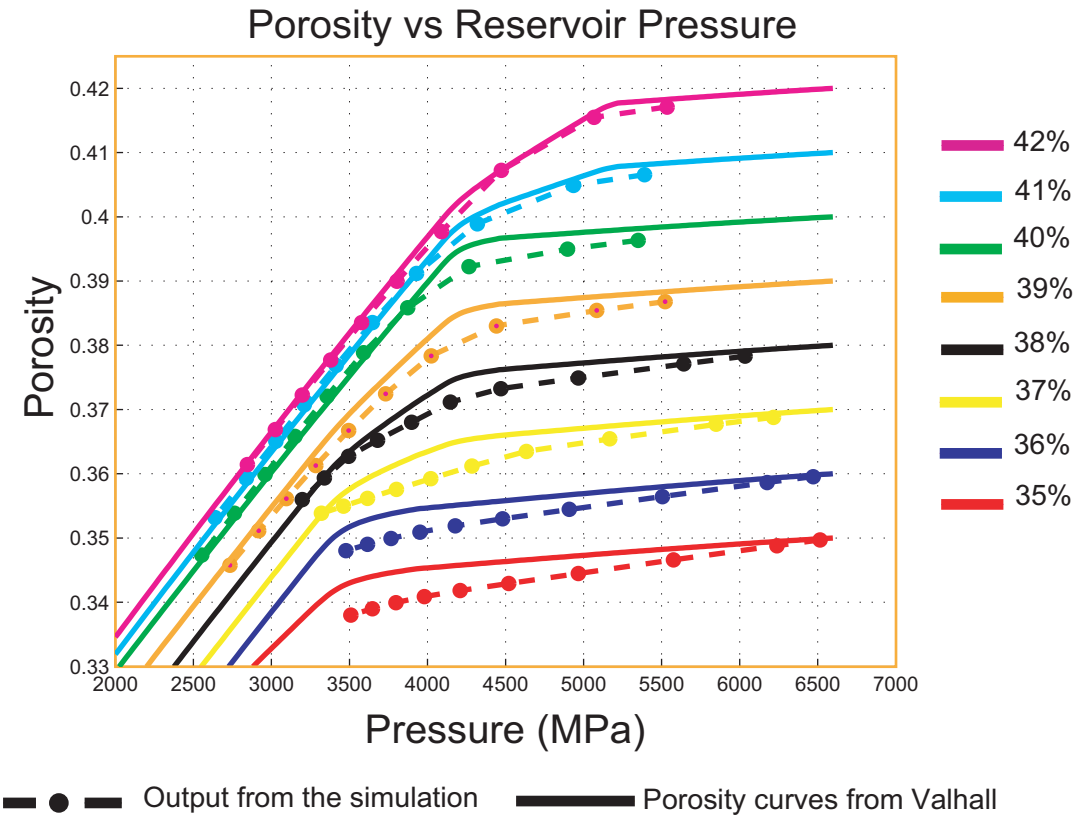

Figure 3.5: The compaction curves from the model (dashed lines) compared with the porosity curves from the Valhall Field (continuous lines). The absolute errors were calculated at specific years during the simulation and are listed in table 3.4.

reduction occurs around that area. Moreover, the porosity reduction varies, as expected, according to the initial porosity. For instance, comparing the percentage of porosity change through time (figure 3.8) between two grid cells from well 3, which differ in initial porosity (42% and 40%), indicates that the rock of 42% porosity compacts faster than the one with 40%, even with both cells having the same pressure depletion profile (figure 3.8).

Effective stress and average normal stress outputs

The effective stress is a function of the mean normal stress and the pore pressure (eq. 1.15). In a conventional reservoir, effective stress variations are normally due to the pore pressure changes, however this is not the case for compacting reservoirs, where the deformation induces average normal stress changes. To illustrate this further, a series of E-W profiles (figure 3.9) are created to analyze

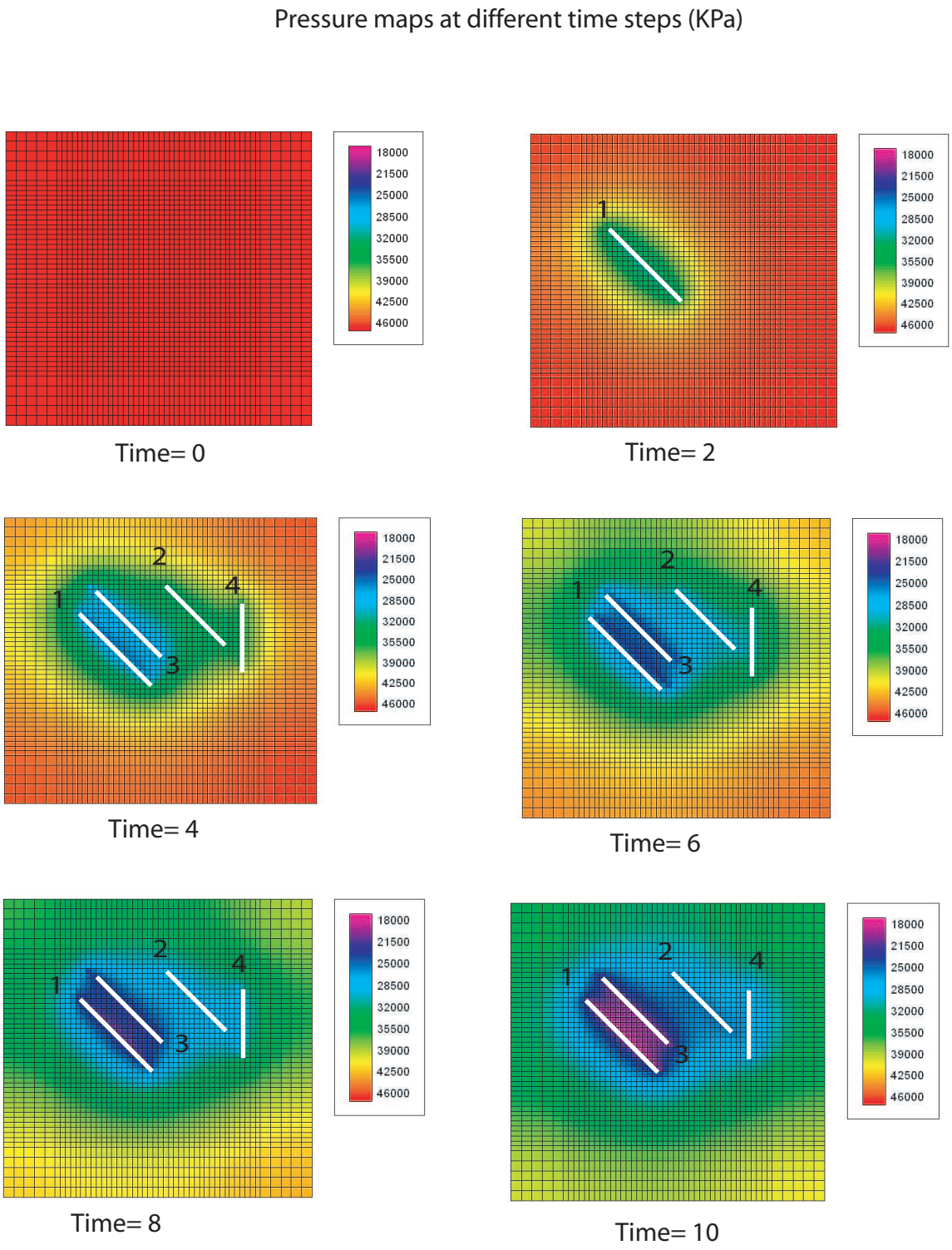

Figure 3.6: Reservoir pressure outputs from year 1 up to year 12.

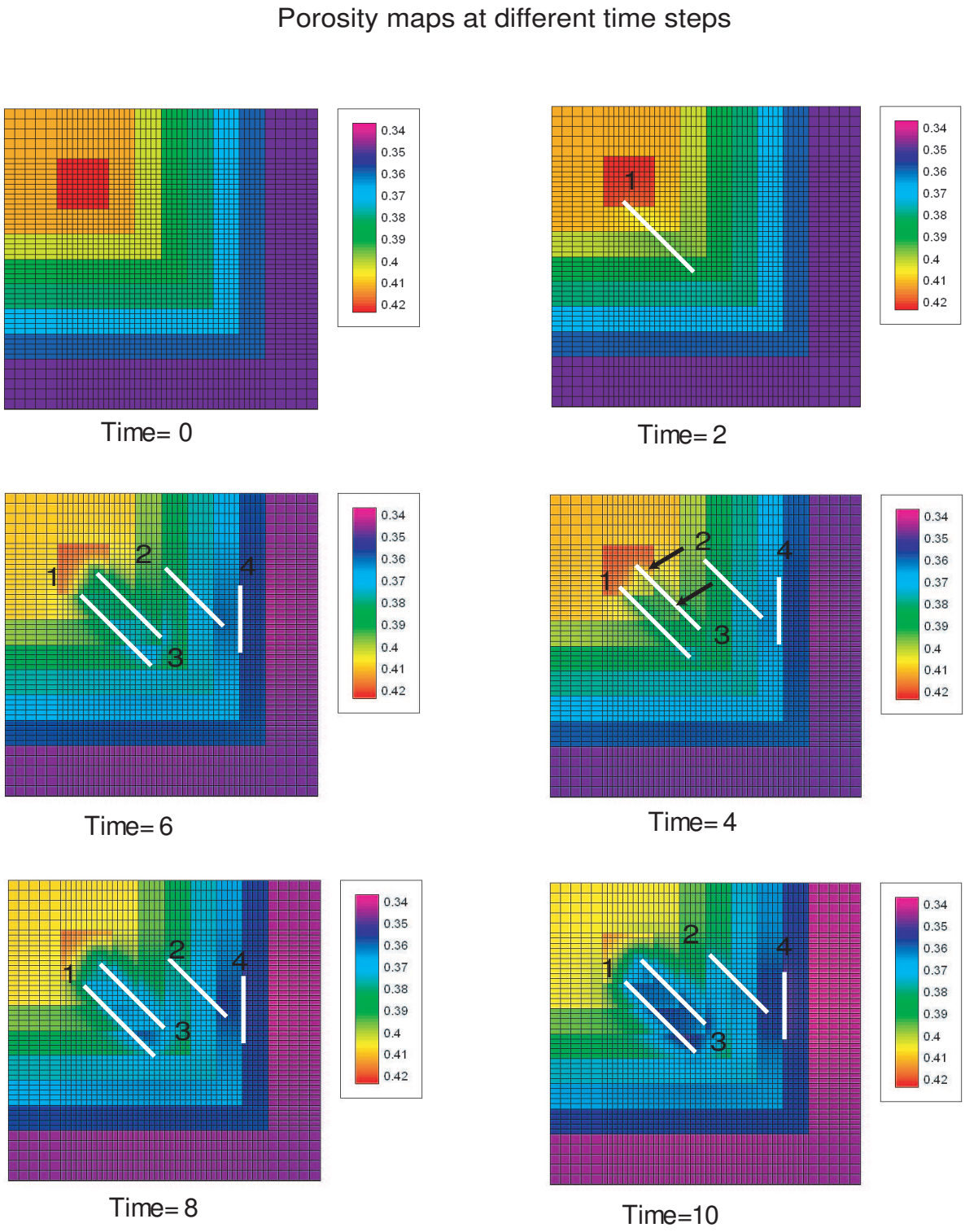

Figure 3.7: Reservoir porosity outputs from year 1 up to year 12. The black arrows on the porosity map at time 4, indicates the position of the grid blocks used in figure 3.8.

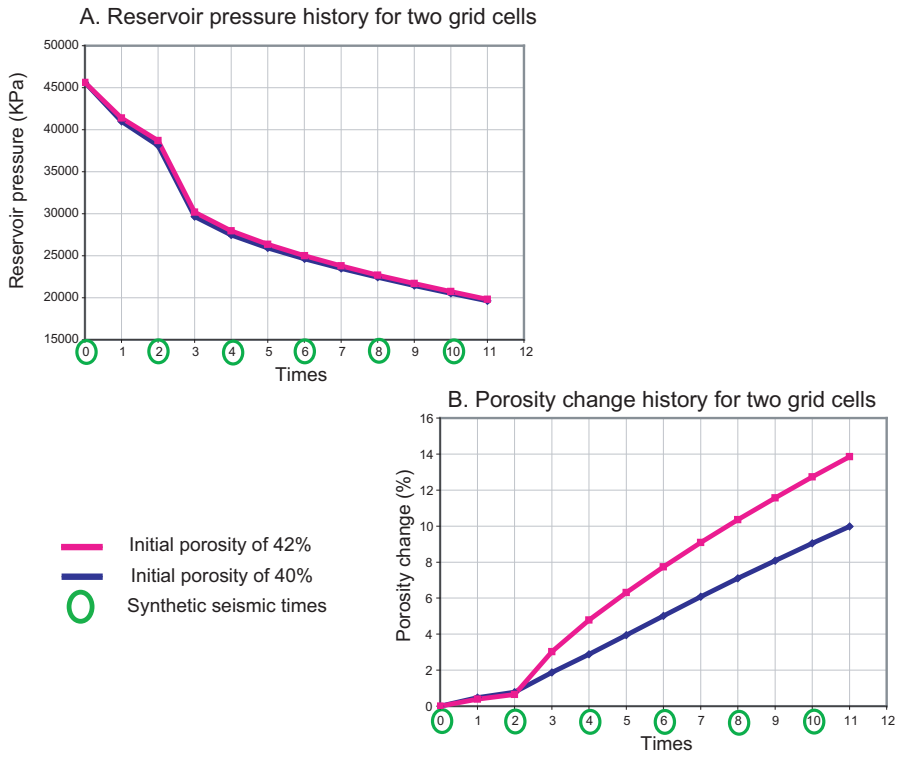

Figure 3.8: Pressure depletion and porosity loss at well 3. A rock with 42 % porosity suffers more compaction than one with 40% porosity even when both materials have the same pressure depletion profile.

the compaction induced-stress-changes during 12 years of production. From top to bottom, the first profile indicates the variation in effective stress, the second one shows the normal vertical stress and the bottom two indicate the normal horizontal stress and pore pressure respectively. In general terms, part of the overburden weight needs to be transferred to the sides of the reservoir, causing a decrease of the vertical and horizontal normal stresses in the whole reservoir. The largest stress changes occurs where the maximum compaction is happening and it is accompanied by a decrease in the normal and vertical stresses in the overburden (between wells 1 and 3). As a convention, ellipses were used to represent the normal stresses at certain time. The vertical normal stress is represented by the long axis of the oval while the horizontal normal stress by the short axis. The red and blue colours indicate the initial and final scenarios respectively. The vertical stress is slightly higher than the horizontal stress (the two horizontal stresses are equal) for the pre-production scenario in the model. After 12 years of production, the redistribution of the normal stresses across the profile is described from left to right as follows:

- The vertical normal stress keeps constant but the horizontal stress is lower than the initial one
- The three normal stresses reduce. Here the maximum reservoir compaction is occurring
- The vertical stress reaches higher values than at pre-production stage but the normal stress decreases
- The vertical normal stress remains constant but the horizontal stress is lower than the initial ones

Normal stress-change patterns are linked to the geometry and geomechanical properties of the rocks. Geomechanical results from a horizontal layered model of high porosity sandstone bounded by salt, conclude that the vertical normal stress decreases while the horizontal stress increases at middle of the model (Schutjens *et al.*, 2007). For a dome shaped reservoir with a hard chalk layer in the overburden, both horizontal and vertical stresses decrease at the center of the reservoir (Schutjens *et al.*, 2007). Undoubtedly these variations will have an impact on the effective stress changes. According to equation 1.15, if the effective stress responds merely to the pressure depletion, the effective stress change (orange profile) would be an exact replica of the reservoir pressure changes (green profile) in figure 3.9, however this is not the case because the effective stress is also influenced by the normal stress changes.

Vertical Displacement

The vertical displacement from the reservoir to the surface evolving through time is displayed in figure 3.10. The reservoir acts as a source point and then the compaction spreads towards the top of the model. The maximum vertical displacement (U_z) after 11 years of production correlates with the high porosity produced area. Figure 3.11 compares the vertical displacement, pressure depletion and effective stress after 11 years of production for the cross-section in figure 3.10. The black arrow indicates where the largest compaction is occurring while the yellow ellipsoids point to where the most depleted and the highest effective stress areas are on the section. The three anomalies do not coincide, because the rock deformation depends on the stress changes and the initial porosity. The maximum displacement is given by the rock of 42% initial porosity. Even though the pressure changes drive the reservoir compaction, the reservoir compaction also depends on the strength of the rock.

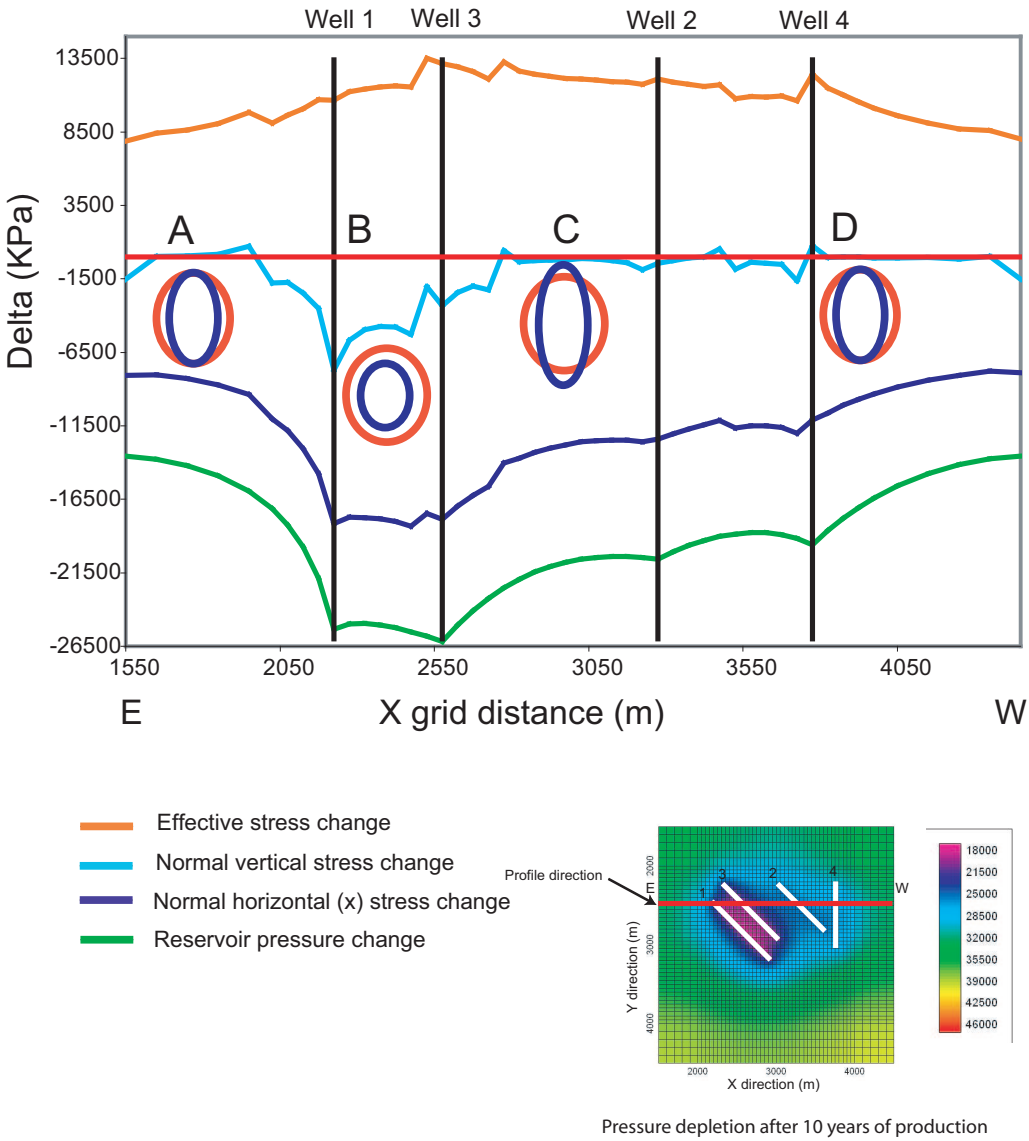

Figure 3.9: Profile E-W across the model to illustrate of the normal and effective stresses variation. A.Profile E-W across the model: Illustration of the normal stress, pore pressure and effective stresses changes after 12 years of production. Ovals were used to represent the normal stresses at certain time. The vertical normal stress is represented by the long axis of the oval while the horizontal normal stress by the short axis. The red and blue colors indicate the initial and final scenarios respectively. The vertical stress is slightly higher than the horizontal stress (the two horizontal stresses are equal) for the pre-production scenario in the model.

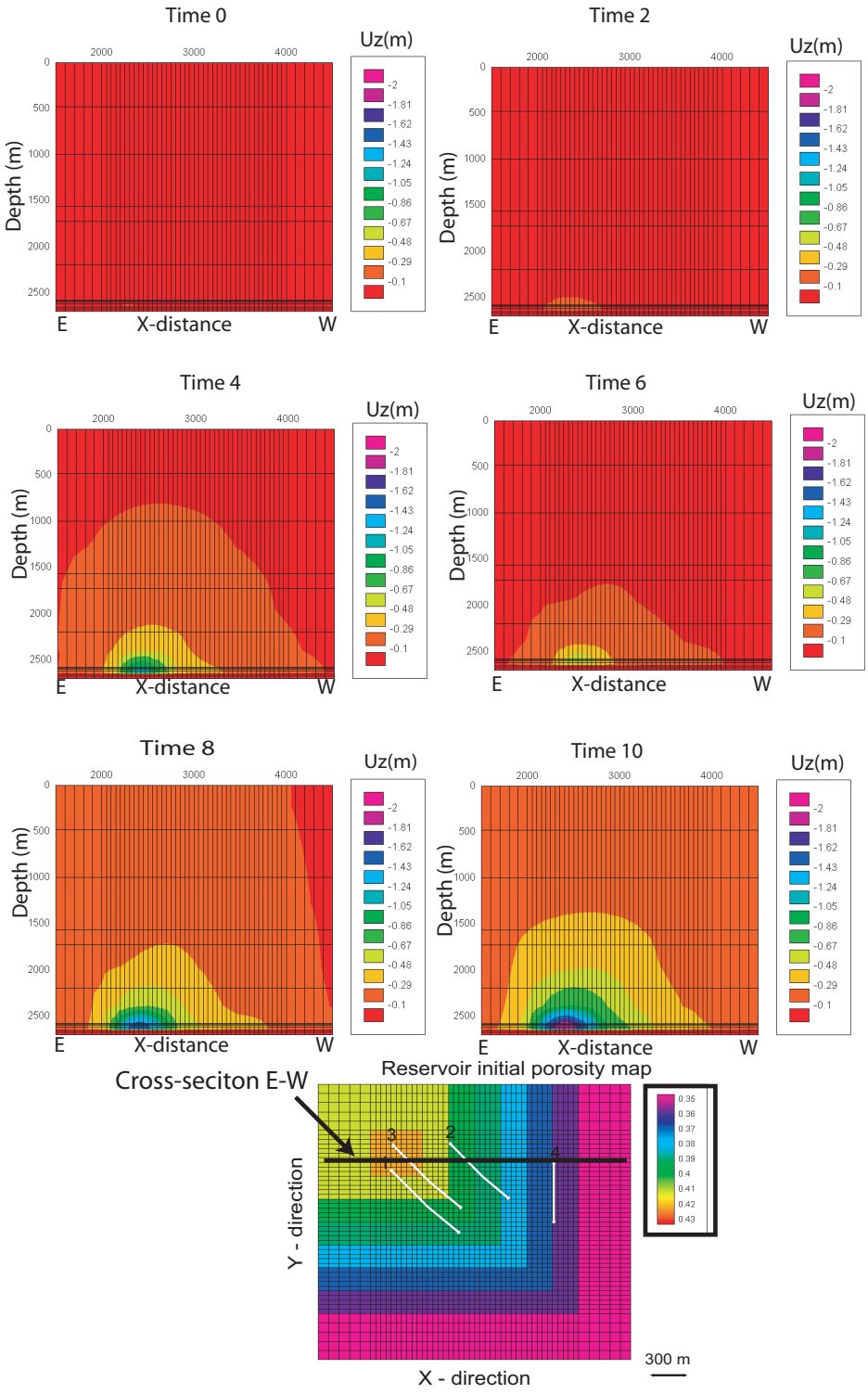

Figure 3.10: Development of the vertical displacement through time for a E-W cross-section.

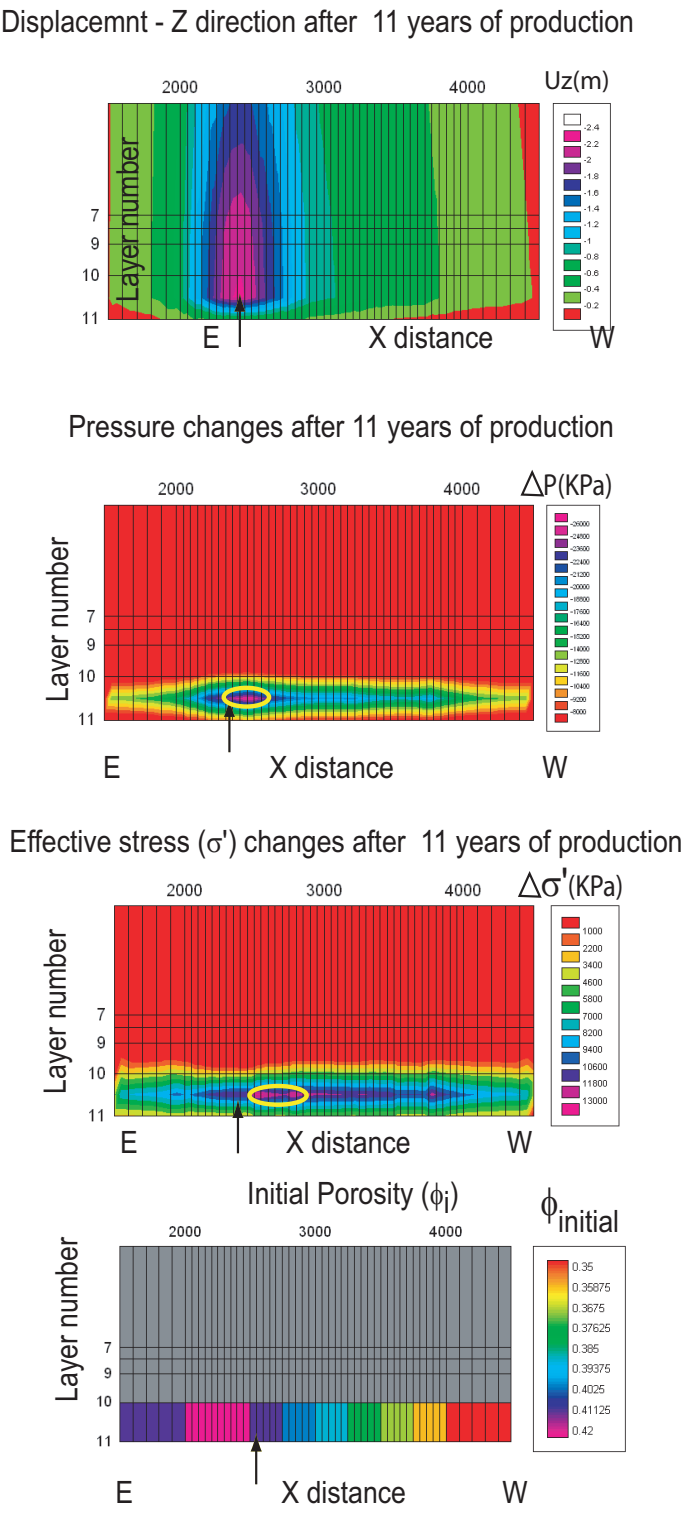

Figure 3.11: E-W cross-sections across the maximum displacement in the reservoir. A. Vertical displacement B Pore pressure changes. D. Effective stress changes D. Initial Porosities. The black arrows locate the maximum reservoir compaction and the yellow ovals highlighted the largest changes for the different properties.

Pressure (psi)	Error (%)	Pressure (psi)	Error (%)
Initial ϕ=0.35		Initial ϕ=0.36	
6514.77	0.05	6470.83	0.06
6239.64	0.19	6175.24	0.17
5575.08	0.51	5504.73	0.42
4967.37	0.79	4908.78	0.64
4521.38	1.00	4481.21	0.79
4208.83	1.14	4178.66	0.91
3979.67	1.28	3950.37	1.03
3797.21	1.38	3767.92	1.08
3646.96	1.46	3615.77	1.09
3508.01	1.47	3476.54	0.97
Initial ϕ=0.37		Initial ϕ=0.38	
6215.85	0.16	6034.55	0.22
5848.33	0.28	5641.36	0.36
5167.81	0.54	4966.36	0.60
4635.24	0.78	4469.46	0.79
4284.97	1.15	4146.61	0.87
4021.30	1.21	3898.30	0.71
3800.84	1.07	3680.46	0.45
3615.34	0.86	3495.39	0.18
3461.16	0.55	3340.20	0.06
3320.33	-0.07	3196.76	-0.18
Initial ϕ=0.39		Initial ϕ=0.40	
5522.43	0.40	5350.12	0.46
5084.56	0.56	4898.33	0.62
4440.31	0.85	4266.55	0.82
4023.04	0.83	3874.66	0.08
3731.22	0.65	3589.96	-0.26
3494.67	0.67	3356.74	-0.30
3284.36	0.57	3150.06	-0.29
3095.38	0.43	2959.33	-0.25
2918.43	0.33	2762.52	-0.25
2734.09	0.24	2553.38	-0.25
Initial ϕ=0.41		Initial ϕ=0.42	
5390.59	0.38	5535.19	0.28
4934.30	0.23	5066.87	0.16
4318.19	0.34	4472.80	0.02
3929.63	0.03	4089.61	0.45
3646.52	-0.16	3804.18	0.28
3415.19	-0.22	3577.34	0.20
3211.70	-0.25	3380.81	0.15
3026.63	-0.24	3198.07	0.12
2838.81	-0.26	3025.47	0.11
2638.80	-0.31	2847.08	0.08

Table 3.4: Porosity error from the iterative coupled simulation

3.2 From the simulator to the seismic data: the workflow

The final objective of running an iterative coupling geomechanical model in this study is to investigate the seismic response.

The simulation is followed by conventional simulator to seismic work-flows as detailed in section 2.3. To determine the seismic velocity changes due to overburden and underburden deformation with a constant R-factor, the relation of Hatchell et al. (2005) is applied, i.e. changes in velocity are proportional to strain (section 2.2). From the final resultant seismograms, relationships are drawn which can then be used to construct guidelines for interpreting the Valhall seismic data.

The calculation of the elastic properties of the rocks (seismic velocities and densities) is followed by seismic modelling of the full stacked data using a convolution-based approach. Seismic data are produced for a pre-production state (baseline volume) and after 2, 4, 6, 8 and 10 years of production (monitor volumes).

3.2.1 Estimation and analysis of the reservoir acoustic properties

Sensitivity of dry frame elastic moduli with effective stress

The variation of the rock frame elastic properties with applied effective stress is a crucial part of the petro-elastic modelling. Generally, in order to find the best equation to describe the sensitivity of the bulk modulus (κ) and the shear modulus (μ) with the effective stress for the dry frame, a mathematical function is created base on core measurements (MacBeth, 2004). In the present study, equations 3.2 and 3.3 are used. These relationships have been previously used and validated in the Valhall Field (Kjelstadli *et al.*, 2005).

$$\kappa_{dry} = \kappa_{norm} * [1 + A_{\kappa} * log(\frac{\sigma^{'}}{\sigma^{'}_{norm}})] \tag{3.2}$$

$$\mu_{dry} = \mu_{norm} * [1 + A_{\mu} * log(\frac{\sigma^{'}}{\sigma^{'}_{norm}})] \tag{3.3}$$

where κ_{dry} and μ_{dry} are bulk and shear dry moduli respectively and $\sigma^{'}$ represents the effective stress. The parameters A_{κ}, A_{μ} are determined from elastic core measurements. The normalized effective stress and elastic moduli ($\sigma^{'}_{norm}$, κ_{norm} and μ_{norm}) are based on the reference conditions used on the core experiment.

Few acoustic laboratory measurements from the Valhall Field have been published, however core data results from an similar chalk field in the North Sea (Ekofisk Field), suggest that there is a correlation between initial porosity and the dry frame elastic moduli (Pedersen & Rhett, 1998). The curves showed a strong influence on the initial porosity for the compressional (V_p) and shear (V_s) wave velocities for a dry samples (figure 3.12). The velocities in the high porosity samples are more sensitive to confining pressure changes. V_p and V_s are expressed as a function of κ and μ (eq.1.31). Therefore, for high porosity rocks, κ and μ are more sensitive to effective stress. This observation is captured by equations 3.2 and 3.3.

Elastic property measurements in cores from the Valhall Field (Askim, 2003) are used to include the effect of initial porosity into the mathematical approximations. Figure 3.13 illustrates the normalized parameters (κ_{norm} and μ_{norm}) and the coefficients (A_K and A_μ) as a function of initial porosity respectively. These are used to generate the curves for the different porosities. These curves are shown in figure 3.14. The laboratory data published by Askim (2003) are used to calibrate the results. Unfortunately the only information regarding how the dry frame moduli varies with effective stress was for a sample of 40 % porosity. Therefore, the uncertainty regarding the way the rock frame elastic properties vary with effective stress for different initial porosities, i.e. the nature of the parameters in equations 3.2 and 3.3 could not be addressed because of the lack of laboratory measurements for the present study,

The P-wave velocities of a saturated rock estimated from the elastic moduli calculated with equations 3.2 and 3.3 were compared with the sonic velocities from a well in the south east flank in figure 3.15. The sonic data (blue asterisks) as well as the model calculations (green squares), indicate a strong dependance of the P-wave velocities with porosity. Furthermore, the velocities from the model are in the range of the sonic log readings.

Influence of the pressure depletion and effective stress changes on the reservoir P-wave velocity and acoustic impedance

After the prediction of the acoustic impedance and seismic velocities, correlations are drawn to analyze which seismic properties are sensitive to the changes in pressure. Cross plots of P-wave velocity and acoustic impedance changes versus pressure and effective stress changes (figure 3.16) show that the initial porosity controls the variations of compressional wave velocities and impedance.

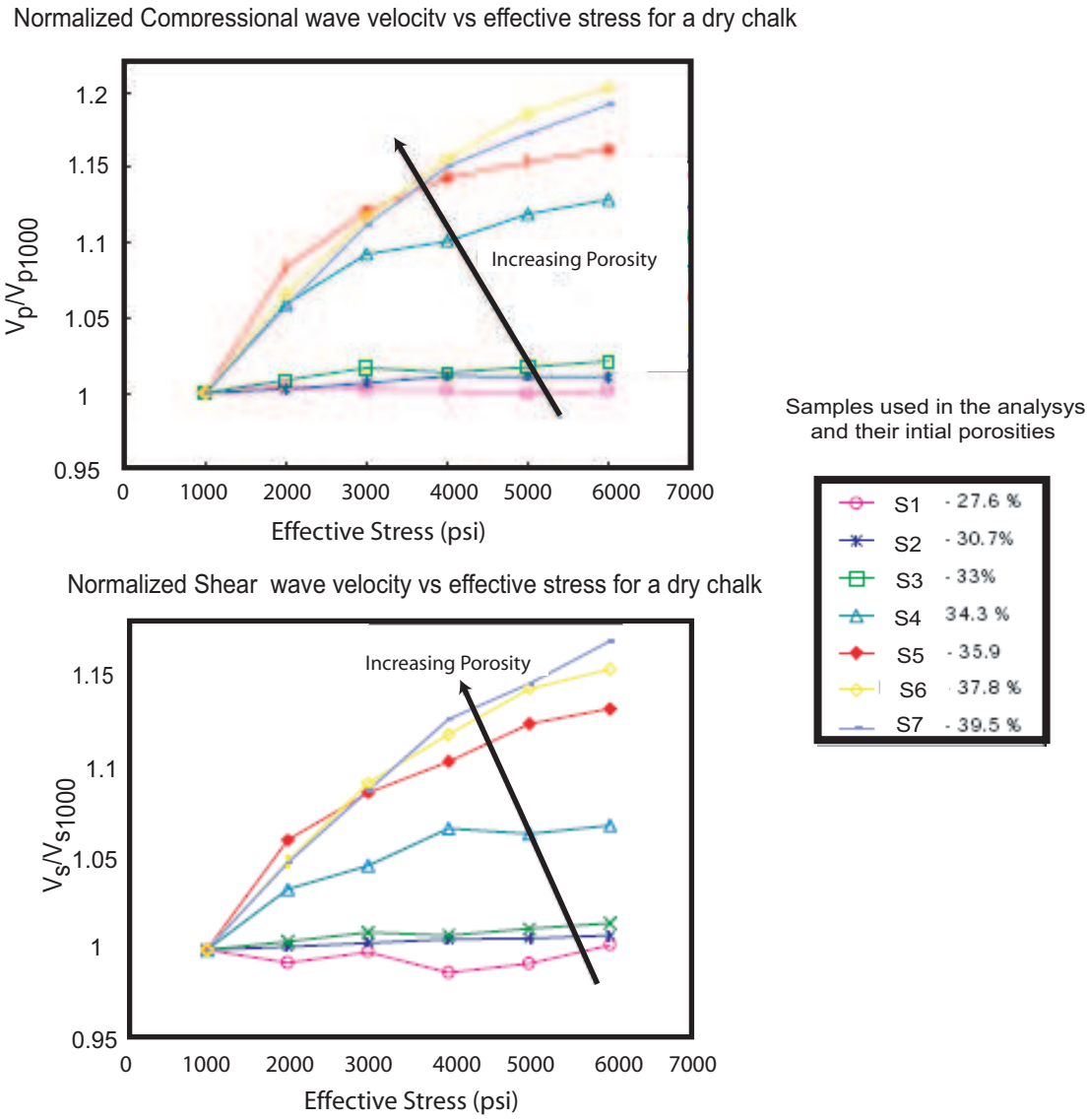

Figure 3.12: Velocities for dry chalk samples from the Ekofisk Field. A. Normalized compressional wave velocity B. Normalized shear wave velocities for dry chalk. The normalization is done by dividing the velocities by the velocity estimated at 1000 psi. The plots indicate that the velocities for the dry samples are strongly influenced by the initial porosities.

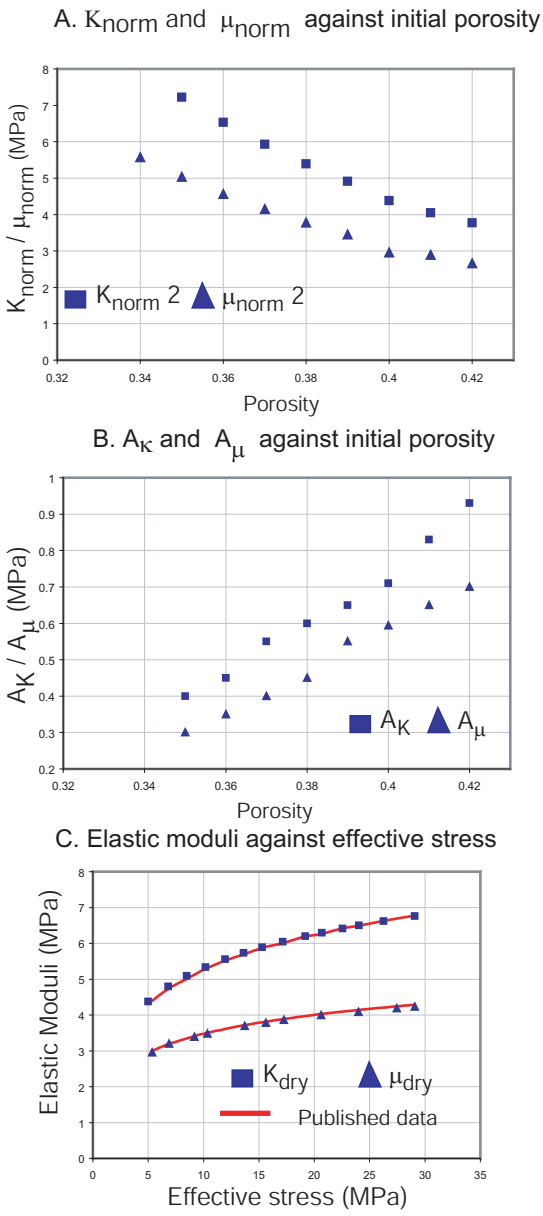

Figure 3.13: Parameters used for equations 3.2 and 3.3 against initial porosity. A. The parameters, K_{norm} and μ_{norm}, as a function of initial porosity. B. Parameters, A_K and A_μ, as a function of initial porosity. C. The elastic moduli versus effective stress. The parameters K_{norm}, μ_{norm}, A_K and A_μ (blue data on plots A and B) are used to estimate the elastic moduli match the published data for a initial porosity of 40% (Askim, 2003) and the sonic log at the well.

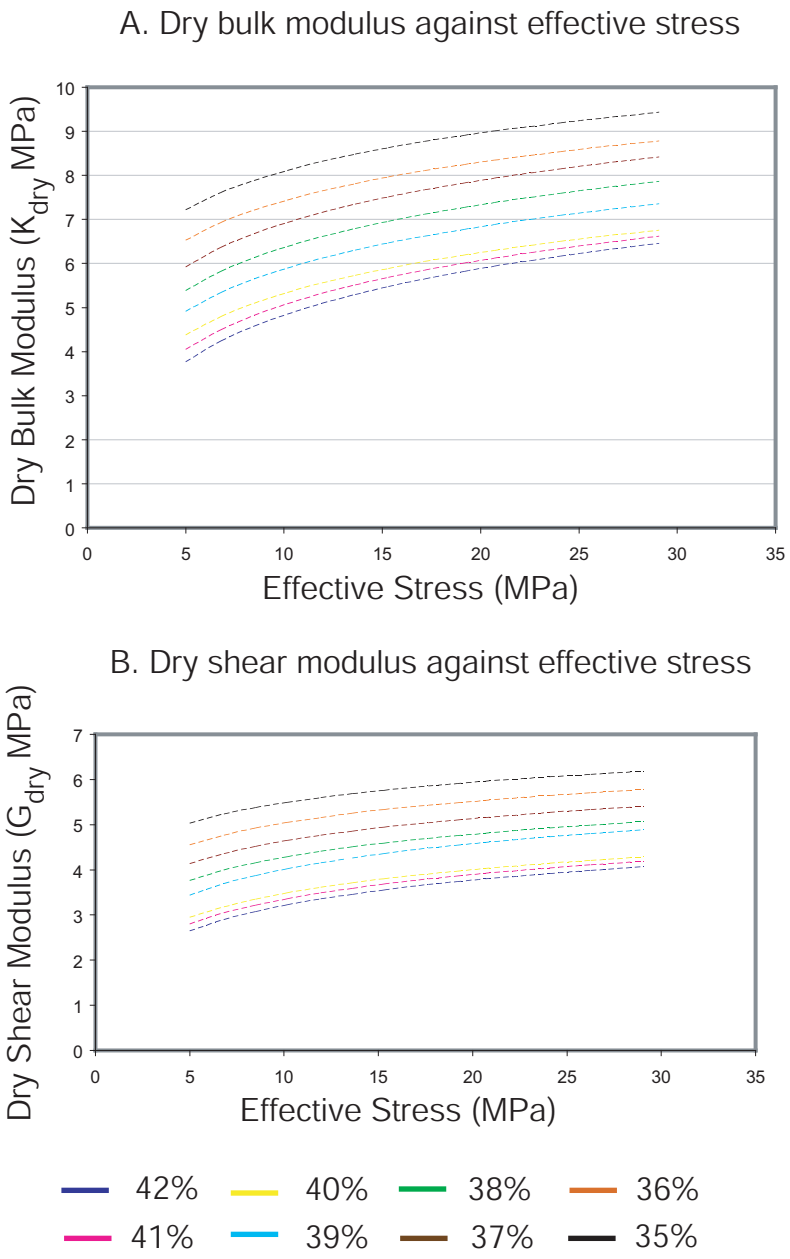

Figure 3.14: Curves for the elastic moduli versus effective stress for different initial porosities. A. Dry bulk modulus versus effective stress. B. Dry shear modulus versus effective stress. These curves are calculated using the equations 3.2 and 3.3.

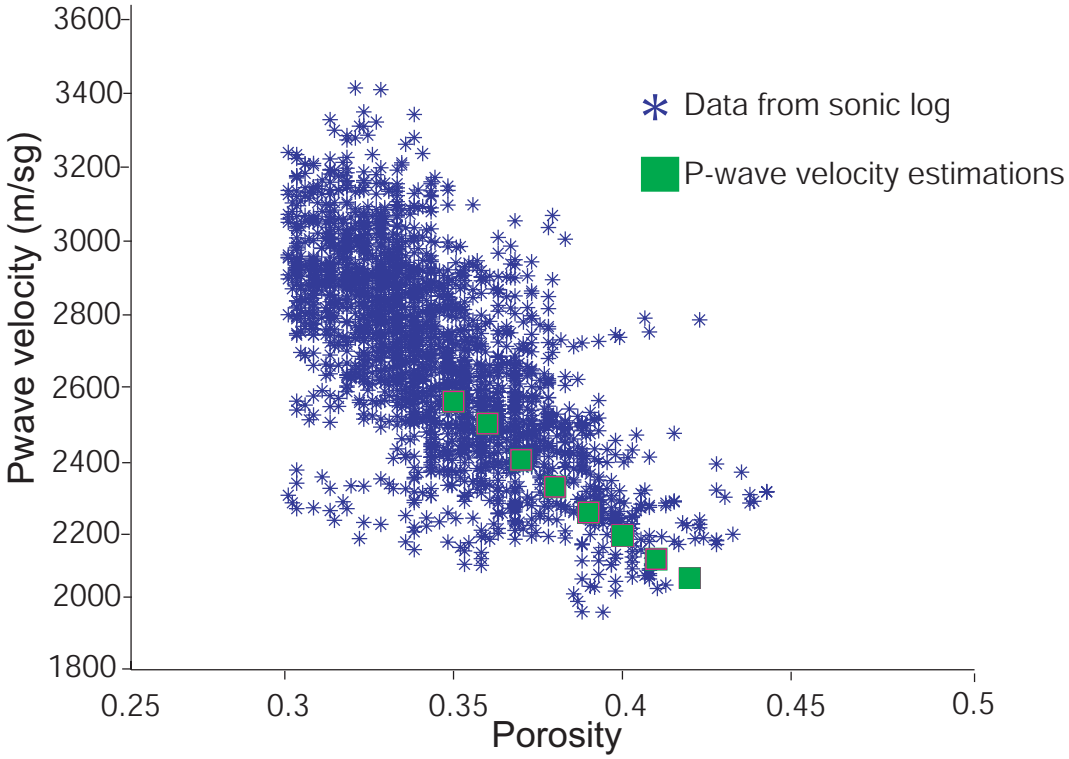

Figure 3.15: Compressional wave velocity vs porosity. Measured sonic log velocities (blue dots) and the model P-wave velocities (green dots). The velocities are calculated using the dry frame moduli curves (figure 3.14). The calculated P-wave velocities of saturated rocks are within the values observed in the sonic log.

The normalized changes of each property ΔX_f were estimated using equation 3.4. For each porosity class, there is a trend showing how the seismic properties respond to pressure/effective stress changes. Furthermore, for the same pressure drop rocks with initial higher porosities will have higher velocity changes due to the porosity loss.

$$\Delta X_f = \frac{X_f - X_i}{X_i} * 100 \tag{3.4}$$

where X_f represents the value of a property (P-wave velocity, acoustic impedance, pore pressure or effective stress) a certain time, X_i is the property value at initial conditions.

Regarding the sensitivity of P-wave velocity and impedance to either pressure or effective stress, the cross-plots between seismic properties and effective stress (figures 3.16C and 3.16D) are well defined and the scatter is minimal, implying that these properties correlate better with effective stress than with pressure changes.

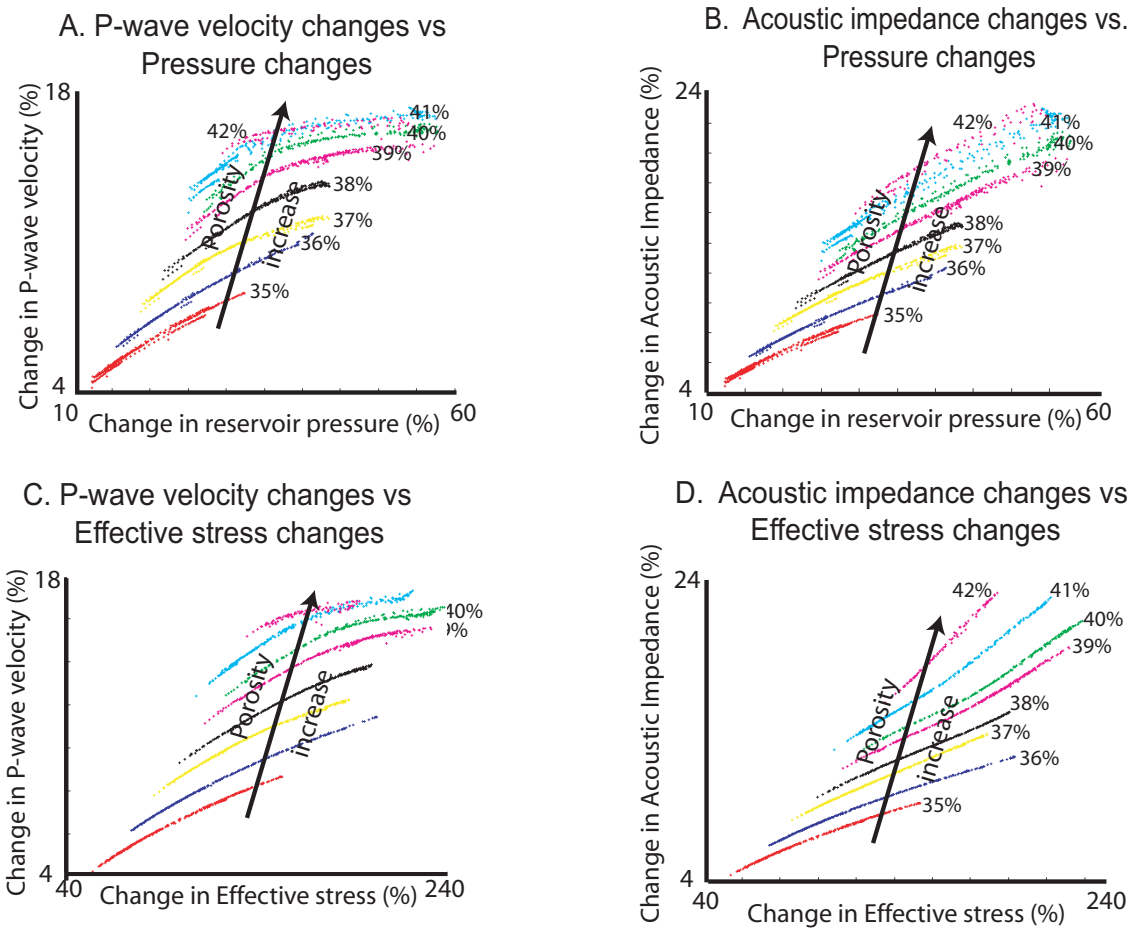

Figure 3.16: Changes in the acoustic reservoir properties vs effective stress and pore pressure changes A. Normalized P-wave velocity changes vs normalized reservoir pressure changes. B. Normalized acoustic impedance changes vs normalized reservoir pressure changes. C. Normalized P-wave velocity changes vs normalized effective stress changes. D. Normalized acoustic impedance changes vs Normalized effective stress changes.

3.2.2 Estimating the acoustic properties for the overburden and underburden rocks

An initial velocity model for the overburden and underburden is created based on the acoustic properties of the overburden in the Valhall Field. The subsequent overburden/underburden velocities were estimated as a function of strain.

Velocity model for the baseline survey

The overburden is described by 9 layers and the underburden consists of 4 layers. Table 3.5 summarizes the initial seismic properties for overburden/underburden rocks. Perhaps the most relevant seismic properties are the ones assigned to the layers immediately above (layer 9) and below (layer 11) of the reservoir, since I am looking for reflectivity changes at reservoir level and interested in obtaining similar time-lapse amplitude changes to those observed at Valhall. The layer 9 represents the Lista Formation; this unit primarily comprises of shale and generally has relatively higher P wave impedance than the reservoir (figure 3.17). The layer 11 (underburden) represents the Hard Chalk. This unit is a very dense low porosity chalk, recognized by an increase of the acoustic impedance.

Overburden			
Layer	P-wave velocity (V_p m/s)	S-wave velocity (V_s m/sg)	Density(ρ kg/m^3)
Layer 1	1800	400	1950
Layer 2	2000	550	1950
Layer 3	2000	550	2010
Layer 4	1850	425	1970
Layer 5	2100	425	1970
Layer 6	2100	650	2030
Layer 7	2600	650	2200
Layer 8	2600	750	2200
Layer 9	2300	750	2200
Under-burden			
Layer	P-wave velocity (V_p m/sg)	S-wave velocity (V_s m/sg)	Density(ρ g/cm^3)
Layer 11	3200	1650	2270
Layer 12	3200	1650	2270
Layer 13	2500	1150	2160
Layer 14	2500	1150	2160

Table 3.5: Initial seismic properties for the non reservoir rocks.

At initial conditions, seismic properties for the overburden and underburden layers are kept constant

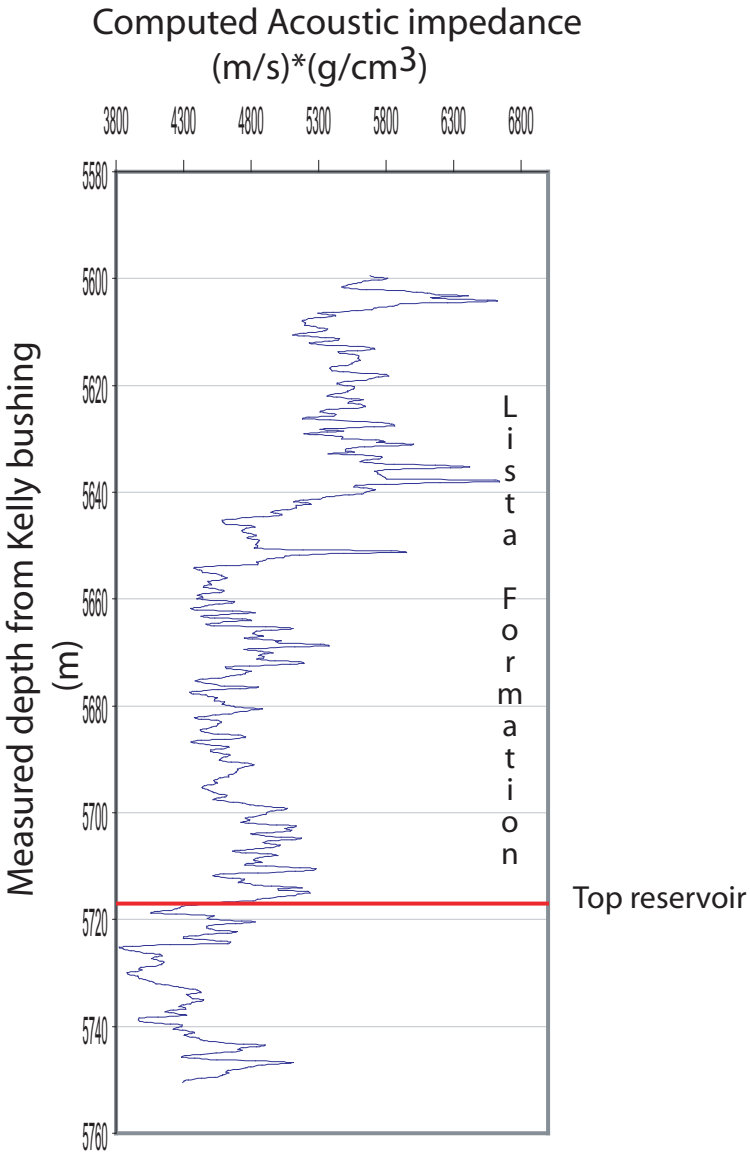

Figure 3.17: Computed P-wave acoustic impedance log for a well in the south flank of the Valhall Field: The top of the reservoir is generally identified as a decrease of the p-impedance.

horizontally.

Velocity model for the monitor surveys

The equation 2.15 is used to determine the seismic velocity changes due to overburden and underburden strain deformation. An R-factor equal to 5 value is adopted for the Valhall Field (Hatchell & Bourne, 2005). Sensitivity analysis to this parameters is presented in chapter 6.

3.3 The final synthetic seismic response

Synthetic seismograms are calculated for a pre-production case and five subsequent time steps. The convolutional method is used. The reflection coefficients were computed using the offset dependant solution for Zoeppritz equation (Zoeppritz, 1919). To obtain the synthetic traces, the reflectivity series in time domain are convolved with a wavelet extracted from the Valhall baseline survey. The final products are six full stacked volumes (1 baseline survey and 5 monitor surveys).

3.3.1 Reflectivity response at the reservoir level at initial conditions

The seismic velocities and density of the reservoir vary depending on the porosity, therefore the wavelet signature of the top and base reservoir varies on the synthetic seismograms. The amount of energy reflected at the top and base of the reservoirs, depends on the reflection coefficients (R_c) at these boundaries. The R_c at the top is defined by the acoustic impedance contrast between layer 9 and the reservoir while the R_c at the base is defined by the acoustic impedance contrast between the reservoir and layer 11. In general, the top of the reservoir is identified as a trough whereas the base is recognized as a peak. The clearest reflections at top and base are expected when the reservoir exhibits an initial porosity of 42 % as this is where the largest contrast between acoustic impedance occurs (figure 3.18)

3.3.2 Reflectivity response at the reservoir level trough time

The six seismic volumes exhibit a characteristic trough-peak doublet, the trough is correlated with the top of the reservoir while the base is identified by a strong peak, as a result of the acoustic

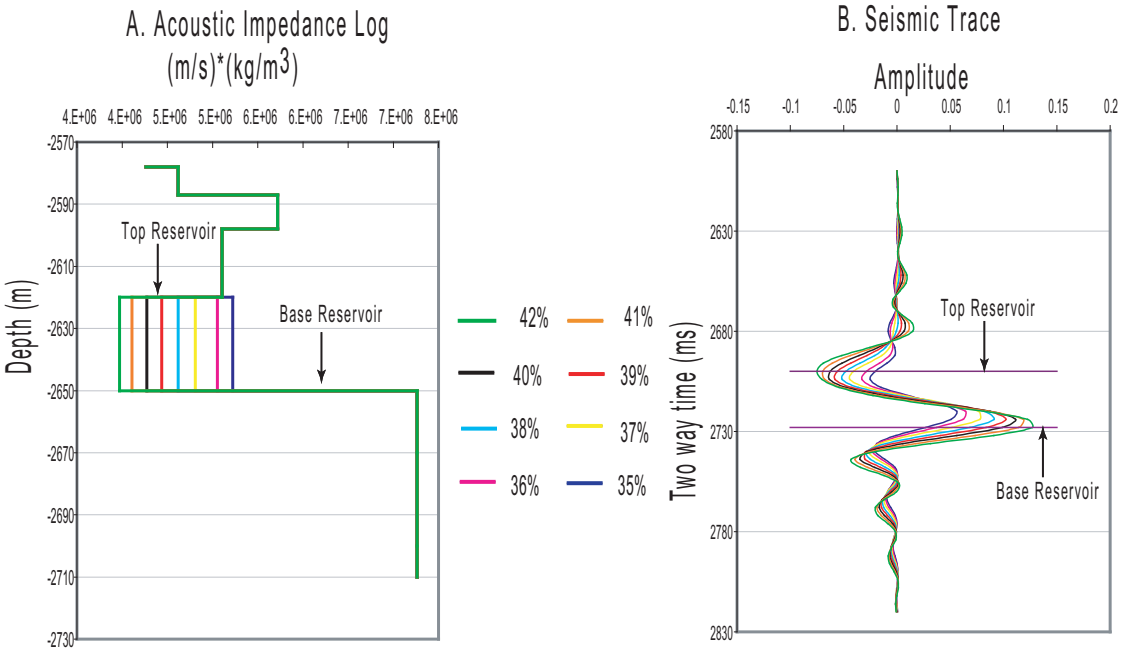

Figure 3.18: Seismic traces for different porosities at pre-production conditions. A. Acoustic impedance profiles: For the baseline volume, the seismic response is controlled by porosity. B. Seismic trace. The trough and peak for top and base respectively, which gain prominence as porosities increase.

impedance increase at layer immediately below the reservoir (layer 11).

Figures 3.19 and 3.20 compare the P wave impedance profiles and their respective seismic traces for the biggest and smallest porosities of the model (42% and 35%). For the 42% porosity rock, the induced compaction has moved the reflectors and decreased the layer 9 P wave impedance while increasing the reservoir P wave impedance. These changes are going to be imprinted on the time-lapse seismic attributes. On the contrary, for the 35% porosity rock, the induced compaction is very small because the rock is "harder", therefore the P wave impedance changes are constrained to the reservoir zone. One can say that the time-lapse seismic attributes generated from the 35% porosity rock are free from undesirable seismic changes caused by reservoir compaction in the layer directly above the reservoir.

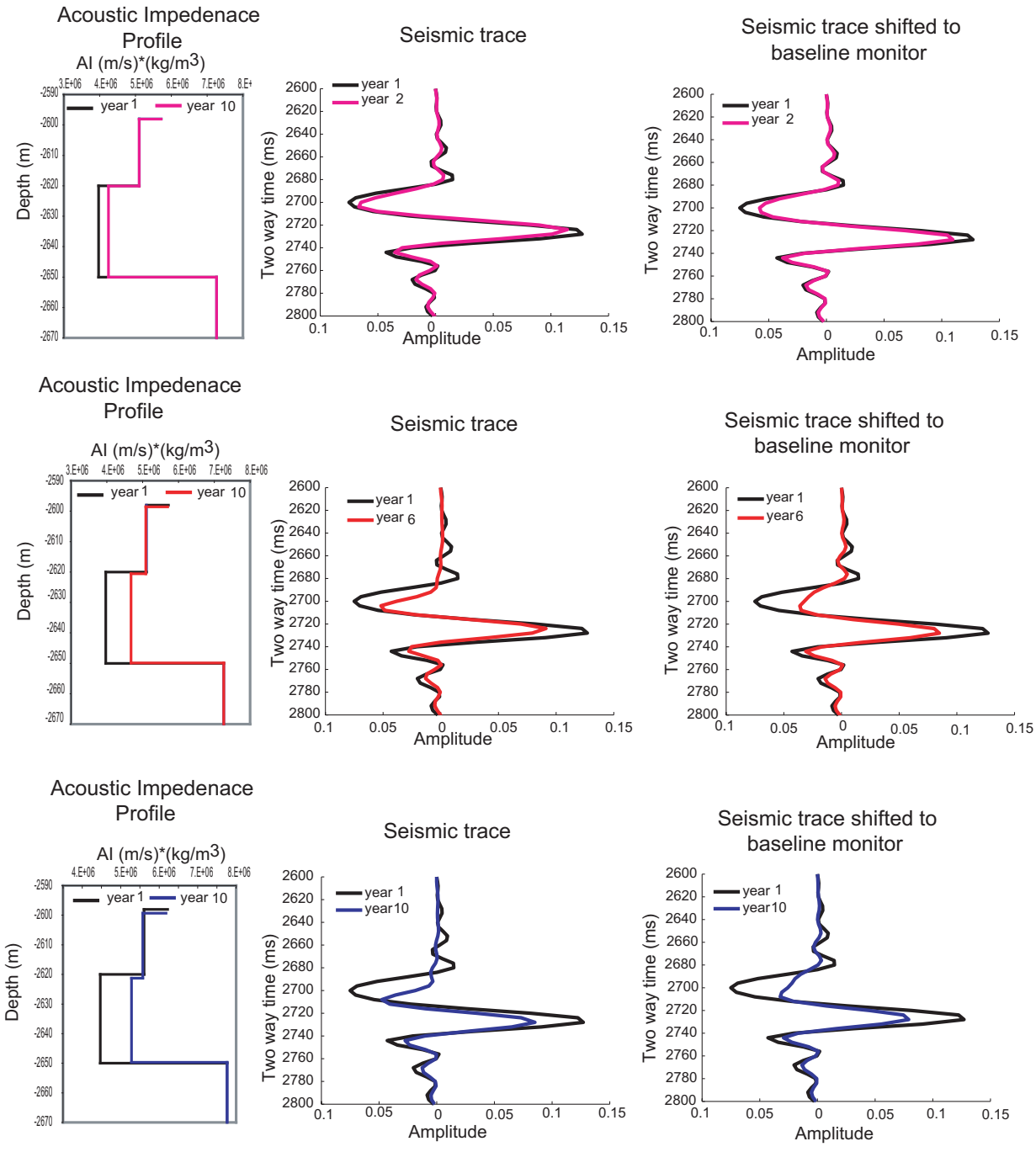

Figure 3.19: Changes in acoustic impedance logs and seismic traces for a rock of 42% porosity during 10 years of production.

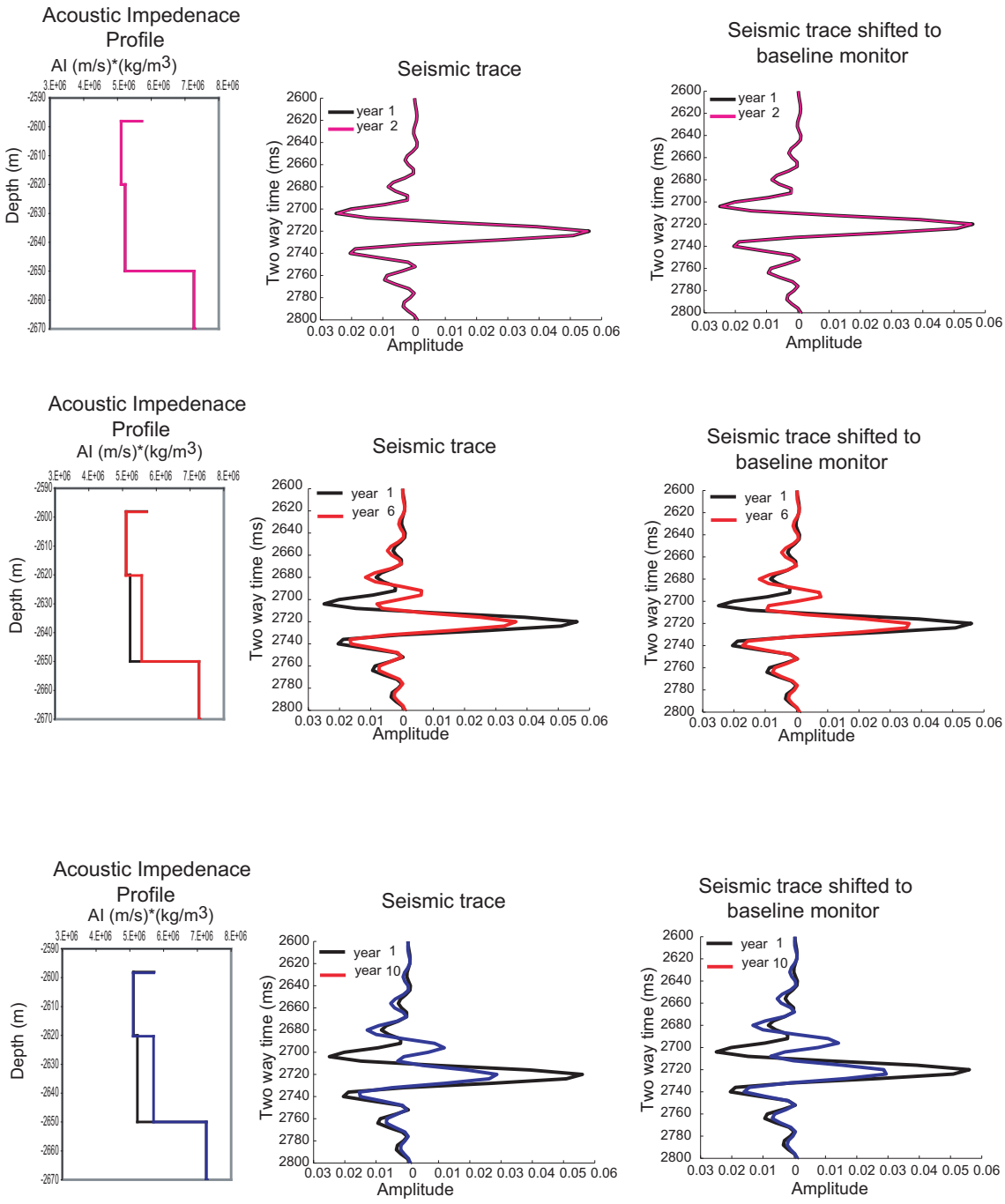

Figure 3.20: Changes in acoustic impedance logs and seismic traces for a rock of 35% porosity during 10 years of production.

3.4 Time-lapse attributes observed on the synthetic example

There are two time-lapse attributes due to pressure depletion and rock deformation that are observed in any compacting reservoir: a) time-lapse amplitude attributes and b) time-shifts. For the synthetic example, I estimated the Largest Positive Value (LPV) as a time-lapse amplitude attribute and the speed-up attribute as a time-shifts attribute. This section explains how these two attributes were extracted.

3.4.1 The Largest Positive Value attribute

Prior to the extraction of any amplitude attribute, it is necessary to align the time-lapse seismic volumes. Time-shifts are corrected in the Valhall Field by using a cross-correlation technique, which aligned all the monitor surveys with the baseline survey and then the time-lapse amplitude attributes are extracted. This method involves the cross correlation of a pair of traces in a sliding window of 60 ms length and the time-shift is picked as the lag in the cross correlation function. However, another approach was used in the synthetic seismic volumes to compensate for the induced time-shifts. The approach used to align the monitors to the baseline was as follows (figure 3.21):

- Step 1: Determine the two-way-time of the horizons on the baseline volume.
- Step 2: Estimate the reflection coefficients (R_c) for each monitor.
- Step 3: The time series for each of the monitor survey is created by combining the two-way-time from the baseline and the reflection coefficients estimated in step 2.
- Step 4: Convolve the time series with the seismic wavelet.

This procedure assures that the monitor surveys are leveled with the baseline, however the effect on the amplitude due to the acoustic impedance changes (reservoir and overburden/underburden) is not removed.

Comparison of the seismic data (figures 3.19 and 3.20) illustrates some differences due to the alignment of the monitor with the baseline. In general, the seismic trace from a 42% porosity rock seems to lose definition at the top of the reservoir when the correction is applied (figure 3.19). Here, the greatest compaction is occurring, therefore the major change wavelet shape are expected. In the seismic traces

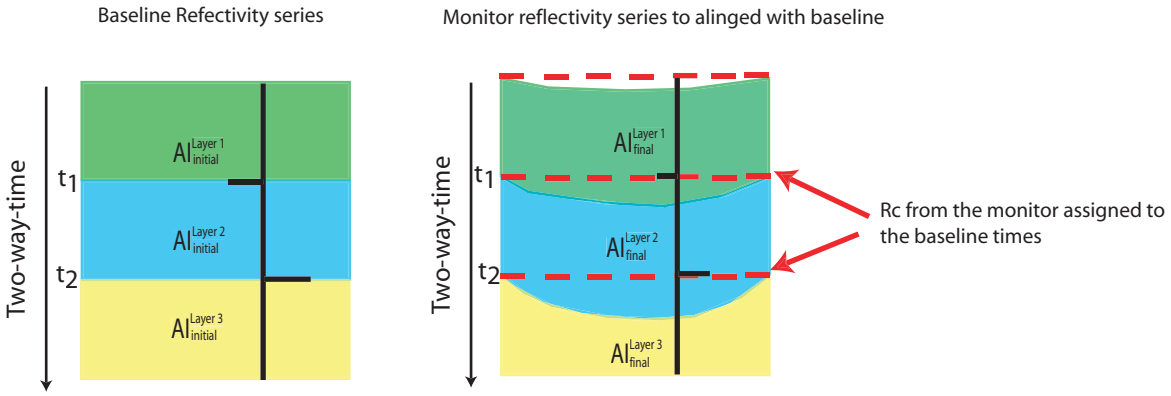

Figure 3.21: Diagram illustrating the approach taken to aligned the monitor volumes to the baseline: The methodology uses a reflectivity series that combines the reflection coefficients (Rc) from the monitor volume with times of the baseline survey.

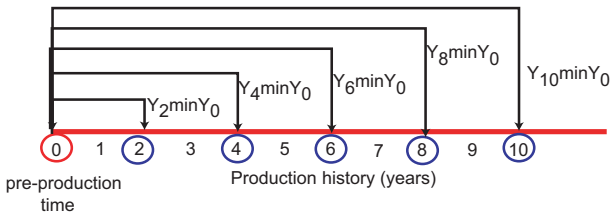

Figure 3.22: Procedure to extract the difference seismic volumes: The baseline volume was generated at pre-production conditions and five subsequent volumes were created every two years of production.

from porosities equal to 35% where the compaction is very low, the effect of shifting the monitor is undetectable (figure 3.20).

After the monitor surveys have been aligned with the baseline, the difference volumes are generated as illustrated in figure 3.22. For simplicity, the difference volumes are referred as "Year of the monitor survey minus Year of the baseline survey", for example Y12minY0 stands for the difference between the seismic volume at 12 years of production minus the seismic volume at pre-production conditions.

Extraction of largest positive amplitude attribute

I am interested in analyzing the time-lapse amplitude signature at top of the reservoir, which corresponds to the interface between the layer 9 and the reservoir. The top of the reservoir is a trough in the baseline survey. After generating the difference volumes, it is noticed that the time-lapse signal at the top of the reservoir, is a peak (figure 3.23). In the baseline survey, the seismic wavelet

crosses from a high acoustic impedance media to a low acoustic impedance media. However, after pressure depletion and rock compaction occurs, the layer 9 P-wave velocity decreases as a function of strain, an unloading / softening effect, while the P-wave velocity and density in the reservoir increase, a loading or hardening effect. This makes the acoustic impedance in layer 9 decrease and the acoustic impedance in the reservoir increase, therefore the trough becomes less negative. If the pressure depletion and the induced rock compaction continue to occur, these P wave impedance changes are accentuated more, and a polarity change can be expected at top of the reservoir (from a seismic trough in the baseline survey to a seismic peak in a monitor survey). This means that the seismic peak observed in the difference volumes becomes stronger as the depletion and the induced compaction increase.

To map the time-lapse amplitude signature, a similar approach to the one adopted for the Valhall Field to generate amplitude attributes is used in the example. The maximum positive amplitude is extracted in a window of 35 ms. The window starts 5 ms above the base of the reservoir and ends 40 ms above the base of the reservoir, in order to capture the time-lapse response at top of the reservoir (figure 3.24).

It is important to notice that I decided to use the Largest Positive Value as the input attribute for developing the technique that uses any time-lapse attributes to determine pressure changes in a compacting reservoir. Therefore, the subsequent sections mainly base their discussions on this attribute.

3.4.2 The speed-up attribute

An adapted version of the time-shift attributes was used in this study. The attribute captures the velocity increase (speed-up) due to pressure depletion in the reservoir. In order to explain this, figure 3.25 shows the way time-shifts evolve from the surface down to the base of the reservoir on a synthetic trace. Firstly, the accumulative time-shifts increase gradually as the wave travels towards the top of the reservoir, due to the decrease of the velocity and physical movement of the reflectors. When the wave is traveling inside the reservoir, the velocity is higher and the travel path is shorter, therefore the accumulative time-shift will decrease from the top to the base of the reservoir. This attribute must be extracted prior to any alignment between the surveys. The speed-up ($speed - up_R$) in the reservoir is extracted by subtracting the time-shift at the base of the reservoir (ΔT_{base}) from the

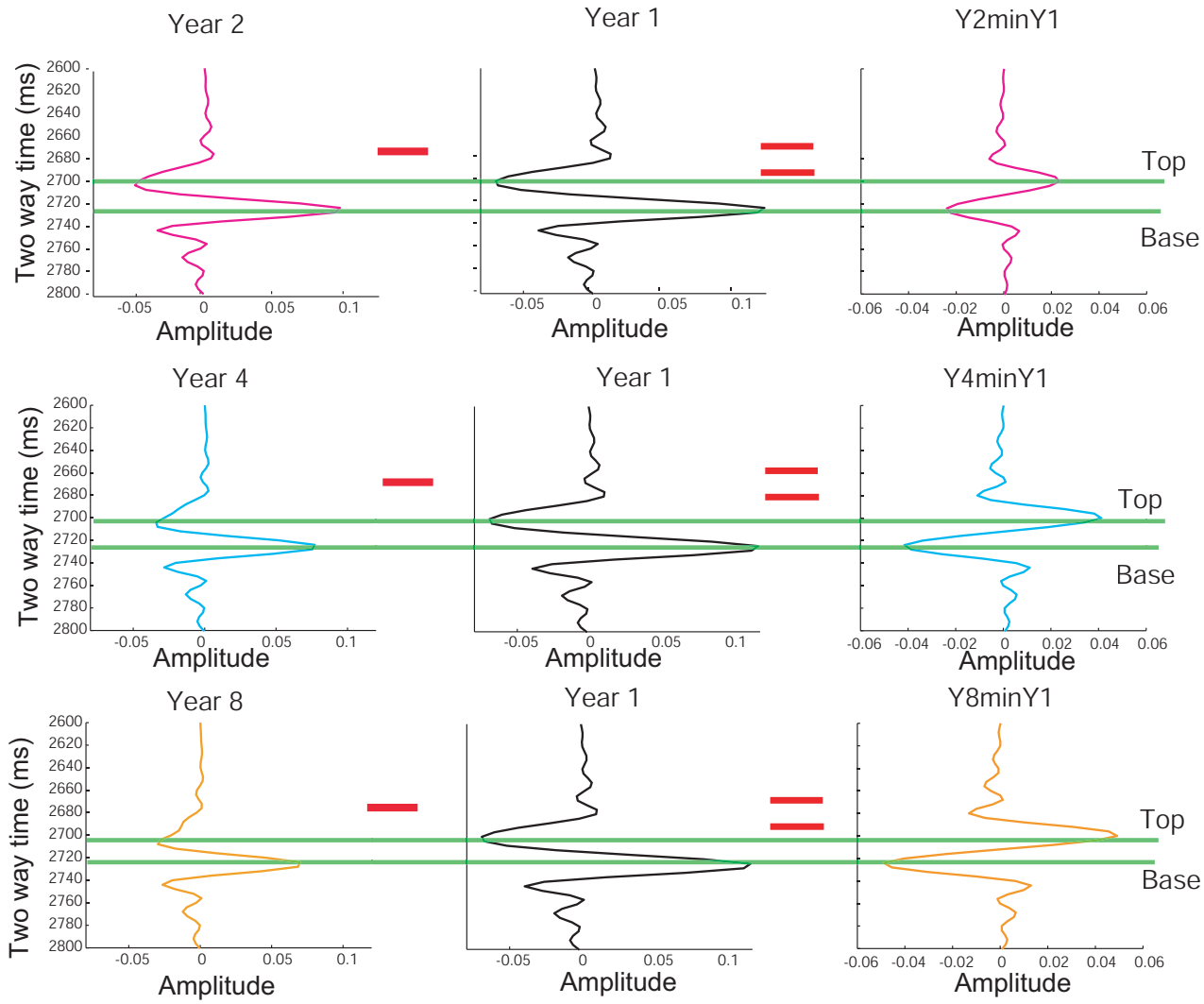

Figure 3.23: Time-lapse seismic response for a 41% porosity rock after 2, 4 and 8 years of production. The desirable time-lapse signal is a peak at the top of the reservoir and in order to capture it, the maximum positive amplitude was extracted in a 35 milliseconds window in each difference volume.

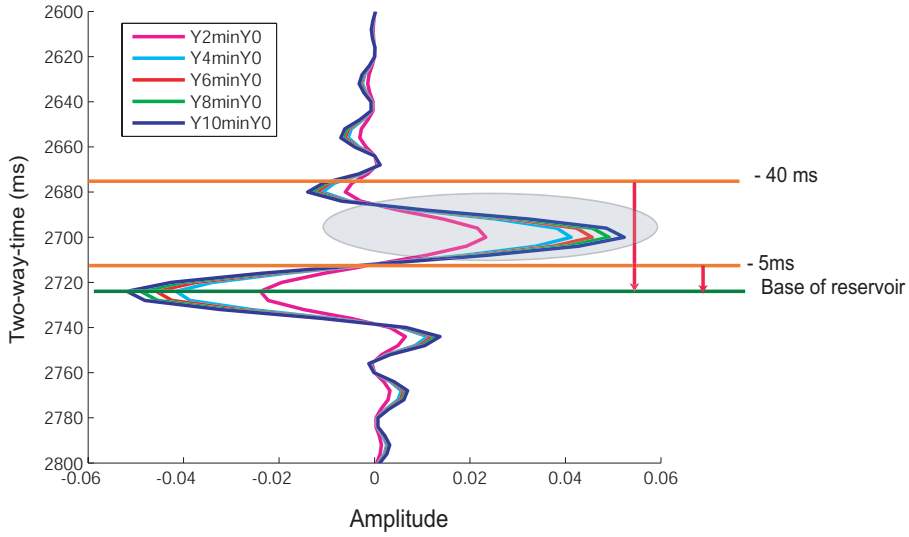

Figure 3.24: Approach taken to extract the maximum positive amplitude attribute. The reservoir base was taken as a reference; The maximum peak was extracted on a window located 5 and 40 milliseconds above the base. The same approach was used for the LoFS data in Valhall to extract the Largest Positive Value (LPV) amplitude attribute.

time-shift at the top of the reservoir (ΔT_{top}) and it can be expressed as follows:

$$speed - up_R = \Delta T_{base} - \Delta T_{top} \tag{3.5}$$

Conventionally, the two-way-time (TWT) at the top of the reservoir is equal to TWT that the wave needs to travel through the overburden. The same way, the reservoir base will be equal to TWT at the top plus the time the seismic wave needs to travel through the reservoir. Therefore, equation 3.5 can be re-written.

$$speed - up_R = \Big((TWT^2_{top} + TWT^2_{res}) - (TWT^{top}_1 + TWT^{res}_1)\Big) - \Big(TWT^2_{top} - TWT^1_{top}\Big) \tag{3.6}$$

where TWT^1_{top} and TWT^2_{top} is the top of the reservoir in time for the baseline and monitor respectively, while TWT^1_{res} and TWT^2_{res} is actual the two-way-time from the top to base reservoir. After eliminating the common terms, equation 3.6 becomes:

$$speed - up_{res} = TWT^2_{res} - TWT^1_{res} \tag{3.7}$$

Finally, two-way-time can be defined in terms of velocity and thickness. Therefore,

$$speed - up_{res} = 2 * \frac{H - \Delta H}{V_p + \Delta V_p} - 2 * \frac{H}{V_p} \tag{3.8}$$

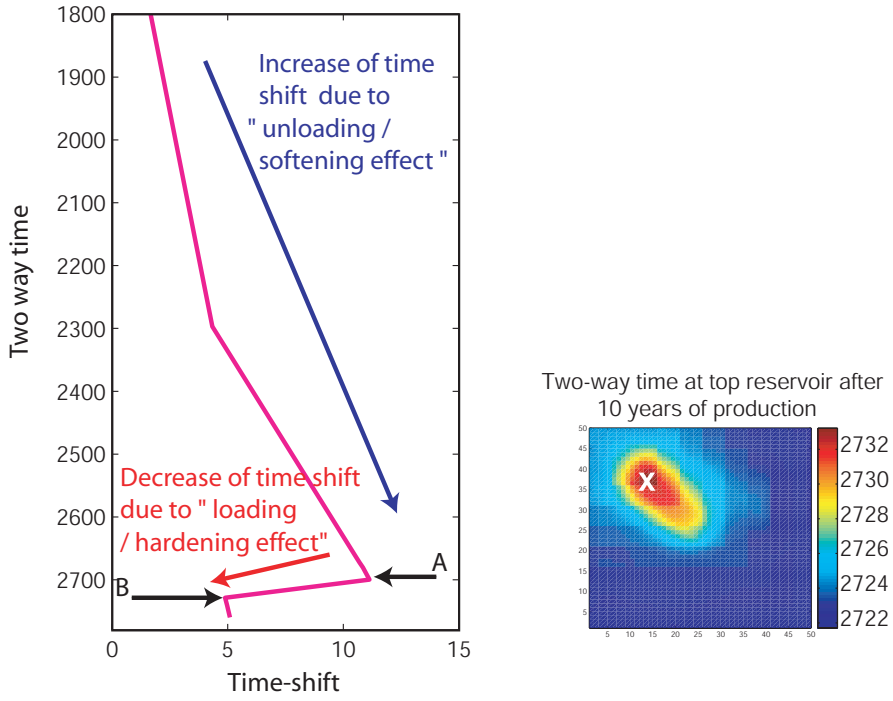

Figure 3.25: Cumulative time-shifts between time 10 and pre-production stage was extracted at the location X. The maximum time-shifts is reached at top of the reservoir due to the unloading effect on the overburden. The decrease in the time-shifts in the reservoir is attributed to the increase in velocity and the reservoir compaction. The speed-up attribute is estimated by subtracting the time-shifts at points A and B.

where H is initial reservoir thickness, ΔH is reservoir compaction, V_p is P-wave velocity and ΔV_p represents the changes in the compressional velocity. Equation 3.8 demonstrates that if the speed-up attribute can be extracted from the time-lapse seismic, the overburden time-shifts are not going to be present in the attribute. Therefore, the impact that overburden velocity changes are having on the time-lapse signal is eliminated. However, additional to the velocity changes in the reservoir, the speed-up attribute will respond to the reservoir compaction, that is the physical movement of the top and base.

3.5 Factors that influence the largest positive amplitude

The largest positive amplitude was selected to be used as the input seismic attribute to estimate pressure changes. Therefore this section discusses which factors other than pressure changes could

influence or vary the 4D amplitude response.

3.5.1 Reservoir thickness and tuning effects

The bed thickness has an effect on the seismic signature and therefore influences the time-lapse signal. For bed thickness equal or greater than a seismic wavelength there is little or no interference between the wavelets from top and bottom of the bed. However for thinner beds, the proximity between top and base causes constructive or destructive interference. The tuning thickness is equal to 1/4 wavelength. This means that beds thinner than 1/4 wavelength causes amplitude interference. To analyze this, the amplitude spectrum for the baseline volume was extracted at the zone of interest (figure 3.26). The dominant frequency is 20 Hz. If the initial P-wave velocity for a rock of 42% porosity is 2000 m/s, the tuning thickness is 25 m. Therefore, if the reservoir is thinner than 25 m, reflections undergo constructive interference and produce a single event of high amplitude. Assuming that the reservoir P-wave velocity increases between 2% and 14% and the dominant frequency is kept constant at 20 Hz. It is expected the reservoir need to be thicker than 25 m in order to be resolved as a two separate events (top and base) on the subsequent seismic volumes (table 3.6). In the model, the initial thickness is 30 m assuring that the top and bottom of the reservoir are imaged at the baseline volume and however for the monitor surveys, the reservoir thickness decreases due to the rock compaction but the tuning thickness increases as the reservoir velocities increase. It is important to be aware of the tuning effect when time-lapse amplitude attributes are cross-plotted against reservoir dynamic properties (i.e. pressure or effective stress) since some of the scatter on the cross-plots can be attributed to the constructive/destructive interference caused by seismic tuning. The thickness influence is further discussed in chapter 5, where a synthetic model was created using the geological structure observed on the south east flank of Valhall Field.

Parameters	Initial	2 %	4 %	8 %	10 %	12 %	14 %
Velocity (m/sg)	2000	2040	2080	2120	2160	2200	2240
Tunning thickness (m)	25	25.5	26	26.5	27	27.5	28

Table 3.6: Tuning thickness as a function of P-wave velocity. The table summarizes the results of estimating the tuning thickness for different P-wave velocities, assuming a constant dominant frequency of 20 Hz.

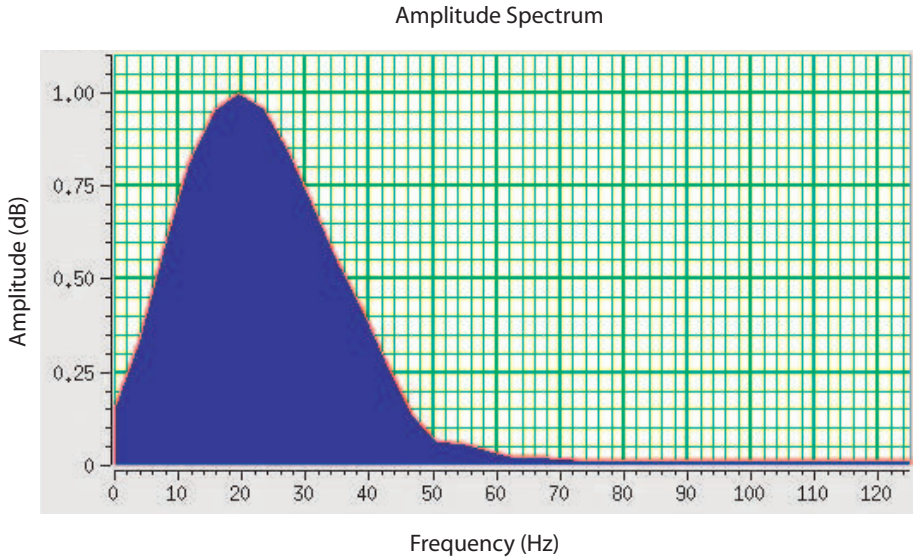

Figure 3.26: The amplitude spectrum of the baseline survey was extracted in a window of 100 ms at the interest zone. The dominant frequency was 20 Hz and the higher frequency is 50 Hz. The dominant frequency was used to estimate the tuning thickness in table 3.6.

3.5.2 Reservoir fluids

The seismic changes will also depend on the presence of gas due to pressure depletion. Gas will decrease the P wave impedance, therefore the combined effect of pressure depletion and gas coming out of solution can produce a small overall change in acoustic impedance. This effect will be further discuss in chapter 6

3.5.3 Seismic properties in the layer immediately above the reservoir

The acoustic properties of layer 9 and the manner this layer responds to the rock deformation (strain) is another element to take into account. If the P wave impedance on layer 9 decreases, the impedance contrast can be accentuated. The top of the reservoir can be undetectable in a monitor survey, if both reflection coefficients at the lithological boundary are equal. This is possible since the P wave impedance contrast can be very small at initial conditions and the production activity could just equalize the acoustic properties for both layers.

3.6 Analysis of the cross-plots of the largest positive amplitude attribute and pressure changes

Figure 3.27 shows the largest positive amplitude attribute maps, generated from the difference seismic cubes between the 5 monitor surveys and the baseline, together with the pressure and porosity changes for those times. A visual comparison between the time-lapse amplitude maps and the pressure depletion maps indicates a strong similarity. However as the production evolves, the porosity and effective stress changes influence the acoustic properties and are captured in the time-lapse signal. Indeed there is also a strong visual correlation between porosity changes and time-lapse amplitudes displays. To investigate this further, pressure changes and time-lapse amplitude response are cross-plotted (figure 3.28A). The selected data points represent the different initial porosities; their locations are shown in figure 3.28B. For each location point, 5 pairs of data are extracted, the pressure and the amplitude changes between the five monitor surveys and the pre-production survey (i.e. Y2minY1, Y4minY1, Y6minY1, Y8minY1 and Y10minY1).

Figure 3.28A exhibits a correlation between the time-lapse attribute and pressure changes for some of the porosity families, it is observed that the trend is influenced by the initial porosity. The data points suggest that the largest positive amplitude attribute recorded between the baseline survey and the monitor surveys can be approximated by a power law equation (eq. 3.9).

$$\Delta A = C_1 * (\Delta P^{C_2}) \tag{3.9}$$

where ΔA and ΔP represent the change in amplitude and pressure respectively and C_1 and C_2 are the constants that depend on the initial porosities. Using this equation, I determined the best fit coefficients for each porosity family. These are listed in table 3.7

Figure 3.28C shows the trend lines for the initial porosity families of the model. Before major compaction occurs (small pressure changes), the amplitude changes are very similar for all the porosity families. However, as the pressure difference increases, the curves begin to separate because the rock deformation starts to significantly influence the P-wave velocity and the rock density. This means that two areas with different initial porosities undergoing the same pressure depletion produce two different time-lapse amplitude anomalies and the largest anomaly corresponds to the highest porosity.

To estimate pressure changes using equation 3.9, one needs to estimate the coefficients (C_1 and C_2)

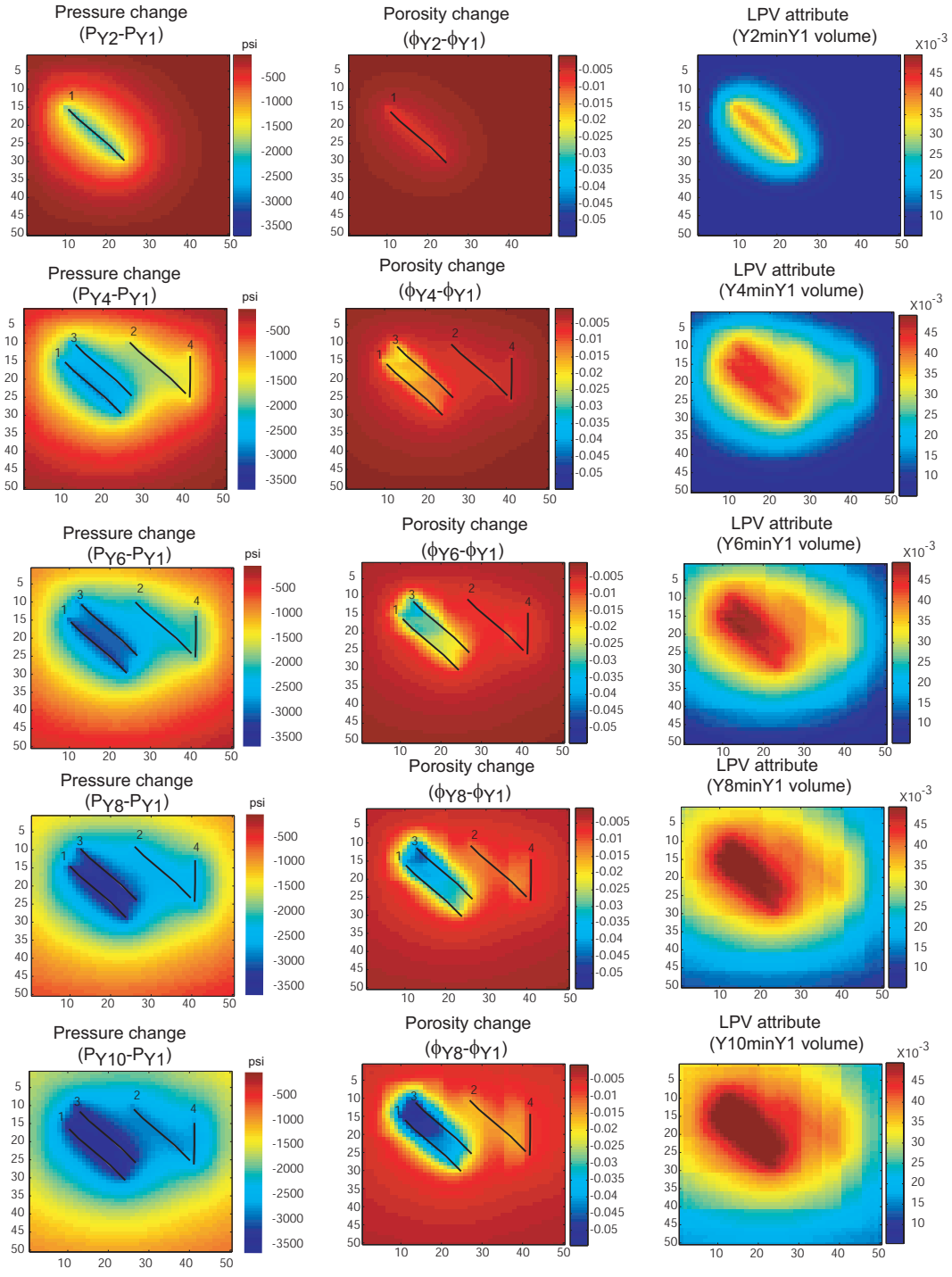

Figure 3.27: Pressure and porosity changes, together with the corresponding largest amplitude value attribute maps.

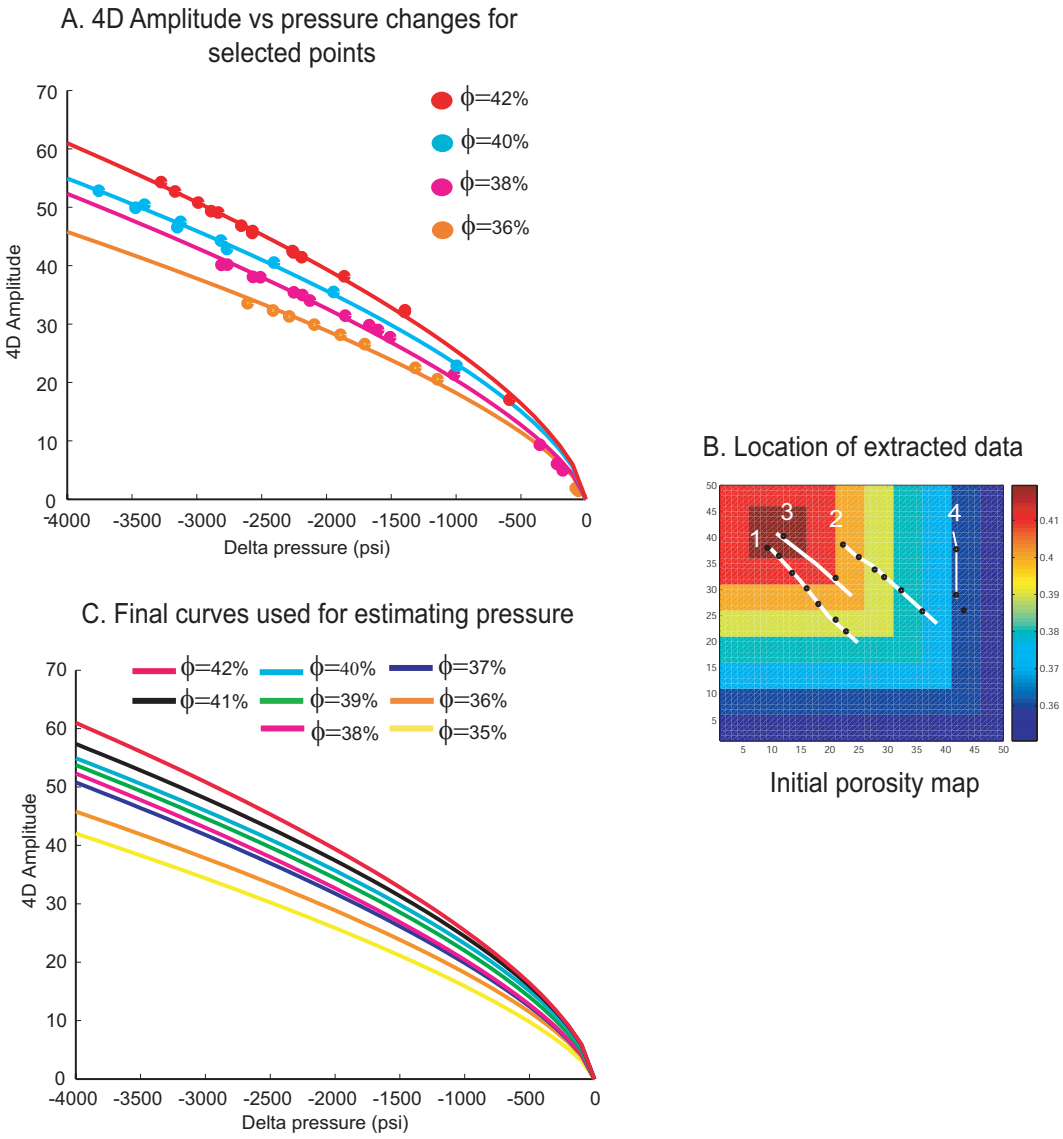

Figure 3.28: Cross plot between the time-lapse amplitude and the pressure changes. The data points suggest that the time-lapse for the amplitude attribute recorded between the baseline survey and the monitor surveys can be approximated by a power law equation (eq. 3.9). The black dots on the porosity map represent the data used in the cross-plots. Most of data were taken around the wells.

ϕ_i (%)	C_1	C_2	R^2	RMSE
35	0.128	0.7019	0.998	0.4147
36	0.1832	0.671	0.995	0.8664
37	0.1844	0.6774	0.995	0.9543
38	0.1864	0.6794	0.995	0.8189
39	0.2543	0.6455	0.995	0.871
40	0.315	0.62223	0.996	0.5757
41	0.336	0.6215	0.971	0.9697
42	0.35	0.621	0.997	0.55

Table 3.7: Coefficients C_1 and C_2 for equation 3.9. The fourth column is the coefficient of multiple determination (R^2). This statistic measures how successful the fit is in explaining the variation of the data. A value closer to 1 indicates a better fit. The fifth column represent the RMSE, the root mean squared error. A value closer to 0 indicates a better fit

for each porosity class present on the model. In a real case study, this might be a very difficult task if the initial porosity distribution is very heterogenous. Therefore finding a correlation between the coefficients and the initial porosity is necessary. Linear best fits were used to estimate the relationship between these coefficients and the porosity families present on the model (figure 3.29) and define the following equations:

$$C_1 = 3.306 * (\phi_i) - 1.031 \tag{3.10}$$

$$C_2 = -1.206 * (\phi_i) + 1.119 \tag{3.11}$$

Assuming that C_1 and C_2 are invariant across the reservoir and replacing equations 3.10 and 3.11 in equation 3.9, the changes in amplitude due to pressure depletion can be re-written as follows:

$$\Delta A = (3.306 * \phi_i + -1.031) * (\Delta {P_f}^{(-1.206 * \phi_i) + 1.119}) \tag{3.12}$$

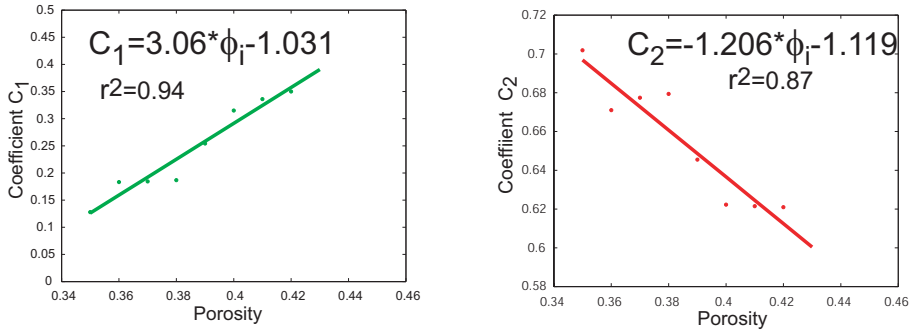

Figure 3.29: Coefficients (C_1 and C_2) against Initial porosity. Linear best fits were used to estimate the relationship between the coefficients (C_1 and C_2) in equation 3.9 and the porosity families. The correlation coefficients (r^2) from the linear fits are close to 1.

3.7 Pressure changes inverted from the largest positive amplitude attribute

The pressure changes maps for times 6, 8 and 10 were generated using two approaches. The first method uses equation 3.9, where the coefficients C_1 and C_2 are determined for each porosity family, whereas the second method is based on equation 3.12, where linear correlations between the initial porosity and C_1 and C_2 are adopted.

The results for both approaches together with the pressure maps from the simulator, are shown in figure 3.30. The predicted pressure maps from the time-lapse are very similar to the simulator outputs. The absolute errors from the estimations using equation 3.12 are slightly higher than the ones originated by inverting with equation 3.9 (figure 3.31). However, both equations prove that it could be possible to invert for pressure from time-lapse seismic on condition the initial porosities are known.

To investigate the error in the pressure predictions, I analyze the uniqueness of the coefficients, C_1 and C_2. The pressure changes at each grid cell of the model were mapped against their corresponding time-lapse response (figure 3.32). Even though the patterns for the each initial porosity can be distinguished, the curves show scatter as the pressure depletion increases, opening the possibility that besides the pressure depletion, other factors can be controlling the time-lapse amplitude response.

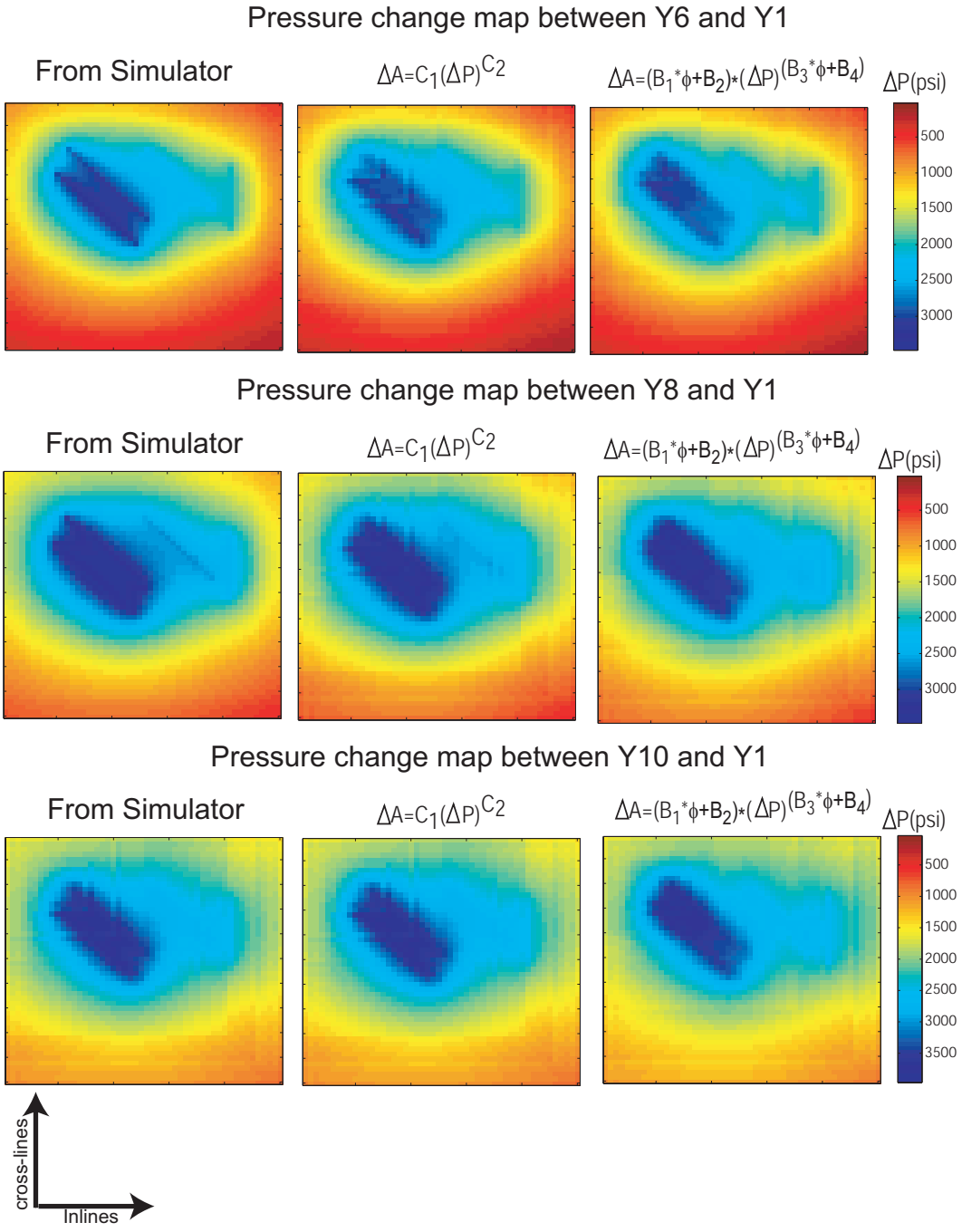

Figure 3.30: Pressure change maps for Y6minY1, Y8minY1 and Y10minY1 seismic volumes.

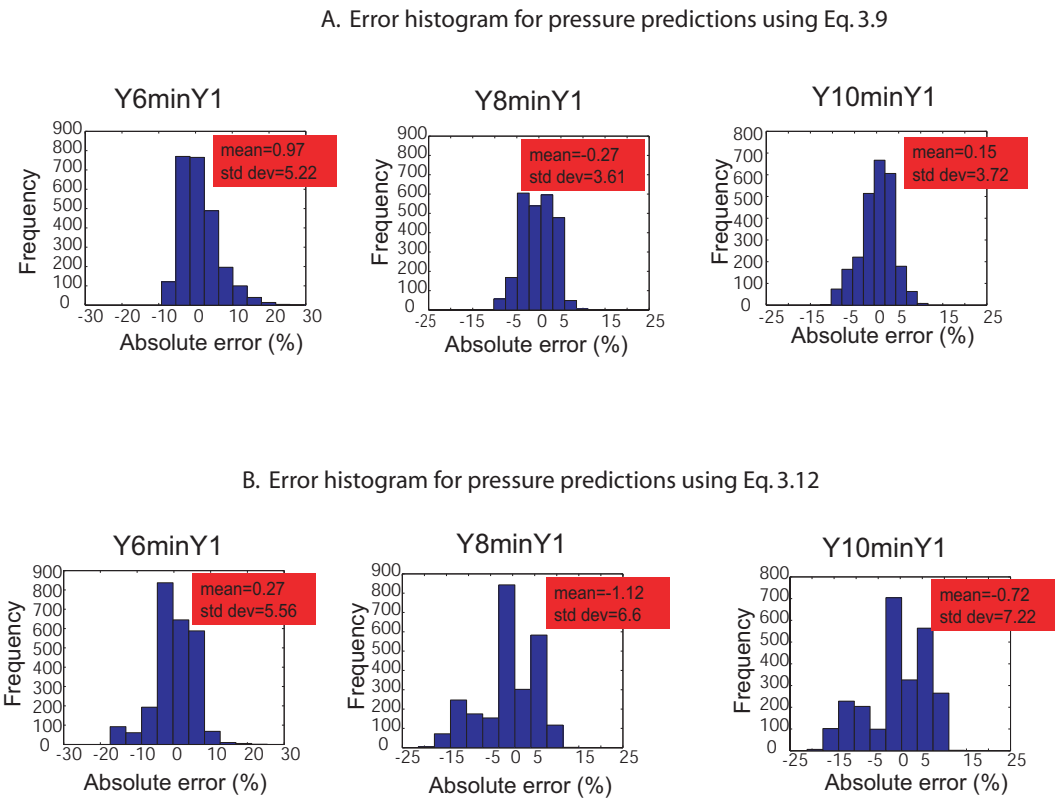

Figure 3.31: A. Error between pressure estimated for seismic and the outputs from the simulator using equation 3.9. B. Error between pressure estimated for seismic and the outputs from the simulator using equation 3.12.

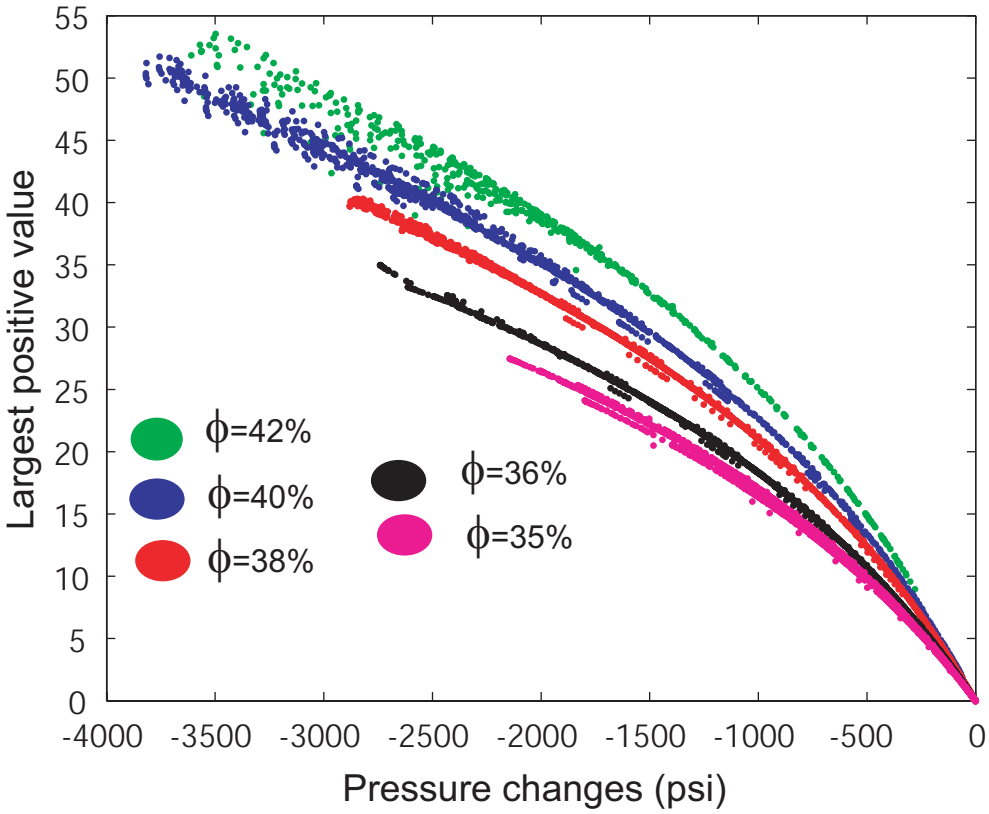

Figure 3.32: Largest positive value attribute vs pressure changes, for all the grid cells which have an initial porosity of 42%, 40%, 38%, 36% and 35%.

3.8 Causes for the errors on the pressure predictions from the largest positive amplitude attribute

This section discusses the factors that causes errors on the pressure prediction from time-lapse amplitude. Those factors are: the effective stress changes and acoustic impedance changes in the layer immediately above the reservoir

3.8.1 The effective stress changes

Figure 3.33 shows cross plots of time-lapse amplitude versus both fluid pressure and effective stress changes. The time-lapse amplitude with effective stress shows less scatter, this is thus a better definition of the trends for each porosity class. The effective stress changes in response to changes in the pressure and the average normal stress. The average normal stress starts to vary since the reservoir begins to compact, however these changes become more important on time-lapse seismic, when the compaction is higher. Therefore, it is concluded that if the reservoir compaction causes considerable changes in the average normal stress, the time-lapse seismic amplitude is more responsive to effective stress changes than pressure depletion. The manner in which the normal stresses responds to compaction induced by pressure depletion, depends on the geological settings, overburden and reservoir geomechanical properties and distribution of faults and fractures. As has been discussed on section 3.1.4, the compaction causes a stress redistribution in the cap rock resulting in changes of the mean normal stress. But why do the normal stress changes influence the seismic response? This can be explained by looking into the Gassmann fluid substitution method (Gassmann, 1951).

Gassmann model considers a saturated rock to be composed of rock grains with a frame modulus and a pore fluid. The bulk modulus of the saturated rock (K_{sat}) is defined in equation 3.13. K_{sat} is used to estimate the P-wave velocity (eq. 3.14). Equation 3.13 shows that K_{sat} depends on the bulk frame modulus (K_{fr}), the grain frame modulus (K_g) and the bulk fluid modulus (K_{fl}). K_{fr} describes the structural integrity of the rock and is function of the effective stress (K_{fr} increases as the effective stress increases). K_{fl} is a function of the pore fluid pressure and the fluid mix present in the rock. The effective stress is the difference between normal average stress and pore pressure. Therefore, the K_{fr} and subsequently K_{sat}, respond to the pore pressure and the normal average stress changes. Furthermore, equation 3.14 shows that the effect of both pore pressure and normal

average stress changes is transferred into the P-wave velocity.

$$Ksat = K_{fr} + \frac{1 - (\frac{K_{fr}}{K_g})^2}{\frac{\phi}{K_{fl}} + \frac{(1-\phi)}{K_g} - \frac{K_{fr}}{K_g^2}} \tag{3.13}$$

$$V_p = \sqrt{\frac{K_{sat} + \frac{4}{3}\mu}{\rho}} \tag{3.14}$$

From Figure 3.33, it is observed that for porosities higher than 39% there is a change in the trend of the curve. To understand this, the effective stress changes, porosity changes and time-lapse amplitude for a initial porosity of 42% were used to create figure 3.34. The effective stress changes are on the x-axis, the porosity changes are on the left y-axis and time-lapse amplitude is on the right y-axis. An important remark from this plot, is that the average effective stress against time-lapse amplitude plot (red data) exhibits a gentle change of the trend at 1200 psi. This change coincides with the faster decrease on porosity (blue data). The reason why this effect is not noticeable for the lower initial porosities is that they have not reached the point when a greater rock compaction occurs.

3.8.2 Acoustic impedance changes in Layer 9

Another important factor that increases the discrepancies in the pressure prediction is the variation of seismic velocities and impedance of the layer immediately above of the reservoir (Layer 9 for the synthetic example). To assess the influence of the overburden velocity changes, I analyzed the main differences between neglecting the overburden velocity changes or considering them on the time-lapse seismic response.

Scenario I has been presented in the previous sections. The time-lapse amplitude attributes from scenario I are extracted from the difference volumes that take into account overburden velocity changes as a function of strain (R-factor=5). In contrast, scenario II describes a case where the time-lapse amplitude attributes were extracted from seismic difference volumes where no changes on the overburden are assumed (R-factor=0).

Figure 3.35 shows the cross-plot for time-lapse amplitude against pressure changes and effective stress changes for scenario II (figure 3.33 is the equivalent plot for scenario I). These graphs show better defined trends for each porosity family for scenario II compared with scenario I. In particular,

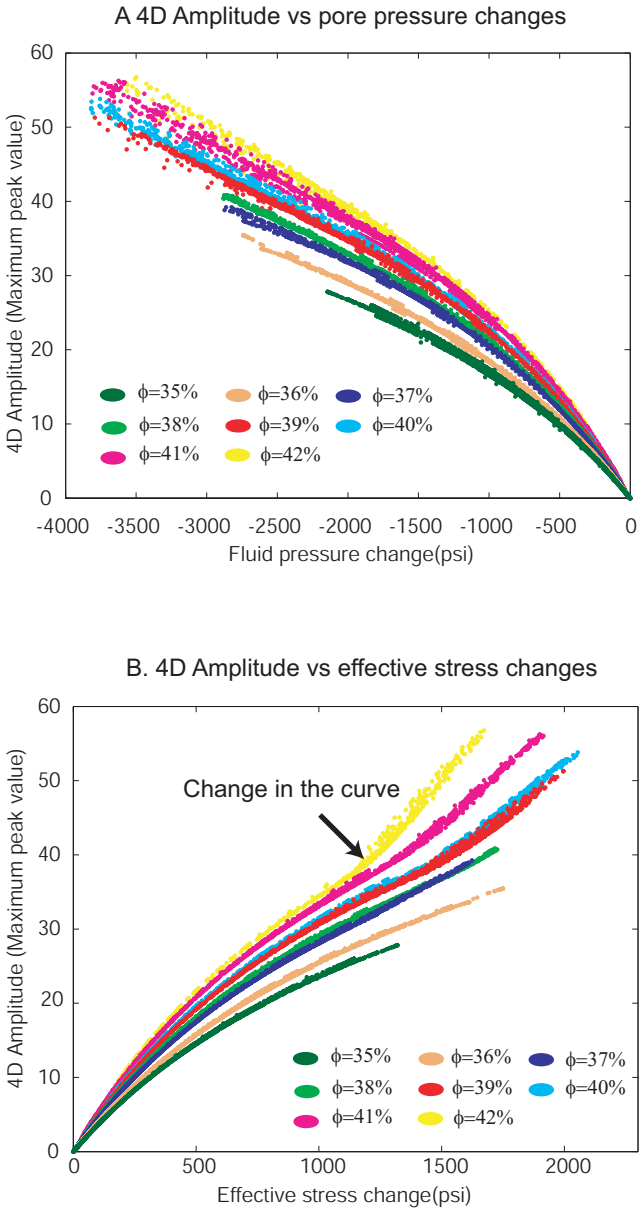

Figure 3.33: Cross-plots between dynamic reservoir properties and time-lapse amplitude for all the initial porosities used on the model I. A. Pressure changes against time-lapse amplitude. B. Effective stress changes against time-lapse amplitude. These two graphs show that the best correlation with the time-lapse seismic attribute is given by the effective stress. In plot B, the black arrow indicates that for high porosity rocks, the curves divert and become more linear. This is caused by the increase in the compaction rate (figure 3.34).

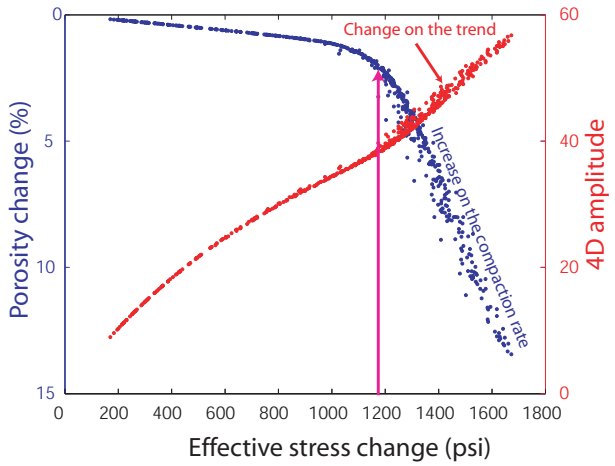

Figure 3.34: Comparison between time-lapse amplitude, effective stress changes and porosity reduction for a initial porosity of 42%. The increase of rate of compaction coincides with the change on the effective stress vs time-lapse amplitude curve (red arrow).

the trends for time-lapse amplitude versus effective stress changes become better defined when the overburden velocity effect is removed (figure 3.35B).

Using the time-lapse amplitude maps from scenario II, new coefficients for equation 3.9 are generated for each initial porosity family (table 3.8). Subsequently, a pressure change map was calculated and compared with the one estimated for scenario I (figure 3.36). The pressure change map for scenario I was generated using the coefficients from table 3.7. Both maps represent the pressure depletion after 8 years of production. Figure 3.37 shows the absolute error distribution between the pore pressure depletion predicted from the time-lapse seismic and the one predicted from the reservoir model. The histogram in figure 3.37A uses the pressure map estimated from time-lapse seismic when the overburden velocities change due to rock compaction (Scenario I). The histogram in figure 3.37B uses the pressure map estimated from time-lapse seismic when the overburden velocities are kept constant through time (Scenario II). The pressure change map generated for scenario II gives a slightly better prediction of the reservoir depletion (mean error=-4.0 and standard deviation=2.0) compared to pressure map estimated for scenario I (mean error=-0.27 and standard deviation=4).

The reduction in error when no overburden velocity changes are assumed indicates that unless the seismic data is compensated for changes in the overburden velocities, an associated error is going to be present on the pressure maps inverted from time-lapse amplitude attributes. Normally, time-shift volumes are calculated and applied to monitor surveys to correct for the overburden velocity changes

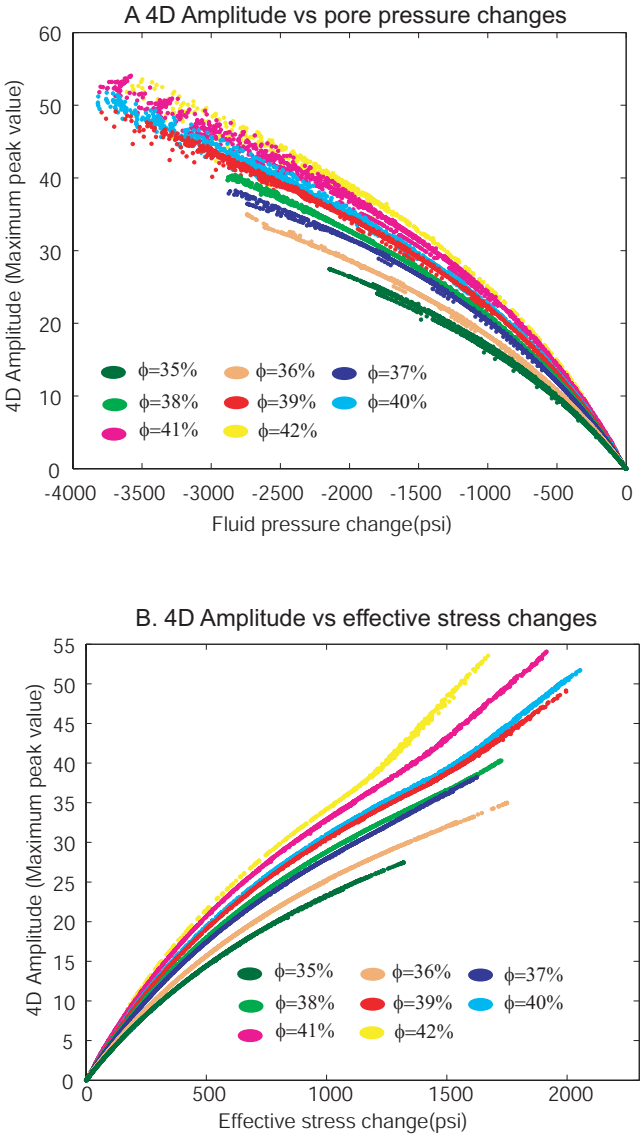

Figure 3.35: Cross-plots between dynamic reservoir properties and time-lapse amplitude for all the initial porosities used on the model II. A. Pressure changes against time-lapse amplitude. B. Effective stress changes against time-lapse amplitude. It was assumed that no changes in the overburden velocities are occurring. These graphs show better defined trends for each porosity family compared with the ones in figure 3.33.

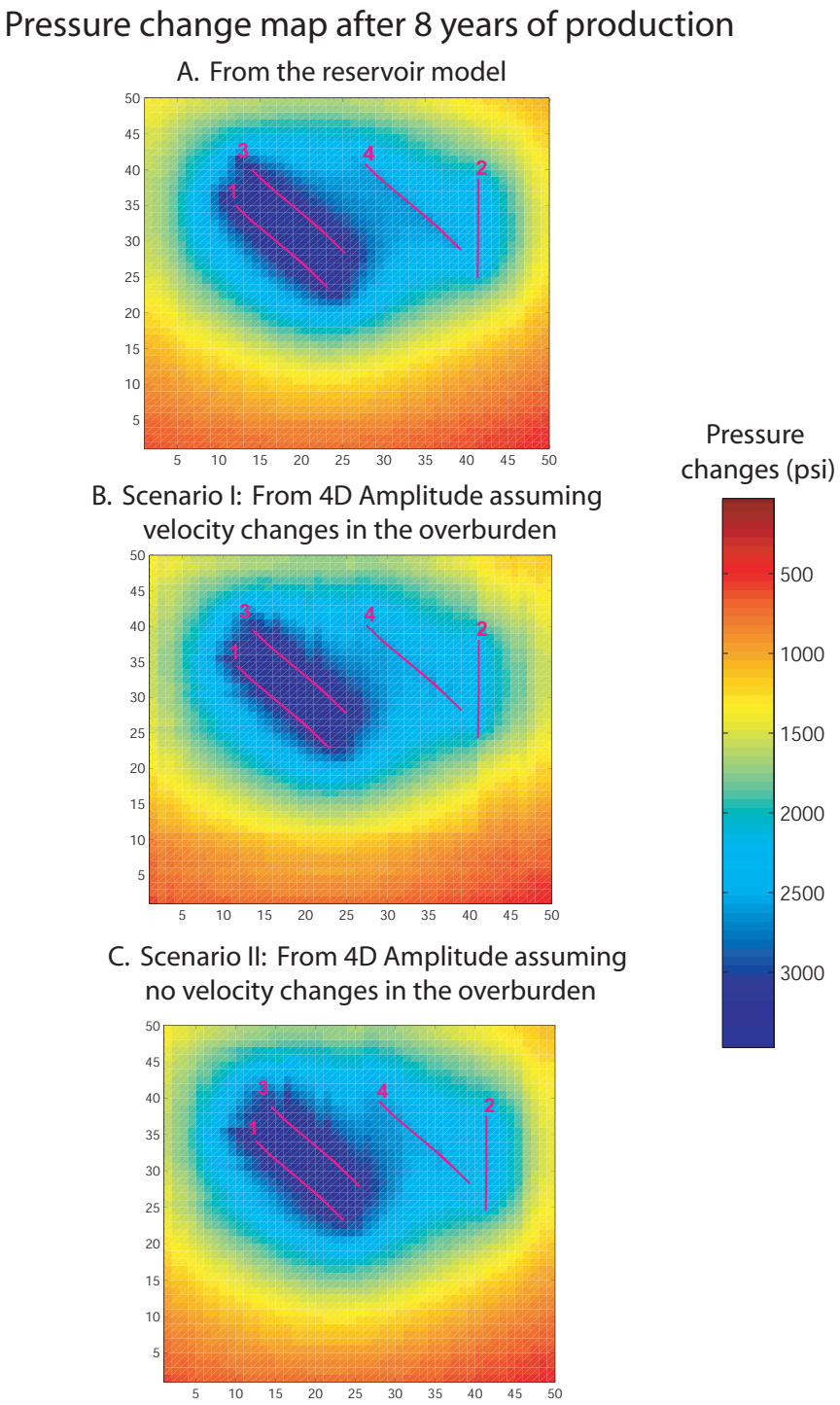

Figure 3.36: Comparison between the pressure change maps estimated for scenarios I and II. A. Pressure change output from the reservoir model. B. Pressure change map for scenario I: This map was generated using the coefficients in table 3.7. B. Pressure change map for scenario II: This map was generated using the coefficients in table 3.8.

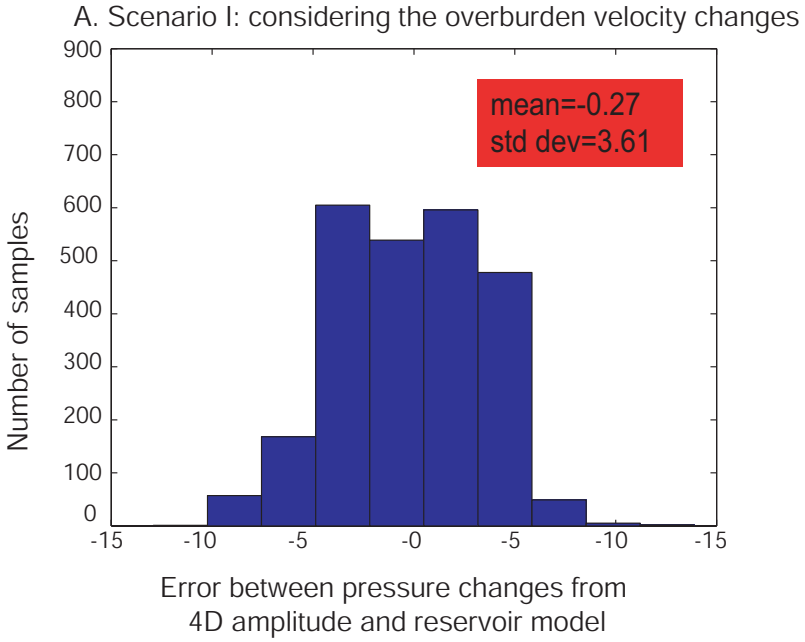

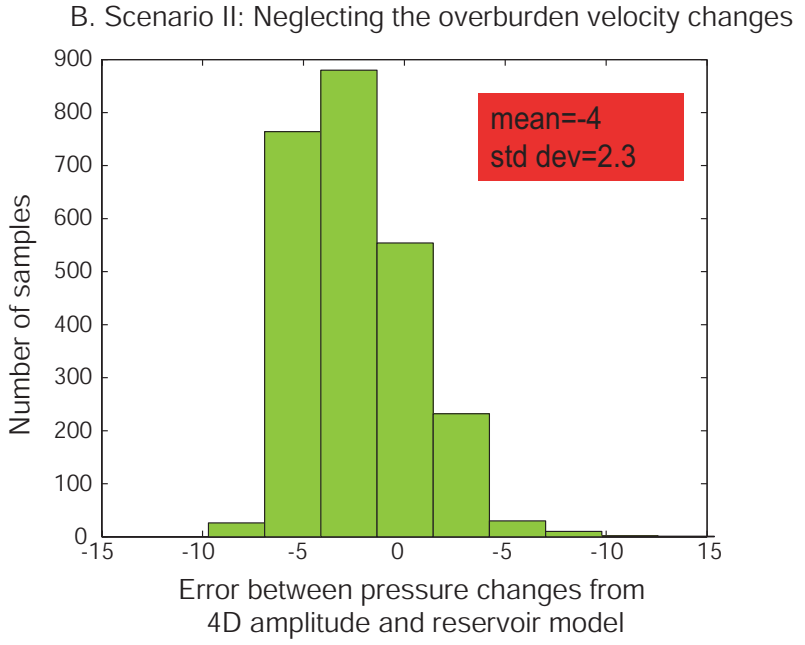

Figure 3.37: Error distribution for scenarios I and II. A. Scenario I: Error between pressure predicted from the reservoir simulator and the pressure map estimated from time-lapse amplitude. B. Scenario II: Error between pressure predicted from the reservoir simulator and the pressure map estimated from time-lapse amplitude.

$\phi_i(\%)$	C_1	C_2	R^2
35	0.09636	0.7439	0.99
36	0.176	0.6684	0.99
37	0.2013	0.6633	0.99
38	0.1927	0.6738	0.99
39	0.3036	0.6193	0.99
40	0.3751	0.5969	0.99
41	0.4351	0.5826	0.99
42	0.4117	0.5962	0.99

Table 3.8: Coefficients C_1 and C_2 for equation 3.9, when overburden velocities changes are ignored (scenario II). These coefficients were used to generate map shown in figure 3.36B.

and physical movement of the reflector due to compaction. This correction aligns the monitor surveys to the baseline volume, however it does not compensate for the changes in the reflectivity at the top of reservoir.

To explain how much the changes in overburden velocities contribute to the time-lapse amplitude response, I estimated the difference (DIF) between the time-lapse amplitude from scenarios I and II as indicated by equation 3.15. The map of DIF is very similar to the vertical strain for the layer immediately above the reservoir (layer 9) as shown in figure 3.38. The strong correlation between DIF and vertical strain is expected because the overburden velocity changes are assumed to be function of vertical strain (eq. 2.15). Figure 3.39 is the cross-plot between strain (ϵ_z) against DIF. There is a linear relationship between these two parameters. The best linear fit is given by the equation 3.16 with a correlation coefficient (r^2) of 0.999. If the changes in 4D amplitude response due to the vertical strain in the layer immediately above the reservoir can be estimated it may be possible to compensate for these changes and get a better pressure prediction from the time-lapse amplitude attributes. For this to be achieved, a calibrated geomechanical model is required in order to get the vertical strain in the overburden. In chapter 6, I will explore more the influence of the overburden by a) assuming different R-factor and b) assuming different linear elastic parameters for layer 9 (Young's modulus and Poisson's ratio).

$$DIF = \Delta A_I - \Delta A_{II} \tag{3.15}$$

$$DIF = 1289 * \epsilon_z \tag{3.16}$$

where ΔA_I is the time-lapse amplitude map for scenario I, ΔA_{II} is the time-lapse amplitude map for scenario II and ϵ_z is the vertical strain in layer 9.

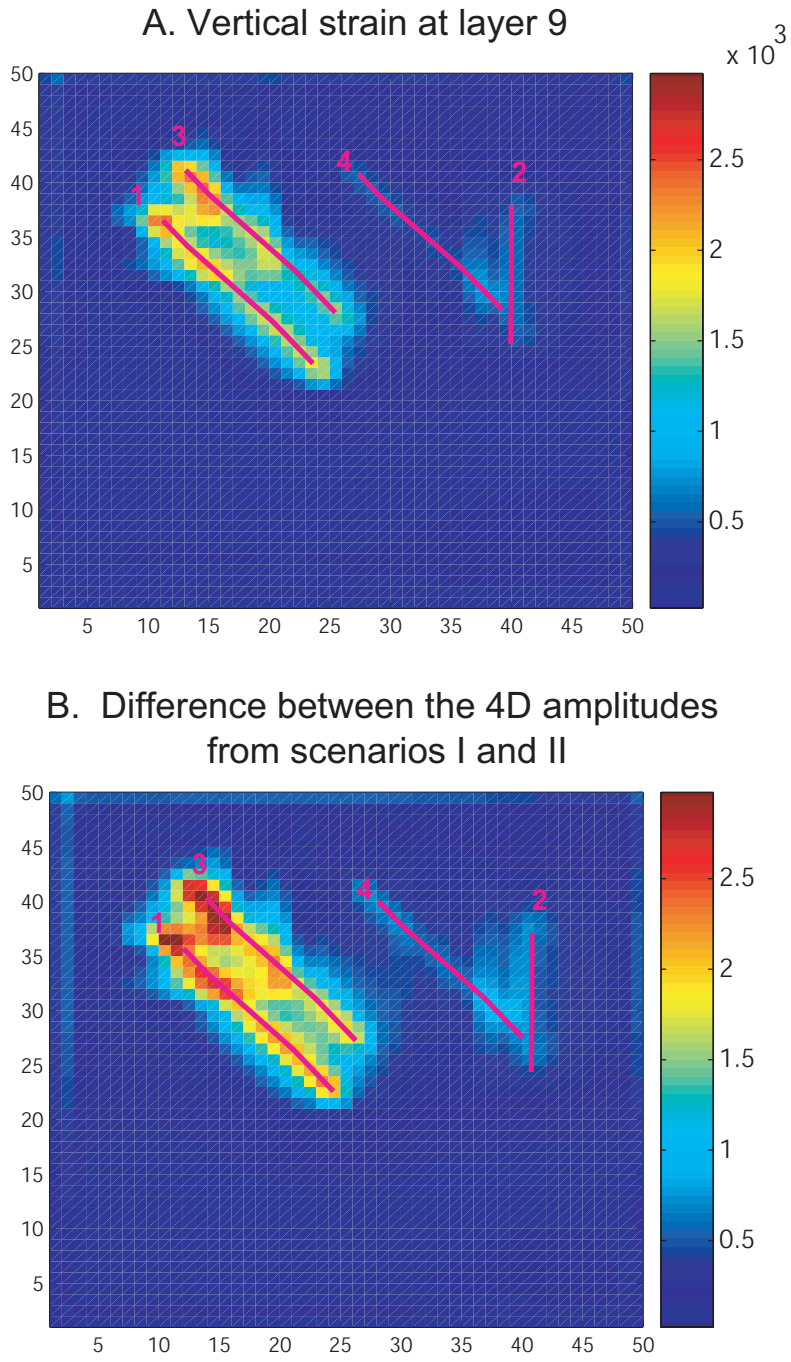

Figure 3.38: Effect of the vertical strain in the time-lapse amplitude response. A. Vertical strain map in the layer 9. Layer 9 is located immediately above the reservoir. B. Difference between the time-lapse amplitude response from scenarios I and II. The strong correlation between the top and bottom map is because the acoustic impedance changes in layer 9 are function of the vertical strain. For the synthetic example, the velocities changes in the overburden causes an increase of the time-lapse amplitudes by up to 6%.

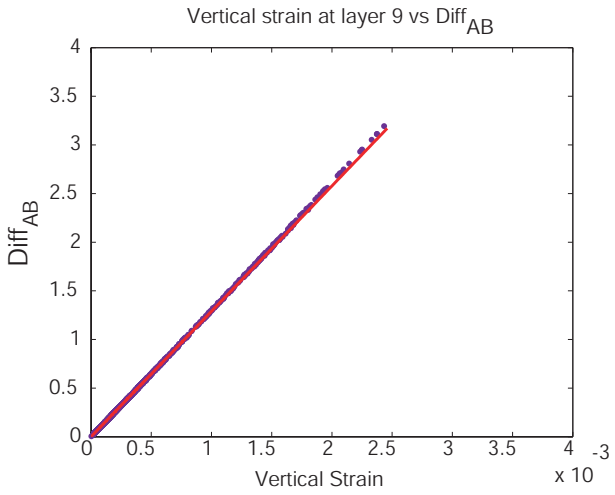

Figure 3.39: Cross-plot between vertical strain in layer 9 and the parameter DIF. There is a linear relationship between the vertical strain at layer 9 and the DIF (eq. 3.16). The parameter DIF is defined as the difference between the time-lapse amplitude response from scenarios I and II. The linearity between vertical strain and DIF opens the possibility of predicting the influence of the overburden velocity changes have in the time-lapse amplitude response. This requires a well calibrated geomechanical model.

3.9 Correlation between speed-up attribute and the pore-pressure and effective stress changes

I investigate the possible relationship that could exist between the speed-up attribute and the dynamic reservoir properties in this section.

Figure 3.40A shows the cross plot of the speed-up attribute against pressure changes. Figure 3.40B shows the cross plot between the 4D amplitude and pressure. The effect that the overburden velocity has on the 4D amplitude has been removed (discussed in section 3.8). For both graphs, a good correlation with pressure for each initial porosity is observed. The scatter on the data at high pressure depletion is due to the normal stress changes caused by the rock compaction. The time-lapse amplitude is sensitive to effective stress changes. The graph of the speed-up attribute versus effective stress illustrates the same behavior (figure 3.40D) and perhaps a better definition of the trends for different porosities is observed. To eliminate the effect that the overburden velocities have on the 4D amplitude attributes, I assume a R-factor equals to 0 and extract the 4D attribute again. For the case of the speed-up attribute, the effect of velocity changes have on the time-shifts are removed when the attribute is derived as shown by equation 3.8.

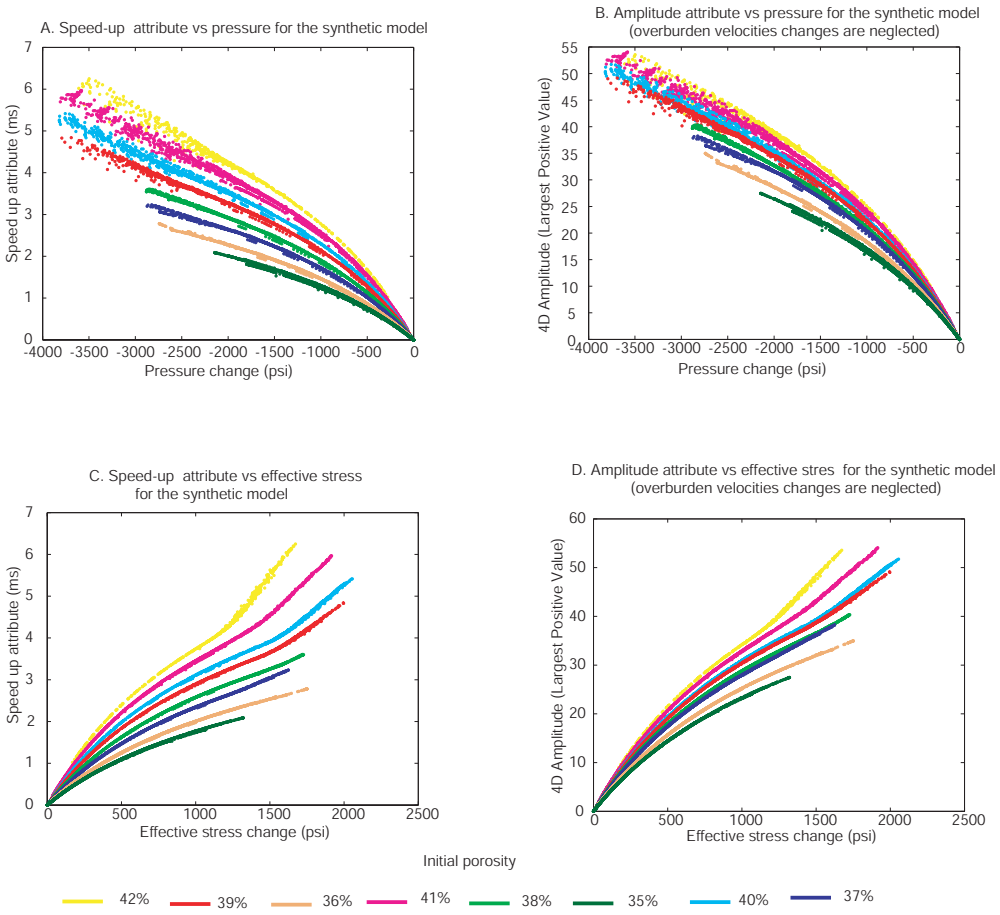

Figure 3.40: Reservoir properties changes (effective stress and fluid pressure) against the speed-up attribute in the synthetic example. A. Speed up attribute vs pressure depletion. B. Time-lapse amplitude vs pressure depletion. C. Speed up attribute vs Effective stress changes. D. Time-lapse amplitude vs effective stress. Graph A and B are very similar, however the definition of the curves for each initial porosity is better on the speed-up attribute cross-plot. Graphs C and D show that the 4D signal (time-shifts and 4D amplitude) correlates better with effective stress changes.

3.10 Summary

In this chapter a synthetic example was presented with the purposes to a) understand the time-lapse seismic response in compacting reservoirs and b) formulate a methodology to estimate pressure depletion from time-lapse amplitude attributes.

The model was created using similar rock and fluid properties from the south east flank of the Valhall Field. An iterative coupled fluid and geomechanical algorithm was used to simulate the rock deformation due to pore pressure depletion. A two slope linear elastic behavior was used to capture the porosity reduction that is occurring in the flank of the Valhall Field.

To determine the time-lapse seismic response, the Gassmann fluid substitution model was first applied to calculate the acoustic properties of the reservoir at different stages of production. Subsequently, a convolutional model was used to create the synthetic seismic volumes and finally, time-lapse amplitude attributes were extracted from the difference volumes.

After investigating which dynamic properties in the reservoir influence the time-lapse amplitude attributes, a methodology was proposed and tested to estimate reservoir pore pressure changes:

- Determine the most suitable amplitude seismic attribute that captures the pressure changes.
- Cross-plot pressure changes vs the time-lapse amplitude at certain locations.
- Define a trend equation that relates time-lapse amplitude and pore pressure changes: This trend equation for the synthetic example was a power law equation and depends on the initial porosity.
- The trend equation was expressed as a function of pressure and initial porosity (eq. 3.12) and was used to generate the pressure change maps for the reservoir.

The pressure maps estimated from the time-lapse amplitude were compared with the pressure maps output from the reservoir simulator, the factors that create the discrepancies between both outcomes are summarized as follows:

- The time-lapse amplitude is more sensitive to effective stress changes than pressure changes. The effective stress changes capture the pore pressure depletion and the normal stress changes.

The normal stress varies due to the rock compaction and the re-distribution of the stress in the reservoir and surrounding rocks. The link between effective stress and acoustic properties can be made by using the Gassmann fluid substitution theory. The bulk modulus of the rock frame responds to the effective stress changes. The acoustic properties of the rock (bulk modulus of the saturated rock, P wave velocity) are affected by the bulk modulus of the rock frame as shown by equations 3.13 and 3.14.

- Variations in the velocities of the layer immediately above the reservoir. According to the synthetic example ignoring the velocity changes in overburden increases the error in the pressure predictions from time-lapse seismic.

The proposed work flow will be tested on real data in chapter 4.

Chapter 4

Pressure estimation in the south east flank of the Valhall Field

The methodology to estimate pressure changes from 4D seismic in compacting reservoirs, developed in chapter 3, will now be applied to a real case study. The area of study is located on the south east flank of the Valhall Field (Norwegian North Sea). The south east flank is an area that has been produced for 10 years and is expected not to have fluid effects on the 4D seismic. No pressure support by injecting water has been carried out and the gas oil ratio has been kept relatively constant through time. This made the area suitable to analyze the influence of compaction and pressure depletion on the time-lapse signal.

Chapter 3 found that the time-lapse response in compacting reservoir is more sensitive to effective stress changes rather than pressure changes. However, I decided to invert for pressure changes. The major justifications for taking this route are:

Firstly, the effective stress inversion requires effective stress measurements linked with the 4D attributes. However, these estimations are extremely difficult to obtain during the daily operations of an oil field and normally the way to determine them is based on laboratory analysis. On the contrary nowadays pressure measurements are frequently gathered for production wells. Secondly with the condition that the reservoir dynamic properties inverted from time-lapse seismic are used as a tool to maximize the productivity of the oil field, the reservoir pressure predictions from time-lapse seismic prove to be more useful than estimating effective stress changes. Besides, there is not a direct

derivation of pressure changes from effective stress changes. The reason is that the effective stress changes capture the variations in the pore pressure and the normal stress, the latter changes depend on the geomechanical properties of surrounding rocks, structural settings and in-situ stresses.

As both pressure depletion and rock compaction affect the seismic properties in the same way (acoustic impedance increases), I am interested to investigate if it is possible to ignore the effective stress changes and correlate the 4D seismic attribute directly with pressure drop. The formulation and validation of a quantitative relationship between pressure changes, initial porosity and seismic attribute changes will help to answer this question.

The data from the south east flank used in this chapter was provided by BP. I required geological, engineering, geomechanical and 4D seismic data. The engineering information comprises well data (logs, deviation surveys, tops), well drilling reports, production data (pressure readings and Gas-Oil ratio estimations) and pressure outputs from the reservoir simulator. The geological data were structural maps, initial porosity and thickness maps. The 4D time-lapse data comprises seismic attributes (amplitude and time-shift) from 6 seismic volumes, which were acquired using permanently installed ocean bottom cables receivers.

The first part of the chapter describes the particular characteristics that lead the Valhall Field to compact. After this, I introduce the development and production history of the south east flank. Subsequently, the seismic data available is described. Then, I explain how the inversion was implemented and which were the most suitable coefficients. Finally, I assess the uncertainties from the final pressure maps.

4.1 Geological description of the Valhall Field

The Valhall Field is one of the chalk fields of the North Sea Central Graben. The field is located approximately 290 km offshore southern most corner of the Norwegian continental shelf (figure 4.1) with a water depth of 70m. The location of the south east flank with respect to the crest of Valhall is shown in figure 4.2.

The Valhall Field was discovered in 1975 and has been on production since 1982. During the first 20 years of production (on primary depletion), 576 MMSTB were produced (Barkved *et al.*, 2003).

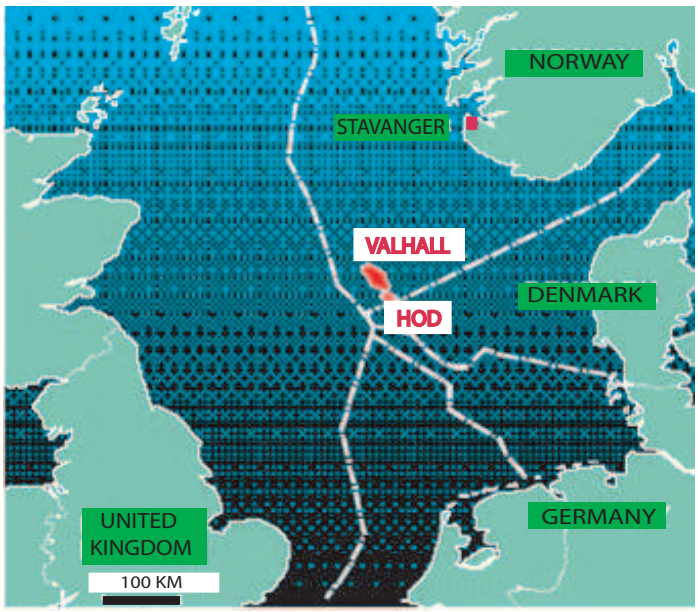

Figure 4.1: The Valhall Field location. The Valhall Field is located approximately 290 km offshore southern most corner of the Norwegian continental shelf. The Valhall structure is associated with the Lindesnes Ridge, a NNW trending elongate antiformal feature which also contains other Chalk fields such as Hod, Eldfisk, Edda and Tommeliten. After Barkved et al. (2003).

The recovery factor is 40% and there are still 500 MMSTB remaining to be produced from the original 2.6 BSTB in place. Approximately 50% of the drive mechanism has come from the rock compaction (Barkved *et al.*, 2003). The field is characterized for its complex structure and for the broken distribution of the main chalk reservoir, the Tor Formation.

The Valhall Field is a double plunging NNW-SSE trending anticline. It is asymmetric, with a steep western flank and a more gently dipping eastern flank. The Valhall Field is divided into compartments by WSW- trending sinistral strike-slip faults. The Tor Formation was deposited in a series of erosional channels but there is also an important stratigraphic component (figure 4.2). The Valhall structure is associated with the Lindesnes Ridge, a NNW trending elongate antiformal feature. The age of Lindesnes Ridge is Mesozoic, a period of active tectonics and when the main structural elements in the Central Graben were formed. Afterwards, during the Tertiary, there was a period of gradual subsidence, when a great thickness of marine shale was deposited in the Central Graben.

The stratigraphy in the Valhall Field is divided into three main subdivisions: the Upper Jurassic to Lower Cretaceous shales of the Rodby Formation; the Upper Cretaceous Chalk Group consisting of

the Hidra, Plenus Marl, Hod and Tor Formations, and the Tertiary shales of the Rogaland, Hordaland and Nordland groups.

The Upper Jurassic Mandal Formation (Kimmeridge Clay) is the hydrocarbon source. Oil generation commenced during the Early Miocene to the present. Migration of the hydrocarbons from the Kimmeridge Clay to the Upper Cretaceous chalk probably occurred along normal faults acting as vertical conduits. The Tertiary shales seal the chalk reservoir, but the existence of a gas cloud overlying the Cretaceous reservoirs indicates that sealing conditions are poor with respect to gas. The Tertiary claystone section is primarily Paleocene, Eocene and Miocene age. Its thickness is approximately 1000 m.

The major reservoir at the Valhall Field is the Tor Formation, containing approximately 70% of the oil in place. This unit is distinguished by high thickness variations across the field and high porosities. The hydrocarbon-bearing zones of the field occur in chalk of Cenomanian-Maastrichtian age. At the base lies the Cenomanian Hidra Formation, then the Tutonian-Coniacian Hod Formation and at the top lies the Late Campanian-Maastrichtian Tor Formation. The Tor Formation has been divided into five-reservoir zones base on detailed biostratigraphy : Tor-D, Tor-M1, Tor-M2, Tor-M3 and Tor-Camp. The Tor Formation is bounded by unconformities at the top and base. The Maastrichtian Tor Formation reservoir zones (Tor-M1, Tor-M2 and Tor-M3) are present over the crest of Valhall. The Hod Formation is divided into 6 reservoir zones (figure 4.3). Low porosity zones known as hardground chalks normally are present between the reservoir layers. The most important hardground chalk is known as the Hard Chalk and it is located between the base of the Tor Formation and the top of the Hod Formation. The Hard Chalk is characterized by a sharp jump in the p-wave velocity and a slight increase in the density, therefore this event is easily identified in seismic data.

At the crestal part of the Valhall Field, the Tor Formation porosities range from almost 50% to 42% in the thickest areas (Farmer & Barkved, 1999). The preservation of high porosities in the Tor Formation is primarily due to the extreme overpressure in the reservoir. Porosities in the Hod Formation range from 20 to 40% with hardground intervals at the Coniacian-Maastrichtian unconformity varying from 25% to less than 10%. However, the matrix permeability in the Tor Formation generally ranges from 2 to 10 mD, whereas it is less than 2 mD in the Hod Formation. Crestal Tor wells have effective permeability of 20-90 mD, indicating the likely contribution of natural fracturing.

The reservoir quality on the flanks of the structure is poorer compared to the crest. The reservoir is

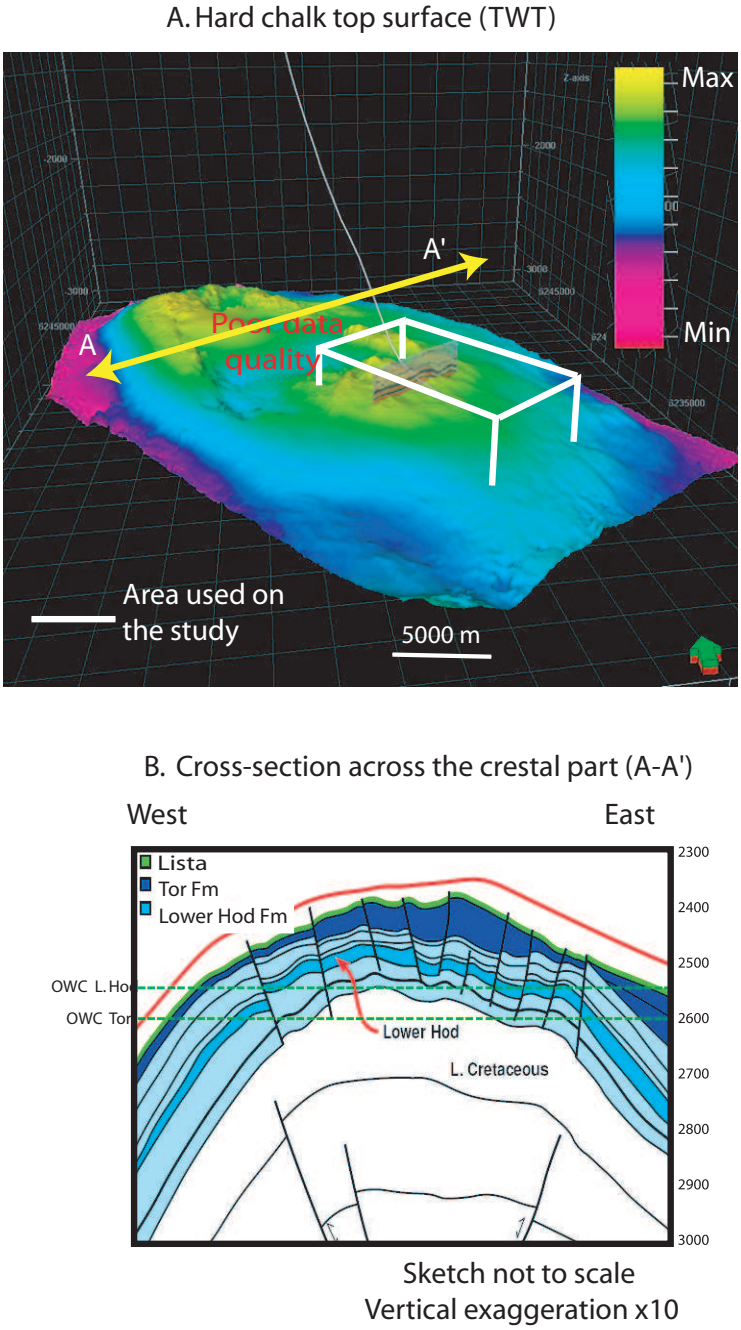

Figure 4.2: The Valhall Field geological settings: A. Two-way-time Hard Chalk top: illustrating the double plunging NNW-SSE anticline. The poor seismic data quality on the crestal part of the field is due to presence of gas on the overburden. The white box indicates the south eastern flank, which is the area of interest for the present work. The Hard Chalk is a non produced unit and is located underneath the Tor Formation. B. Schematic and simplified cross section from the crest of the structure. After Barkved and Kristiansen (2005).

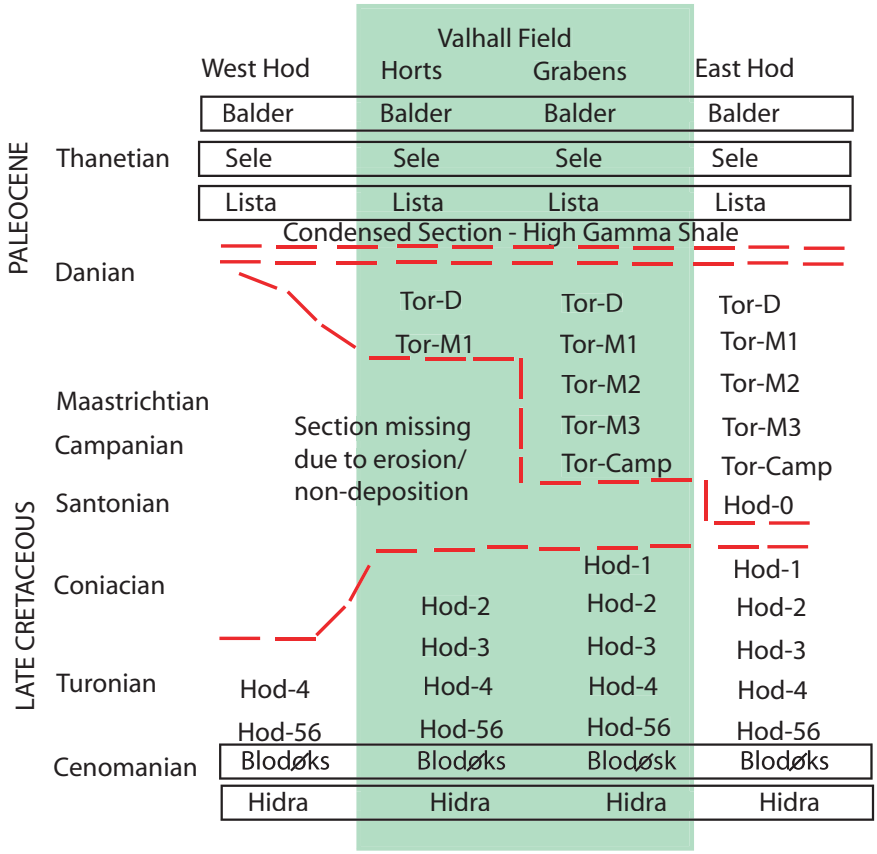

Figure 4.3: Late Cretaceous and Paleocene stratigraphy for the Valhall-Hod area. The Valhall zonation is highlighted on green. The major reservoir at Valhall Field is the Tor Formation. This unit is distinguished by high thickness variations across the field and high porosities. The Tor Formation has been divided into five-reservoir zones base on detailed biostratigraphy: Tor-D, Tor-M1, Tor-M2, Tor-M3 and Tor-Camp. Figure modified from Farmer and Barkved (1999).

thinner than on the crest and varies from 0 to 40 m. The initial porosity within the reservoir is in the range of 35% to 43%. Also, the structural complexity is low and therefore there is good continuity of the main seismic reflectors (Top of Hard Chalk and Top Balder Formation). There are some normal faults present in the area that can be easily recognized at seismic scale.

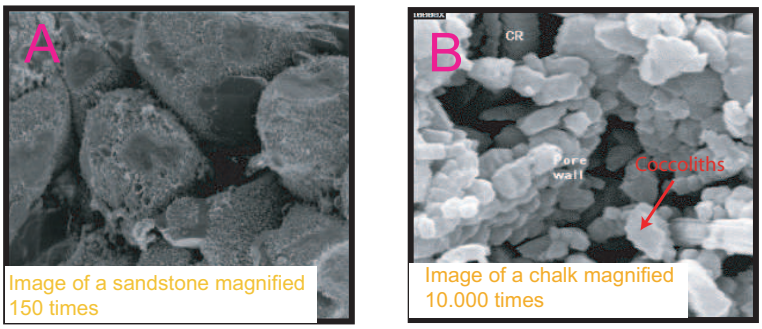

Figure 4.4: Comparison between two SEM images from a North Sea Chalk and a sandstone rock. A. Sandstone sample: The inter-locking grains form strong support beams. B. North Sea Chalk sample: The coccoliths make mechanical weak pore walls. For high porous chalks, the pore wall will collapse decreasing the pore volume dramatically when the reservoir is produced (Patzek & Barenblatt, 2001).

4.2 Compaction of the Valhall Field

A major production challenge in the Valhall Field is the reservoir compaction attributed to the porosity reduction. The associated sea floor subsidence was first measured in 1985 after only three years of the field being put on production. It was found to be approximately 50 cm. Nowadays based on pressure gauges at the seafloor, infrared sensing and GPS, it has been established that the subsidence rate is around 25 cm/year. The overpressure and the mechanically weak structure of the chalk are the elements that trigger the reservoir compaction. The compaction has the positive effect of being the drive energy to produce Valhall for more than 20 years without any other recovery mechanism. This compensates for the negative consequences such as chalk production, influx failures and casing collapse problems.

Because of the depositional processes, the chalks vary from weak, high porosity chalk to well-cemented low porosity chalk (hard grounds). Two Scanning Electro Microscope (SEM) images of a North Sea chalk and a sandstone sample are shown in figure 4.4. The sandstone pores are protected by a network of grains that are large with respect to the pore size. If the pore pressure drops, the walls are strong enough to support the effective stress increment. In contrast, the pore walls on the chalk sample are protected by a large number of coccolith platelets that are poorly cemented. In the case of pressure depletion, the pore wall will collapse, decreasing the pore volume dramatically.

The high initial porosity (reported at higher than 53 % in some localized areas) is caused by over-pressures. The principle of effective stress states that the stress acting on a porous medium is partly

supported by the pore pressure. The effective vertical stress acting on the high porosity chalk is approximately the difference between the weight of the overburden and the pore pressure. For the North Sea chalk, the overburden stress gradient is approximately 0.91 psi/ft (20.6 Kpa/m) and the fluid pressure gradient which is normally obtained from the density of the brine, approximately 0.46 psi/ft (10.5 kPa/m) so the normal effective pressure gradient is 0.45 psi/ft (10.1 kPa/m) (Fjær *et al.*, 1992).

A reservoir is over-pressured when the pore pressure is higher than the hydrostatic pressure. Comparing different chalk reservoirs in the North Sea (table 4.1), it is observed that Valhall Field is the most over-pressured reservoir. The pressure in Valhall is 44.5 MPa at 2400 m, whereas the brine hydrostatic gradient would predict a pore pressure of 25.2 MPa. The 19.3 MPa overpressure means more support of the overburden weight by the fluid and less porosity loss due to burial. However, the effective stress felt by the matrix is 3.8 MPa. This is converted to the effective depth by dividing the effective stress by the effective overburden gradient. This value represents the equivalent burial depth for a normally pressured material with the same effective stress. The results listed on the sixth column of table 4.1, suggest that the effective depth is about half the actual depth for the some of the North Sea chalk reservoirs but significantly less so for the Valhall Field.

Eldfisk					
Depth	Porosity	Pressure (MPa)		Effective	
(m)	(%)	OB	Pore	OB Pressure (MPa)	Depth (m)
2820	43	58.1	46.3	11.8	1165
2990	27	61.6	49	12.6	1249
3040	24	62.6	49.7	12.8	1274
Ekofisk					
Depth	Porosity	Pressure		Effective	
(m)	(%)	OB	Pore	OB Pressure (MPa)	Depth (m)
3050	35.5	62.8	46.6	16.1	1601
3260	18	67.1	49.9	17.2	1707
3350	26.5	69	51.3	17.7	1752
3400	21.5	70	52.1	17.9	1777
Valhall					
Depth	Porosity	Pressure		Effective	
(m)	(%)	OB	Pore	OB Pressure (MPa)	Depth (m)
2400	42	48.3	49.4	4.9	485
2700	40	54.3	55.6	9.10	910
Dan/Kraka					
Depth	Porosity	Pressure		Effective	
(m)	(%)	OB	Pore	OB Pressure (MPa)	Depth (m)
1814	40	37.3	25.7	11.6	1154
1890	25	38.9	26.2	12.7	1260

Table 4.1: Calculated stresses for some North Sea fields. Source data from Parker, J.R (1993) and Fjær, E.(1992). Estimations assume an overburden stress gradient of 0.91 psi/ft and a fluid pressure gradient of 0.46 psi/ft

4.3 Description of the Life of Field Seismic (LoFS)

A full field permanently installed 3D-4C Ocean Bottom Cable (OBC) system was implemented at Valhall in 2003, covering 70% of the field. The project was called Life of Field Seismic (LoFS). The baseline survey was shot in the autumn of 2005 and 3D surveys have subsequently been acquired every three months. The seismic data available for this study are the first six surveys. Table 4.2 shows the dates when each survey was acquired. Seismic attributes from full stack seismic (time and depth) and time-shift volumes were available.

The main objectives of the LoFS project was firstly to monitor and optimize depletion of the reservoir. Secondly to help understanding the fluid movement since water injection started in 2004 and thirdly to better image beneath the gas cloud using PS data (Barkved & Kristiansen, 2003; Kommedal

et al., 2005). The major areas where the LoFS of programme has made an impact are defining new well targets, monitoring well performance and updating and history matching the reservoir model (Barkved *et al.*, 2004).

Survey	Started	Ended
LoFS 1	27.09.2003	23.11.2003
LoFS 2	19.02.2004	13.04.2004
LoFS 3	29.05.2004	29.06.2004
LoFS 4	25.09.2004	24.11.2004
LoFS 5	06.03.2005	18.04.2005
LoFS 6	02.10.2005	20.11.2005

Table 4.2: LoFS surveys that were acquired between 2003 and 2005. Six seismic surveys are used on the study. The time separation between them is approximately 3 months.

4.3.1 Installation

The LoFS project has 120 km of GeoRes cables which were fixed one metre into the seabed during the summer of 2003. There are 2304 receiver stations in total. Each station consists of a 4 component (4C) sensor (three orthogonal and non-gimbaled geophones and a hydrophone); they are connected to a GeoRes Imagine recording system on the Quarters Platform at Valhall. The layout of the array covers an area of 45 sq. km. One geophone and the hydrophone detect incoming compressional P-waves. The remaining two geophones can detect converted waves in two directions perpendicular to each other and the vertically moving P-wave. The station spacing is 50 m and the separation between the parallel cables is 300 m (figure 4.5). The outside cables are located 600 m from their neighbors and were added to provide some additional coverage. The sources are installed on a standby vessel and these being a 2000 in^3 array of Bolt Annular Port Guns operated at 2000 psi by a I/O DigitShot gun control system. The source depth is 5 m below sea level. For the acquisition a grid of shot points of 50 m by 50 m is used. Each survey has approximately 50000 shots. The recording length is 8 seconds and sample interval is 2 or 4 ms. (Kommedal *et al.*, 2004).

4.3.2 Acquisition and processing to optimize 4D repeatability

The LoFS acquisition was designed to have the same the receivers and shot point locations in order to minimize negative impact on the 4D repeatability. However errors during the acquisition phase

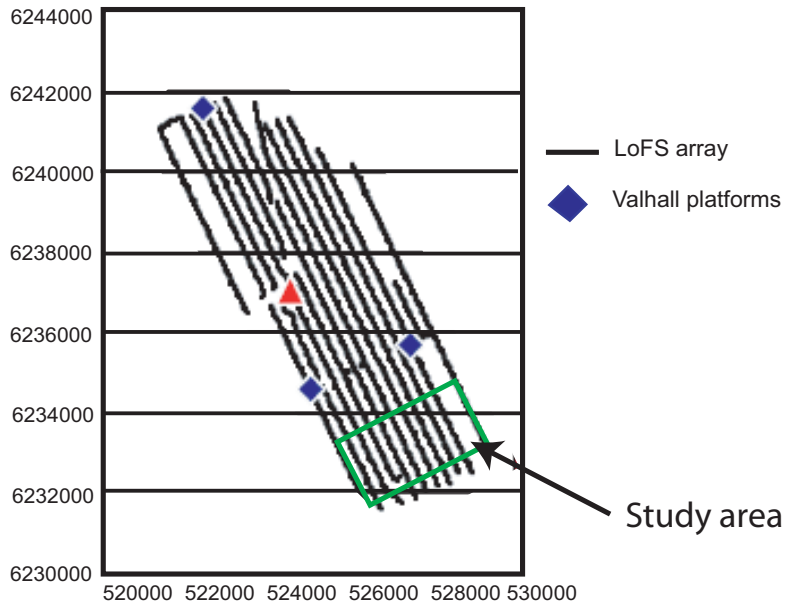

Figure 4.5: Design of the geophone array for the LoFS project. There are 2304 receiver stations and each station consists of a 4 component (4C) sensors. After Kommedal,J. et al (2004).

related to the shot location and bad receivers location have been reported.

The shot point error distribution for survey 3 is shown in figure 4.6. The differences are estimated between the location of the actual shot and the planned one. The errors are greater in the cross line direction than in the in line direction. In the cross-line direction, the shot point error varies from -6.5 m to 5.5 m while in the inline direction they are close to zero (Kommedal *et al.*, 2007). By comparison, these results are lower than the ones reported by Goto, et al (2005) for the Norne Field (North Sea). In the Norne Field, the 3D surveys were acquired with steered streamers to reduce the acquisition differences. For this case, the reported error in the cross line direction is approximately -/+ 9 m.

Kommendal et al. (2004) estimate the error due to the bad receivers locations for the first 6 surveys. The location and orientation of the receivers were kept constant for the first surveys. Error in the receiver position between the second survey and the baseline were -0.24 m north and 0.16 m east, both with a standard deviation of 0.26 m. However, after survey 5 some cables were lifted to replace damaged stations, and then re-trenched at their original position. The total affected receiver stations were 117. Based on the survey six records, these stations had moved on average 1.46 m north, with a standard deviation of 0.85 m and 1.78 m east with standard deviation of 1.45 m.

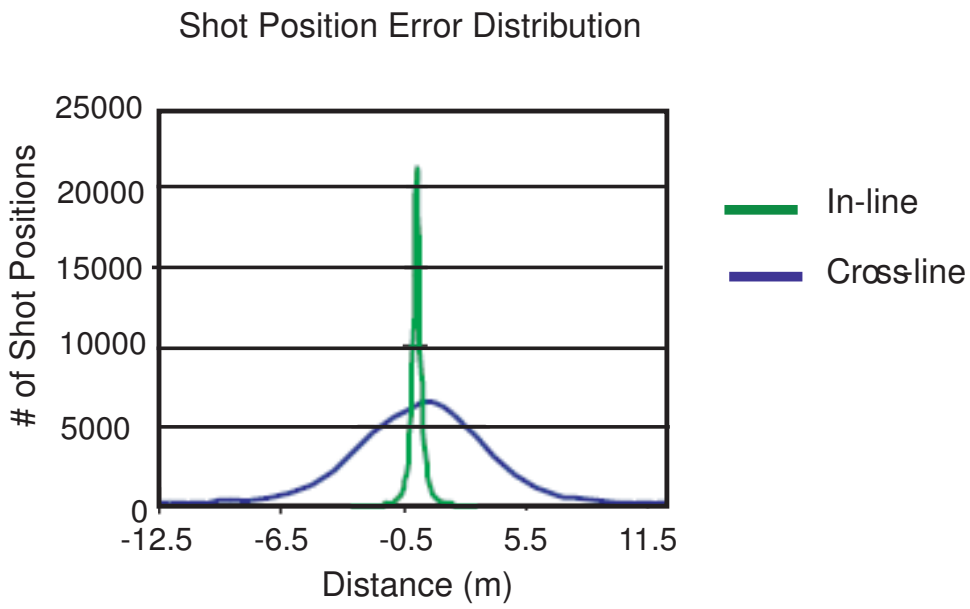

Figure 4.6: Error distribution for the shot position on survey 3. The mean of the error distribution is close to zero, however the highest error are observed on the cross-line direction (standard deviation of 4.3 m). After Kommedal et al. (2007).

Two parallel processing efforts with different flows were carried out. The first processing flow was done by BP in-house specialists and involves a pre-stack depth migration (PreSDM) to produce results with very short delivery time (Kommedal *et al.*, 2004). The main idea of this flow is to sort the data to common receiver gathers, such that non-repeatable noise will be randomized and can be removed by standard noise reduction methods. Multiple removal steps are also included. Finally the common receiver gathers are migrated using a wave equation shot algorithm.

The second approach involves a rigorous pre-processing flow, more similar to standard for streamer 4D processing (Calvert, 2005). For each survey this flow includes checking of navigation data, orientation of the 4C receivers, tidal statics corrections, shot and receiver static corrections, and changes to the mute functions due to changes in water velocity. The non-repeatable noise, such as vessel noise, rig noise, seismic interference, was reduced using f-k dip or frequency filters with the parameters being optimized for each survey. The migration algorithm used was Kirchhoff pre-stack depth migration.

An automated workflow for loading and extracting the seismic information has been implemented to handle all the data coming from the LoFS project (van Gestel *et al.*, 2007). The workflow consists of five basic steps (figure 4.7). Step 1 comprises loading the new LoFS depth migrated volume into the

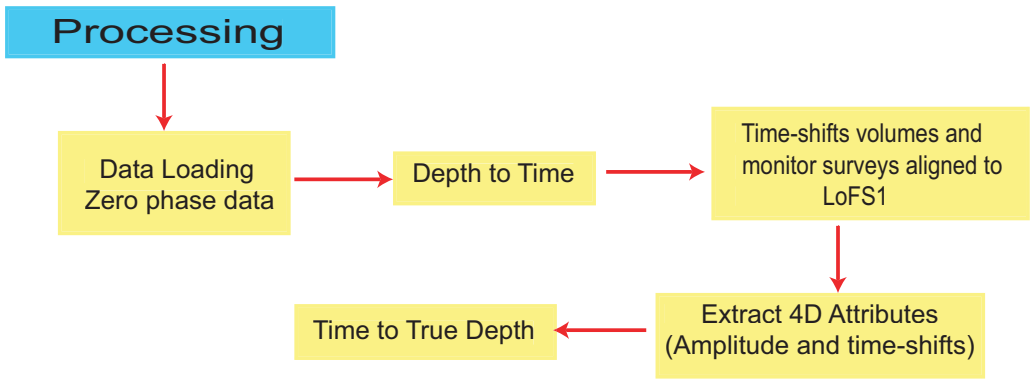

Figure 4.7: Workflow implemented to assist the LoFS interpretation. It consist of 5 principal steps. The final outcome are four different time-lapse volumes (time-shifts, amplitude, acoustic impedance and coherency) which are used during the interpretation phase.

interpretation package and adjusting the phase to make the data zero-phase. Steps 2 and 3 involve converting the data into time and estimating the time-shift volumes. The time-shifts are determined using a sliding window cross-correlation of 300 ms, they are applied to the monitor survey to align it with the baseline (LoFS1). Module 4 involves extracting amplitude and time-shift attributes in the time domain. Module 5 involves converting the seismic data from time to true depth domain, tying to the well tops and reservoir model horizons. Additional intermediate steps have been developed to create acoustic impedance volumes and coherency volumes.

4.4 Time-lapse seismic responses due to pressure depletion, compaction and water injection observed in the LoFS data in the Valhall Field

Before I start to correlate the 4D seismic effects with production activity in the south east flank, I describe some of the most significant 4D anomalies (time-shifts and amplitude changes) due to pressure depletion, compaction and water injection across the Valhall Field.

The Valhall Field is an actively compacting reservoir. Therefore to understand the 4D signature it is necessary to take into account not only fluid and pressure changes but also, porosity reduction, stress and strain redistribution inside the reservoir and in the surrounding rocks. It was observed that the amplitude difference maps shows the biggest anomalies around the producing and injecting

wells (figure 4.8A). For the depleted areas, this difference is due to an acoustic impedance increase due to pressure depletion (velocity increases due to effective stress increase and density changes). For the injectors, the increase in amplitude can be explained due to water replacing oil (water velocity is higher than oil velocity). On the contrary, the time-shift attributes are positive near to a water-injection well, whereas negative time-shift differences are observed on the depleted areas (figure 4.8B).

Furthermore, there are special cases where the pressure increase due to water injection can be observed as shown in figure 4.9. The traces represent inverted acoustic impedance volumes using the Coloured Inversion approach (Lancaster & Whitcombe, 2000). The blue traces are LoFS4 and the yellow traces are LoFS5. There was no water injection in the I_2 well while the LoFS 4 was acquired, but during the acquisition of LoFS 5 the well started injecting at very high pressures. This caused a decrease in acoustic impedance, which is in evidence when LoFS 4 and LoFS 5 are compared.

As was discussed in section 4.3, two different processing approaches were carried out for the LoFS data. Figure 4.10A compares the 4D amplitude map between the sixth and the first survey, for BP and PGS processing. Even though both displays highlighted the 4D amplitude response due to production, the BP processed data appear to have a better Signal to Noise ratio (S/N). Kommedal et al. (2007) suggest that this can be attributed to the fact that the data have full fold, including offsets up to 5 Km and a more sophisticated migration algorithm was used in the in-house processing. On the contrary, the time-shift attributes from PGS processing (figure 4.10B) seems to show a better correlation with the well activity and a higher S/N. Kommedal et al. (2007) attributes this to the more careful pre-processing including static corrections. Consequently, I decided to use the BP processed data for extracting amplitude attributes and the PGS data for time-shift related attributes.

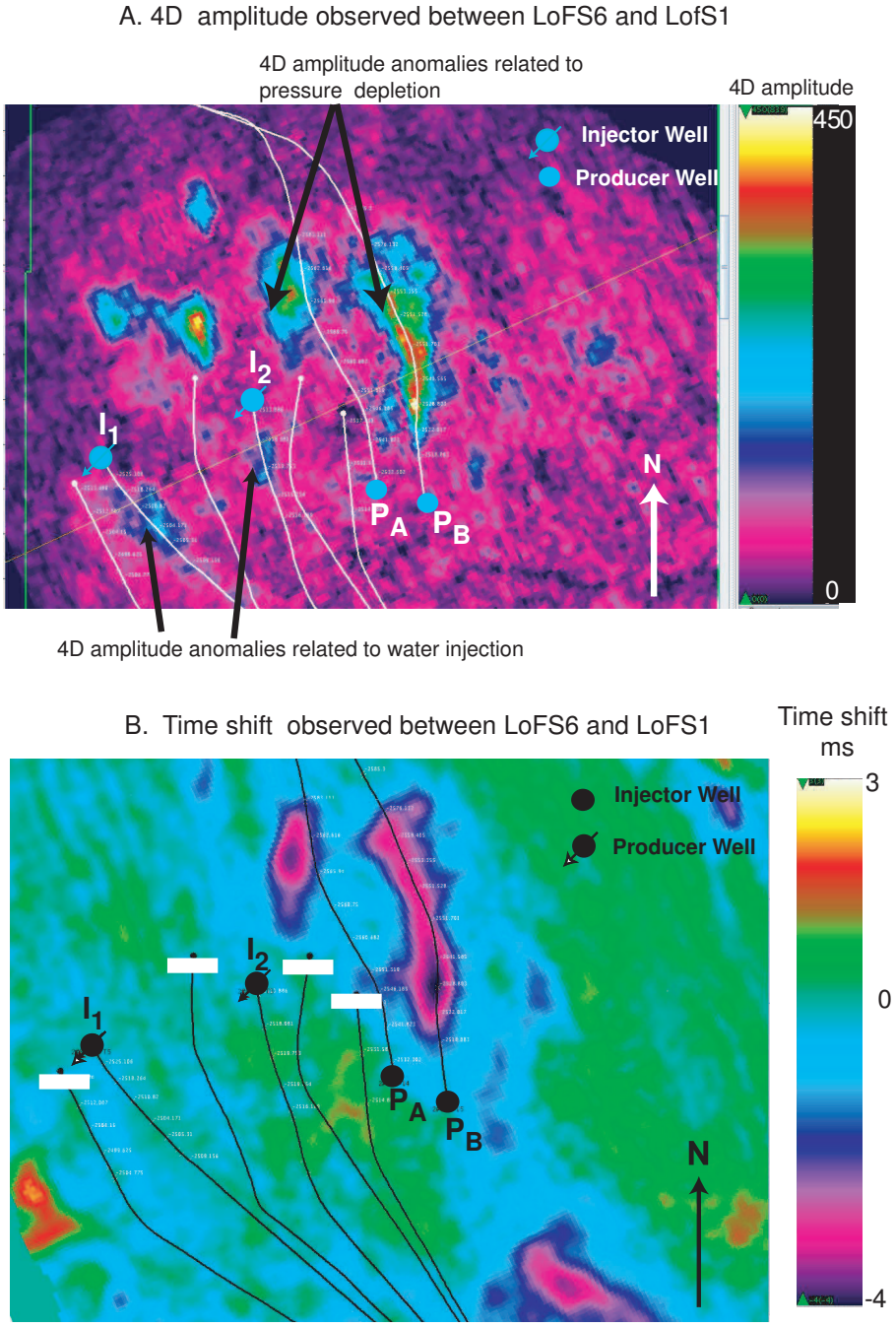

Figure 4.8: Time-lapse response in the north area of the Valhall Field. A. Amplitude difference between LoFS6 and LoFS1 in the north area: The 4D amplitude for both the injectors (I_1 and I_2) and the producers (P_A and P_B) is positive due to water injection and pressure depletion causing an acoustic impedance increase. The 4D amplitude were extracted in a time window of 35 ms using the approach explained in section 3.4.1. B. Time-shifts in the north area: Near water-injection wells (I_1 and I_2) the time-shift differences are positive or close to zero, whereas negative time-shift differences are observed in the depleted areas (P_A and P_B).

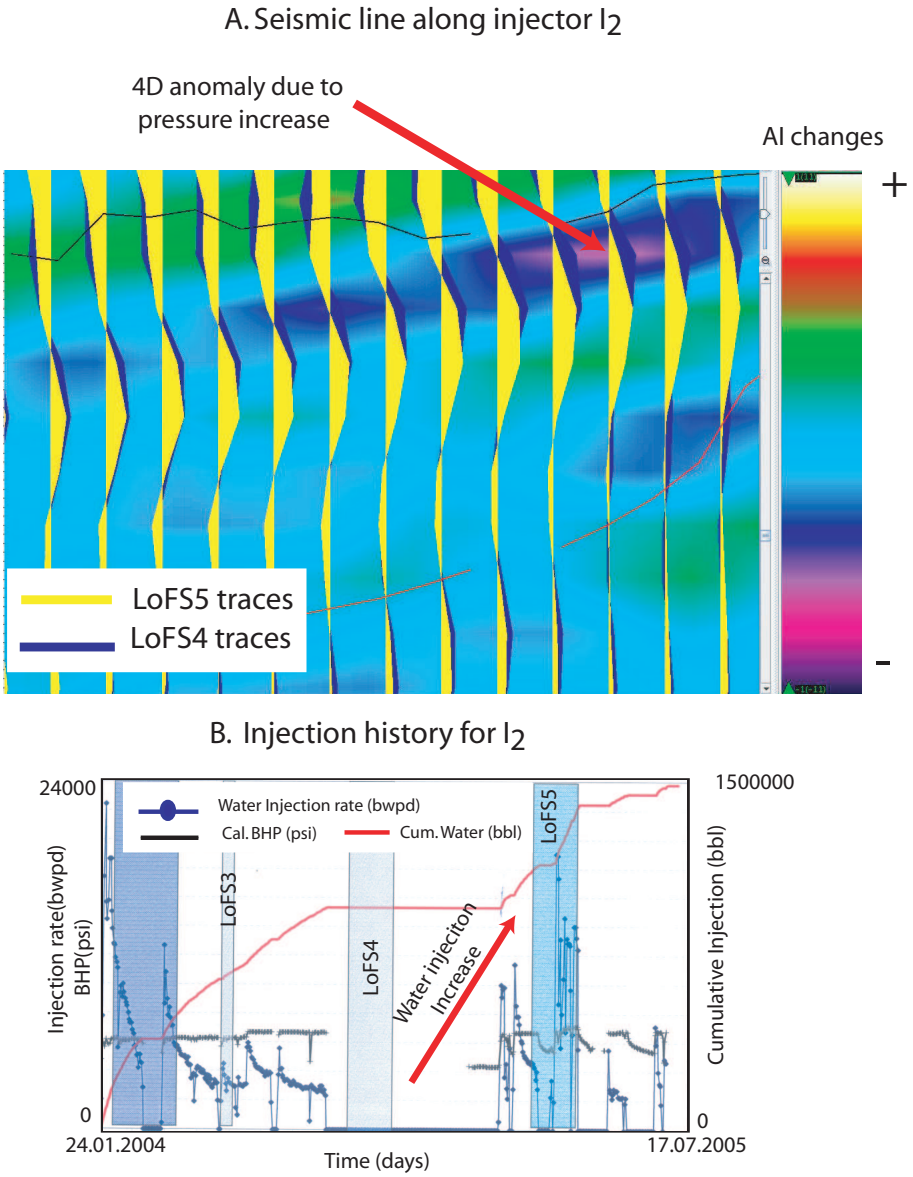

Figure 4.9: Seismic section along the injector well I_2 showing the acoustic impedance decrease at the reservoir due to pressure increase. A. Seismic traces along the injector, I_2. The seismic data are acoustic impedance volumes. The background volume is the difference AI volume between LoFS5 and LoFS4. The blue traces are LoFS4 volume and the yellow traces are LoFS5 volume. The acoustic impedance decreases as pressure increases. This decrease in AI is due to the high pressure around the borehole. Also, the velocity reduction is perceptible as the time arrivals are larger for LoFs5 (The yellow traces are shifted down few milliseconds with respect to the blue traces). B. The injection profile for I_2. The injection rate was increased immediately before and during the acquisition of LoFS5. This caused a pressure increase (velocity decrease) that was recorded by the LoFS 4 and 5.

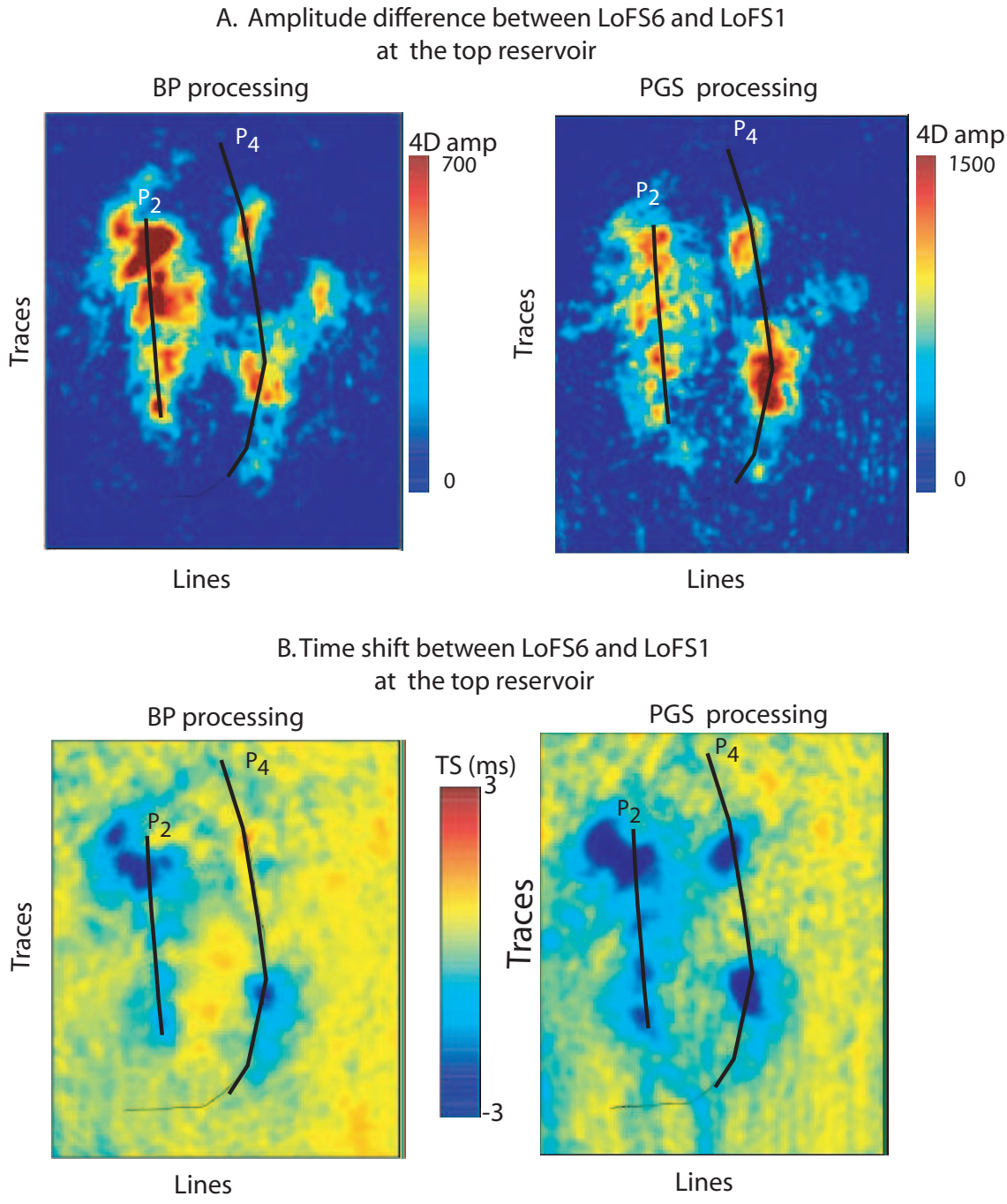

Figure 4.10: Comparison between the time-lapse attributes from BP and PGS processing approaches A. Comparison between the 4D amplitudes from BP and PGS processing approaches. Even though both displays highlight the 4D amplitude response due to production, the BP processed data appears to have a better Signal to Noise ratio (S/N). The 4D amplitude were extracted in a time window of 35 ms using the approach explained in section 3.4.1. B. Comparison between the time-shifts from BP and PGS processing approaches. The time-shift attributes from PGS processing seems to show a better correlation with the well activity and has a higher S/N . After Kommedal et al. (2007).

4.5 Development and production history in the south east flank of the Valhall Field

Significant compaction has resulted in high intrinsic reservoir energy that has allowed the flank to be produced on primary depletion (no water injection) since 1994 but this compaction has been confined at reservoir level since no sea floor subsidence has been reported for this part of the field. In 2003 a wellhead platform was installed in the southern part of the field and a corresponding infill drilling campaign targeting flank areas was carried out (Kjelstadli *et al.*, 2005). Six horizontal wells have been drilled in this area (figure 4.11). The first producer was perforated in 1994 and has been on production for nearly 14 years. The first dedicated time-lapse study at Valhall (streamer data) has shown a strong 4D signal interpreted to be the result of the pressure drop and the reservoir compaction around that well. Figure 4.12 shows the RMS amplitude difference map at the producer. The RMS amplitude was extracted using a time window of 35 ms above the base of the reservoir and the monitor volume was corrected for time-shift before the amplitude extraction.

The remaining wells have been on production for less than 5 years and their 4D response due to pressure depletion and reservoir compaction has been captured by the six surveys acquired using permanently installed ocean bottom cables (section 4.3) between October 2003 and June 2005. Figure 4.13 shows the cumulative oil production for wells P_2, P_3, P_4, P_5 between January 2003 and March 2006. The first seismic surveys were acquired approximately 1 month after the wells P_2 and P_3 were put on production. P_4 and P_5 started to produce while the first survey was being acquired. P_6 was not taken into the analysis because it was put on production after LoFS5.

The location of the wells are shown in figure 4.14. The horizontal separation between the wells is around 300 m and the horizontal section drilled by the wells reaches up to 2 km. The wells produce from the Tor Formation. In the reservoir model, the Tor Formation has been divided into eight zones and the average total thickness is 25 m. Zones 2, 4 and 8 are very low porosity zones less than 15%. Table 4.3 shows the equivalent stratigraphic interval for each zone. The hardground layers (zone 2 and 4) are very thin and towards the north of the flank are not present (figure 4.11B). The producers have been perforated on zones 2 and 3 which are the Tor-M1 and Tor-M2. The wells are fractured and opened with proppant materials and are thought to see the entire Tor package.

The producer wells have never produced at the same period of time. They are switched on and off

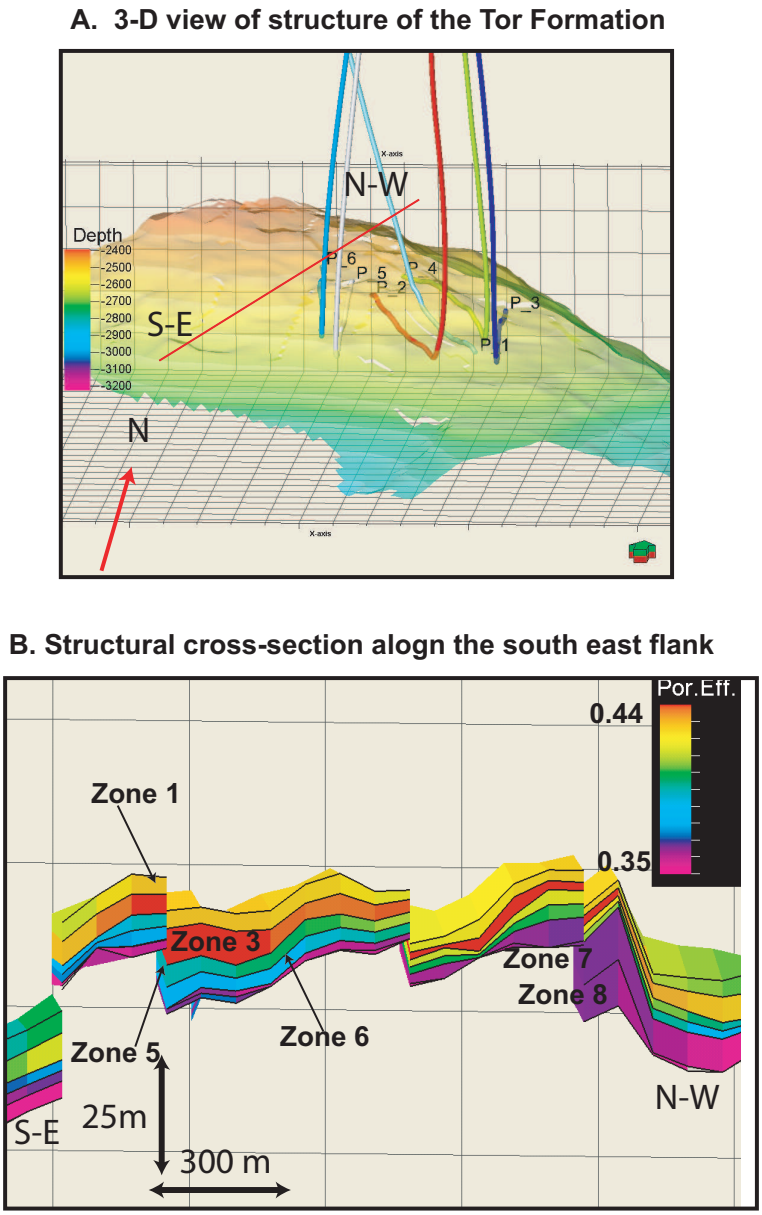

Figure 4.11: Structural cross-section along the south east flank of the Valhall Field. A. 3D view of structure of the Tor Formation in the south east flank. B. SE-NW structural cross section. Six horizontal wells have been perforated in the flank. The wells produce from the Tor Formation. The direction of the cross section is shown on the 3D view as a red line. The structure has low complexity, however there are some faults offsetting the Tor Formation. The Tor average thickness is 25 m on the flank. In the reservoir model, the Tor has been divided into 8 zones and the equivalent stratigraphic units for the zones are listed in table 4.3.

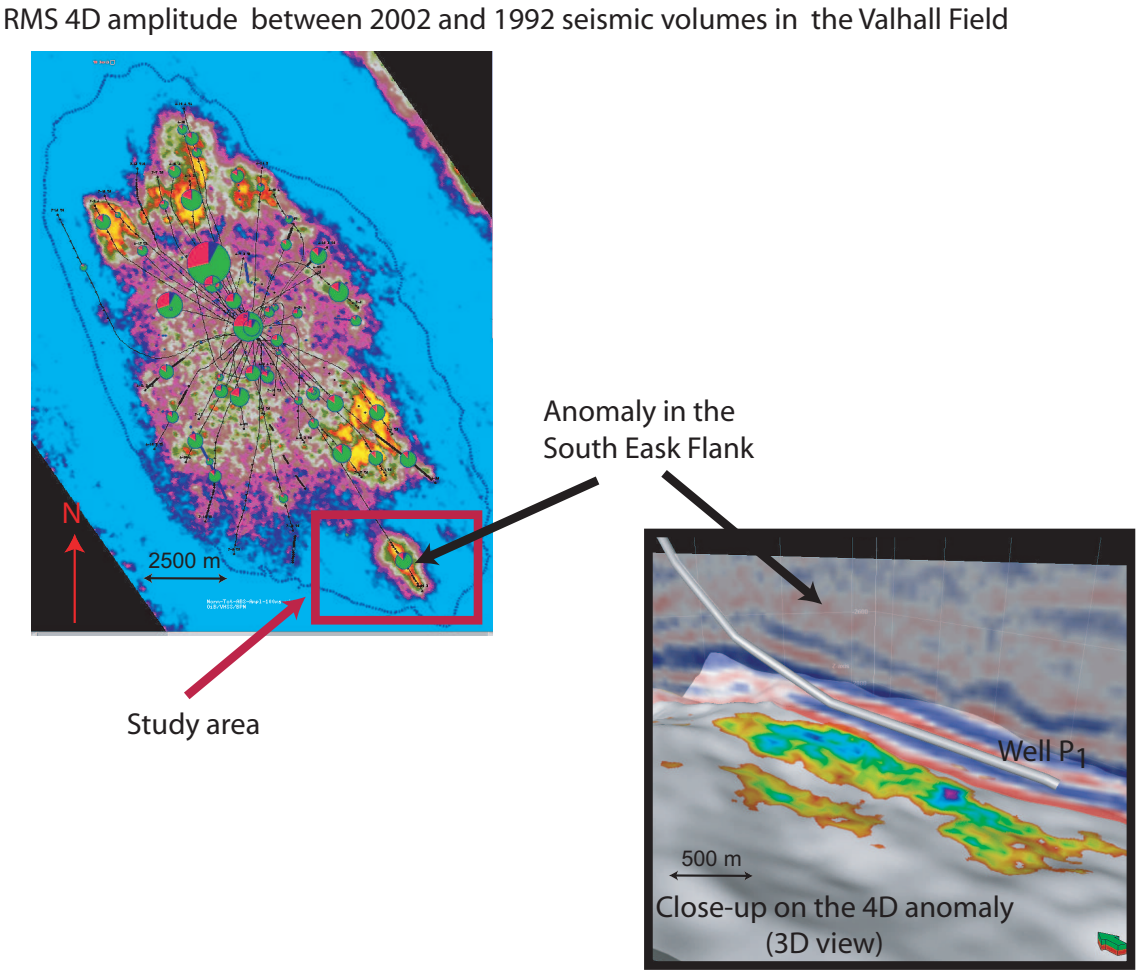

Figure 4.12: 4D RMS amplitude attribute extracted from the first time-lapse seismic study in the Valhall Field. The seismic amplitude changes induced by pressure depletion due to the activity of first horizontal well (P_1) on the south east flank. Two streamer seismic data were used (1992 and 2002). The RMS 4D amplitude (monitor-baseline) shows a positive anomaly due to pressure depletion and its associated rock compaction. The top-left figure shows the RMS 4D amplitude map for the Valhall Field. The right-bottom figure is a 3D-view of the amplitude anomaly at P_1. The 3D seismic in the background is a line of the baseline survey.

Zones in the reservoir model	Stratigraphic interval
1	Tor-D
2	Hardground
3	Tor-M1
4	Hardground
5	Tor-M2
6	Tor-M2
7	Tor-M3
8	Tor-Camp

Table 4.3: Zones used on the reservoir Model for the south east flank of the Valhall Field. Zones 2,4 and 8 are very low porosity zones less than 15%. The hardground layers (zone 2 and 4) are very thin and towards the north of the flank are not presence (figure 4.11). The producers have been perforated on zones 2 and 3 which are analogous to Tor-M1 and Tor-M2

in order to maintain a good production rate; therefore the pressure depletion pattern is not uniform. During the time the well is shutdown, the reservoir pressure can build up and hence higher pressures are often observed when the well is re-opened.

Water saturation changes do not play a major role in this part of the field, since pressure support by water injection has not been carried out.

The average gas oil ratio (GOR) for this part of the field is generally low, around 780 MSCF/BBLS (the maximum GOR has been 1200 MSCF/BBLS). In general for the Valhall Field, the GOR has increased after 20 years of depletion only 35%. The low GOR is due to the relatively low gas mobility. Although a high porosity rock, the low gas mobility is caused by a very low matrix permeability (Barkved *et al.*, 2003). Also, other reason for the low GOR is that reservoir pressure is above the bubble point pressure (which for the flank is estimated to be 3112 psi/21457 MPa). As table 4.6 illustrates, the fluid pressure at the well perforations during the time the 6 surveys were acquired, are higher than the bubble point pressure.

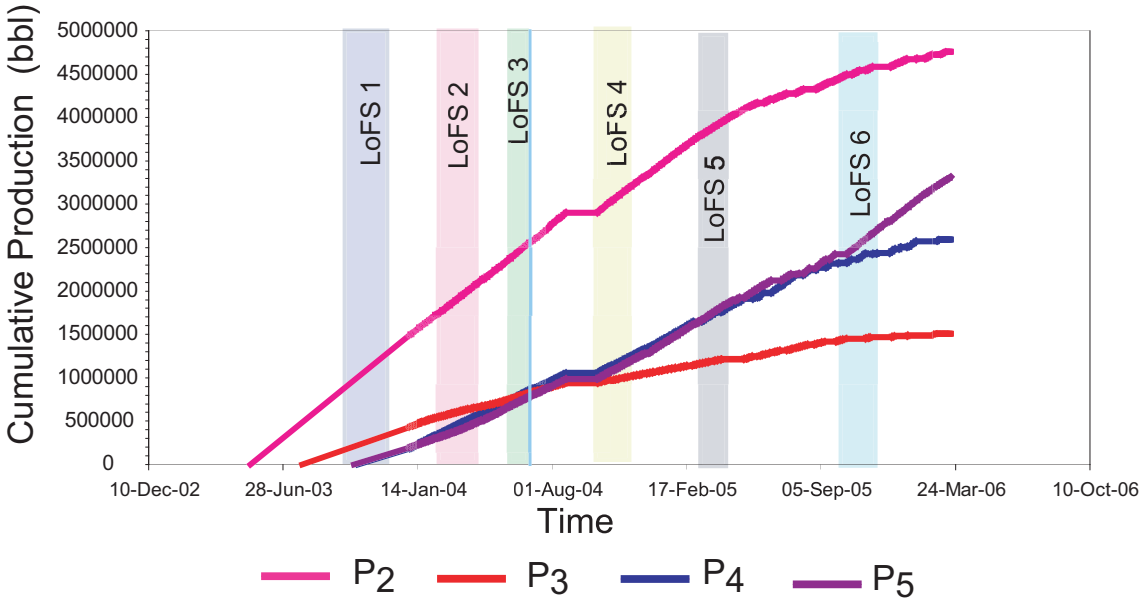

Figure 4.13: LoFS acquisition schedule and accumulative production for the wells that have been drilled in the south east flank, after the Life of seismic project started. Wells P_2 and P_3 started to produced one month before the first seismic survey (LoFS1) was acquired. Wells P_4 and P_5 were put on production during the acquisition of LoFS1.

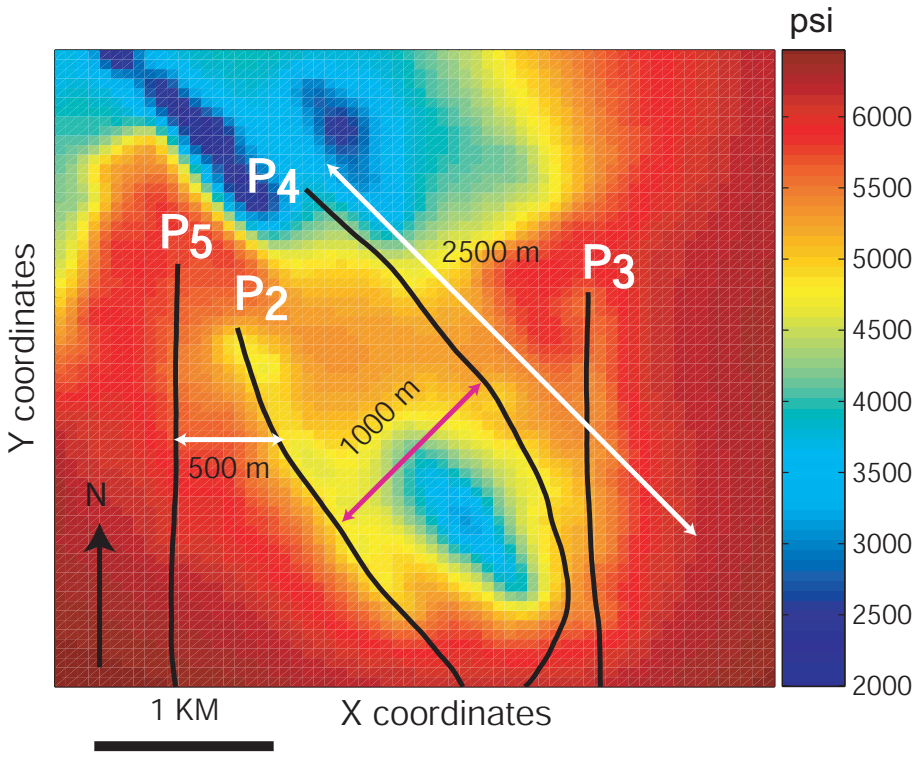

Figure 4.14: Reservoir pressure map for the south east flank of the Valhall Field. The map shows the pore pressure when LoFS1 was acquired. The production had already started in P_2 and P_3 when the first seismic volume was acquired. The low pore pressures (blue color) observed between wells P_2 and P_4 is caused by the production from P_1, which is the oldest producer in the area.

4.6 Time-lapse seismic attributes due to pressure depletion in the south east flank

Time-shifts and amplitude changes are the time-lapse signal expected for compacting reservoirs. So far in the study of compacting reservoirs, the time-shifts have been the most used 4D attribute and they have provided an important tool to understand the geomechanical response in the reservoir and surrounding rocks (Hatchell *et al.*, 2005b). Little effort has been made to use these time-shifts as a mechanism to estimate pressure or fluid saturation changes in the reservoir (Hodgson *et al.*, 2007). Seismic amplitude attributes have not been used to predict reservoir dynamic properties (pressure and fluid saturation) in such compacting reservoirs. The majority of work using 4D amplitudes has directed towards synthetic examples and relatively little has been reported on real data. Perhaps this is because the amplitude signal does not respond exclusively to the reservoir seismic properties but is contaminated with the changes from the layer above the reservoir. However, as was shown by the synthetic model in chapter 3, under certain circumstances the amplitude response can show a strong relationship with the reservoir's dynamic properties (pressure or more accurately, effective stress changes). This relationship is controlled by the initial porosity. In this section, I introduce the two time-lapse attributes from the LoFS data used to estimate pressure depletion on the south eastern flank of Valhall. The first attribute is the Largest Positive Value (LPV) which is a time-lapse amplitude attribute. The second one is the speed-up attribute which is a time-shift attribute.

4.6.1 The Largest Positive Value: the time-lapse amplitude attribute used to predict pressure changes in the south east flank of the Valhall Field

In the south east flank, the time-lapse signal in the reflectivity domain is recorded as the Largest Positive Value (LPV) in the differences volume. This time-lapse response is similar to the one observed in the numerical example (figure 3.23). Softening of the layer immediately above the reservoir (acoustic impedance decrease) and hardening in the reservoir (acoustic impedance increase), result in a peak on the differences volume (monitor-baseline). Because the top of Tor is not very easy to interpret on the seismic, the extraction of the amplitude was done over a time window above top of Hard Chalk, which is a very good seismic reflector (figure 4.21). A 35 milliseconds window assures that the top of the reservoir is included. However the reservoir thickness varies considerably, so it is

important to have in mind that the reliability of this attribute is reduced in very thin areas, where information from the overburden/underburden might extracted.

Figures 4.15 and 4.16 illustrate the LPV attribute against the pressure depletion for the different times. In a visual comparison, the relationship between both maps is obvious. The 4D amplitude intensifies with time as the pressure depletion progresses. However there are areas where the pressure depletion seems unperceived by the time-lapse (highlighted as black ellipsoids in the figures). In addition, while the pressure maps from the reservoir simulator are broader and the pressure front is observable, the amplitude changes appear more confined to specific areas. These areas are generally correlated with high porosity and the thickest zones on the reservoir (figure 4.17).

4.6.2 The speed-up attribute: the time-shift attribute used to predict pressure changes in the south east flank of the Valhall Field

Time-shift cubes were generated from a cross-correlation procedure between the monitor surveys (LoFS 2, 3, 4, 5 and 6) and the LoFS 1. These volumes were used to extract maximum and minimum time-shifts. The maximum time-shift corresponds to ΔT_{top} in equation 3.5 while the minimum time-shift is ΔT_{base} in equation 3.5, and the speed-up attribute is equal to the difference between them. Figure 4.18 shows the approach taken to search for the maximum and minimum time-shifts. The maximum time-shift was extracted by applying a window of 60 ms centered on the Hard Chalk top while the minimum time-shift used a window of 80 ms centered on the same horizon.

The speed-up attribute for each of the volumes are displayed on the left side of figures 4.19 and 4.20. These are compared with the 4D amplitude maps (right side of figures 4.19 and 4.20). The close agreements between the speed-up and amplitude attributes are numerous; however several discrepancies can be observed between both outputs. The 4D time anomalies observed around wells 2 and 5 (red circles on the maps) are more noticeable than the ones shown by the 4D amplitude maps. The amplitude attributes exhibit time-lapse signal in areas where the speed-up attribute has detected none (white circles on the maps). The amplitude anomaly present at the toe of well P_4 seems to be shifted to the left on the time attribute maps (black circles on the maps).

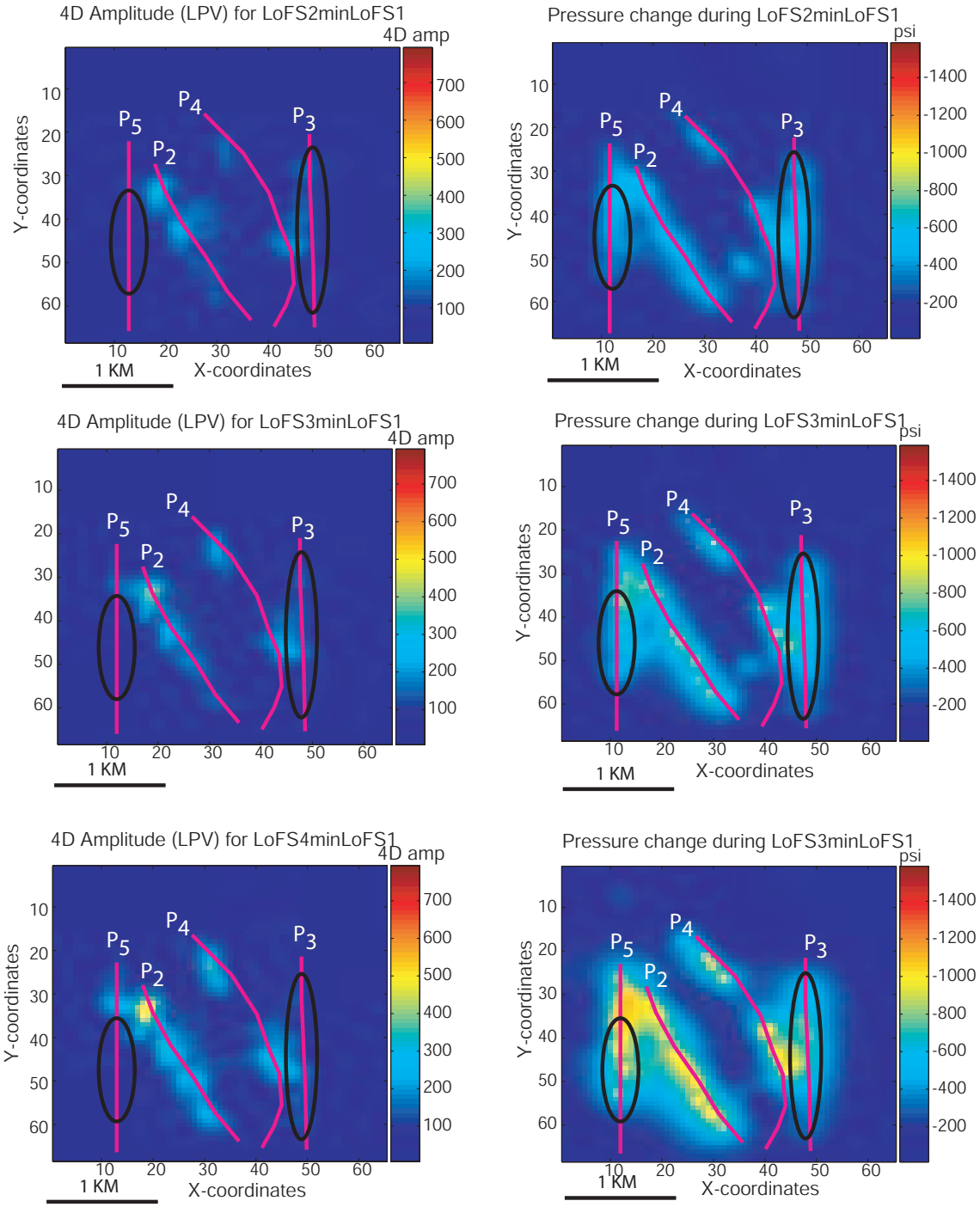

Figure 4.15: Largest positive value (amplitude attribute) for the time-lapse volumes: LoFS2minLoFS1, LoFS3minLoFS1 and LoFS4minLoFS1. The black ellipsoids denote the main discrepancies between the seismic attribute and the pressure changes. Pressure depletion was expected in these areas however the 4D amplitude did not detect any changes in the seismic properties. The pressure changes maps are outputs from the reservoir model (section 4.8).

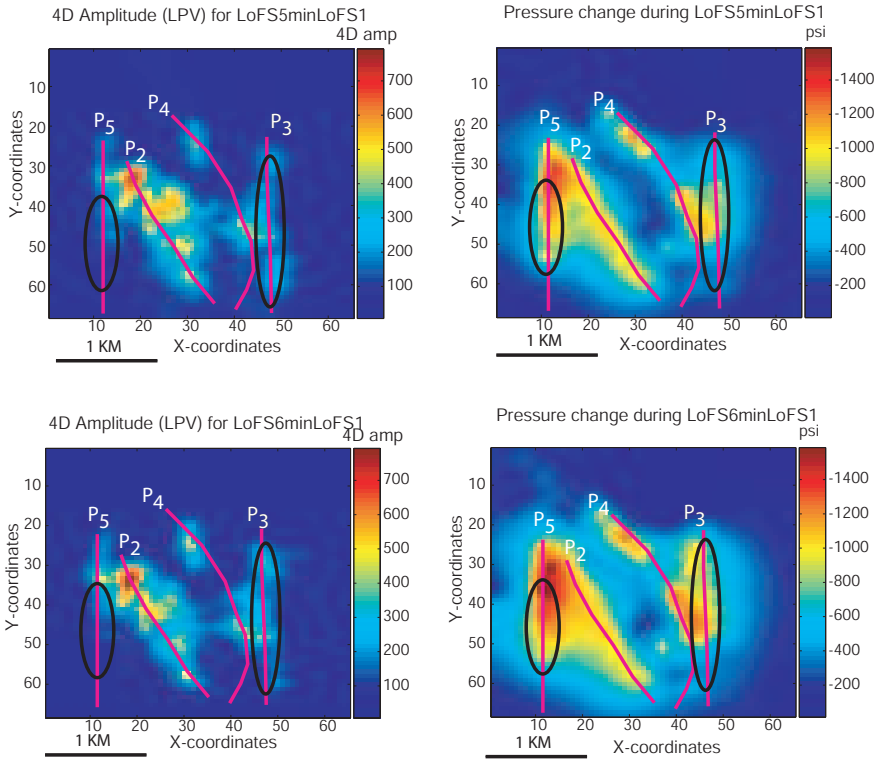

Figure 4.16: Largest positive value (amplitude attribute) for the time-lapse volumes: LoFS5minLoFS1 and LoFS6minLoFS1. The black ellipsoids denote the main discrepancies between the seismic attribute and the pressure changes. The pressure changes maps are outputs from the reservoir model.

4.6.3 Impact of the horizon seismic interpretation on the quality of the 4D seismic attributes extraction

The seismic attributes used in this study are based on pre-interpreted horizons. Therefore, it is important to investigate the reliability of the seismic interpretation. Since, the LoFS seismic volumes were not available for me, I decided to use the streamer data-sets to assess the structural complexity in the area and impact on the seismic interpretation. The two reflectors that are easily recognized on a standard 3D seismic volume are Balder Formation and the top Hard Chalk. These horizons serve as guide to locate the oil bearing zone since the base and top of the reservoir are generally not resolved at seismic scale because of the reservoir thickness and the low impedance contrast between the Lista Formation and Tor Formation. The time thickness between the Balder Formation and the Hard Chalk is around 60 ms on the South Flank. Two seismic cross-lines (E-W) in the south flank are shown in figure 4.21. The displays are from the streamer data acquired in 2002. In general terms

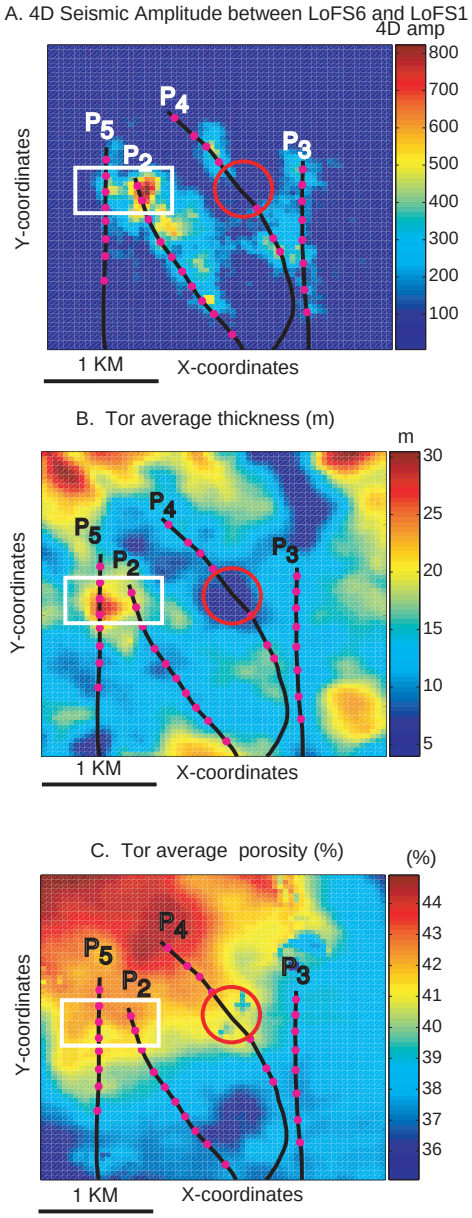

Figure 4.17: Comparison between the Largest positive value for LoFS6minLoFS1 and the reservoir properties (porosity and thickness). A. Largest positive value (amplitude attribute) for LoFS6minLoFS1. B.Tor average thickness. C.Tor average porosity. The large anomalies observed at the end of wells P_2 and P_5 correlate very well with the thickest and most porous Tor in the flank (White rectangle). The area located at the middle of P_4 does not have a very strong 4D signal. This area correlates with a very thin Tor Formation (red circle).

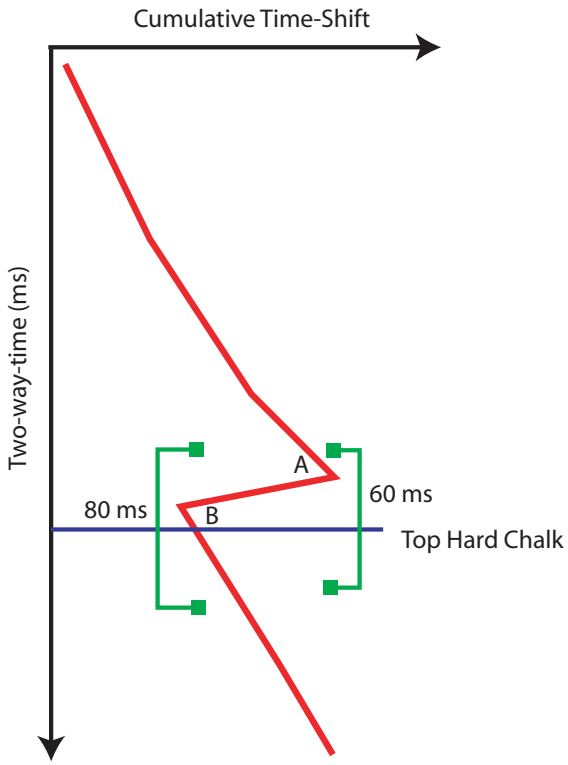

Figure 4.18: Extraction of the maximum and minimum time-shift attribute. Centered windows on the Hard Chalk top were used to estimate the maximum (labeled A on the graph) and minimum (labeled B on the graph) time-shifts. The minimum time-shifts were subtracted from the maximum time-shifts to get the speed-up attribute.

for this part of the field the seismic quality is high as the first seismic line illustrates; the Top of Hard Chalk and Balder show very good continuity and even some strong reflectors can be followed between both horizons. However, towards the TD of the P_5 and P_4 wells the seismic quality decreases due to the gas cloud affecting the crest of the field; furthermore some faulting is observed and the reflectors become broken and weak. This lack of continuity in the reflectors affects the interpretation of the reservoir zones and decreases the reliability of the 4D seismic attributes. Perhaps another issue that might affect the seismic attribute extraction is the thickness of the reservoir. In the flank, the thickness variation is very difficult to quantify on a seismic scale, however based on the well drilling reports, it was determined that P_5 found the Tor Formation with a thickness less than 10 m for the first 1000 m of the well. P_3 also found a very thin Tor at the beginning of the horizontal section (7 m), the net pay seems to increase to 15 m towards the toe of this well.

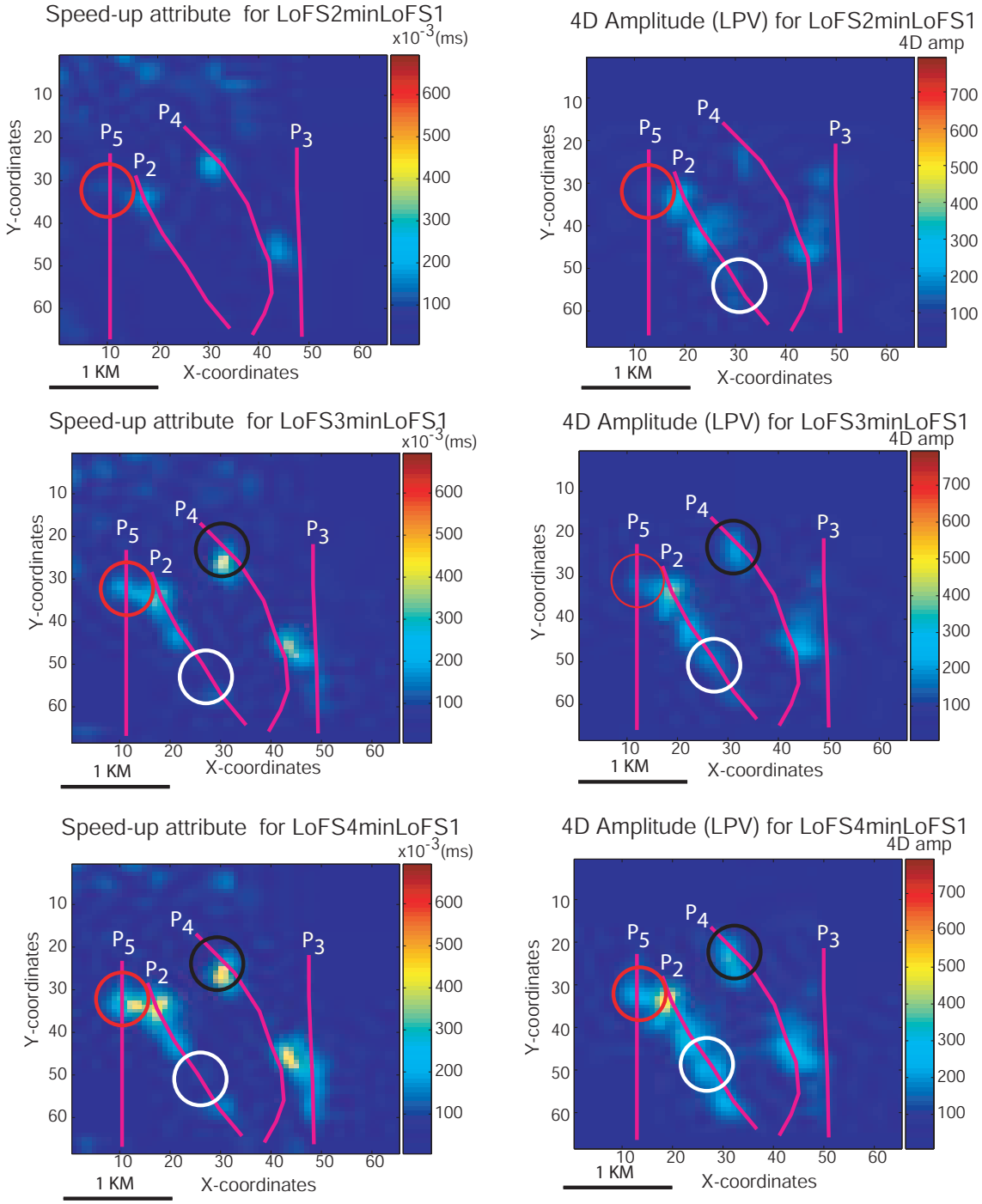

Figure 4.19: Speed-up (left side) and amplitude (right side) attributes for the time-lapse volumes: LoFS2minLoFS1, LoFS3minLoFS1, LoFS4minLoFS1. The circles denote the main discrepancies between both attributes. The most significant one occurs around well P_5 (red circle). In this area, there is an anomaly when the speed-up attribute is mapped however nothing is observed on the 4D amplitude map. A possible explanation is that the velocities in the Lista Formation are increasing (discussed in section 4.8).

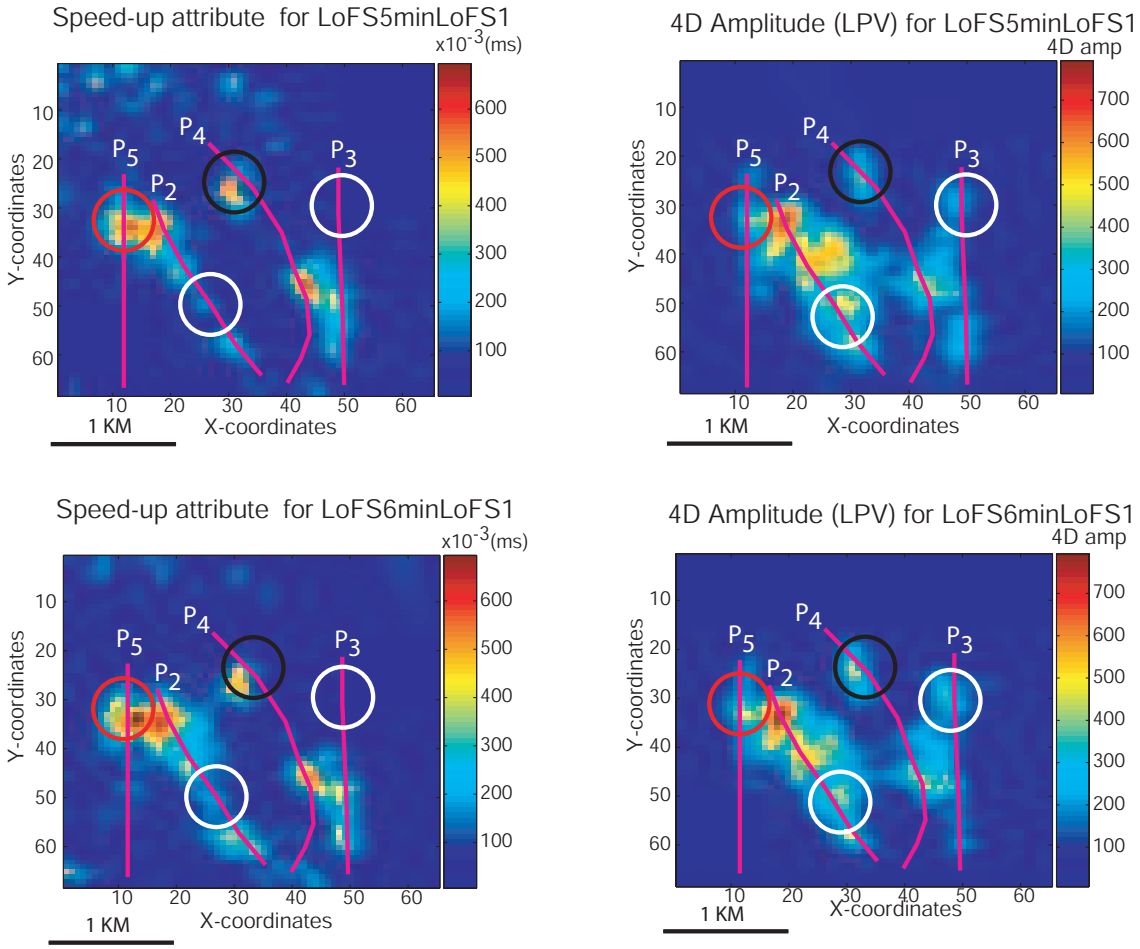

Figure 4.20: Speed-up (left side) and amplitude (right side) attributes for the time-lapse volumes: LoFS5minLoFS1 and LoFS6minLoFS1. The circles denote the main discrepancies between both attributes.

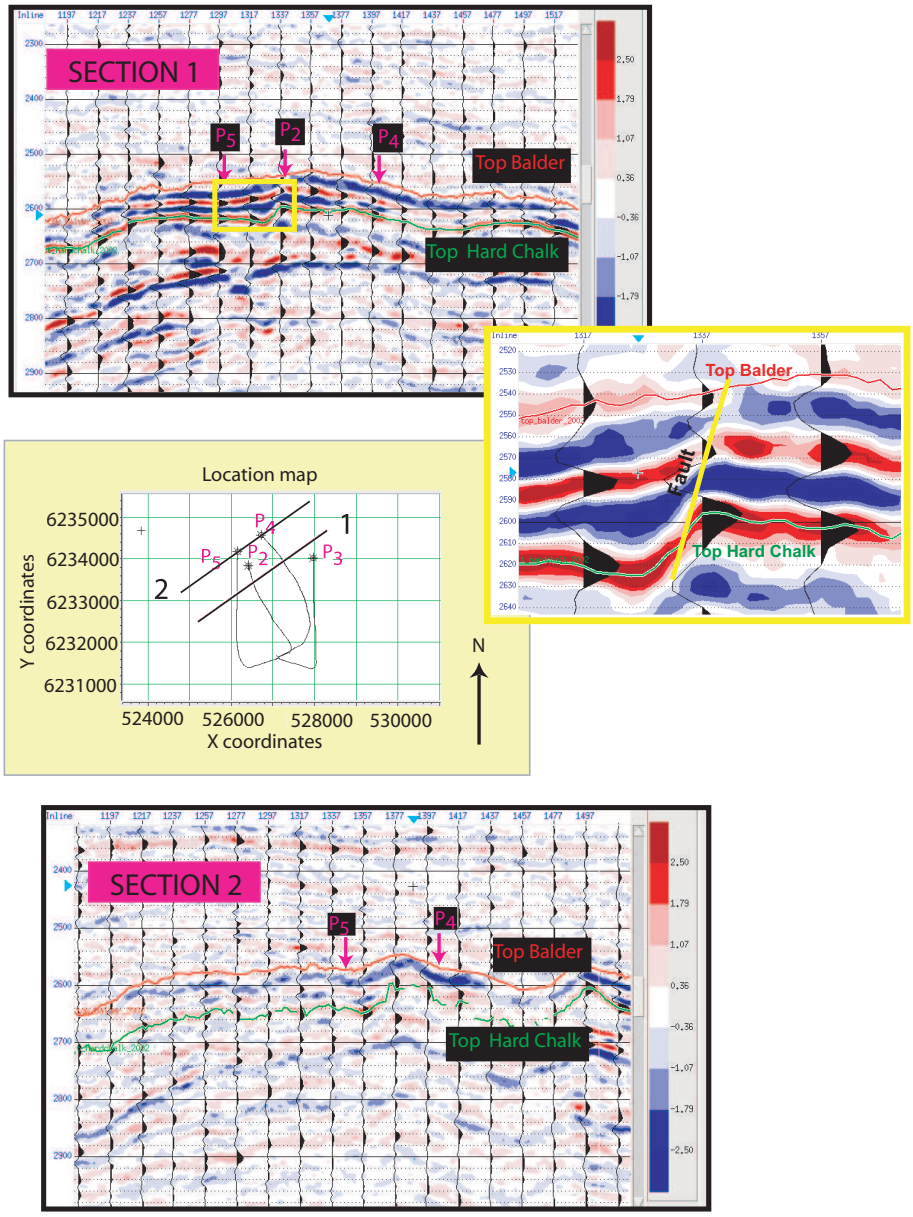

Figure 4.21: SE-NW seismic sections in the south east flank (2002 streamer seismic data). The seismic quality decreases towards the highest part of the flank (toe of the wells). The top Balder and top Hard Chalk reflectors are very continuous and easy to recognize in section 1. For section 2, the seismic quality decreases due to the gas cloud. The zoom in (yellow polygon) shows one of the small faults present around well P_5. These small structures might be affecting the fluid flow from the best pay found on the well (discussed in section 4.8).

4.7 A methodology to map reservoir pressure change from the time-lapse amplitude attribute

Determining the 4D signal that is to be cross-plotted against pressure changes is normally done by defining a threshold value. The threshold value represents the background (no changes) in an attribute map. Amplitudes higher than the threshold value are considered to be 4D signal related to production activity. Therefore the selection of the threshold value can affect the formulation of the trend equation used to compute the pressure maps from 4D seismic amplitude. For the south east flank, the initial threshold was 125. This value was determined by selecting an area where 4D signal due to production is not expected. Then, extracting the Largest Positive Value attribute in this area and finally, calculating the mean of the attribute.

I assess the impact that varying the threshold value has on the trend equation by including a threshold value range. A normal distribution of threshold values was generated using a mean of 125 and a standard deviation is 20. The number of samples in the normal distribution is 1000 (figure 4.24A). LoFS6minLoFS1 attribute map is used to define which bin locations have amplitude values higher than a specific threshold. LoFS6minLoFS1 map was chosen because it has the largest time difference therefore the 4D signal is better defined. For instance, the selected threshold is equal to 100. Then, if the 4D amplitude for LoFS6minLoFS1 is less than 100 at certain bin location inside a polygon, previously defined around a producer well, this bin location is identified and is not taken into account when the average 4D amplitude is calculated for all the difference volumes. This step is carried out for each sample in the normal distribution (i.e. 1000 times).

The methodology used to generate pressure maps from 4D amplitude in the south east flank, is comprised of the following six steps.

- Step 1 Definition of polygons around the producer wells and extraction of average porosity and pressure: Polygons are defined around the producer wells where 4D anomalies could be observed. Based on these polygons, mean values of pressure changes and initial porosity using the reservoir simulator outputs are estimated at the different times.
- Step 2 Calculate the average 4D amplitude at the different times for each polygon around the producer wells: The average 4D amplitude is calculated using the threshold approach previously

explained.

- Step 3 Correlating 4D amplitude against pressure changes and defining the equation: The pressure changes against 4D amplitude plots are created and a linear fit each for initial porosity was used to correlate the data (eq. 4.2). Finally, the gradients from equation 4.2 are cross-plotted against initial porosity and the coefficients D_1 and D_2 from equation 4.3 are computed.
- Step 4 Estimation of the final pressure changes map from 4D seismic amplitude

Steps 2,3 are repeated for each sample in the normal distribution (i.e. 1000 times). Then normal distributions for the coefficients D_1 and D_2 are obtained (figures 4.24B and 4.24C). The pressure changes from 4D amplitude are computed using each sample of the normal distributions for the coefficients (D_1 and D_2). Therefore, a distribution of possible pressure changes at each bin location is calculated. From this distribution a mean and a standard deviation maps are estimated (figure 4.25). The mean pressure map is compared with the pressure outcome from the reservoir model.

For simplicity, I describe the methodology using a threshold amplitude value of to 125. However the final pressure map shown in figure 4.25A is created taking into account a range of threshold values in the 4D amplitude attribute.

4.7.1 Steps 1 and 2: Definition of polygons around the producer wells and extraction of average porosity, pressure and 4D amplitude

Polygons were defined around each production well where 4D anomalies could be observed. Based on these polygons, mean values of pressure depletion, initial porosity and 4D signal (amplitude and time-shifts) were calculated at the different times. Since the reservoir model was available, fluid pressure and porosity information were taken from it. I assume that the wells produce from the entire Tor Formation and therefore an initial porosity representative of the formation in each polygon was estimated. The reservoir thickness, as derived from the thickness maps, were used to weight the average porosities as shown by equation 4.1.

$$\overline{\phi_0} = \sum_{k=1}^{6} \frac{\phi_k * h_k}{H} \tag{4.1}$$

where the initial average porosity is represented by $\overline{\phi_0}$, ϕ_k and h_k are the porosity and thickness from

layer k respectively, and H is the thickness of the Tor Formation.

Regarding the accuracy of the initial porosity and thickness maps, it is important to mention that the wells are horizontal and are normally drilled along a specific zone thus, the log data rarely brings information about the entire Tor Formation. This requires to incorporate data from neighboring wells to extrapolate the porosity and thickness of the non-drilled zones.

The reservoir simulation model was used to give fluid pressure at well locations. Although reservoir fluid pressure directly measured at wells is not available, down hole gauges are installed and constantly provided bottom hole pressure information. Furthermore, the initial reservoir pressure was measured as part of the logging programme while drilling. Both sets of data were used for the history matching process during the runs of the simulator. This gives some assurance that the simulated pressure outputs are close to the real reservoir pressure around the producers.

4.7.2 Step 3: Correlating 4D amplitude against pressure changes and defining the equation

Figure 4.22A shows the cross plot of reservoir pressure changes against 4D amplitude. Each point represents the pressure drop and the amplitude change between a monitor LoFS and LoFS1. For each area, there are 5 points identified by different symbols representing the 5 difference LoFS volumes. The location of the six polygons is shown in figure 4.22B.

The initial porosity for each polygon was extracted using the average porosity map for layers 1, 3, 5 and 6 and the results are listed on the second column of table 4.4. The data with the same initial porosity were grouped. This means that the highest porosity of 42% was given by polygon 1. Polygons 2 and 5 correspond to a initial porosity of 40%. Polygons 4 and 6 represent an initial porosity of 38%. The lowest porosity was 36% and was given by polygon 3.

Figure 4.23A shows that each initial porosity data set can be fit by a linear trend that intercepts the origin. This agrees with the observation made on chapter 3 since clear trends are observed for each porosity family. For the synthetic example, the trend equation to describe the 4D amplitude changes with pressure was power law equation as shown by equation 3.9. However on the real data, the maximum data points to define the relationship between 4D amplitude and pressure for each initial porosity family were 5. Therefore, I decided to hold C_2 equal to 1 and allow C_1 to vary as a

Polygon	Average initial porosity using Layers 1,3,5,6	Initial Porosity using Layer 5
1	42%	41%
2	40%	39%
3	36%	35%
4	38%	36%
5	40%	39%
6	38%	36%

Table 4.4: Average initial porosity for each polygon. Second Column: the initial porosity was estimated using an average porosity of 1, 3, 5 and 6. Third Column: Initial porosity from zone 5

function of initial porosity. Therefore, equation 3.9 becomes equation 4.2. This equation was used to fit the four data sets and the results are listed in table 4.5.

$$\Delta A = C_1^{\phi_i} * \Delta P \tag{4.2}$$

where ΔA and ΔP are the changes in seismic amplitude and pressure respectively and $C_1^{\phi_i}$ is the gradient that depends on the initial porosity. One observation that can be made from the plot of

ϕ_i	C_1	r^2
42	0.57	0.93
40	0.41	0.87
38	0.32	0.88
36	0.24	0.84

Table 4.5: C_1 as a function of Initial porosity estimated using equation 4.2. The initial porosity was estimated using an average porosity of 1, 3, 5 and 6. The correlation coefficient is shown in column 3.

pressure changes versus the 4D attribute, is that the 4D amplitude estimated using LoFS5minLoFS1 volume is out of the trend delineated by the other data points (star marker in figure 4.22). The reason is that a linear amplitude gain was applied to the LoFS5 volume (Olav Barkved, personal conversation). To improve the linear fit, I applied a weighted least squares regression where an additional scale factor (the weight) is included in the fitting process. The weights determine how much each 4D amplitude value influences the final parameter estimations. The data coming from LoFS2minLoFS1, LoFS3minLoFS1, LoFS4minLoFS1, LoFS6minLoFS1 were considered high-quality data points (assigned weight=1) and they influence the linear fit more than the low-quality data point coming from LoFS5minLoFS1 (assigned weight=0.4)

The final step is to correlate the different gradients found by equation 4.2 with the initial porosities (figure 4.23B). This produces the trend equation that captures the 4D amplitude changes as a function of the initial porosity, the two coefficients (D_1 and D_2) and pressure changes. The relationship can be written as follows:

$$\Delta A = (D_1 * \phi_i + D_2) * \Delta P \tag{4.3}$$

where ΔA is the 4D amplitude, ϕ_i is the initial porosity and ΔP is the pressure changes. D_1 is equal to 0.052 and D_2 is equal to -1.632

4.7.3 Step 4: Estimation of the final pressure changes map from 4D seismic amplitude

Steps 2 and 3 are repeated many times as the number of samples corresponding to the distribution of threshold values (figure 4.24A). Therefore for each bin location, there is going to be a distribution of coefficients D_1 and a distribution of coefficients D_2 (figures 4.24B and 4.24C). Using these two distributions, a pressure changes distribution is computed at each bin location. The map in figure 4.25A corresponds to the reservoir pressure changes for the period of time between LoFS4 and LoFS1. This pressure map results from selecting the mean of the pressure estimations at each bin location. The map in figure 4.25B is the standard deviation of the pressure estimations at each bin location. The final pressure changes map was computed under the following assumptions:

- There is no gas coming out of solution
- The entire Tor is producing.
- The initial porosity classes are computed by averaging the porosities from the different Tor zones.

Figure 4.26A is compared with figure 4.26C which represents the pressure output from the reservoir simulator for the period of time between LoFS4 and LoFS1. There is a good match between both outputs, however there are some discrepancies that need to be investigated. In the following section, I will discuss how these differences can be understood. Pressure predictions from 4D seismic in compacting reservoirs carry intrinsic errors due to acquisition together with effects such as the undesirable

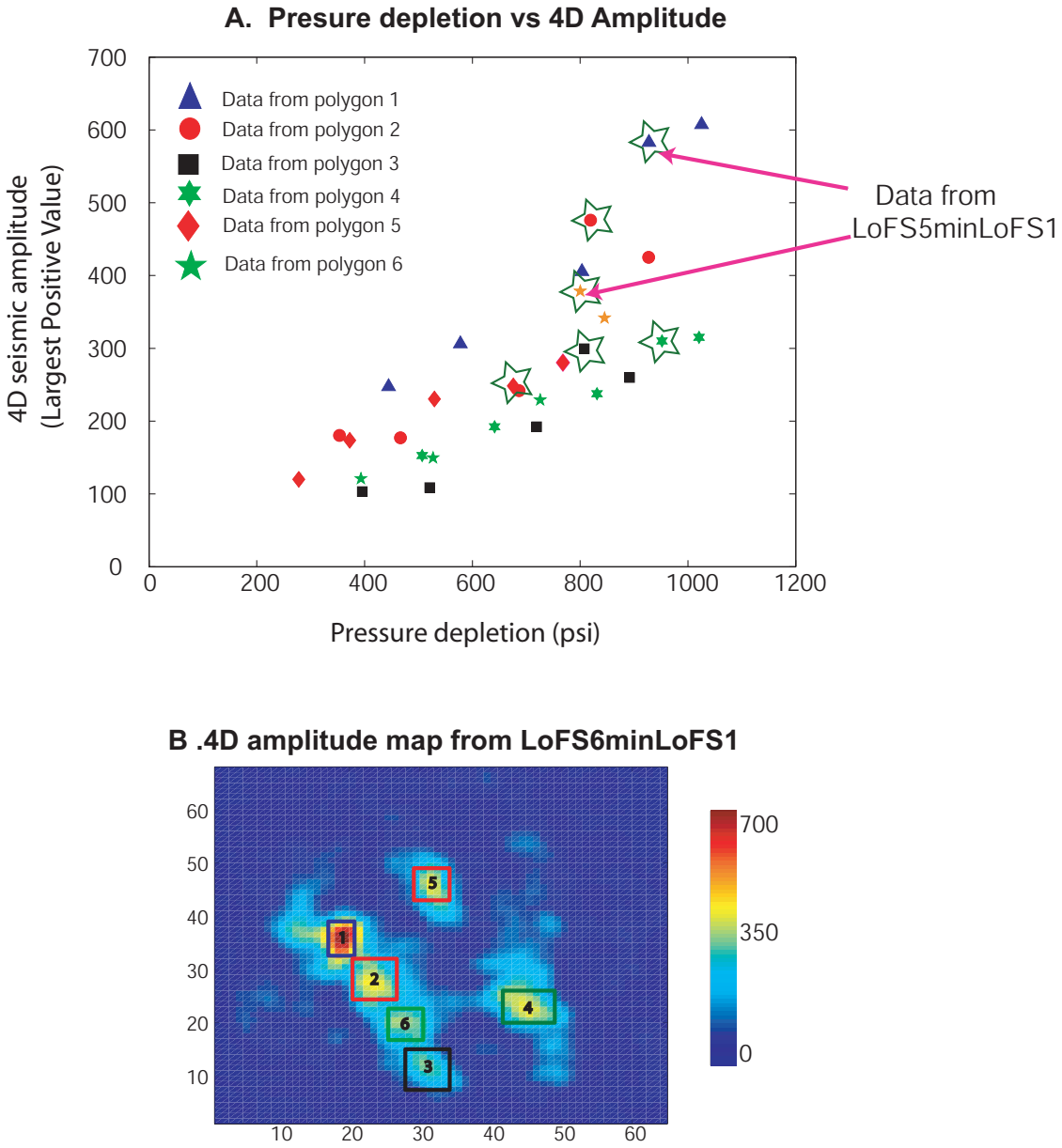

Figure 4.22: A. Cross-plot between pressure changes and time-lapse seismic amplitude for the south east flank of the Valhall Field. The average time-lapse seismic amplitude of each difference volume is cross-plotted against the pore pressure depletion occurring during the same lapse of time. These data are extracted for seven areas. The stars highlight the data from LoFS5minLoFS1, which is normally out of the linear trend. B. Location of selected zones are shown on the 4D amplitude map: the polygons were selected around the largest time-lapse anomalies.

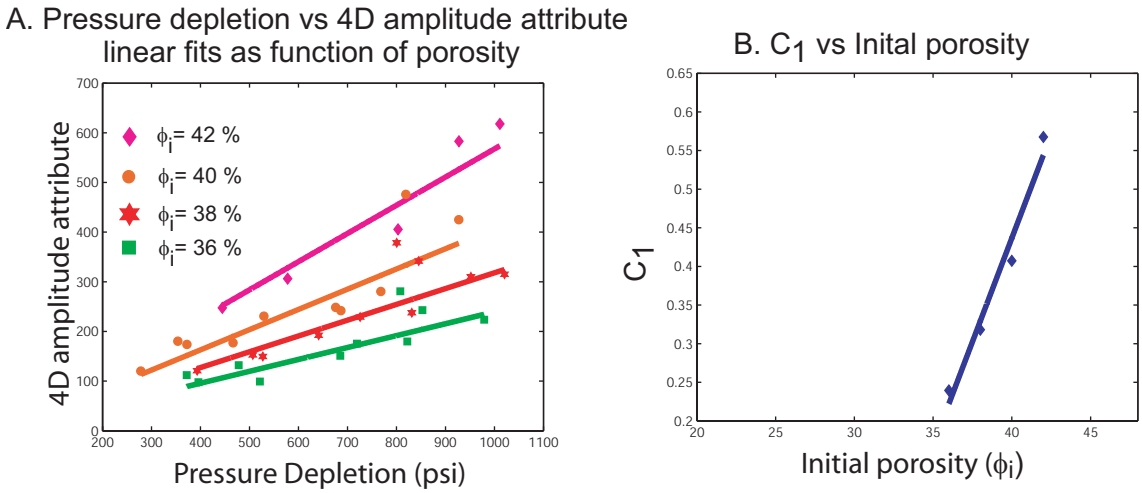

Figure 4.23: A. Linear approximations for pressure depletion vs 4D amplitude using equation 4.2. The gradient (C_1) for each porosity family is listed in table 4.5. B. Gradient (C_1) vs Initial porosity plot, equation 4.3 was used to fit the data.

overburden velocity changes and rock deformation. However the 4D signal provides invaluable information on the spatial distribution of pressure that combined with well data may produce a better and different insight into the reservoir compared to the predictions from the reservoir model.

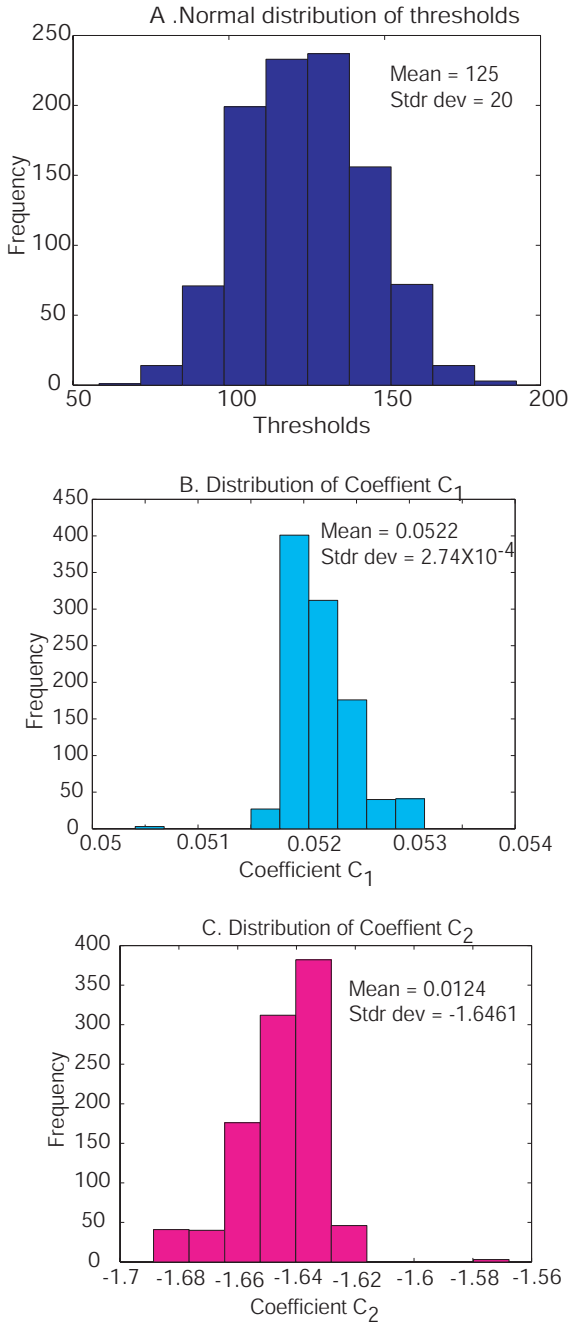

Figure 4.24: A. Normal distribution of the threshold values for the 4D amplitude between LofS6minLofS1. B. Distribution of the coefficient D_1. C. Distribution of the coefficient D_2.

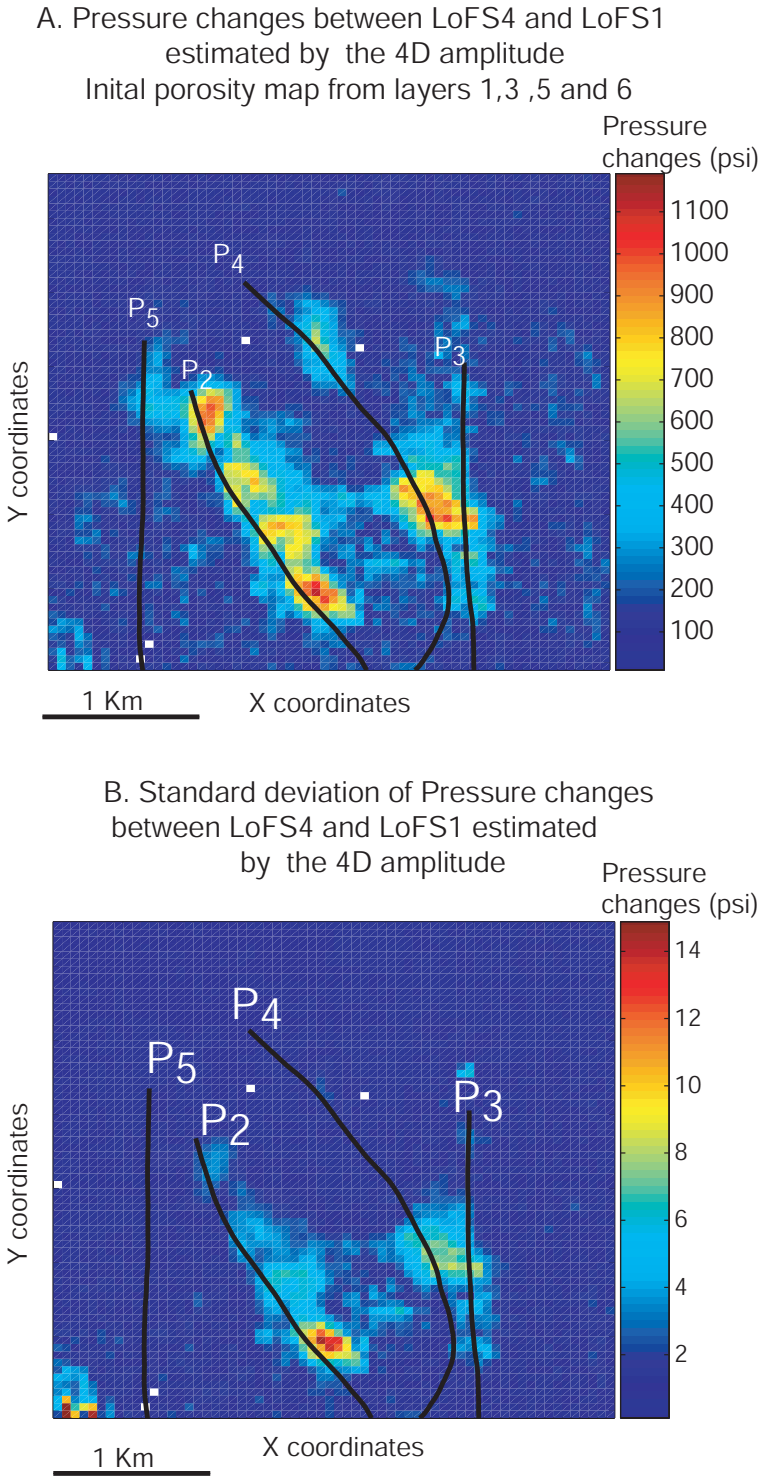

Figure 4.25: A. Pressure changes estimated from 4D seismic amplitude for the period of time between LoFS4 and LoSF1 using the methodology described in section 4.7. This map is the mean pressure change at each bin location. B. Standard deviation of the pressure changes estimated from 4D seismic amplitude at each bin location.

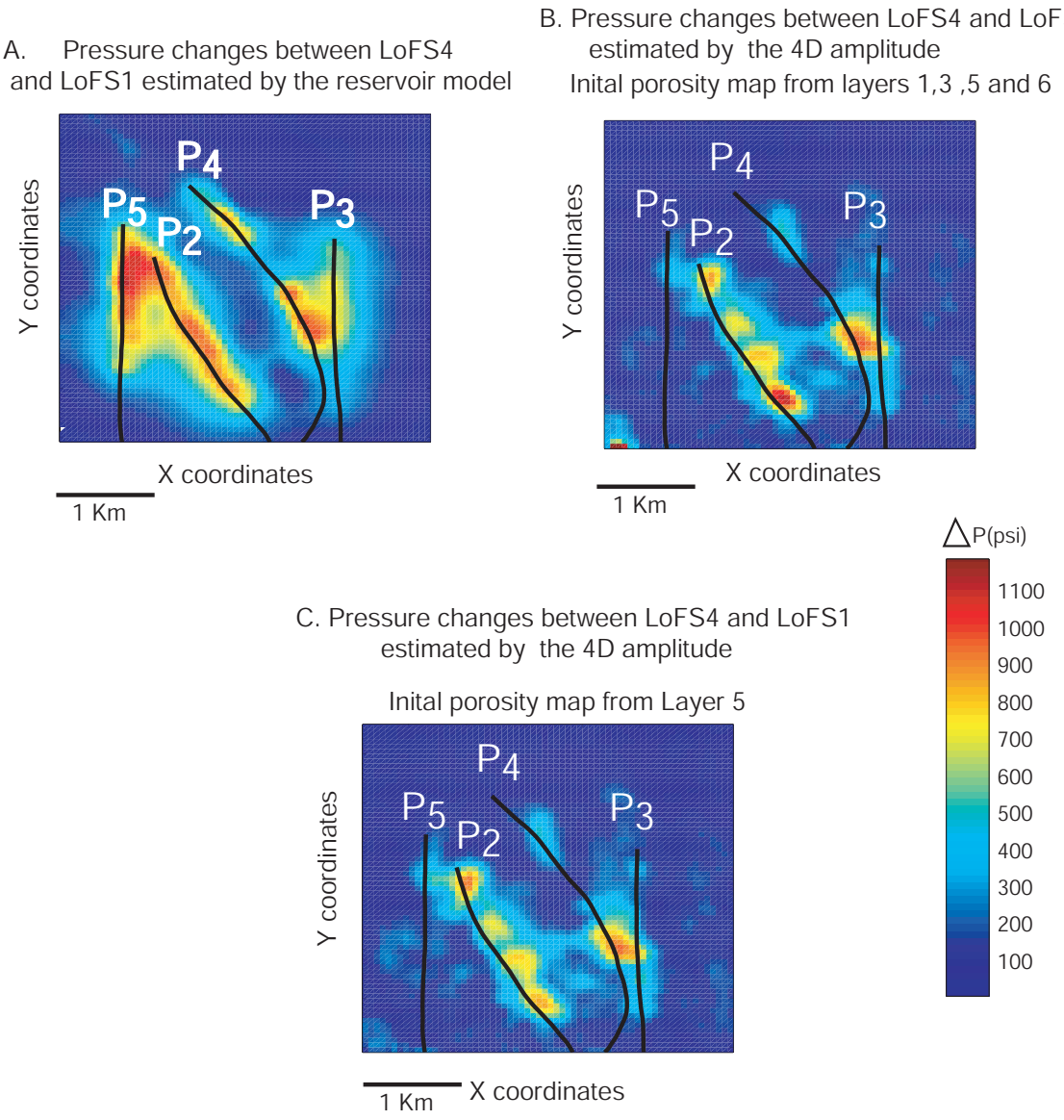

Figure 4.26: A. Pressure changes from the reservoir model for the period of time between LoFS4 and LoSF1. B. Pressure changes estimated from 4D seismic amplitude for the period of time between LoFS4 and LoSF1. The input initial porosity was an average porosity of zones 1, 3, 5 and 6. C. Pressure changes estimated from 4D seismic amplitude for the period of time between LoFS4 and LoSF1. The input initial porosity was the porosity of zones 5. This was decided after analyzing the zones where the wells were perforated. In general, the pressure estimations from 4D seismic seems to be localized around the wells. The pressure front observed from the output of the reservoir model is not seen on either map B or map C.

4.8 Analysis of the discrepancies between the pressure changes estimated from the 4D amplitude attribute and the pressure outputs from the reservoir model

The differences between the pressure changes estimated from the 4D amplitude attribute and the pressure map from reservoir model can be due to a) the way initial porosity was determined, b) the known uncertainty due to using pore pressure changes rather than effective stress changes and c) the amplitude response is influenced more by the velocity changes in the layer immediately above the reservoir (Lista Formation) rather than by the reservoir acoustic property changes.

Figure 4.27 displays the 4D amplitude maps and the porosity logs. It is observed that each 4D anomaly is correlated with a perforated area. For instance, the strongest time-lapse signal recognized at the toe of well P_2 can be linked with the high porosity Tor perforated in that area (red circle). Furthermore, a low porosity section was drilled by well P_4 but never perforated (blue circle) therefore no 4D signal is recorded there. Normally, the perforated well sections are decided based on the reservoir quality, for the south east flank the perforation are made into the high porous zones 3 and 5 and probably these zones are the most depleted ones. Therefore there is the possibility that the differences between the pressure maps are accentuated by choosing an initial porosity map which was the average porosity for zones 1, 3, 5 and 6, instead of map that represents the zones 3 and 5.

According to the porosity reduction curves shown in figure 4.32, the rock compaction has already started before the first survey was shot for a porosity of 42% in well P_3. However the greatest porosity lost has been recorded by the LoFS surveys. The total pressure depletion is around 2500 psi during a time window of 2.2 years. In the numerical model (chapter 3) similar pressure depletion ranges were reached and the areas of high initial porous chalk suffer more changes in the effective stress changes compared to the areas of low initial porosity. These changes in the effective stress are due to the changes in the average normal stress caused by the rock compaction. Therefore, it is possible that the 4D amplitude shows better correlation with the effective stress rather than the pore pressure depletion in the high porosity areas in the south east flank.

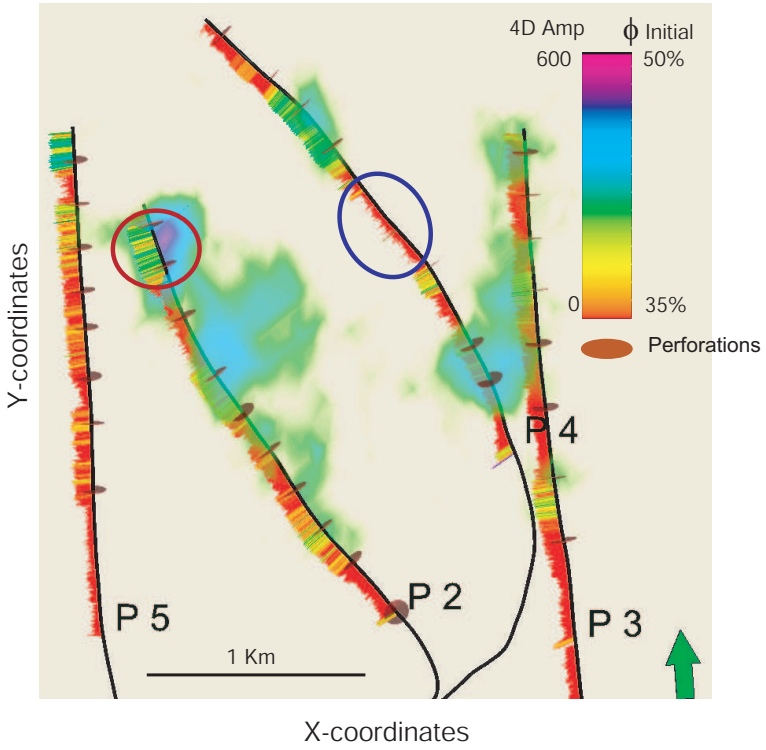

Figure 4.27: 4D seismic amplitude map for LoFS2minLoFS1: The neutron porosity log is displayed along the borehole. The background map is the 4D amplitude map for LoFS2minLoFS1. The perforations are the brown disk shapes. A general observation is that the 4D anomalies are occurring in areas where high porosity chalk has been perforated.

4.8.1 Initial porosity map

To assess the effect that adopting a different porosity map has on the pressure maps generated from 4D amplitude seismic, I decided to use the porosity maps from the penetrated and perforated zones in the wells. Figure 4.28 displays the porosity and gamma-ray logs for the P_2 well. The perforations are represented by squares. A series of histograms were generated at specific areas around the wells (for their location see figure 4.30). The histograms represent the absolute differences between the pressure changes from the reservoir model and the pressure estimations using as an initial porosity of: a) average porosity map from layers 1, 3, 5 and 6 (magenta bars), b) porosity map from layer 1 (blue bars), c) porosity map from layer 3 (orange bars) and d) porosity map from layer 5 (green bars). Generally, the results indicate that the differences between the pressure maps decrease when the initial porosity of the layers 5 and 3 are used during the calculations. All three diagrams (A, B and C) demonstrate that poorer results (bigger mismatches) are obtained when zone 1 is used

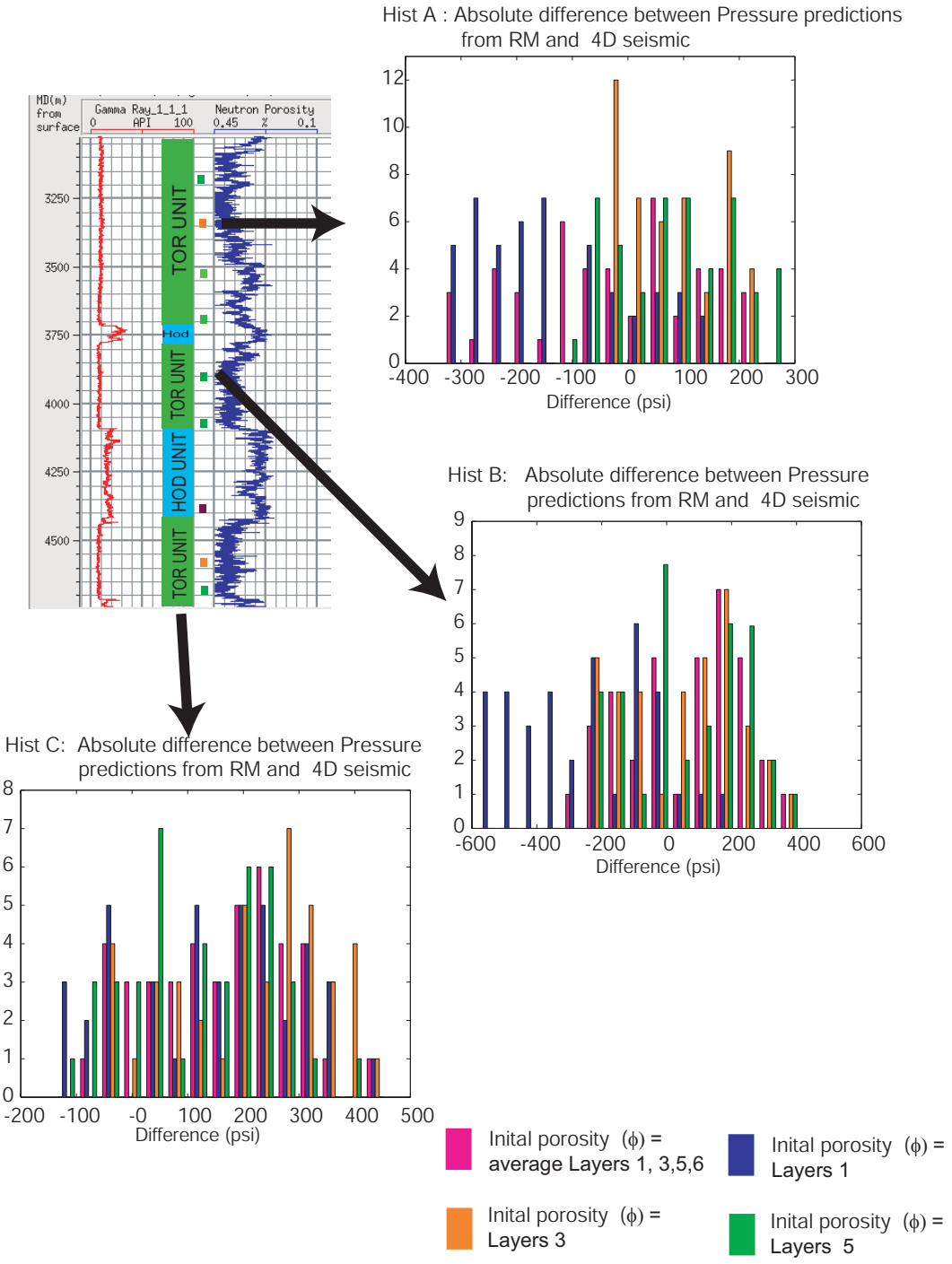

Figure 4.28: Analysis of the differences between the pressure changes estimated by the reservoir model and the ones predicted with 4D seismic amplitude at well P_2. This well was drilled in the Tor Formation, however a small portion penetrated the Hod Formation (at 4300 m). The perforation depths are shown between the gamma-ray and neutron porosity log. The majority of the perforations were made on zone 5 (green color). Each colored histogram represents the absolute differences between the pressure changes predicted by the reservoir model (RM) and the pressure changes predicted from 4D seismic using a different initial porosity map.

as input for the pressure estimation. For instance, the histogram A illustrates how the mismatch is reduced when either layer 3 or layer 5 initial porosity is used. An equal approach was taken to generate histograms around well P_4 (figure 4.29). These also confirm that a better match between the pressure changes maps from reservoir model and 4D amplitude will be obtained if either the initial porosity of zone 3 or zone 5 is used. According to the well reports, both wells have been drilled mainly on zones 3 and 5. However, most of the perforations have made in zone 5. Therefore, I can conclude that probably the best initial porosity map to be used for the pressure estimations will be from zone 5. Figure 4.30 shows the average porosity from zone 5. This map was used to re-calculate the pressure change from 4D seismic, using the methodology explained in section 4.7.

The third column in table 4.4 shows the initial porosities for zone 5 in each of the polygons. Using these initial porosities, the coefficients C_1 and C_2 of equation 4.3 were calculated and a new the pressure depletion map for the time between LoFS4 and LoFS1 was generated (figure 4.26C).

4.8.2 Low porosity effect

So far, it has been demonstrated that is possible to decrease the mismatch between the pressure prediction from the reservoir model and 4D seismic by considering that layer 5 is the most produced zone. However, this assumption does not reduce the differences in some areas where the main concern is that no 4D amplitude anomalies are recorded. The two most obvious areas where this is happening is around wells P_3 and P_5. According to figure 4.13, P_3 has the lowest accumulative production, followed by P_5. Furthermore, P_3 was the second producer on the Valhall South Platform and the reservoir pressure readings during drilling suggest that the well found the highest pressures in the area (table 4.6). So, if the initial pressure is high and the well was put on production just a month before the first LofS was acquired, why is 4D seismic response relatively low? Looking at figures 4.19 and 4.20, it is observed that a 4D signal at P_3 starts to appear after LoFS 4. Because the 4D signal seems to be located around the perforations and is influenced by the initial porosity, I decided to estimate the porosity distribution around the perforations for both wells. The neutron porosity log was used and the porosities were extracted along the borehole averaged in a 20m window. The window was created, having the perforation depth as the centre and porosity data from 10 m above and below this were averaged. Figure 4.31 shows the initial porosity distribution around the 8 perforations for well P_3. In general, the porosities are lower than 35% except for perforation 5 that has some porosities

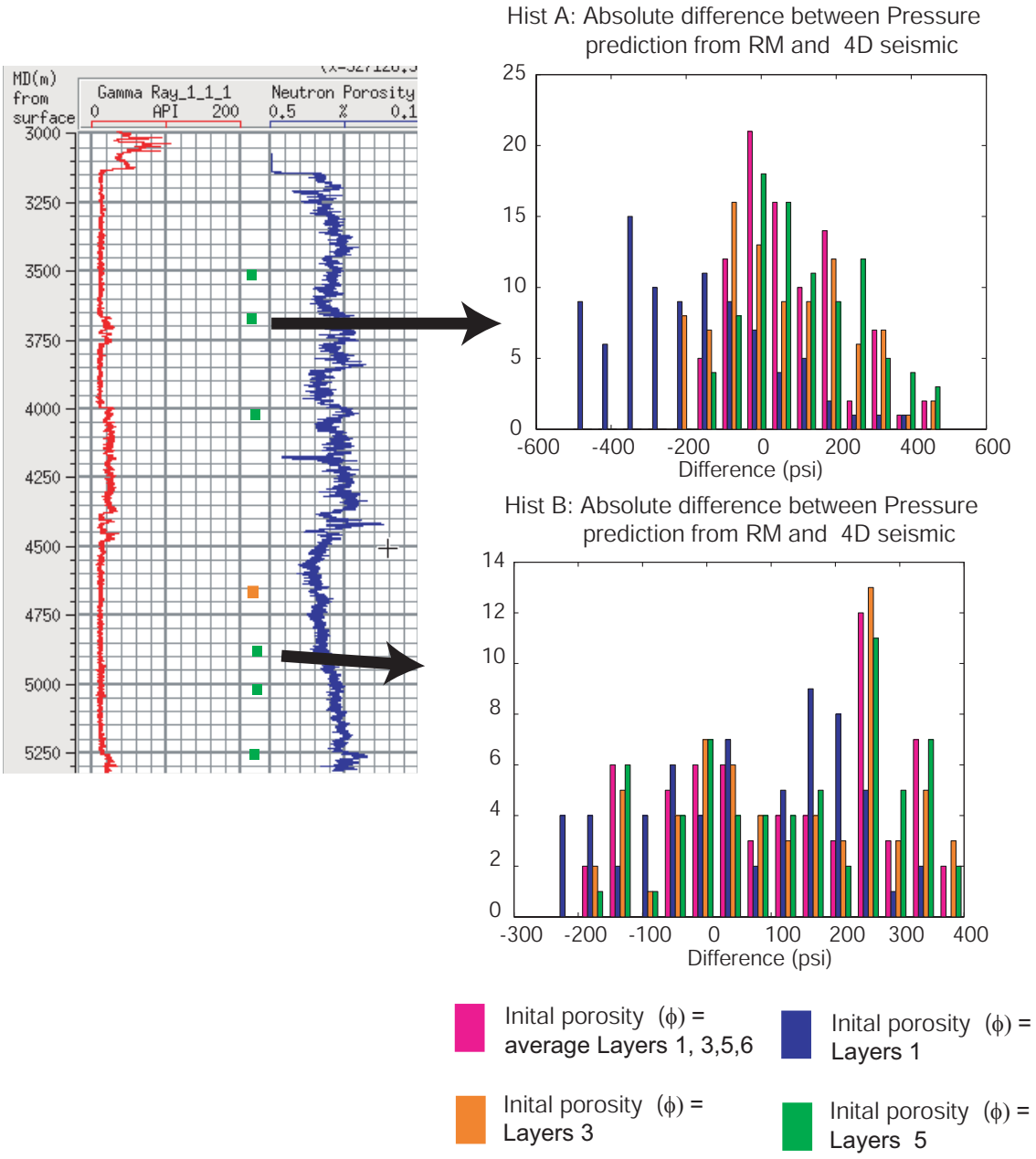

Figure 4.29: Analysis of the differences between the pressure changes estimated by the reservoir model with the ones predicted with 4D seismic amplitude at well P_4. This well was drilled on Tor Formation. The perforation depths are shown between the gamma-ray and neutron porosity log. A total of 7 perforation were place along the reservoir section. The majority of the perforation were made on zone 5 (green color). Each colored histograms represents the absolute differences between the pressure changes predicted by the reservoir model and the pressure changes predicted from 4D seismic using a different initial porosity map.

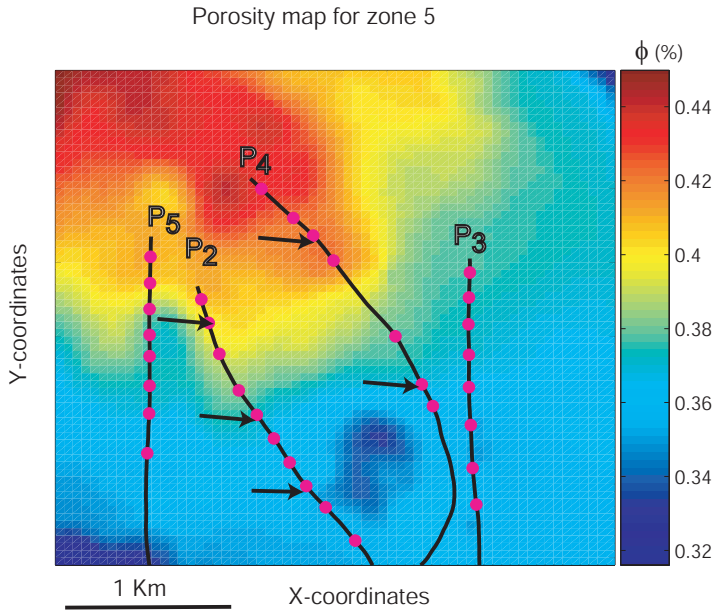

Figure 4.30: Initial porosity map for layer 5. The highest porosities were found by P_2, P_4 and P_5. The areas used to generate the histograms shown in figures 4.28 and 4.29, are indicated with the black arrows.

higher than 40%.

Based in chapter 3, I know that the time-lapse signal is responding to the pressure changes and the rock deformation, in fact the 4D response is enhanced by the compaction. In well P_3 the reservoir has been depleted but how much rock compaction has occurred? A simple way to determine the rock compaction is by using the synthetic porosity curves together with the pressure information. These curves have been used by the reservoir engineers to estimate the porosity reduction as a function of pore pressure for calculations of the pore volume and the matrix permeability.

The porosity loss curves have been calibrated with geomechanical tests on core data, sea floor subsidence records and bullet markers. Some discrepancies between the real rock deformation and the one predicted by the curves have been reported on the crest of field (Barkved *et al.*, 2003), where the structure is very complex (high density of fractures and faults) and other geomechanical effects might influence the compaction. However on the flanks due to the fairly simple structure, these curves are considered a valid approximation to describe the compaction phenomena.

Figures 4.32A and 4.32B illustrate how the porosity evolves as the pressure decreases for initial porosities of 32% and 42% using the porosity loss curves. These porosities families were found

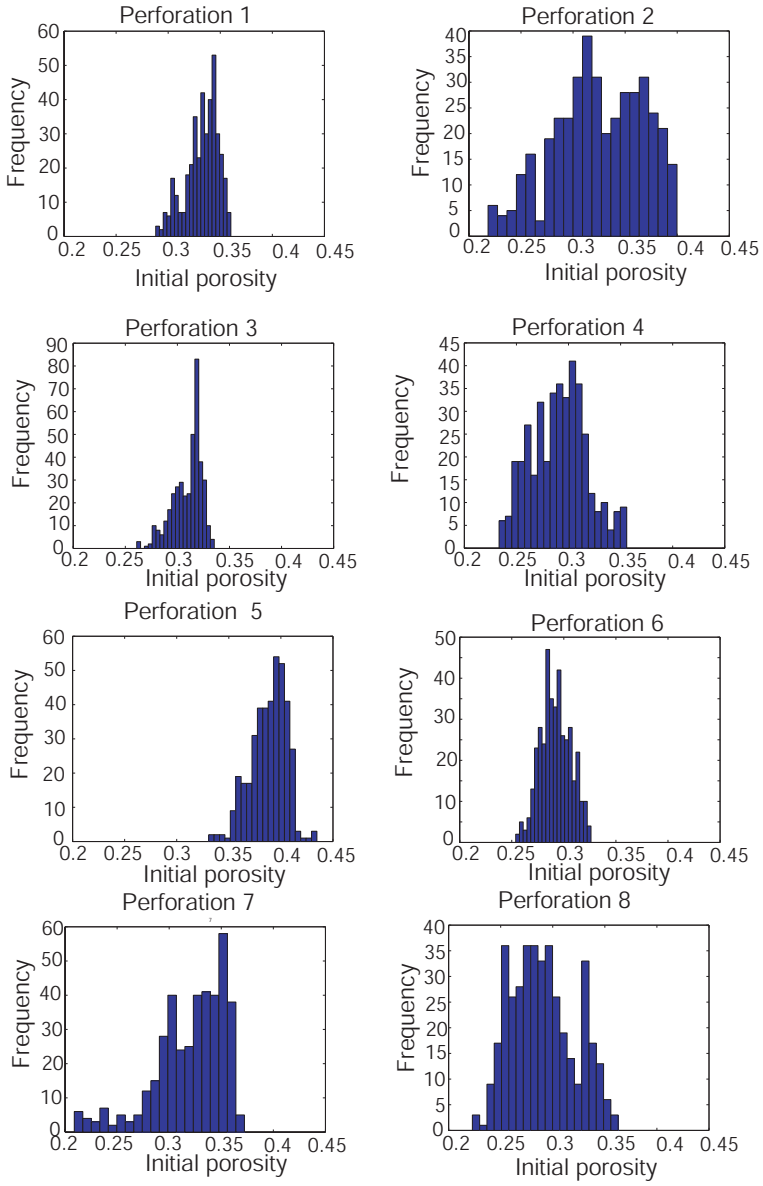

Figure 4.31: Porosity distribution for the perforations in well P_3. The porosities are lower than 35% except for perforation 5 that has some porosities higher than 40%.

around the perforation 7 in P_3 and the perforation 10 in P_2 respectively. The lines on the curves define the reservoir pressure when the wells were put on production for the first time and when the LoFS volumes were acquired (table 4.6). For an initial porosity of 32%, the graph suggests that small porosity loss has occurred during the acquisition of the six volumes. On the contrary, for a initial porosity of 42%, the porosity has reduced from 42% to 39% during the same period of time. Figure 4.32C shows the 4D anomaly produced by 585 psi of pressure depletion in perforation 7 (well P_3) while figure 4.32D shows the 4D amplitude for a pressure depletion of 555 psi in well P_2 (perforation 10). The amount of pressure depletion is very similar, however the 4D amplitude anomaly is smaller in well P_3 than the one produced by well P_2. This is evidence that the porosity collapse added to the pressure depletion of perforation 10 in well P_2 is enhancing the 4D signal. The same phenomenon is captured by figure 4.33, where the initial porosity distribution for some 4D anomalies in wells P_2 and P_4 are displayed. The best defined 4D amplitudes are located around perforations 3, 9 and 10 for well P_2 and perforations 2 and 5 for well P_4. The common characteristic between these perforation is that the porosities are generally higher than 35%.

Figure 4.34 shows how the 4D amplitude progresses through time for perforations 9 and 10 in well P_2. In this area, the porosities are above of 42%. The 4D amplitude starts to be noticeable since LoFS2minLoFS1 and intensifies through time. According to figure 4.32B, this initial porosity began to reduce simultaneously as the production started. Therefore the 4D anomaly is intensified by the porosity loss.

Another obvious observation made from figure 4.33, is the way the time-lapse signal keeps confined to the high porosity zones. In well P_2, perforation 9 is right after a very low porosity area. The low porosity zone probably has been produced by perforation 8. Even though this zone is depleted, the 4D anomaly is fairly weak here because the porosity is lower than 35%

Figure 4.35 compiles the initial porosity distribution for the eight perforations made on well P_5. This well does not have a strong 4D signal (figure 4.33). The producer P_5 was designed to drain a graben identified on the seismic data and penetrated by an abandoned producer. In this area, the Tor Formation is very thin (around 10 m). Also, the porosities are lower than 35% for perforations located on the upper part of the well (perforations 1 to 6). Therefore the thickness and the lower porosities can explain the small the 4D amplitude. In contrast however, perforation 8 (at the toe of the well) found a high porosity zone which does not correlate with a time-lapse signal. Based on

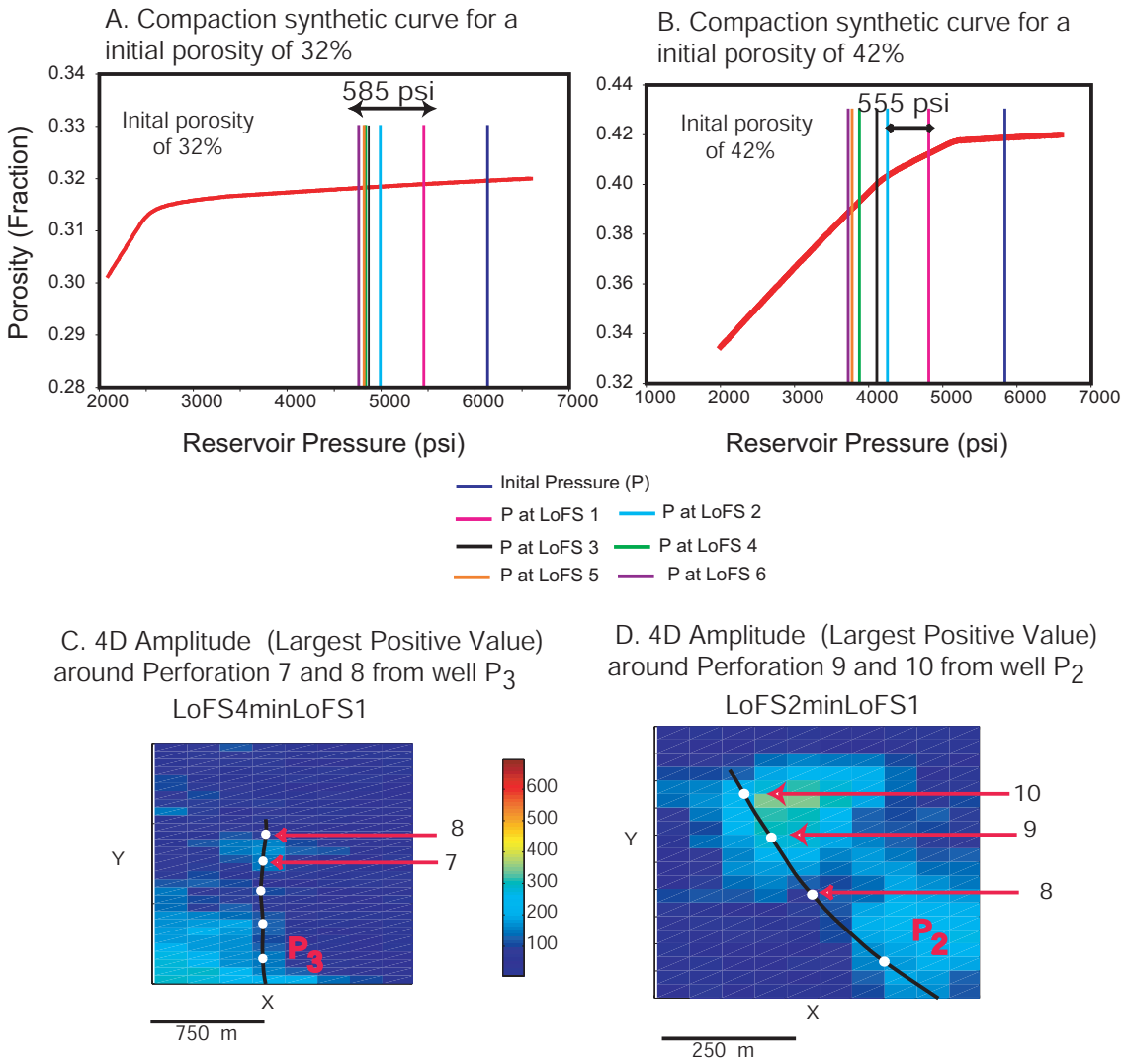

Figure 4.32: Comparison between a 4D amplitude anomaly caused by two different initial porosity families. Figures A and B illustrate how the porosity evolves as the pressure decreases for initial porosities of 32% and 42% using the porosity loss curves. The lines on the curves define the reservoir pressure when the wells were put on production for the first time and when the LoFS volumes were acquired (table 4.6). Figure C shows the 4D anomaly produced by 585 psi of pressure depletion in perforation 7 (well P_3) while figure D shows the 4D amplitude for a pressure depletion of 555 psi in well P_2 (perforation 10).

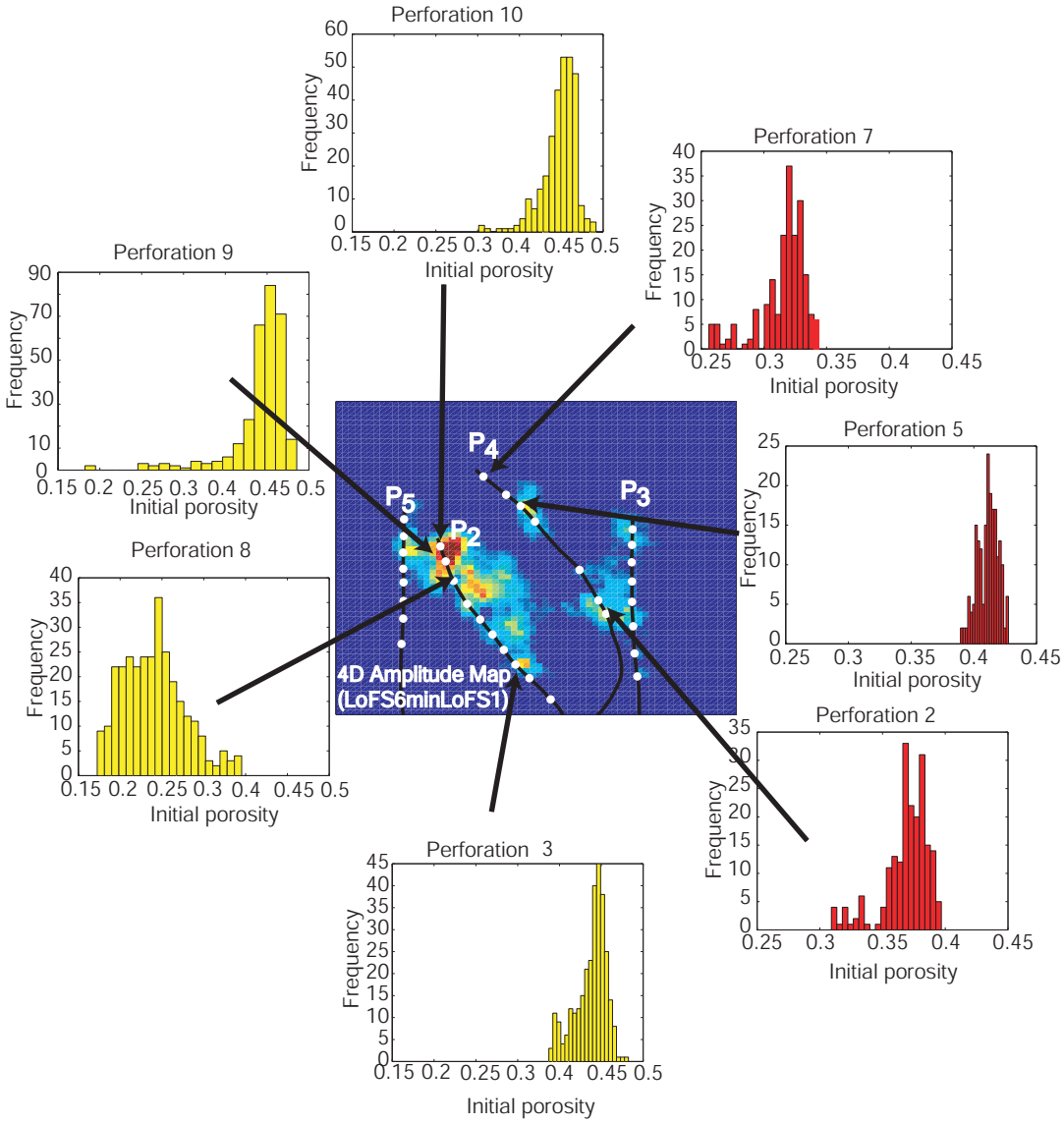

Figure 4.33: Comparison between a 4D amplitude anomaly caused by two different initial porosity families. The initial porosity distribution for some 4D anomalies in wells P_2 and P_4 are displayed. The best defined 4D amplitudes are located around perforations 3, 9 and 10 for well P_2 and perforations 2 and 5 for well P_4. The common characteristic between these perforations is that the porosities are generally higher than 35%.

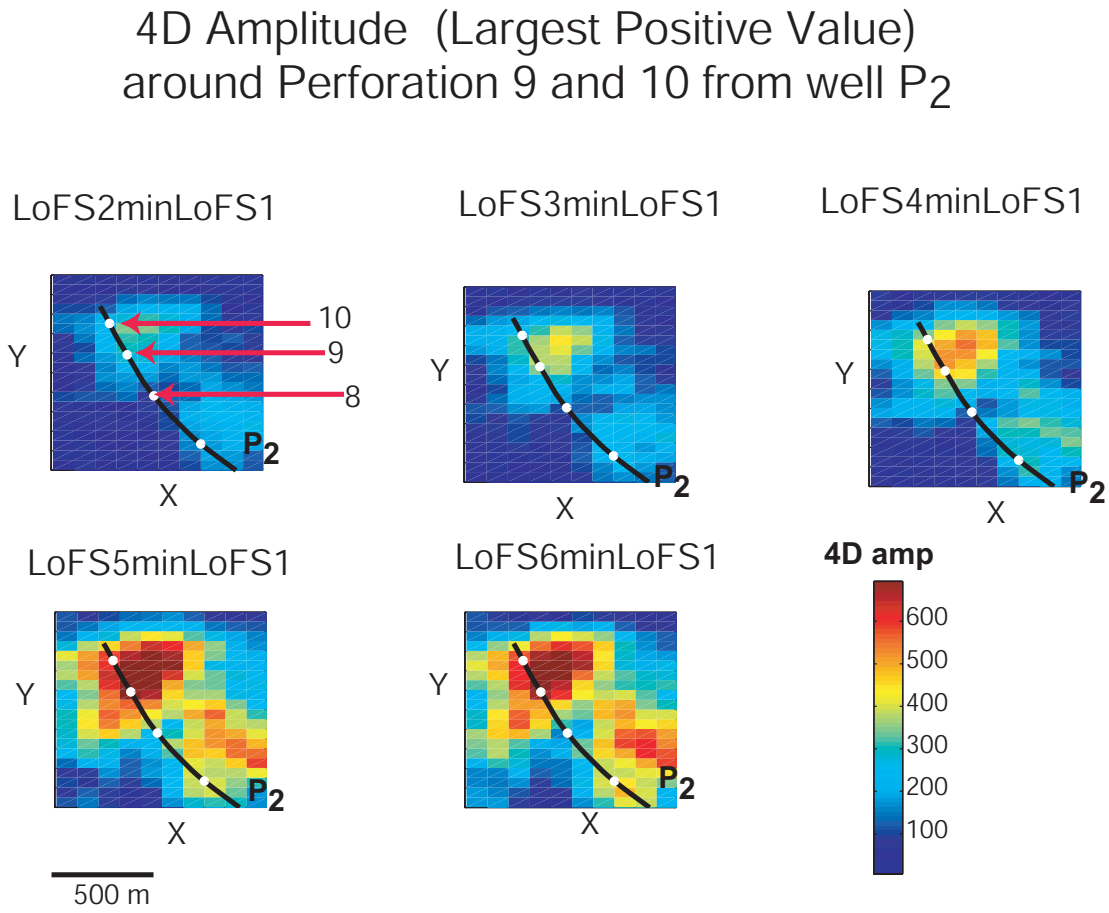

Figure 4.34: Evolution of 4D amplitude anomaly through time for perforations 9 and 10 in well P_2. In this area, the porosities are higher than 42%. The 4D amplitude starts to be noticeable since LoFS2minLoFS1 and intensifies through time due to induced compaction.

the 4D response of similar porous zones (perforations 9 and 10 from well P_2 and perforation 5 from well P_4 in figure 4.33), I conclude that this zone has probably not been produced but unfortunately there is no PLT information to validate this conclusion. Nevertheless, the drilling report mentioned that towards the toe of the well (after perforation 7) small faults were crossed and perhaps these structures are affecting the fluid flow over that area (figure 4.21).

4.8.3 Normal stress changes and overburden velocity changes

The speed-up attribute explained in section 4.6 was used to estimate pressure and compared with the output from 4D amplitude. However it is necessary to be aware that some of the time-shifts measured are smaller than 1 ms, which is less than the sample rate (4 ms) and probably in some areas this signal is below the noise level. This attribute can be of low confidence in thin reservoir areas such as the zones drilled in the first half of wells P_4 and P_3. Furthermore, the speed-up attribute should be positive if it is only due to pore pressure depletion and reservoir compaction, therefore the pressure estimation was carried out considering only positive time-shifts, which is in general the case around the producers.

The polygons used to extract are shown in figure 4.36A. The initial porosities come from layer 5 and the cross-plot between the speed-up and the pressure changes is shown in figure 4.36B. As with the amplitude attribute, the pressure depletion was estimated between LoFS4 and LoFS1.

Figure 4.37 compares the pressure depletion from the reservoir simulator and the ones estimated from 4D amplitude and the speed-up attribute. Pressure predictions in areas A and B (red and blue squares in figure 4.37) from 4D amplitude agree more with the reservoir simulator than the estimations from the speed-up attribute. These areas correspond to a thin reservoir found by wells P_4 and P_3 and therefore the accuracy of the speed-up attribute is low.

Pressure predictions around perforation 6 for well P_5 and at the toe of well P_2 (area C) correlate better when the speed-up attribute is used (black square in figure 4.37). From figure 4.19, I notice that the time-shift anomaly appears around well P_5 while nothing is observed on the 4D amplitude map. However, both seismic attributes have a good chance of capturing the pressure effect since the reservoir is thick and porous. According to the well reports, a very good net pay was perforated by both wells. So why is there a difference between the 4D amplitude and the speed-up attributes?

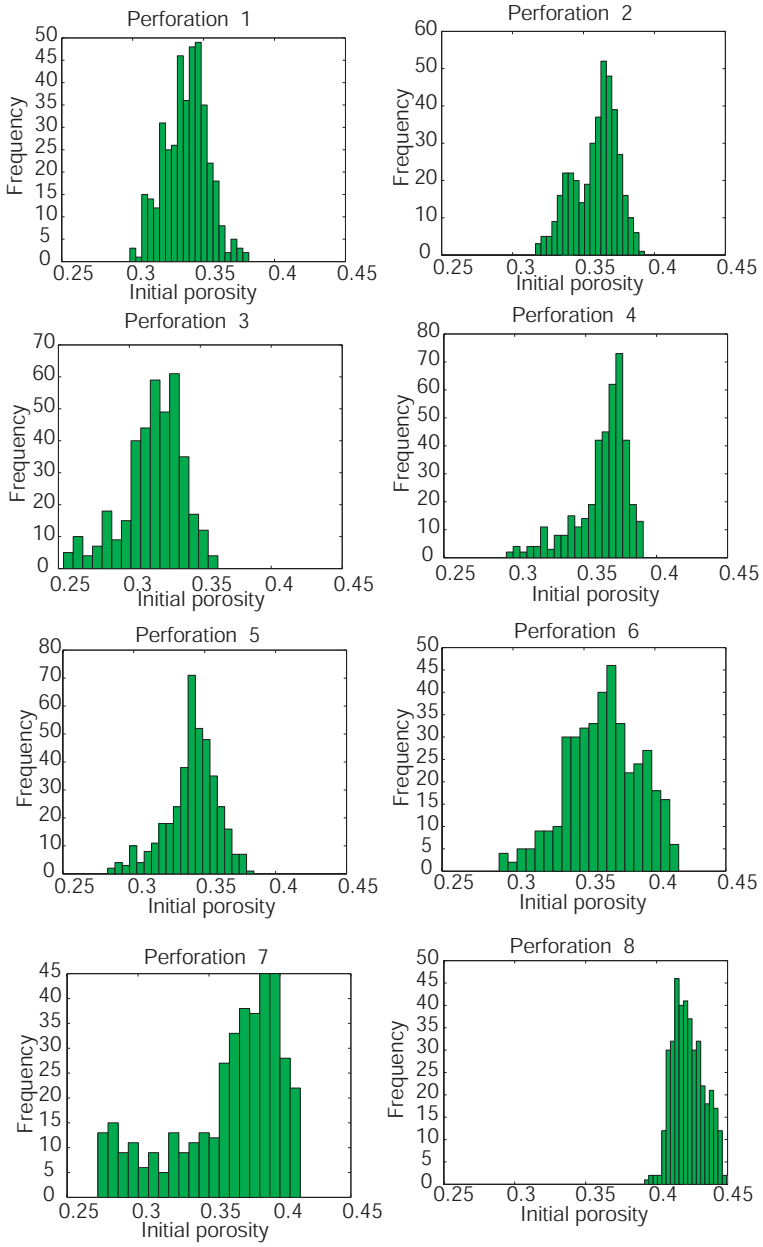

Figure 4.35: Porosity distribution for the perforations in well P_5. The porosities are lower than 35% for perforations located on the upper part of the well (perforations 1 to 6). However, perforation 8 (at the toe of the well) found a high porosity zone.

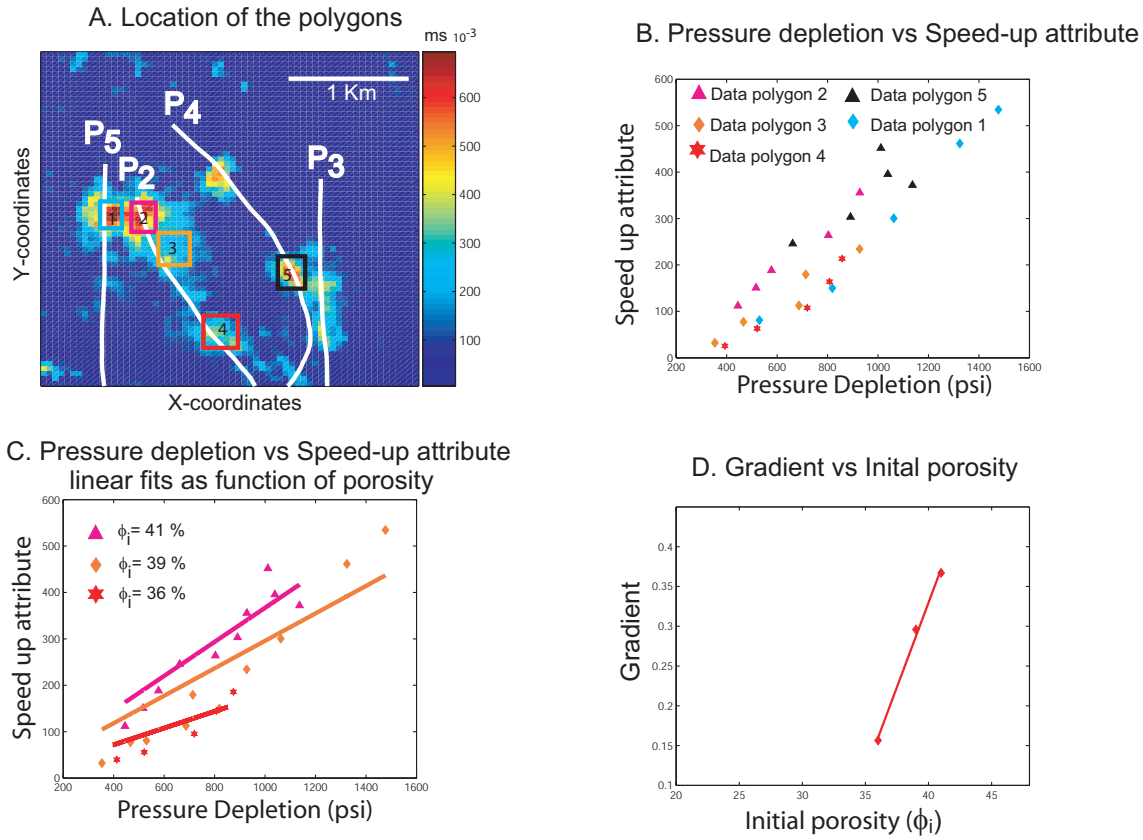

Figure 4.36: A. Location of the areas (polygons) used to cross plot pressure vs speed-up attribute B.Cross-plot of pressure depletion vs the speed-up attribute C. Best Linear fit for the different initial porosities. D. Gradient vs Initial Porosity.

So far I have considered that when a high porous chalk compacts due to pressure depletion, the reservoir acoustic impedance increases while the acoustic impedance in the layer immediately above (the Lista Formation for the Valhall Field) decreases due to the unloading process. This process enhances the 4D signal since the contrast at interface will get increased. If this was the case for well P_2, an amplitude anomaly similar to the one shown by the speed-up attribute could be seen. One possible explanation is that the P-wave velocity in Lista Formation is actually increasing due to loading effect (rock compaction), making the acoustic impedance contrast smaller. Therefore no 4D amplitude is observed but the speed-up anomaly will still be present.

Compaction in the overburden shale has been previously considered in the Valhall Field (Kristiansen, 1998). The curve predicting the drainage from these shales using laboratory data, estimates a compaction of the Lista Formation in the order of 0.75 to 1.75 m, assuming a pressure drop in the

cap-rock of 1500 psi. This compaction must be added to the reservoir compaction to determine the seafloor subsidence. Even though the cap rock does not accumulate the hydrocarbon, it is permeable and theoretically a large pressure differential between the shales and the reservoir could cause the drainage of the cap rock.

If the shales are drained and compacted, I could expect to have an increase of P-wave velocities and a decrease on the impedance contrast at the top of the reservoir. Barkved and Kristiansen, (2005) showed an example where the uploading effect (decrease in P-wave velocity) was reversed 100 meters above the reservoir but so far this effect immediately above the reservoir has not been observed.

Pettersen (2006) used the time-shift volumes to extract and stack traces around the toe of well P_2 (figure 4.38), the maximum time-shift is observed at 2450 ms, after that there is a decrease until 2550 ms, where the time-shift starts to increase again. This point could be interpreted as the base of the Tor Formation located 70 ms above the Hard top chalk. Therefore, there is a 100 ms window where an increase in P-wave velocity is occurring. Now, is the reservoir as thick as that window? From the reservoir model, the thickness of the porous chalk in this area is around is 22 m. In order for the reservoir to have time thickness of 100 ms, the velocity should be of 440 ms. This value is very low for a high porous chalk.

The most optimal way to estimate the reservoir velocity would be to use a check-shot in the well but it was not available, therefore I decided to used a sonic log acquired on P_1 (the first producer drilled on the flank). Figure 4.39 shows that there is a linear correlation between P-wave velocity (V_p) and initial porosity (ϕ_i) that can be expressed as follows:

$$V_p = -5.76\phi_i + 4.67 \tag{4.4}$$

From equation 4.4, the P-wave velocity is equal to 2035 m/s for an initial porosity of 44% (average porosity observed around the anomaly). This velocity and a reservoir thickness of 22m, give a time thickness of 21 ms. Assuming the base of the reservoir is located at 2550 ms, the reservoir top is located approximately at 2525 ms. So why does the decrease in time-shifts start to appear at 2450? One possible answer is that the velocity in the Lista Formation is increasing due to shale compaction as pointed out by Kristiansen (1998). Therefore, a possible compaction in the Lista Formation combined with the pressure depletion and reservoir compaction can explain why there is

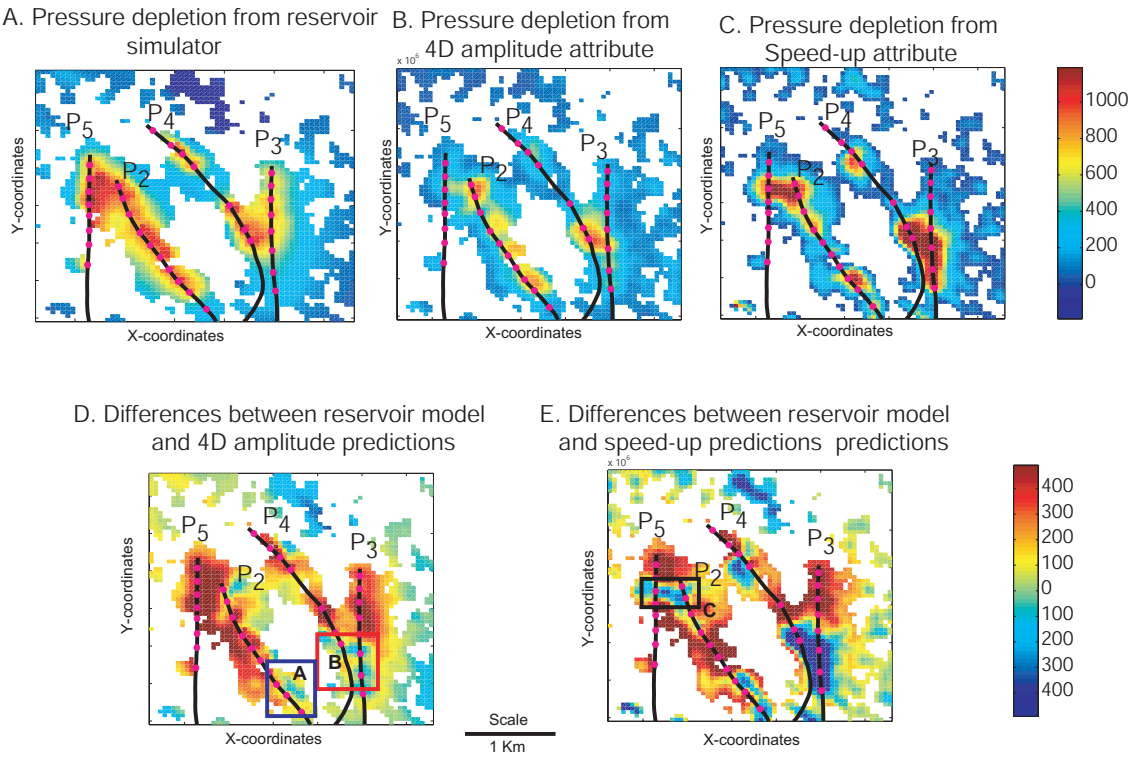

Figure 4.37: Comparison between the pressure predicted from the speed-up attribute and the 4D amplitude attribute. A. Pressure depletion from the reservoir simulator between LoFS4minLoFS1, B. Pressure depletion estimated form the 4D amplitude attribute (Largest Positive Value) between LoFS4minLoFS1, C. Pressure depletion estimated form the speed-up attribute between LoFS4minLoFS1, D.Absolute differences between Map A and Map B, D.Absolute differences between Map A and Map C.

an anomaly in the speed-up attribute map while there is nothing in the 4D amplitude map (figure 4.19).

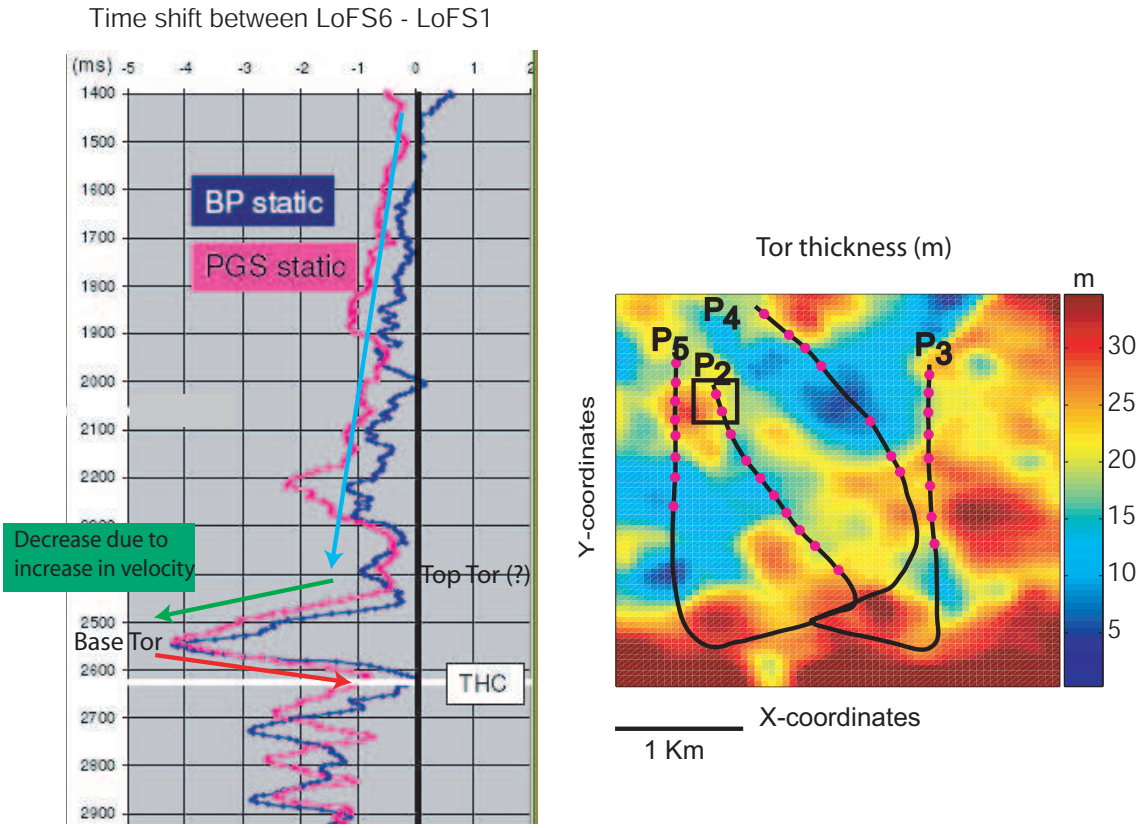

Figure 4.38: A. Time-Shift between LoFS1 and LoFS2 around P_2 and P_5.

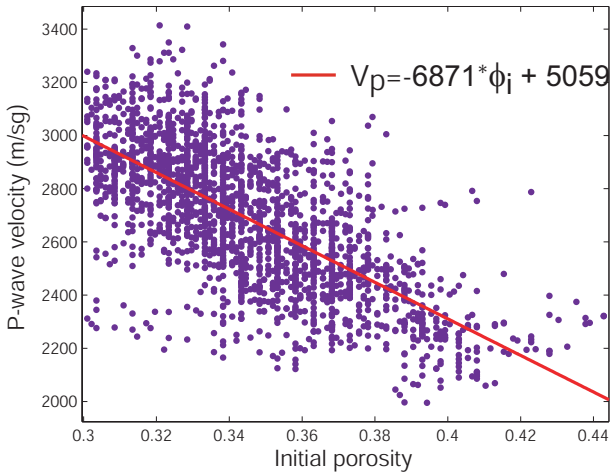

Figure 4.39: Cross-plot between P-wave velocity and initial porosity. The data come from a sonic and neutron porosity logs acquired on P_1 (the first producer drilled on the flank). The data were used to estimate equation 4.4.

Well	#	Depth	Reservoir Pressure (psi)						
Name		MD	Initial	LoFS 1	LoSF 2	LoFS 3	LoFS 4	LoFS 5	LoFS 6
P_2	1	2880	5850.00	5904.28	5762.23	5721.07	5622.09	5550.44	5459.28
P_2	2	3160	5665.00	4845.36	4346.91	4153.32	3937.95	3912.87	3948.98
P_2	3	3340	5836.00	4585.59	3981.80	3772.63	3545.54	3525.51	3605.22
P_2	4	3530	5588.00	4487.97	3931.92	3734.96	3494.06	3462.31	3527.64
P_2	5	3720	5837.00	4642.45	4138.02	3929.85	3666.65	3622.76	3653.56
P_2	6	3910	5745.00	4732.01	4152.99	3991.74	3725.92	3678.74	3677.20
P_2	7	4100	5799.00	4703.01	4164.32	3947.72	3747.82	3663.77	3619.96
P_2	8	4370	6003.00	4610.89	4034.88	3889.85	3634.80	3518.77	3524.85
P_2	9	4590	5902.00	4518.27	3848.98	3683.62	3469.39	3402.56	3421.56
P_2	10	4745	5838.00	4809.59	4253.73	4109.52	3875.26	3778.33	3722.19
P_3	1	3600	5145.00	5535.13	5276.18	5209.06	5218.24	5199.07	5227.03
P_3	2	3855	5308.00	5358.96	5018.83	4929.49	4958.35	4977.24	5007.91
P_3	3	4130	5498.00	5100.07	4616.06	4497.83	4495.41	4432.20	4587.80
P_3	4	4405	5744.00	5273.40	4779.71	4658.96	4550.61	4464.76	4460.47
P_3	5	4620	5926.00	5328.45	4693.16	4563.75	4487.52	4396.77	4560.34
P_3	6	4830	6106.00	5322.84	4782.46	4660.58	4599.17	4522.11	4608.42
P_3	7	5005	6133.00	5453.61	4991.74	4868.59	4836.18	4761.91	4819.26
P_3	8	5180	6077.00	5453.61	4991.74	4868.59	4836.18	4761.91	4819.26
P_4	1	3520	5188.00	4730.12	4072.11	3880.28	3597.10	3424.06	3397.26
P_4	2	3680	5272.00	4881.09	4284.93	4099.23	3830.54	3647.74	3550.90
P_4	3	4040	5438.00	5010.07	4481.17	4316.16	4077.32	3918.46	3837.41
P_4	4	4670	5381.00	4817.42	4387.37	4235.09	4022.05	3851.53	3779.22
P_4	5	4870	4901.00	4476.22	3961.81	3810.94	3608.23	3370.58	3292.20
P_4	6	5040	4113.00	4124.90	3637.76	3526.20	3312.46	3010.53	2935.88
P_4	7	5305	4077.00	3979.70	3662.02	3573.28	3362.52	3078.87	2987.66
P_5	1	3950	6560.00	5907.75	5439.35	5254.30	5020.53	4795.05	4921.17
P_5	2	4190	6393.00	5851.52	5391.56	5230.93	4990.10	4727.36	4708.38
P_5	3	4380	5989.00	5726.08	5210.83	5040.05	4732.72	4472.39	4398.96
P_5	4	4580	5949.00	5578.29	5024.50	4849.89	4532.37	4210.01	4114.76
P_5	5	4730	5969.00	5500.21	4869.22	4690.88	4353.93	4022.50	3870.61
P_5	6	4905	6033.00	5475.97	4929.91	4718.73	4332.63	4002.41	3943.18
P_5	7	5080	5941.00	5599.86	5197.78	5028.32	4690.35	4428.38	4244.42
P_5	8	5260	5755.00	5592.28	5050.04	4840.87	4475.70	4128.87	4154.21

Table 4.6: .

Pore fluid pressure for the wells in the south east flank

4.9 Summary

In this chapter I applied the methodology derived in chapter 3 to estimate pressure depletion from 4D seismic in compacting reservoirs to real data. The area of study is located in the South East flank of the Valhall Field. The Valhall Field is a chalk reservoir that undergoes compaction when produced. The 4D amplitude and the speed-up attribute were used. The seismic attributes were extracted from one baseline survey and 6 monitor surveys. Initial porosity maps and pressure estimations from the reservoir model together with 4D seismic attributes were used to generate an equation that correlates pressure changes with the time-lapse response. This equation was found to be approximately linear (eq. 4.3). The pressure maps estimated from 4D amplitude and using the derived equation were compared with the ones output from the reservoir model. The principal observations from this comparison are:

- The 4D amplitude response is controlled by the initial porosity.
- Higher initial porosity zones appear to have a strong 4D signal due to the rock compaction associated with the pressure depletion.
- The depleted areas where there is not an observable 4D seismic signal can be explained by a thin and low porous reservoir (initial porosity lower than 35%)
- The perforation 8 in producer P_5 (at the toe of the well) found a high porosity zone which does not correlate with a time-lapse signal. Based on the 4D response of similar porous zones, it is possible that this zone has probably not been produced but unfortunately there is no PLT information to validate this conclusion. Nevertheless, the drilling report mentioned that towards the toe of the well (after perforation 7) small faults were crossed and perhaps these structures are affecting the fluid flow over that area.
- The speed-up attribute captures the P-wave velocity increase due to pressure depletion and reservoir compaction. The overburden velocity changes are not affecting the speed-up attribute. However, the accuracy of this attribute depends on how well the top and base of the reservoir are defined.
- The comparison between the pressure maps predicted from 4D amplitude and the ones from the speed-up attribute, suggests that the rock deformation in the Lista Formation can influence the

pressure predictions. The speed-up attribute appears around well P_5 while nothing is observed on the 4D amplitude map. However, both seismic attributes have a good chance of capturing the pressure effect since the reservoir is thick and porous. The difference between the 4D amplitude and the speed-up attributes can be caused by an increase in the P-wave velocity in the Lista Formation due to loading effect (rock compaction). If the acoustic impedance increases in the reservoir and in the Lista Formation, the acoustic impedance contrast will be small and will not generate a 4D amplitude response. However, the speed-up attribute is not confined to the reservoir zone.

Chapter 5

Effect of structure and the presence of gas on the pore pressure predictions from time-lapse amplitude attributes

After developing the technique to estimate pressure from 4D seismic attributes, the next step in this thesis involves investigating under which circumstances the trend equation varies. The two situations that I evaluate in this chapter are: a) the thickness and structure and b) the presence of gas in the reservoir. The conclusions from this chapter may explain some of the discrepancies in the pressure inversion results for the south east flank (chapter 4).

Thickness variation is one of the major challenges in chalk reservoirs and it has an impact on the time-lapse seismic response. Corzo and MacBeth, (2006) found out that thickness variation can accentuate the tuning effect, making the 4D attribute noisier and increases the error when empirical linear fits are used to estimate pressure from time-lapse amplitude. To investigate these findings further, two models are compared in this chapter. The first model assumes flat layers and the second model is based on the structure of the south east flank of the Valhall Field.

In the Valhall Field, the gas oil ratio (GOR) has been kept fairly low due to the low mobility of the gas; furthermore according to pressure outputs from reservoir modelling, the pore pressure in the south east flank has been above the bubble point during the acquisition of the first six LoFS surveys. However, the presence of gas can not be totally ruled out, especially close to the borehole, where

there are large pressure drops and at crest of the field where the maximum depletion occurs. To evaluate the gas effect, the model explored in chapter 3, was modified to have three fluid phases.

5.1 Effect of structure and thickness on pore pressure estimations from time-lapse amplitude attributes

5.1.1 Description of the synthetic models: Model I (constant thickness) and model II (variable thickness)

The two examples used were based on a sector model taken from the south east flank of the Valhall Oil Field. In the first model example (model I), initial thickness is held constant with a horizontal well producing from a high porosity reservoir zone. The thickness for each layer is determined by taking an average thickness from the Valhall sector model. In the second model example (model II), the variations in the geological structure of the southeastern part of the Valhall Field are emulated figure 5.2). Both models include 23 layers that are arranged as follows: 9 layers above the reservoir (which means that layer 9 is the layer immediately above the reservoir), 13 layers comprise the reservoir and 1 layer is below the reservoir. Both models have 41 grid cells in the x direction and 23 grid cells in y direction (41x23x23). The total of grid cells is 21689. The x and y dimensions of each grid bock decrease towards the reservoir area. The reservoir grid is a subset of the finite element stress grid and its size is 33x15x13. The reservoir consists of 13 layers, which represent the zones that describe the reservoir in the south east flank of the Valhall Field. They are distributed as shown in figure 5.1. The Tor formation is represented by the first 7 layers which have a initial porosity of 40 %. The Hod formation is represented by the 6 remaining layers which have an initial porosity of 15 %. The Hod formation is not a producer unit in the model. A horizontal well is located in the same position for both models and produces from the most porous layers (figure 5.2). The fluid and reservoir properties are the same as the ones used for the model in chapter 3 (table 3.2). The well produces 500 bbl/day during 10 years.

The overburden and underburden consist of 10 linear elastic materials. For the reservoir, the 40% initial porosity layers are modelled assuming two different linear elastic behavior as described in section 3.1 and figure 3.2. The 15% initial porosity layers were considered as linear elastic materials.

Layer distribution in the full grid	Layer distribution in the reservoir grid	Observations		
1		Overburden		
2				
3				
4				
5				
6				
7				
8				
9				
10	1	TOR	ϕ=40%	Well produces from these layers
11	2			
13	4			
14	5			
15	6			
16	7			
17	8	HOD	ϕ=15%	
18	9			
19	10			
20	11			
21	12			
22	13			
23		Underburden		

Figure 5.1: Layers distribution for models I and II: The only producing layers are the ones which represent the Tor formation (layers 1 to 7 in the reservoir grid

Table 5.1 summarizes the elastic properties for each layer. The boundary conditions for both models are set to assume uniaxial strain deformation.

The output from the iterative couple geomechanical fluid simulation is used to determine the seismic properties of the reservoir and non-reservoir rocks. Calculation of the reservoir seismic properties is carried out using conventional fluid substitution. For the non-reservoir rocks, the changes in P-wave velocity is calculated as a function of strain. This is followed by seismic modelling of the full stacked data using a convolution-based approach. This methodology has been explained in section 2.4. Seismic data are produced for a pre-production state (baseline volume) and after 2, 4, 6, 8 and 10 years of production (monitor volumes).

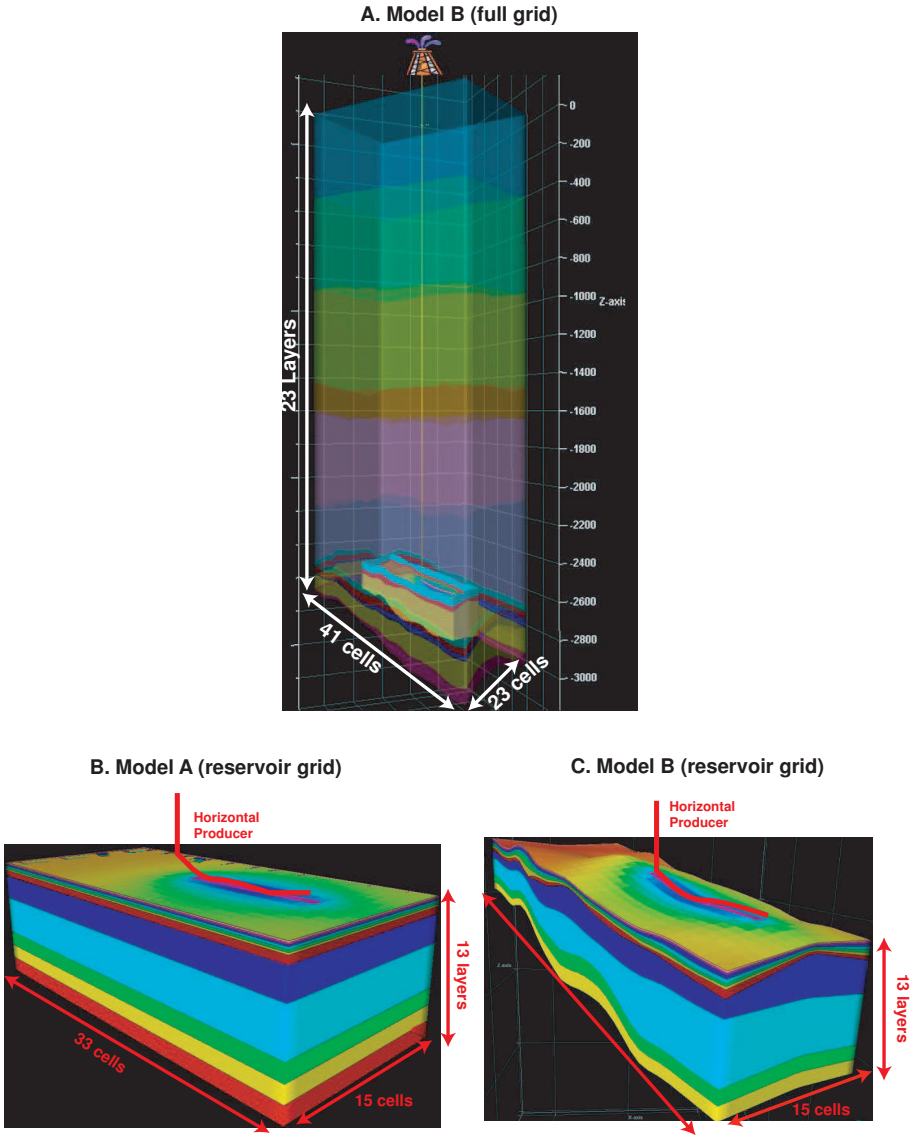

Figure 5.2: Geometry of models I and II: The dimensions of both models are 41x23x23, the reservoir is confined within the stress grid and consists of 33x15x13 cells. For model I, initial thickness is held constant in a plane horizontal layered model. For Model II, the variations in the geological structure of the southeastern part of Valhall Field are emulated. The well trajectory is shown in red

Layer	Young modulus (E) (KPa)	Poisson's ratio (ν)
	Overburden	
Layers 1-3	800000	0.4
Layer 4	600000	0.4
Layer 5	920000	0.43
Layer 6	600000	0.4
Layers 7-9	810000	0.46
	Reservoir	
Layers 10 -16	Two slope linear elastic	Two slope linear elastic
Layers 17-22	600000	0.18
	Under-burden	
Layer 23	2000000	0.3

Table 5.1: Linear elastic parameters used for models I and II. The producer layers (10 -16) are assumed to have two linear elastic behaviors. The elastic parameters for layers 10 to 16 are estimated using the porosity compaction curves (figure 3.2)

5.1.2 Influence of the structure and thickness in the stress and strain distribution during hydrocarbon production

Comparison of the pore pressure, effective stress and average normal stress at initial conditions between model I (constant thickness) and model II (variable thickness)

The initial reservoir conditions are established by gravity-capillary pressure equilibrium. This means use of a oil pore pressure at a known datum ($P_{o-datum}$) and calculate the oil pore pressure (P_o) for all the cells using a density gradient adjustment (eq. 5.1). Additionally, a pressure for each phase (water and oil) must be calculated. The pressure in the water phase (P_w) is related to the oil pressure by the oil-water capillary pressure (P_{cwo}) (eq. 5.2). To initialize both models, I used a $P_{o-datum}$ equal to 45.5 MPa at 2620 m. P_{cwo} was 20.7 MPa at initial conditions (S_w=0.05).

$$P_o = P_{o-datum} + \frac{\Delta D * \rho_o}{144} \tag{5.1}$$

Where ΔD is the change in elevation (ft and positive is down) and ρ_o is the oil density ($\frac{lb}{ft^3}$).

$$P_w = P_o + P_{cwo} \tag{5.2}$$

The effect of the structure on the pore pressure at initial conditions is illustrated in figure 5.3. Figure 5.3A is a structure profile (A-A') at the top of the reservoir (layer 1) for models A (red line) and B (blue line). Figure 5.3B shows the initial pore pressure for layer 1 along profile A-A'. The pore pressure in the layer is constant for model I (red line). However for the same layer, the pore pressure varies in model II (blue line). As equation 5.2 indicates there is a variation in the initial pore pressure that depends on the structure of the reservoir. The profiles from model II (blue lines in figures 5.3A and 5.3B) show the correlation between initial pressure distribution and structure. The effective stress depends on the average normal stress and the pore pressure. The average normal stress is a function of the horizontal and vertical stresses. At initial conditions a gradient with depth is used to estimate the horizontal and vertical normal stresses. If initial pore pressure and average normal stress are governed by the structure, the effective stress is also influenced by it. Therefore, the initial effective stress varies across each layer of the reservoir in model II.

Comparison of pore pressure, effective stress and average normal stress during production between model I (constant thickness) and model II (variable thickness)

Both models are produced by a single well in the middle of the models. The daily production rate is fixed to 500 bbl. However the pore pressure depletion is not the same for models I and II. Firstly, both models do not start with the same initial pressure as explained previously. Secondly, the pore volume is different for each model. Even though both models have the same porosity and matrix permeability, the reservoir thickness is different between the two models.

Figure 5.4 shows two profiles along the well after 10 years of production for models I and II. Profile A-A$'$ is east-west direction and the profile B-B$'$ has a south-north direction. For model II, the thickness is fairly constant along the profile A-A$'$. On the contrary, the thickness varies considerable in the profile B-B$'$ (figure 5.4F). The red profiles are from the model I while the blue profiles correspond to the model II. The pore pressure depletion in model II is lower than in model I. However, the pore pressure profiles from both models show identical trends (figures 5.4A and 5.4C). The effective stress profiles for models I and II are very similar if the thickness and the structure does not vary significantly in model II (i.e. along profile A-A$'$). There are considerable changes in reservoir thickness and the structure along profile B-B$'$. Therefore, the effective stress changes in model II are not as

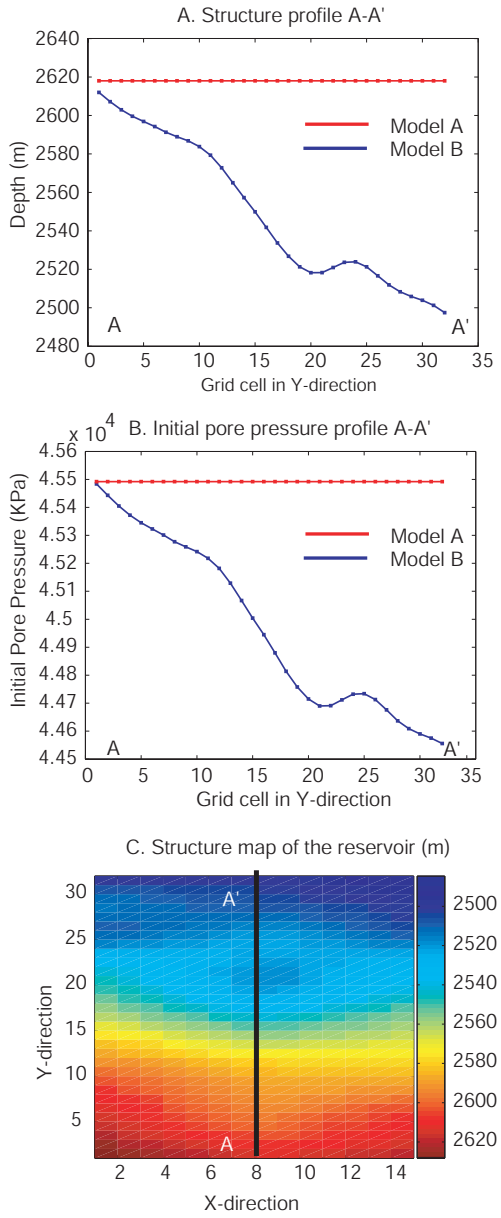

Figure 5.3: A. Depth changes along the profile A-A′ (from south to north) B. Initial pressure along the profile A-A′. C. Structure map of the reservoir. The initial pore pressure depends on the structure.

smooth as the ones in model I along this profile (figures 5.4B and 5.4D).

Analysis of the vertical strain due to pressure depletion in models A (constant thickness) and B (variable thickness)

The vertical strain controls the changes in the acoustic properties of the non-reservoir rocks. Therefore investigating the effect that the structure has on the rock deformation, helps to understand the 4D signal. Figures 5.5, 5.6A and 5.6B show the vertical strain of the reservoir and non reservoir rocks for both models. The vertical strain for 10 years of depletion is shown in the figures. The reservoir and the non-reservoir rocks undergo more vertical deformation in model II since the pressure depletion is higher in this model (figures 5.5 and 5.6B). In both models, it is observed that a) the overburden rocks are relaxing (positive strain) while the reservoir rocks are compacted (negative strain) and b) the rock deformation decrease upwards. However, the vertical strain distribution is more heterogenous when the initial thickness of the model is not constant (model II).

Several north-south profiles along the producer well were created to analyze the vertical strain. The direction and location of the profiles are shown in figure 5.4F. Figure 5.7A shows the pore pressure changes profile. Figure 5.8A shows the reservoir vertical strain profile and figure 5.8B shows the profile for the vertical strain in layer immediately above the reservoir. The pore pressure profiles from models A (red line) and B (blue line) have very similar shape and are symmetric. The major pressure depletion for both models is located from grid cell number 8 to grid cell number 14 (at the well location). At the reservoir, the vertical strain profile from model II is more asymmetric than the one from model I (figure 5.8A). Furthermore, the maximum depletion and reservoir compaction is not associated with the same grid block in both models. For model I, the maximum rock deformation and the most depleted grid cell is 11. However for model II, the most pressure depleted and the highest rock compaction occurs at grid cell 10 (this grid cell is the thickest reservoir cell along the well). According to figure 5.8B, the vertical strain profiles for layer 9 (i.e. the layer immediately above the reservoir) vary significantly between the two models. For model I, the maximum vertical strain in layer 9 coincides with where the maximum depletion occurs (i.e. grid cell number 10). On the contrary, for model II, the maximum vertical strain in layer 9 occurs in grid cell 15 (at the end of the well) while the maximum depletion was observed at grid cell 10. As discussed in chapter 3, the velocity changes for layer 9 are estimated as a function of vertical strain (eq. 2.15). This implies that

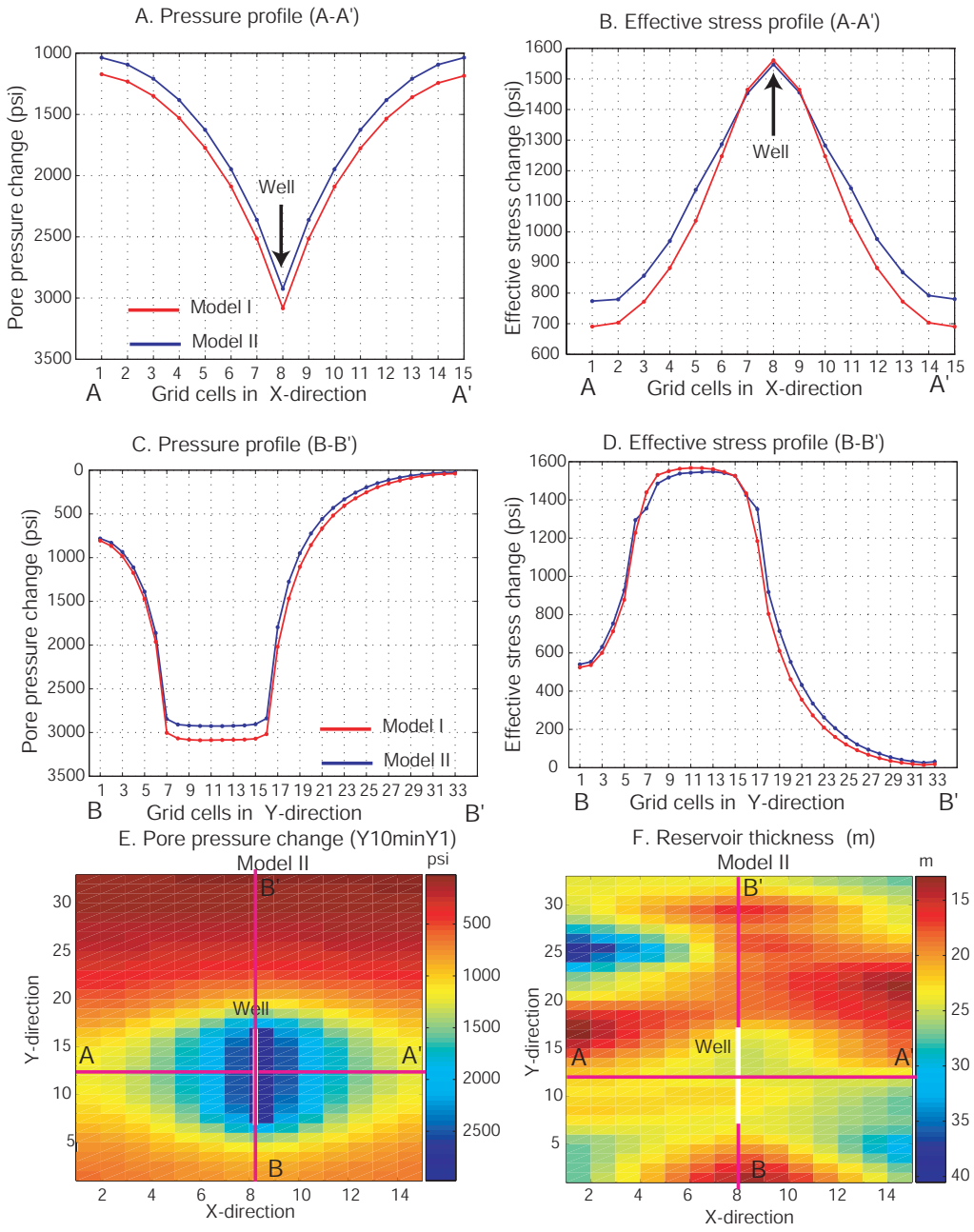

Figure 5.4: Pressure and effective stress profiles along models I and II. A. Pore-pressure changes between initial pressure and 10 years of production along profile A-A′. B. Effective stress change between initial pressure and 10 years of production along profile A-A′. C. Pore-pressure changes between initial pressure and 10 years of production along profile B-B′. D. Effective stress change between initial pressure and 10 years of production along profile B-B′. E. Pore pressure depletion after 10 years of production for model II. F. Initial reservoir thickness map for model II.

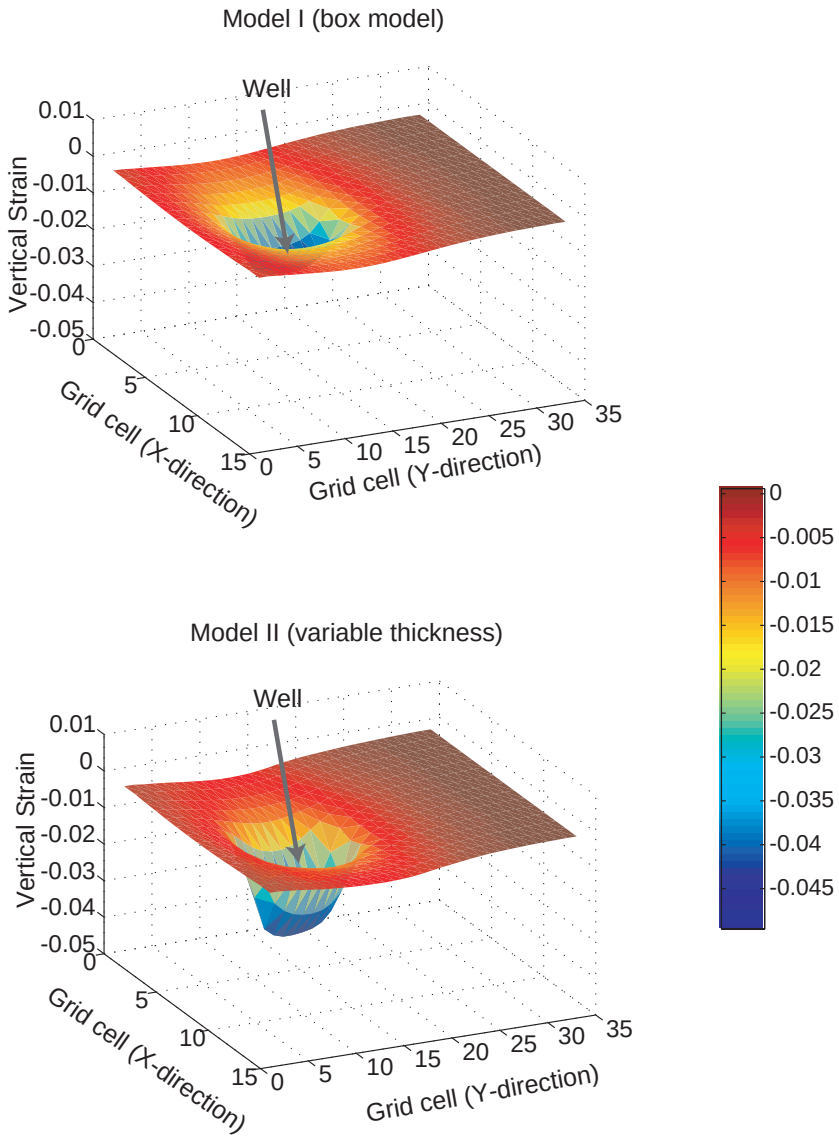

Figure 5.5: 3D view of the reservoir vertical strain. The negative vertical strain in the reservoir indicates the rock compaction while the positive vertical strain in the overburden is related to the uploading effect in the cap rock (figure 5.6)

the maximum velocity changes in layer 9 do not correspond with the most depleted area for model II.

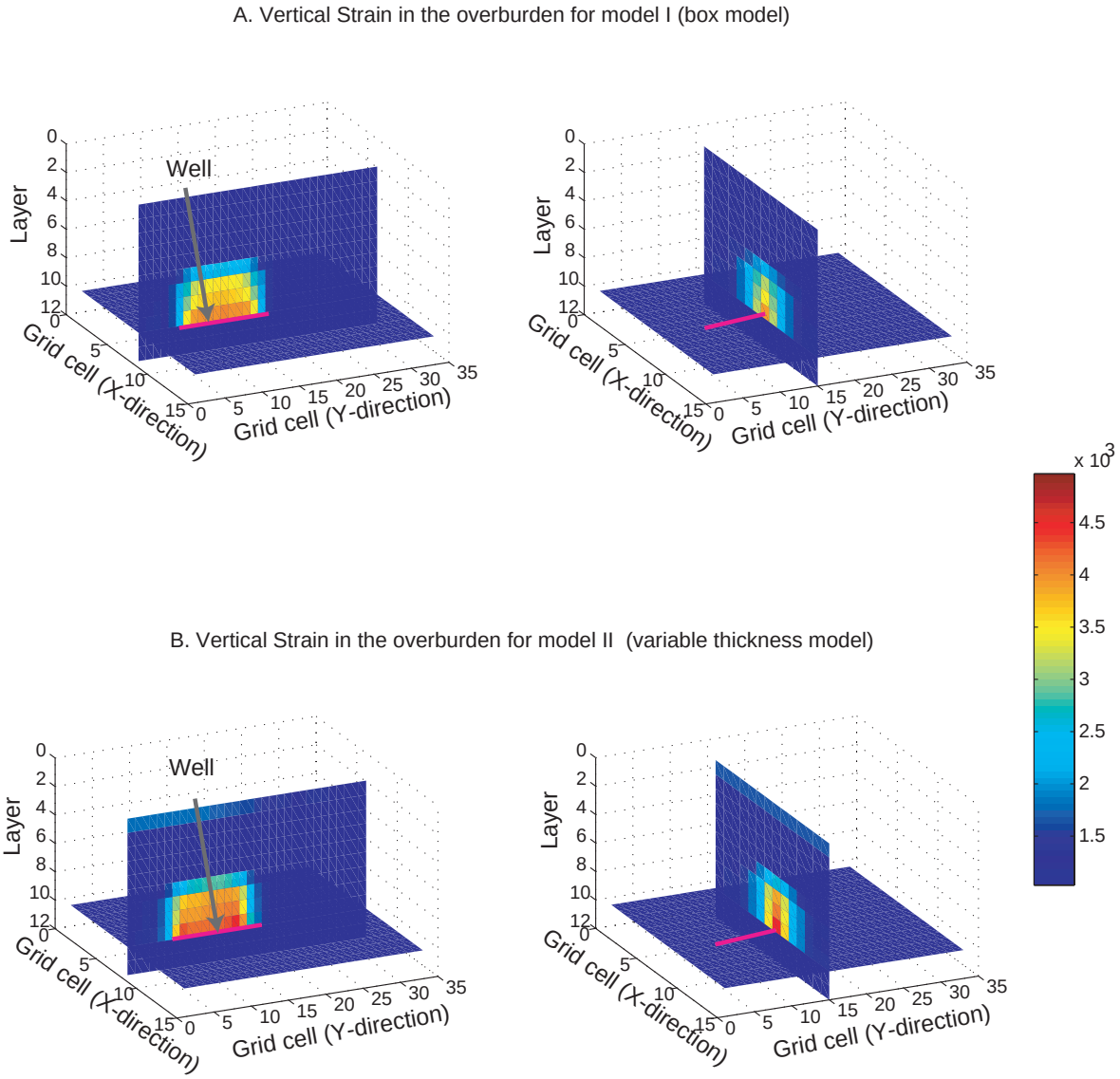

Figure 5.6: Vertical strain in the reservoir and non-reservoir rocks. A. Overburden vertical strain in model I. B. Overburden vertical strain in model II. The positive vertical strain in the overburden is due to the uploading effect caused by the reservoir rock compaction.

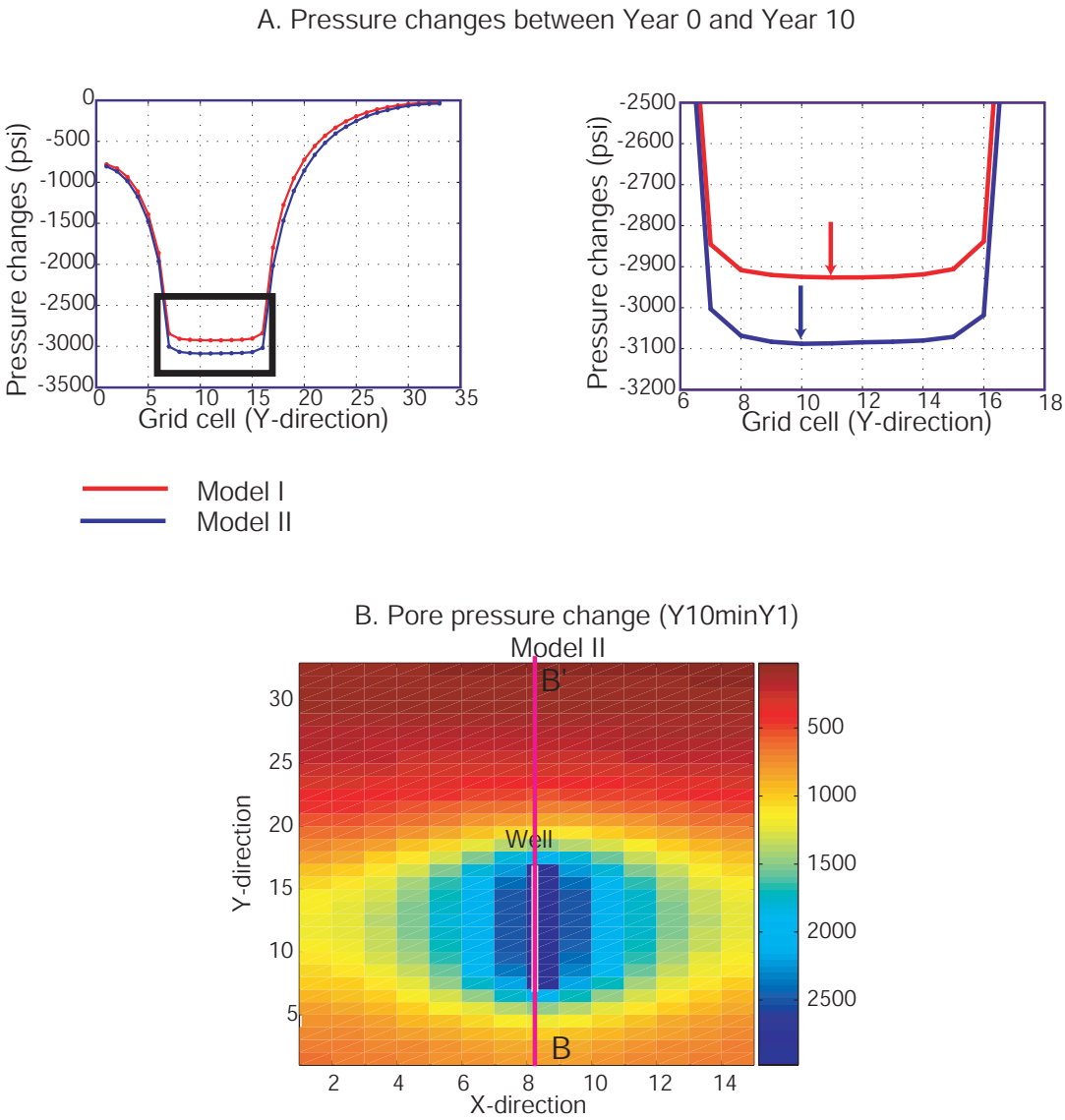

Figure 5.7: Pore pressure change along profile B-B′ for models I and II. A. Pore pressure change profiles. B. Location of profile B-B′

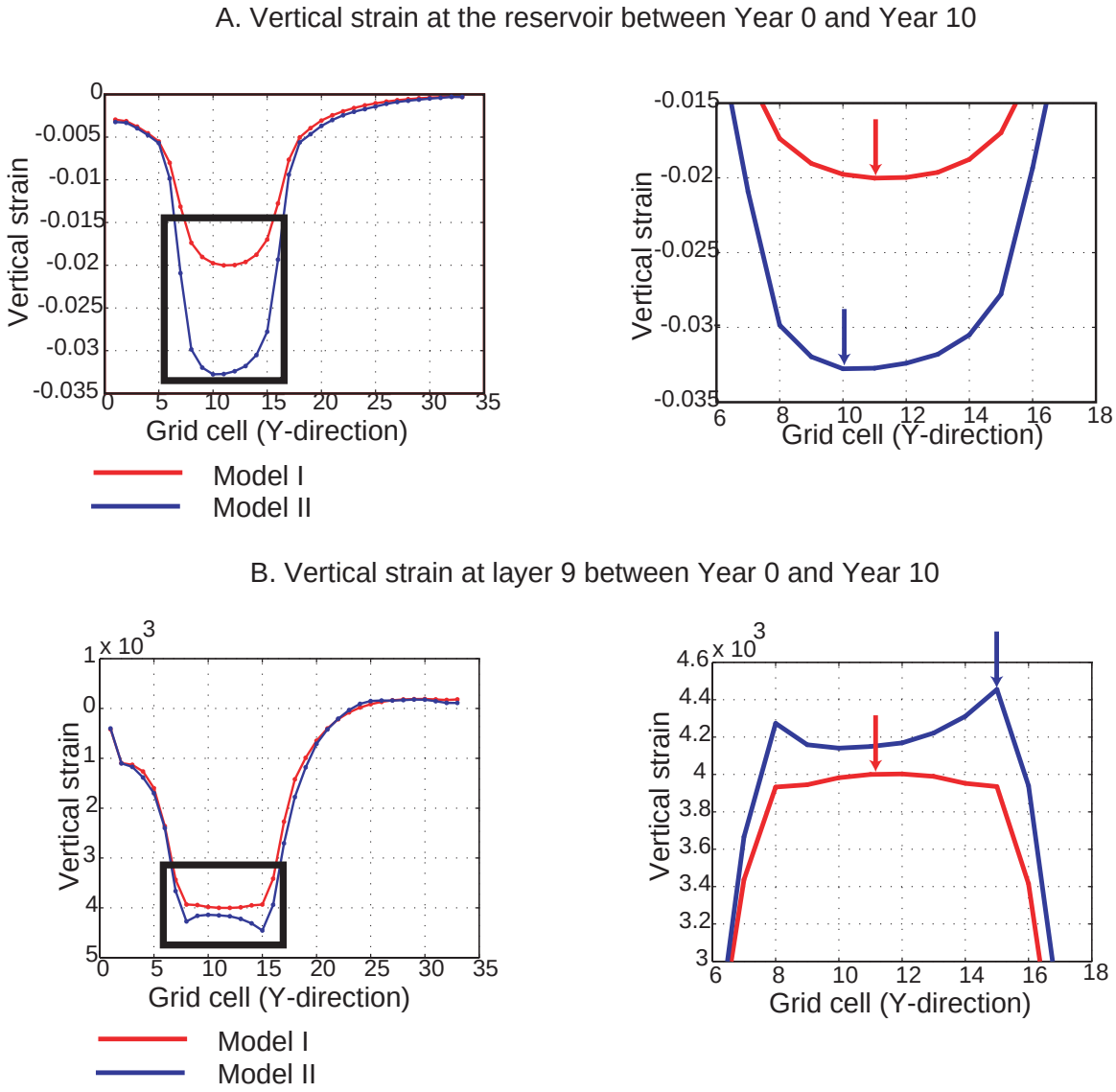

Figure 5.8: Vertical strain along profile B-B′ for models I and II. A. Reservoir vertical strain along profile B-B′. B. Layer 9 vertical strain along profile B-B′. For model I, the maximum pressure change shown in figure 5.7A coincides with the largest vertical strain in the reservoir and layer 9 (red arrow). For model II, the maximum pressure change shown in figure 5.7A correlates with the maximum vertical strain at the reservoir, however the largest vertical strain in layer 9 does not correlate with the most depleted area (blue arrows). The location of the profile is shown in figure 5.7B

5.1.3 Variation of the elastic properties during production due to the structure

Analysis of the P-wave velocity and acoustic impedance changes in the reservoir for models A (constant thickness) and model II (variable thickness)

In the previous chapters, it has been discussed that the acoustic property changes are influenced by the pore pressure depletion, the porosity reduction and the effective stress changes in the compacting reservoirs. Figure 5.9 shows that the initial P-wave velocity from models I and II are different. This is because the structure and thickness variation influence pore pressure and effective stress, therefore the P-wave initial velocity varies as well.

To investigate the influence that the structure has on the reservoir seismic properties during production, the acoustic impedance changes were cross-plotted against effective stress changes for models I and II. Figure 5.10A shows the acoustic impedance absolute changes against the effective stress absolute changes. Figure 5.10B shows the acoustic impedance relative changes against the effective stress relative changes. Both figures represent the changes due to 10 years of production. The relative changes were estimated dividing the absolute changes by the initial values. The red points correspond to model I and the blue ones to model II. Model I shows a single trend while the model II has more scatter and two trends are observed (blue and black lines). Furthermore acoustic impedance changes from model II are lower than the ones from model I. This is because the initial P-wave velocity varies across model II while it is constant in model I. However the acoustic impedance differences between models I and II decrease when relative changes are cross-plotted instead of absolute changes (figure 5.10B). Moreover the two different trends in model II are correlated with the effect that reservoir thickness has on the seismic acoustic properties. Figures 5.11 and 5.12 illustrate this effect. For model II, the effective stress changes and the initial reservoir thickness map are shown in figures 5.11B and 5.11C respectively. The colored square points in the figures correspond to the same set of points cross-plotted in figure 5.11A. The blue points lay on the south part of the model. The yellow points are located on the middle of the model. The green points correspond to the producer well. For model I, the effective stress changes map is shown in figure 5.12B. The black points on the map are also highlighted in figure 5.12A. The yellow and blue points from model II, have the same amount of effective stress changes as the black points from model I. Also, all three set of points occupied the same area in both models. However, the data from model II are not defined by a single trend as the

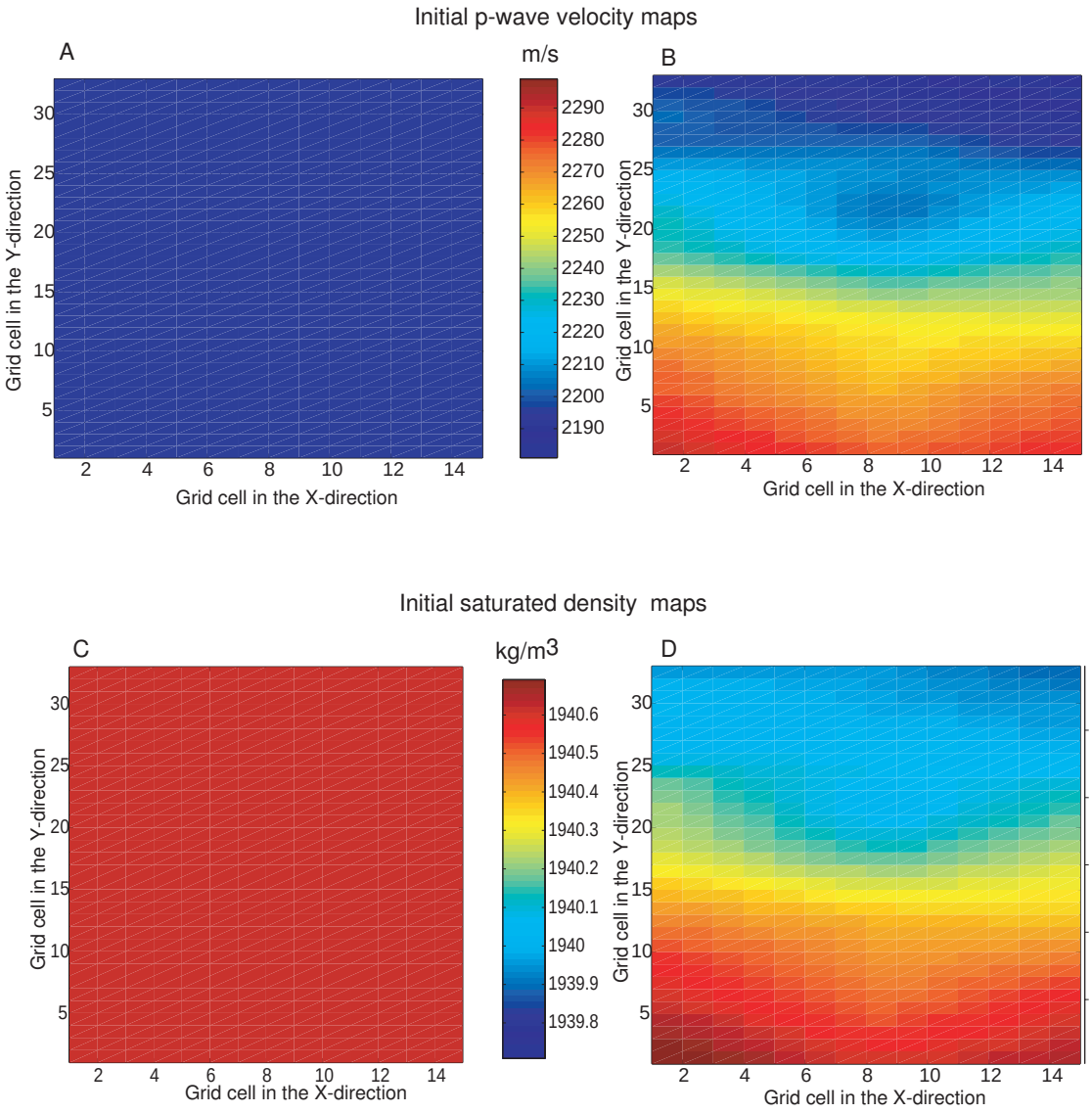

Figure 5.9: Effect of the reservoir thickness on the initial acoustic properties. A. Initial P-wave velocity for model I. B. Initial P-wave velocity for model II. C. Initial saturated density for model I. D. Initial saturated density for model II. P-wave velocity and saturated density change across model II due to the structure and thickness variation

data from model I. The reason is that yellow points are located on thinner reservoir that the blue points (figure 5.11).

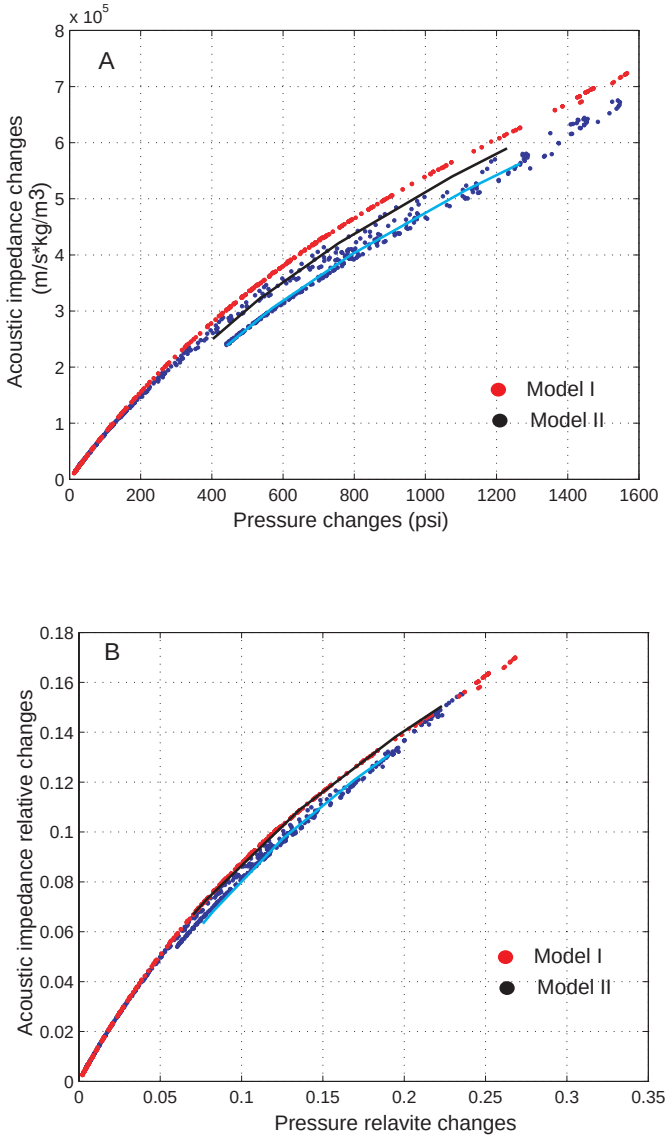

Figure 5.10: Acoustic impedance against effective stress cross-plots. A. Acoustic impedance absolute changes vs. effective stress absolute changes. B. Acoustic impedance relative changes vs. effective stress relative changes. Notice the two trends for model II. The differences between both models become less obvious when relative changes are cross-plotted.

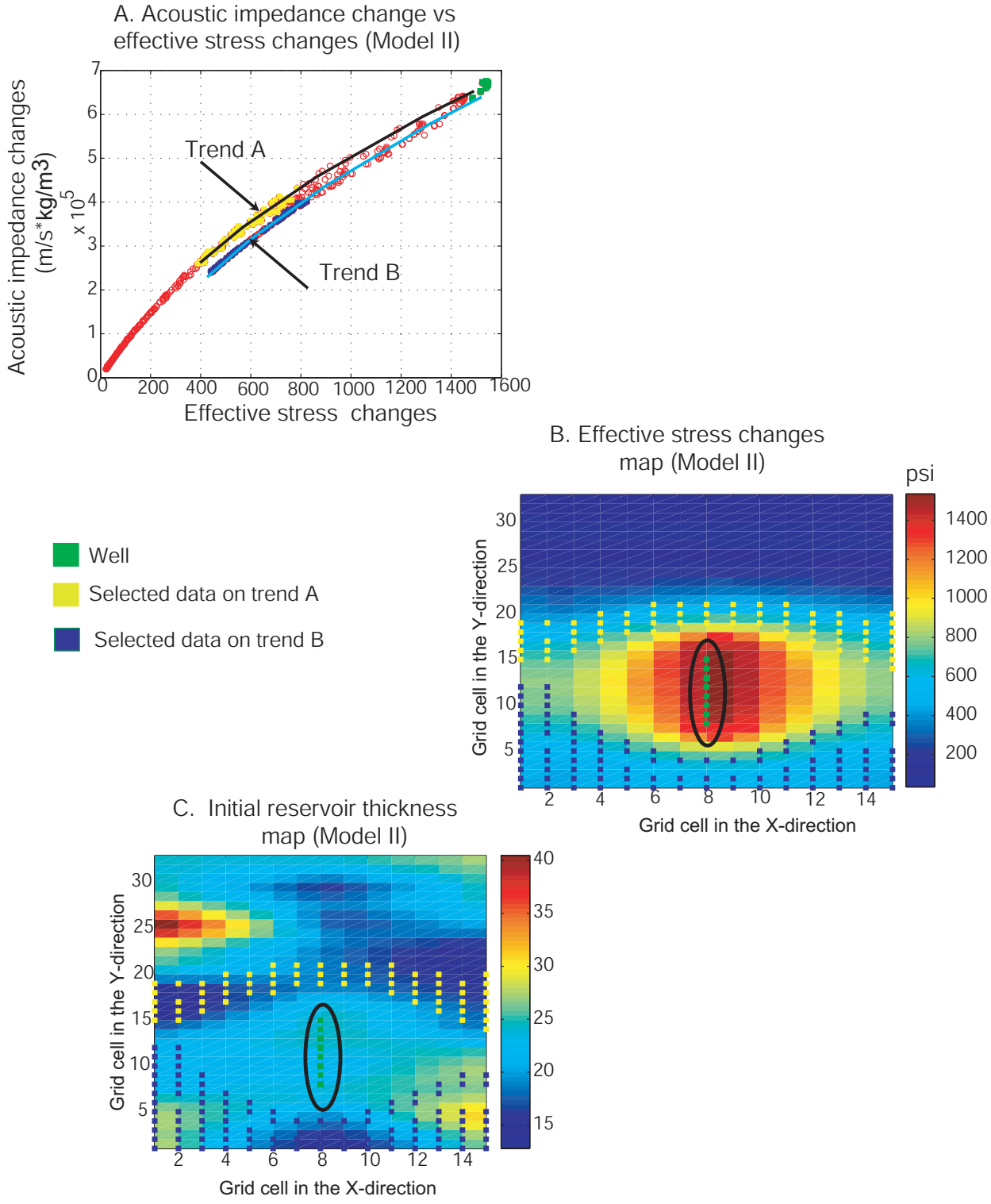

Figure 5.11: Acoustic impedance changes against effective stress changes for models I and II. A. Acoustic impedance changes against effective stress changes for model II. B. Effective stress changes map for model II. C. Initial reservoir thickness map for model II.

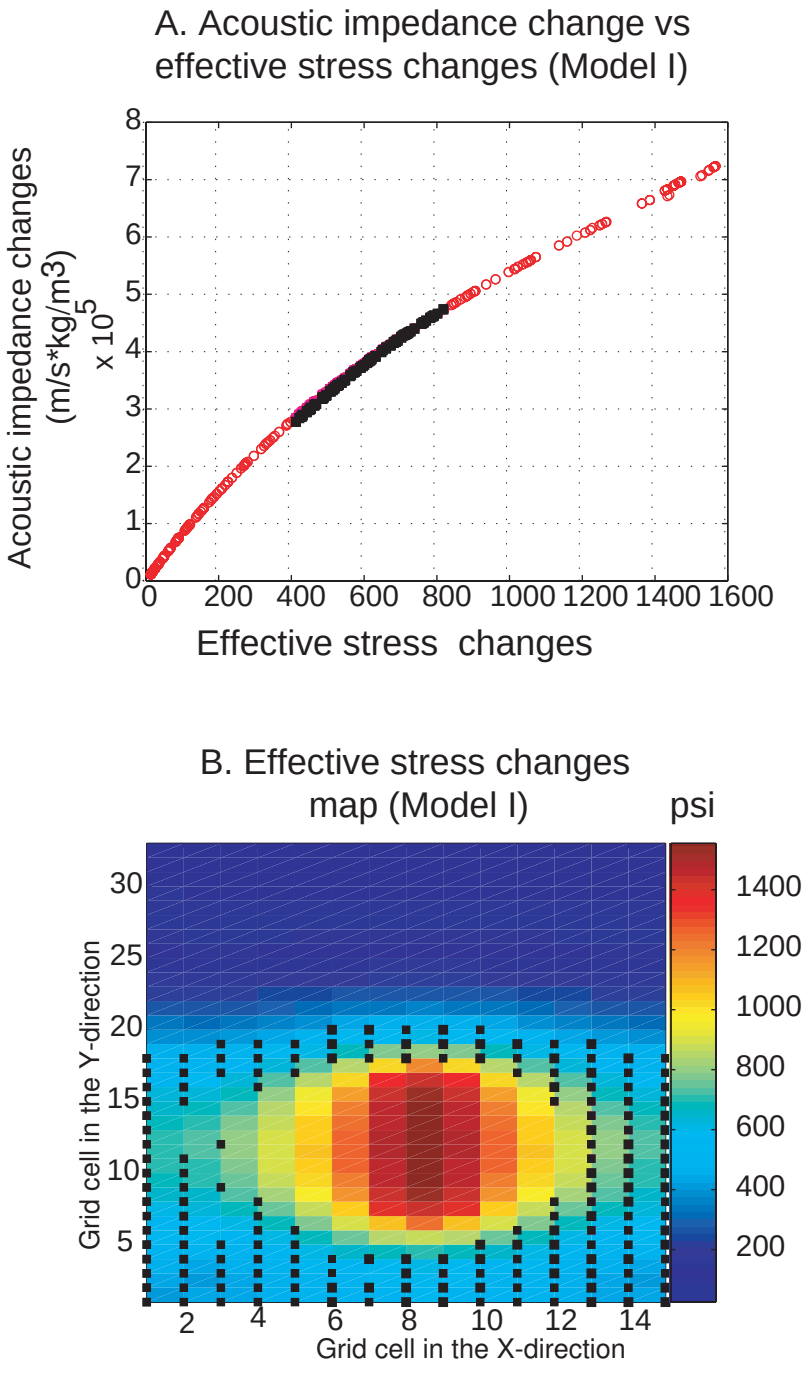

Figure 5.12: A. Acoustic impedance changes against effective stress changes for model I. B. Effective stress changes map for model I.

Analysis of the 4D amplitude attribute extracted from models A (constant thickness) and B (variable thickness)

Synthetic seismic volumes were created every two years of production and subsequently time-lapse volumes were calculated. The baseline survey was the pre-production stage (year 0) and the monitor surveys were the volumes coming from year 2, year 4, year 6 and year 10 of production. For convention, the time-lapse volumes are named as follows: Y2minY1, Y4minY1, Y6minY1, Y8minY1 and Y10minY1. After that, the 4D amplitude attribute (Largest Positive Value) was extracted for each volume. This attribute was extracted at the top of the reservoir using the methodology explained in section 3.4.

Figure 5.13 shows the Largest Positive Value attribute from Y10minY1 volume against pore pressure (figure 5.13A) and effective stress (figure 5.13B) for both models. The blue points are from model I and red points from model II. There is considerably more scatter on the data from model II due to the structure and thickness variation. Also, the 4D amplitude attribute correlates better with effective stress than with pressure changes as previously discussed in chapter 3. Similar trends in figure 5.13B to the ones in figure 5.13A can be defined for both models. However when the pressure depletion causes enough compaction to significantly change the normal stresses, a better correlation with 4D amplitude response is given by the effective stress. This effect is better observed on model I. Due to the large depletion on the producer well (yellow points in figures 5.13A and 5.13B), which produces large changes in the normal stress, the effective stress against 4D amplitude graph exhibits a better trend than the cross-plot using pore pressure.

Time-lapse amplitude response as result of the arching effect

The rock compaction is smaller or null at the outside of the hydrocarbon production area and the compaction bowl is formed because of the constrained effect of the side-burden and the arching effect in the overburden. The stress arching effect causes an increase in the vertical stress (the overburden compacts) and possibly the pore pressure builds up in the reservoir.

The effect of pressure increases in time-lapse seismic studies is very difficult to observe and normally is linked to the effect of fluid injection (water or gas). However, in compacting reservoirs, the increase of pressure can also occur due to the re-distribution of stresses in the overburden and the reservoir

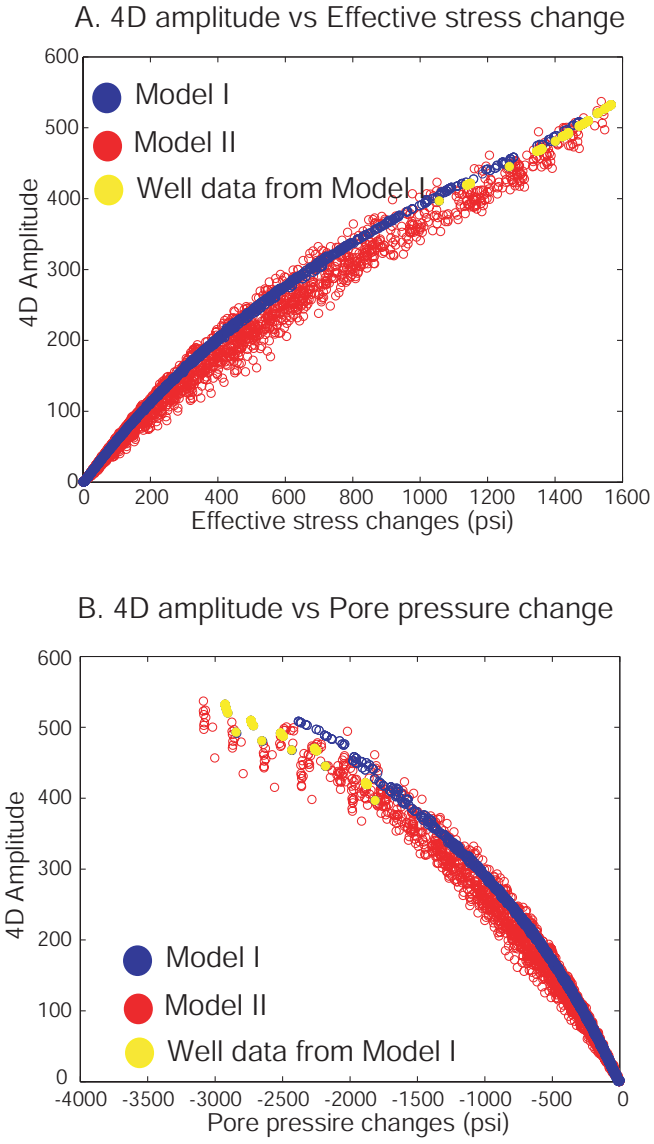

Figure 5.13: 4D amplitude attribute vs fluid pressure and effective stress. A. 4D amplitude attribute (Largest Positive Value) vs pore pressure changes. B. 4D amplitude attribute (Largest Positive Value) vs effective stress changes. Less scatter with the 4D amplitude attribute and the effective stress changes is cross-plotted

rocks (arching effect). Higher pressures than the initial pore pressure are observed away from the producer for models I and II. A similar effect has been observed in a fully coupled geomechanical model presented by Gutierrez et al. (2001). Furthermore new producer wells in the south east of Valhall Field have found higher or similar pore pressure than wells previously drilled close by.

In the synthetic example, the 4D amplitude response is negative due to over pressurization (amplitude of the monitor survey < amplitude of the baseline survey). The reservoir acoustic impedance decreases because the P-wave velocity decreases as the pressure increases. The vertical strain in layer 9 is compressive (positive sign), therefore its acoustic impedance increases since the velocity changes are a function of vertical strain. This means that the amplitude at the top of the reservoir is decreasing with time, therefore the 4D amplitude response is a trough. However, this response is not properly captured by the 4D amplitude attribute that has been used so far. The Largest Positive Value amplitude attribute captured the effect of the pressure depletion since it looks for the maximum peak in a time window (the decrease of the layer 9 acoustic impedance and the increase of the reservoir acoustic impedance). In order to map the pressure increase at the edges of the compaction bowl, the maximum negative value needs to be extracted from the same time window. However it is possible to observe both pressure effects (increase and depletion) in a 4D amplitude map if the time-lapse amplitude value is extracted at the exact time of the top of the reservoir. Figure 5.14 shows the 4D amplitude changes at the top of the reservoir for model II after 4 years of depletion. In general, there is an amplitude increase (positive values) due to the pressure depletion and associated rock compaction. However, towards the north of the reservoir the 4D amplitude decreases (negative values) associated with the arching effect. These changes are very small compared with ones from the pressure depletion in the model.

Another 4D attribute that is affected by the arching effect is the time-shift. Instead of the slow down in the overburden due to the pressure depletion, a speed up is observed due to the stress increase and thereby negative strain (compression) outside the depletion zone. Staples et al. (2007) observed a negative or upward time-shift in the Shearwater Field (North Sea), these time-shift anomalies were the Cretaceous and Jurassic sections in the Shearwater Field. The magnitudes of the time-shifts were very small (-0.3 ms) and the authors associated them with the stress arching in the overburden. However, negative time-shift or 4D amplitude response due to the arching effect have not been reported in chalks reservoirs; perhaps, the seismic response is very small and below the noise

level to create a reliable 4D response. The impact that stress arching have on the changes of rocks acoustic properties depends on a) the structure, b) contrast between the geomechanical properties of the reservoir and surrounding rocks, c) presence of faults, d) the amount of pressure depletion and e) the sensitivity of overburden/side-burden and reservoir velocities to the stress/strain. In the Valhall Field, this effect can not be totally neglected. However it may be difficult to observe since the top of the reservoir (Tor Formation) is not easily to interpret on the seismic. Therefore, the most common approach to observed the 4D amplitude changes is to extract the Largest Positive Value (LPV) (chapter 4) in a time window. For model I the largest positive amplitude (LPV) and the amplitude response exactly at the top of the reservoir were extracted from the Y1minY4 seismic volume. The 4D attributes were cross-plot against pressure and effective stress changes (figure 5.15). The red circles represent the LPV attribute and the red crosses are the 4D amplitude at the top of the reservoir. Both amplitude attributes coincide when the reservoir is depleting, however the LPV does not identify the pressure building up in the reservoir. The empirical relationship between pore pressure and the LPV attribute (eq. 5.3) was found by cross plotting data point located at the producer wells, where only pressure depletion occurs. Therefore, the trend equation is conditioned to be used merely for predicting pressure depletion from 4D amplitude changes.

5.1.4 Accuracy of the methodology of predicting pressure changes from 4D amplitude attributes when the structure and thickness vary across the reservoir

The methodology used in chapters 3 and 4 to predict pressure depletion from 4D seismic, is applied to models I and II. The approach finds an empirical fit between pore pressure changes and the 4D amplitude attribute around the wells and then, this relationship is used to predict the pressure depletion across the field. The pressure maps obtained from each of the models help to quantify the influence that the thickness and the structure have on the trend equation. Figure 5.16 shows the cross-plot between pressure changes and 4D amplitude. The points represent the differences in pressure and 4D amplitude between a pre-production baseline survey (year=0) and 5 monitor surveys (years 2, 4, 6, 8 and 10). The set of points were extracted at the producer location. The data suggest that the Largest Positive Value attribute (ΔA) and the pressure changes (ΔP) can be approximated by a power law equation, the same type of fit used in chapter 3 (eq. 5.3). The best fit coefficients (C_1

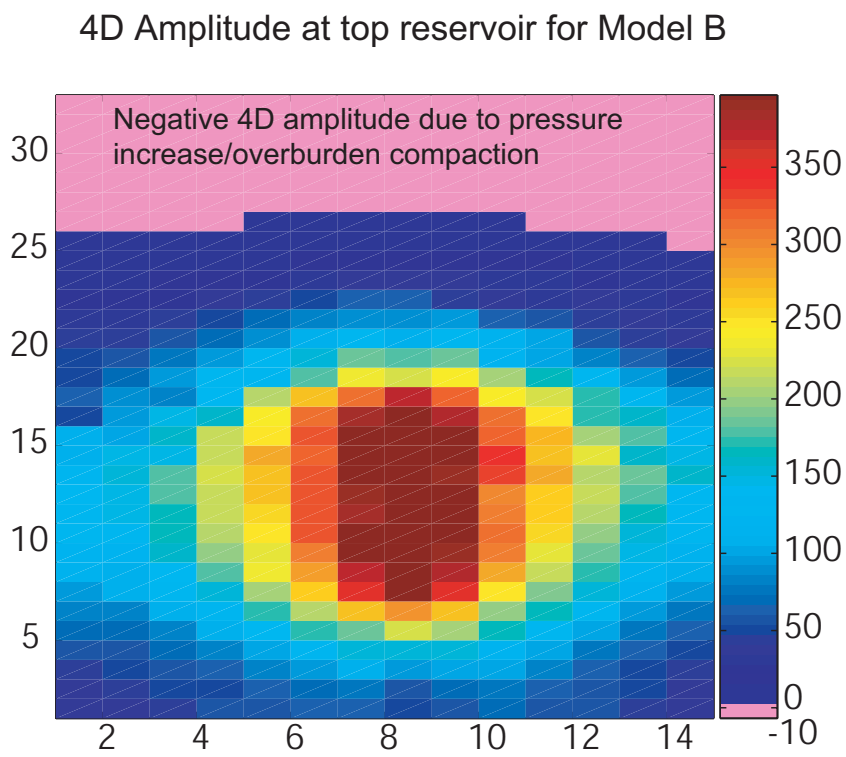

Figure 5.14: 4D amplitude response extracted at the top of reservoir for model II. The amplitude attribute was extracted at the exact time for the top of the reservoir. The pink area highlights the zone where the pressure increases and the 4D amplitude anomaly is negative (values between -10 to 0)

and C_2) for each model are listed in table 5.2. In this case is not required to define the coefficients as a function of initial porosity since models I and II are using a single initial porosity of 40%.

$$\Delta A = C_1 * (\Delta P^{C_2}) \tag{5.3}$$

ϕ_i (%)	C_1	C_2	R^2	RMSE
Model I	4.64	0.5961	0.983	17.03
Model II	2.574	0.6599	0.9791	19.05

Table 5.2: Coefficients C_1 and C_2 for equation 5.3. The fourth column is the coefficient of multiple determination (R^2). This statistic measures how successful the fit is in explaining the variation of the data. A value closer to 1 indicates a better fit. The fifth column represent the RMSE, the root mean squared error. A value closer to 0 indicates a better fit

Figures 5.17A and 5.17C show the pressure depletion maps after four years of depletion for models I and II. These maps are compared with the ones in figures 5.17B and 5.17D. All pressure maps show

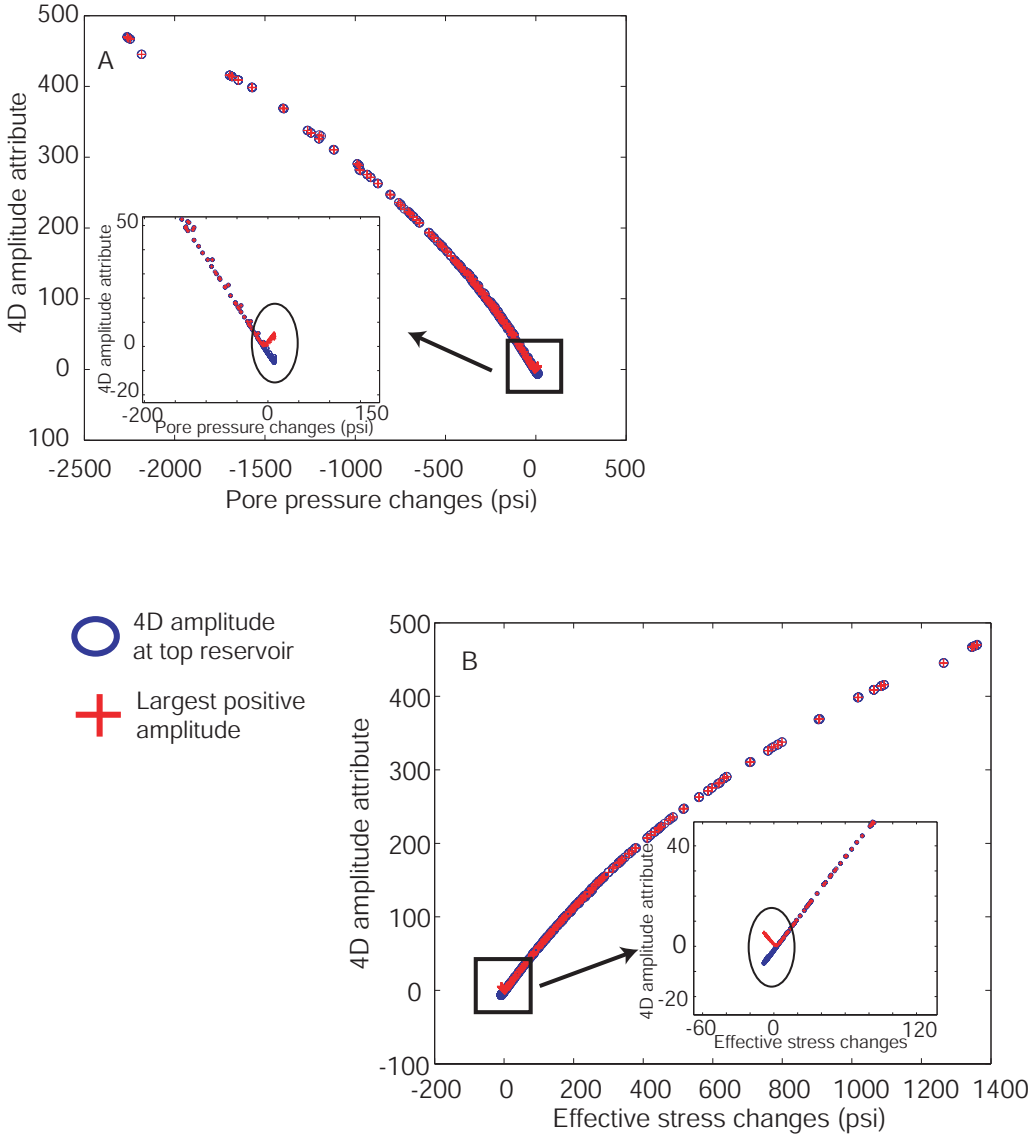

Figure 5.15: A. 4D amplitude attributes vs pore pressure changes after 4 years of depletion. B. 4D amplitude attributes vs effective stress changes after 4 years of depletion.

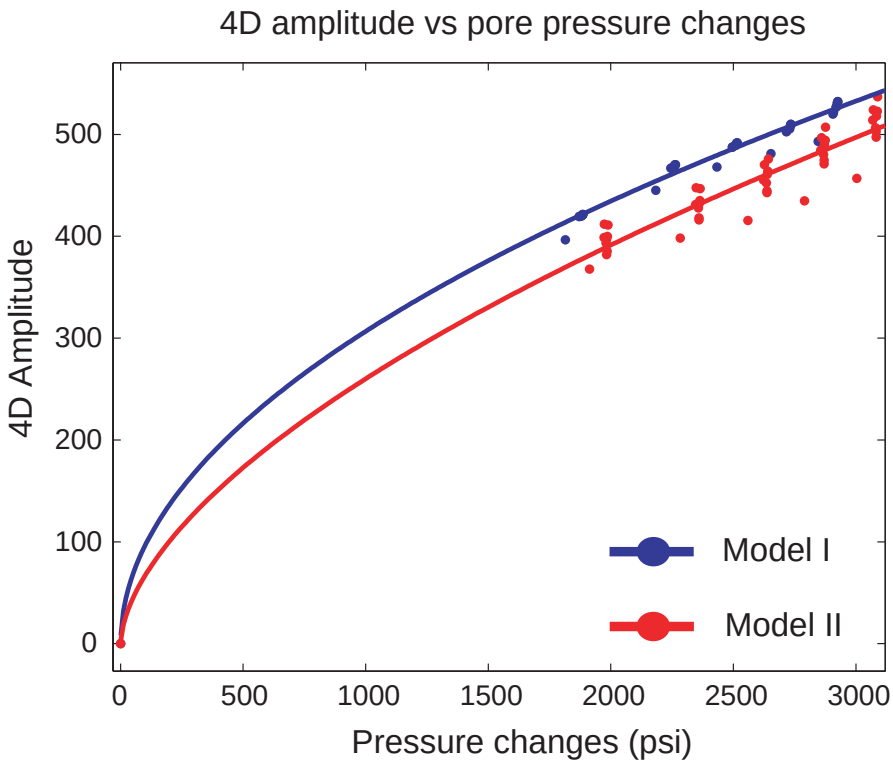

Figure 5.16: 4D amplitude attribute vs pore pressure cross-plot. Data extracted along the well trajectory. More scatter in model II due to the structure and thickness variation.

the maximum depletion at producer and the pressure front decreasing towards the boundaries of the model. However, the pressure estimates from 4D amplitude for model II over predicts the pressure drop around the producer. The error was estimated using equation 5.4.

$$error = (P_{RM} - P_{4DAMP}) \tag{5.4}$$

Where P_{RM} is the pressure from the reservoir model and P_{4DAMP} is the pressure estimated from 4D amplitude using equation 5.3. The error maps for models I and II are shown in figures 5.18A and 5.18C respectively. The greatest errors are due to the large variations in the normal average stress.

Errors on the pressure changes estimations from time-lapse amplitude attributes due to thickness and structure

Even though both models have the same fluid and reservoir properties, identical geomechanical properties were used and the producer well is producing at the same rate in the two models, there

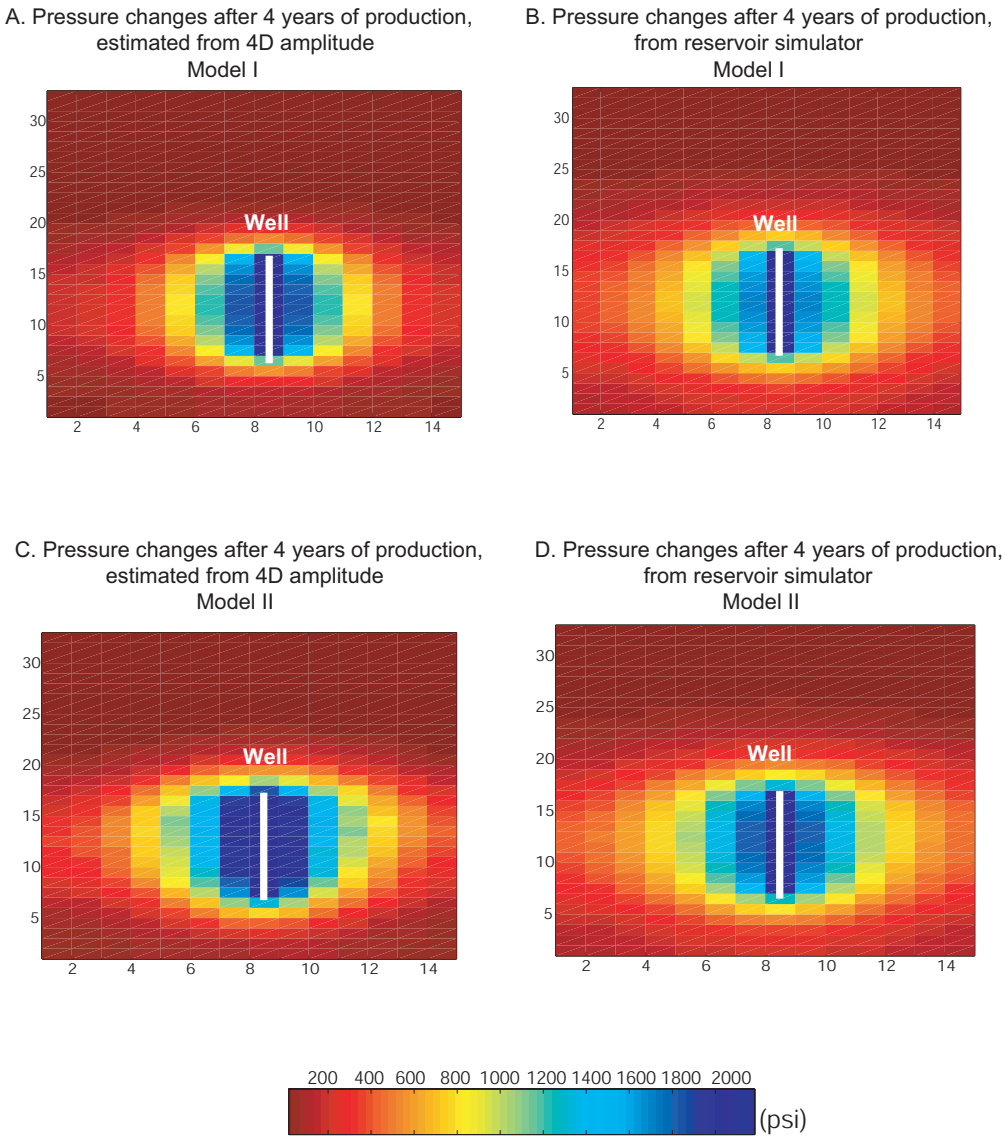

Figure 5.17: A. Pressure depletion map estimated from 4D amplitude for model I. B. Pressure depletion map output from the reservoir simulator for model I. C. Pressure depletion map estimated from 4D amplitude for Model II. D. Pressure depletion map output from the reservoir simulator from model II.

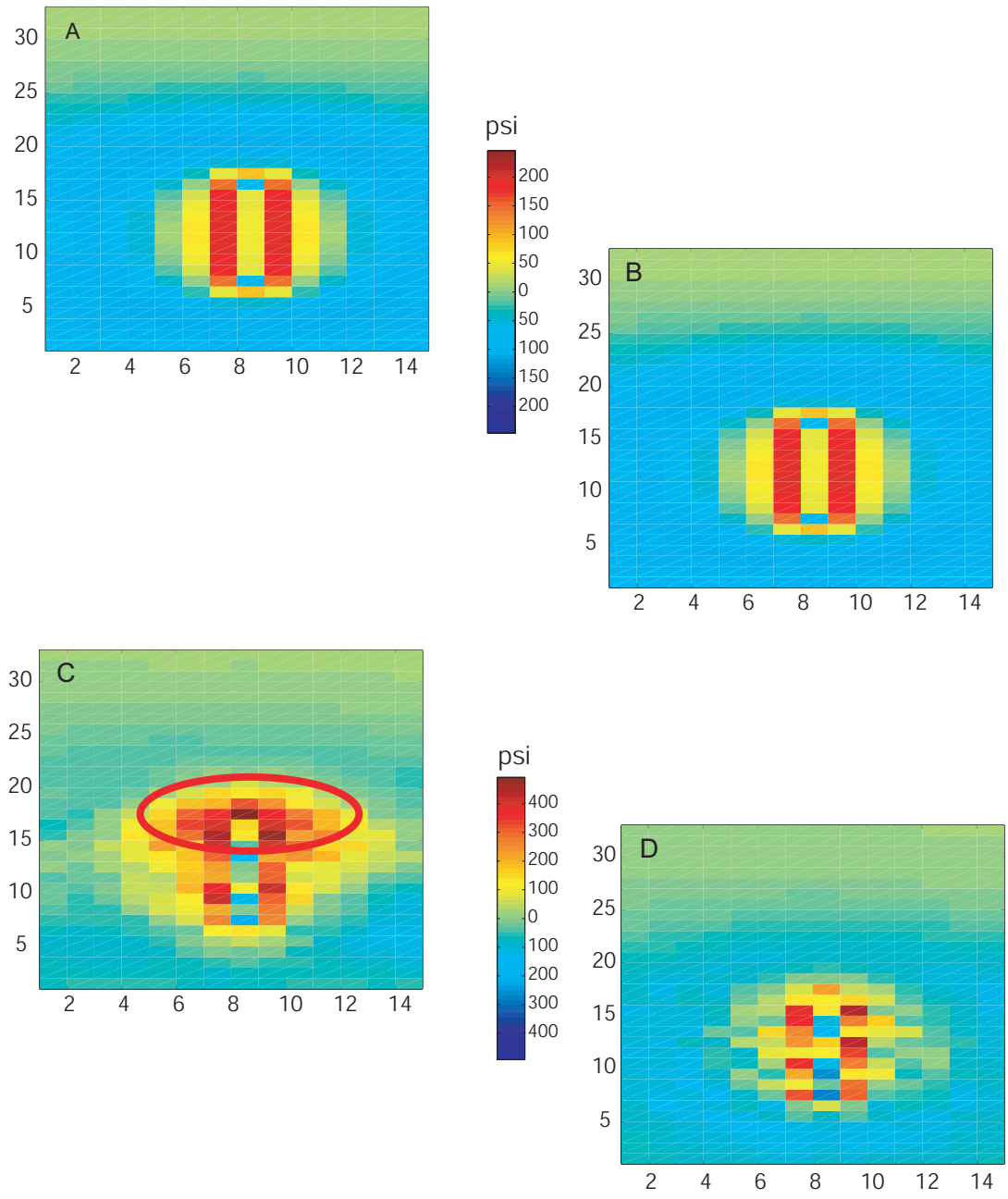

Figure 5.18: A.Error of pressure changes estimated from 4D amplitude for model I (using absolute values). B. Error of pressure changes estimated from 4D amplitude for model I (using relative values) C. Error of pressure changes estimated from 4D amplitude for model I (using absolute values). D. Error of pressure changes estimated from 4D amplitude for model I (using relative values)

are differences in the pressure depletion pattern and the stress and strain distribution through time. These differences affect the 4D amplitude response and are caused by the structure. To quantify the influence that thickness and structure have on the predicting pressure changes, the trend equation was re-written in terms of relative changes of amplitude and pressure (eq. 5.5), where the relative changes of the 4D signal ($\frac{\Delta A}{A_i}$) is equal to the relative changes of the reservoir pressure ($\frac{\Delta P}{P_i}$). The relative changes of the properties were estimated by dividing the pressure and amplitude change (ΔA and ΔP) into the initial values of pressure and amplitude (P_1 and A_1). Equation 5.5 is a modification of the one proposed by MacBeth et al.(2004) for siliciclastic reservoirs (eq. 2.1). They used the average initial values instead of using the initial values.

A set of coefficients (C_1 and C_2) was estimated for both models (table 5.3). The new coefficients from models I and II are similar, indicating that estimating relative changes instead of absolute changes, compensates the influence of the structure on the pressure estimations. Figure 5.18 shows the absolute errors (eq. 5.4) between the pressure estimations using equations 5.3 (absolute changes) and 5.5 (relative changes) for both models. For model I, there is no difference between the pressure estimations using either of the equations (figures 5.18A and 5.18B), since the amplitude and pressure at initial conditions is constant across the model. However, for model II the error maps are different. When equation 5.3 is used to predict the pressure changes, the outcome is more affected by the structure, specially in the middle part of the model (red circle in figure 5.18C). On the contrary, equation 5.5 reduces the structure influence on the results figure (5.18D). Figure 5.19 shows the absolute error for model II using equations 5.3 and 5.5 on a histogram. When relative values are used, the errors are smaller (magenta columns) than the errors when absolute values are used (green columns).

For the pressure predictions carried out in the south east flank of the Valhall Field (chapter 4) using relative values to estimate the coefficients is probably the most appropriate approach. However, the top of the reservoir on the baseline seismic (LoFS1) is not easy to interpret due to the initial impedance contrast between the Lista formation (layer immediately above the reservoir) and the Tor Formation is very low.

$$\frac{\Delta A}{A_1} = C_1 * (\frac{\Delta P}{P_1})^{C_2} \tag{5.5}$$

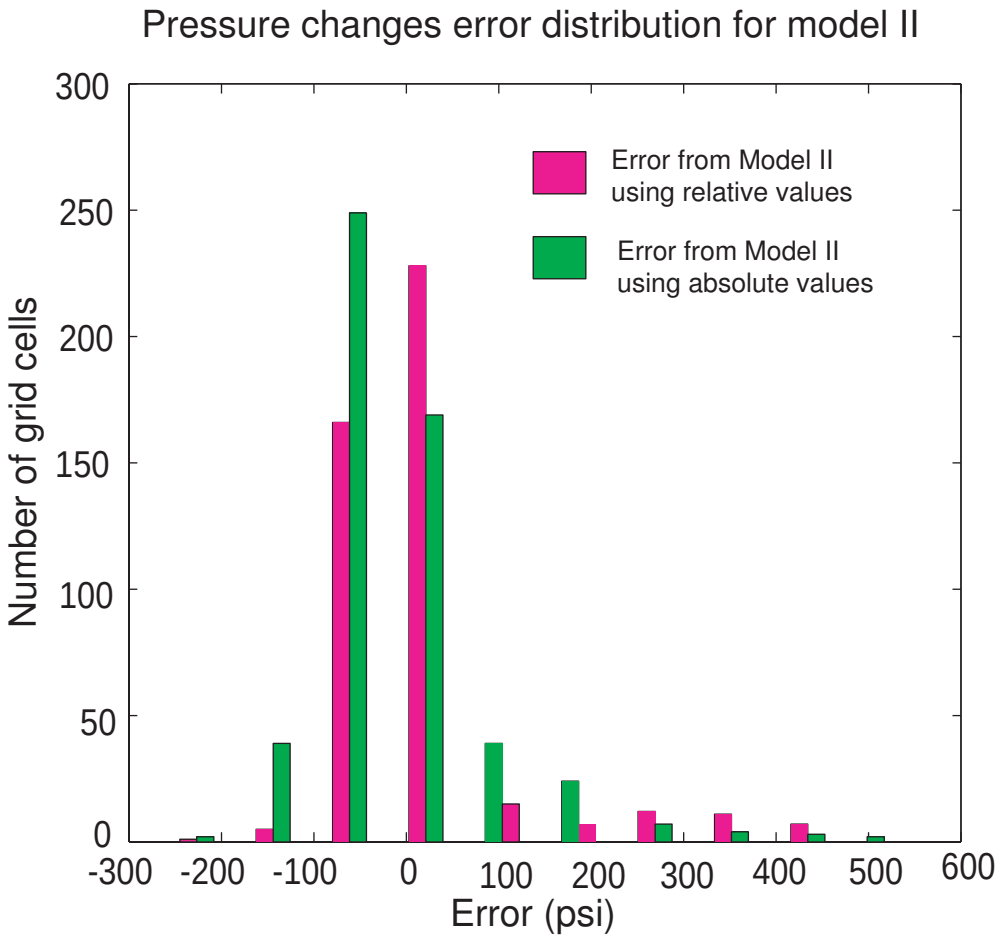

Figure 5.19: Error distribution of the pressure changes predictions for model II. The pressure changes errors using relative values (magenta bars) are smaller than when absolute values (green bars) are used.

ϕ_i (%)	C_1	C_2	R^2	RMSE
model I	0.9393	0.5961	0.983	0.018
Model II	0.8844	0.6045	0.97	0.023

Table 5.3: Coefficients C_1 and C_2 for equation 5.5. The fourth column is the coefficient of multiple determination (R^2). This statistic measures how successful the fit is in explaining the variation of the data. A value closer to 1 indicates a better fit. The fifth column represent the RMSE, the root mean squared error. A value closer to 0 indicates a better fit

5.2 Pressure changes predicted from time-lapse amplitudes on a three phase reservoir

The second part of this chapter investigates the effect that gas coming out of solution has on the pressure changes estimated from 4D amplitude. For doing this, I used a synthetic model that has identical geometry and reservoir and geomechanical properties to the one used in chapter 3. However, the oil is treated as a live oil and when the bubble point pressure is reached, gas is released into the system. Therefore three phase coexist at some point during the life of the field. After the iterative couple geomechanical and fluid simulation is run. The same methodology explained in section 2.4 was used to create the full stack synthetic data. Firstly, the acoustic properties for the reservoir and non-reservoir rocks are calculated. For the reservoir rocks a fluid substitution model is used for estimating the elastic properties. The overburden P-wave velocities were calculated as a function of vertical strain (eq. 2.15). Finally, synthetic seismic volumes for the different times were created using a convolutional model. The input wavelet used to convolve with the reflectivity series, was extracted from the LoFS data.

5.2.1 Description of the synthetic model

The model has 60 grid cells in the x and y directions. In the vertical direction, there are 14 layers, arranged as follows: 10 layers above the reservoir (overburden), 1 layer for the reservoir and 3 layer below the reservoir (underburden). The total of grid cells is 50400 (60X60X14). The x and y dimensions of each grid bock decrease towards the reservoir area. The reservoir grid is a subset of the finite element stress grid and its size was 50x50x1.

The model is considered a three-phase (oil-gas-water) system undergoing primary depletion with no

gas cap at initial conditions but there is gas dissolved in the oil phase. The PVT properties for both oil and gas are considered functions of pressure only and not of composition. The PVT data from the south east of the Valhall Field were used to assign the fluid properties such as solution gas-oil ratio (Rs), oil formation volumetric factor (Bo) and gas formation volume factor (Bg). The additional input data required for the fluid flow modelling, are summarized in table 5.4. The initial porosity varies across the model from 35% up to 42%. The reservoir is produced by a single well for 24 years (figure 5.20B for well location). The initial production rate is 6800 bbl/day.

Regarding the geomechanical data, this model uses linear elastic materials with the same parameters as the model in chapter 3 (table 3.1). The overburden and underburden are described as linear elastic materials and for the reservoir, a two slope elastic behavior is adopted to capture the rock deformation due to the pressure depletion (section 3.1 for a detailed description).

Property	**Description / Value**
Type of oil	Live
Oil viscosity (cp)	2.05
Oil gravity (API)	36
Thickness (m)	25
Reservoir depth (m)	2600
Initial pressure (MPa)	45.5
Temperature	90
Vertical and Horizontal permeability	5
Oil density ($\frac{Kg}{m^3}$)	844
Gas density ($\frac{Kg}{m^3}$)	0.96
Water density ($\frac{Kg}{m^3}$)	1009.163
Connate water (%)	5

Table 5.4: Fluid and reservoir properties for the live oil model. All the properties are based on the data from south east flank of the Valhall Field

5.2.2 Analysis of pore pressure and fluid saturation during production

The pressure at initial conditions is higher than the bubble point pressure (BPP), in other words, there is no gas cap. Also, the reservoir is not connected to an aquifer. As the reservoir is depleted and the pore pressure reaches values below BPP of the liquid, gas is formed and migrates to the top of the reservoir. Figure 5.20A shows the production data (pore pressure and gas saturation) at one grid cell along the well. The location of the grid cell is shown in figure 5.20B. The plot of the

gas saturation exhibits two different slopes (green line). The pressure at which the slopes change is the bubble point pressure (BBP=3112 psi). For pressures lower than BBP, the saturation of gas increases. The fluid saturation (S_{fluid}) on the reservoir is constrained by equation 5.6. At initial conditions, the only two phases present in the model are oil and water. The initial oil saturation is 0.95 (S_o) and the initial water saturation (S_w) is equal to the residual saturation (0.05). The residual saturation is the amount of water that is trapped in the pore spaces. At 12 years of production, the reservoir reaches the BBP, the saturation of gas (S_g) increases and the oil saturation decreases by the same amount since the water saturation is kept constant during the simulation time (figure 5.21).

$$S_{fluid} = S_o + S_g + S_w = 1 \tag{5.6}$$

5.2.3 Analysis of the stresses and strain distribution during production

Changes in pore pressure are accompanied by changes in the total stress and effective stress. The total stress is the average of the vertical stress and the two horizontal stresses. Observing the changes in the vertical stress and one of the horizontal stresses along the producer gives an idea how the total stress is varying during the simulation. Figure 5.22A shows the changes in the vertical stress (blue line), the horizontal minimum stress (green line) and pressure (red line). Figure 5.22B shows the changes in the effective stress. All of these changes are measured after 18 years of production. From the cross-plots it is observed that the pore pressure depletion causes the vertical and the horizontal stresses to decrease. However, the vertical stress varies more than the horizontal stress. The black arrow in the figures indicates that due to a pressure depletion of 3800 psi, the vertical stress has decreased up to 2600 psi while the minimum horizontal stress has decreased only 400 psi. This produces an effective stress increase of 2000 psi. In general, the pore pressure decrease causes a decrease in both normal stresses (vertical and horizontal).

5.2.4 Calculation and analysis of the acoustic property changes for a three phase reservoir

The outputs from the fluid flow and geomechanical simulators are used to determine the seismic properties of the reservoir rocks using the standard rock physics equations (Batzle & Wang, 1992).

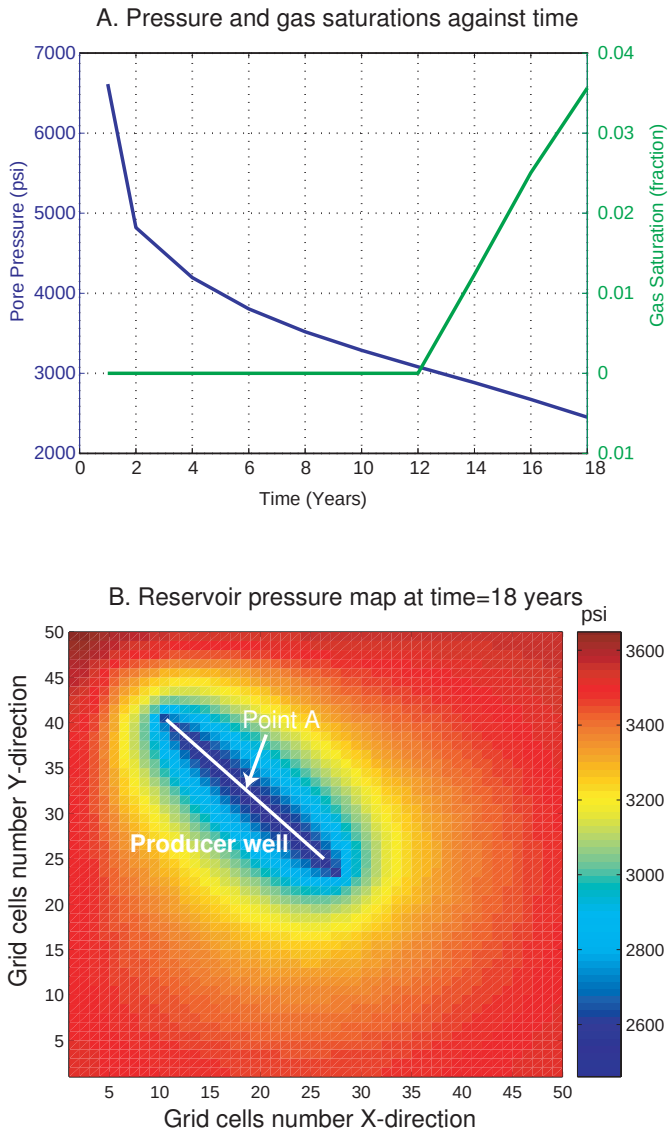

Figure 5.20: Production data at the well location from the reservoir simulator. A. Pressure and gas saturation at one grid cell along the well. B.Pore pressure map at 18 years of production. Point A is the data used in the cross-plot. At point A, after 12 years of production, reservoir pressure goes below BPP.

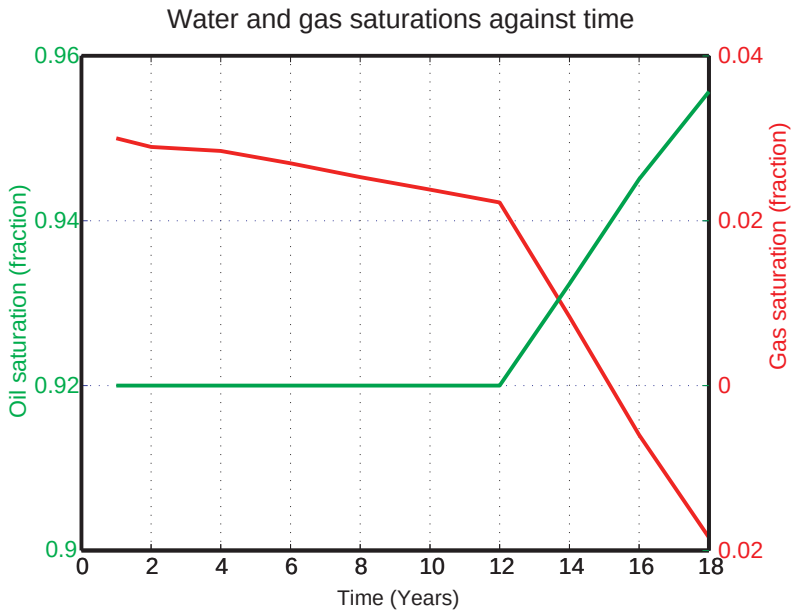

Figure 5.21: Fluid saturations (oil and gas) at one grid cell along the well. The well location is shown in figure 5.20B. Gas production starts after 12 years. The water saturation is equal to the residual saturation (0.05) during the simulation time.

In the previous chapters, I have dealt only with a dead oil, where no gas was dissolved in the oil phase. The present model considers the oil as live oil type. Live oils have significantly different properties than dead oils because the dissolved gas into the oil solution and the free gas expelled after BPP is reached have an effect on the acoustic properties of the fluid. Several authors have reported decrease in bulk modulus, density and ultrasonic velocities with increasing dissolved gas in the oil (Hwang & Lellis, 1988; Clark, 1992). I have used the mathematical expressions proposed by Batzle and Wang. (1992) to determine the seismic properties of a live oil (eq. 5.7 and eq. 5.8). Their approach is based on assuming that a live oil is considered to be a mixture of the original gas-free oil and a light liquid representing the gas component. The velocities of the dead oil are significantly higher than the ones for live oil. For the dead oil case, the P-wave velocity of the oil phase changes only as a function of pressure and temperature (eq. 5.7). However, for the live oil case the oil saturation density (ρ_{oil}) needs to be substituted by ρ_G shown in equation 5.8. Therefore, the P-wave live oil velocities depends in addition to the pore pressure, on the gas gravity (G), the gas-oil ratio (R_s) and oil formation volumetric factor (B_o). These two last parameters are pressure dependent and are

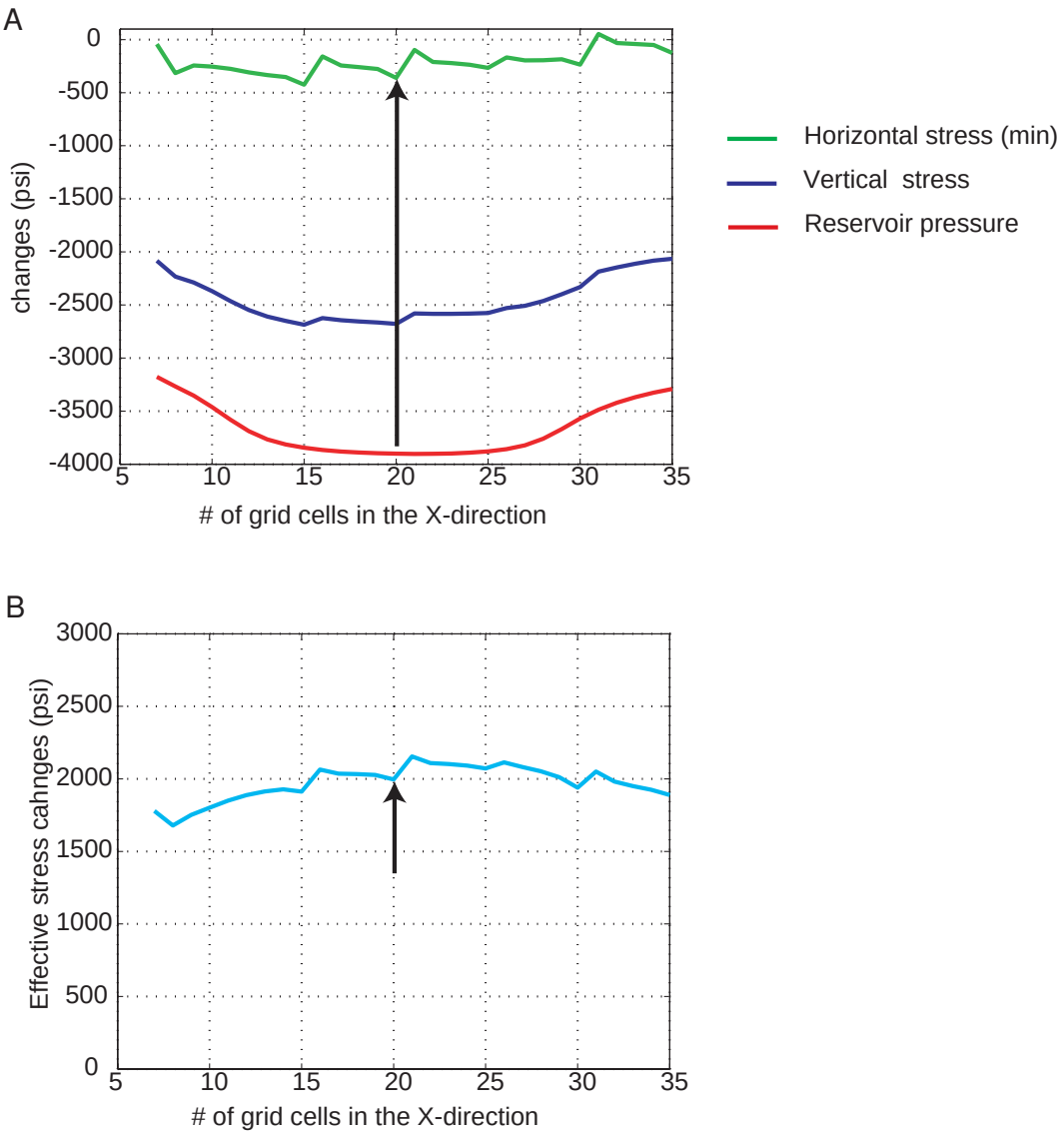

Figure 5.22: Variation in the total stress due to pressure depletion. A. Vertical and horizontal stress changes along the well. B. Effective stress changes along the well. The profile location is shown in figure 5.20B. The minimum horizontal stress, the vertical stress and the reservoir pore pressure decrease while the effective stress increases along the well.

determined by PVT analysis.

$$V_p = 2096(\frac{\rho_{oil}}{2.6 - \rho_{oil}})^{\frac{1}{2}} - 3.7T + 4.64P + 0.0115[(\frac{18.33}{\rho_{oil}})^{\frac{1}{2}} - 1]TP \tag{5.7}$$

$$\rho_G = \frac{\rho_{oil} + 0.0012R_sG}{B_o} \tag{5.8}$$

P-wave velocity and acoustic impedance changes in the reservoir

Figure 5.23A shows the relative changes in seismic properties (%) against pore pressure from pre-production up to 16 years of production. The data were extracted from the location shown in figure 5.23B. Each data point represents the percentage change in P-wave velocity (red) and acoustic impedance (blue) between a monitor survey and the baseline survey, cross-plots against the pore pressure in the monitor volume. The plot exhibits three different slopes, the first slope change is when the rock starts to compact, the second slope change coincides with the bubble point pressure. After gas starts coming out of solution, the P-wave velocity and the impedance decrease. The velocity decreases more rapidly than the impedance decreases. This is because the impedance is not only influenced by the velocity decrease but is also affected by the density, which is increasing due to the rock compaction.

Extraction and analysis of the time-lapse amplitude attribute used to predict pore pressure changes

The model produced for 18 years and synthetic seismic was created every 2 years (8 seismic volumes). Seismic data are generated for a pre-production state (baseline volume) and after 2, 4, 6, 8, 10, 12, 14, 16 and 18 years of production (monitor volumes). The same name nomenclature previously used was adopted for the time-lapse volumes (i.e. YxminY1, where x is the monitor survey). Pressure below BPP around the well are reached after 14 years of production. Therefore the effect of the gas coming out of solution is observed in the following difference volumes: Y14minY1, Y16minY1 and Y18minY1.

Figures 5.24A and 5.24B show a trace extracted from 9 difference seismic volumes. The trace was extracted from the grid cell shown in figure 5.23B. For the first five time-lapse seismic volumes, the 4D amplitude response is a peak at the top of the reservoir that increases with time, due to

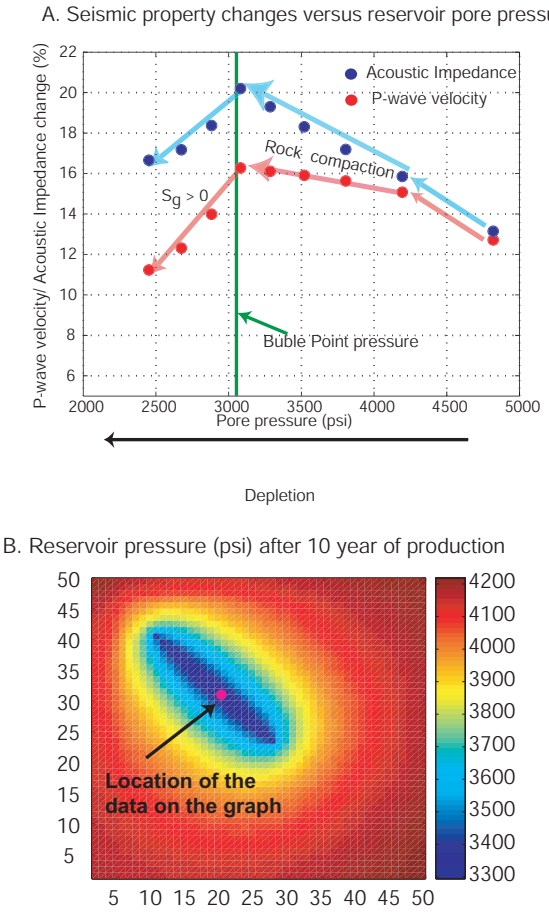

Figure 5.23: Elastic properties changes against pore pressure. A. P-wave velocity and acoustic impedance changes versus pore pressure. B. Location of the data used in the cross-plot

the acoustic impedance decreases in layer 9 and the acoustic impedance increases in the reservoir (figure 5.24A). The 4D amplitude attribute used during the analysis is the Largest Positive Value. This is the same type of attribute that has been extracted in previous synthetic examples (chapter 3 and section 5.1). The 4D amplitude response at the top of the reservoir decreases with time on the last three time-lapse seismic volumes (figure 5.24B). The 4D signature remains a peak but the magnitude decreases as the reservoir depletes and the gas saturation increases. This means that if the gas saturation keeps increasing due to pressure depletion, a change from peak to trough in the 4D amplitude response could occur even if the reservoir continues compacting and the overburden stretching.

5.2.5 Estimation of pressure changes from 4D amplitude attributes in a three phase reservoir

The methodology used for estimating the pressure changes has been explained in chapter 3. The approach is based on finding a trend equation to relate changes in 4D amplitude with pressure changes and initial porosity. This is achieved by cross plotting pressure changes and 4D amplitude around the wells. For this model, there is a single well that has been producing from the highest initial porosities on the reservoir (from 39% up to 42 %). I have selected more points in the model in order to know how 4D amplitude against pressure changes correlates for the other initial porosities (from 35% up to 38 %). Figure 5.25 shows the data used in the analysis.

In order to investigate how much the trend equation varies from a dead oil scenario to a live oil scenario, I create a parallel model which has the same reservoir and geomechanical characteristics as the live oil model but only oil and water are in the system during the life of the field. For this model, the synthetic seismic volumes were created after the simulation was completed. Then, the 4D amplitude response was extracted from the time-lapse volumes. Figure 5.26 shows the cross-plot between pressure depletion and 4D amplitude. The data points are colour coded by initial porosity. The squares represent the live oil model and circles represent the dead oil model. The data points along the well were extracted at the periods of times when 4D seismic was available (i.e. every two years). The 4D amplitude and pressure changes are estimated relative to the initial conditions. For the live oil case, the data exhibits two different slopes. Before BPP, the 4D amplitude increases with pressure depletion and after BPP, the 4D amplitudes decrease with pressure depletion due to the gas

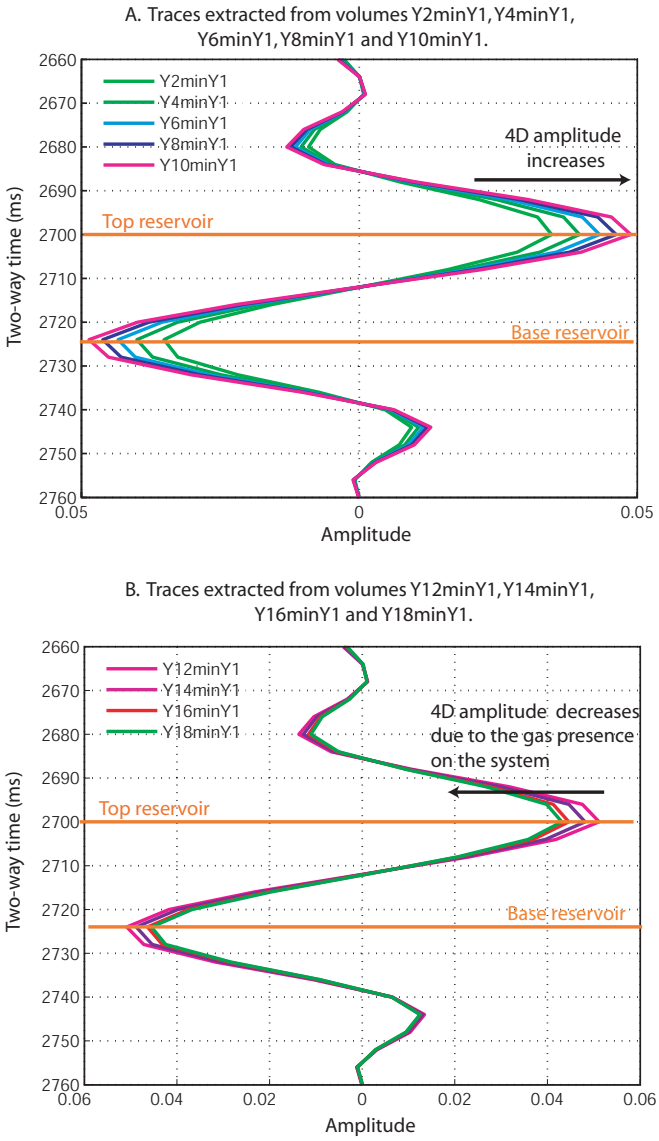

Figure 5.24: Seismic traces extracted around the well location. A. Seismic traces from volumes Y2minY1, Y4minY1, Y6minY1 and Y8minY1. B. Seismic traces from volumes Y10minY1, Y12minY1, Y14minY1, Y16minY1 and Y18minY1. The 4D amplitude increases prior to 12 years. After 12 years, the 4D amplitude decreases but remains as a peak on the seismic.

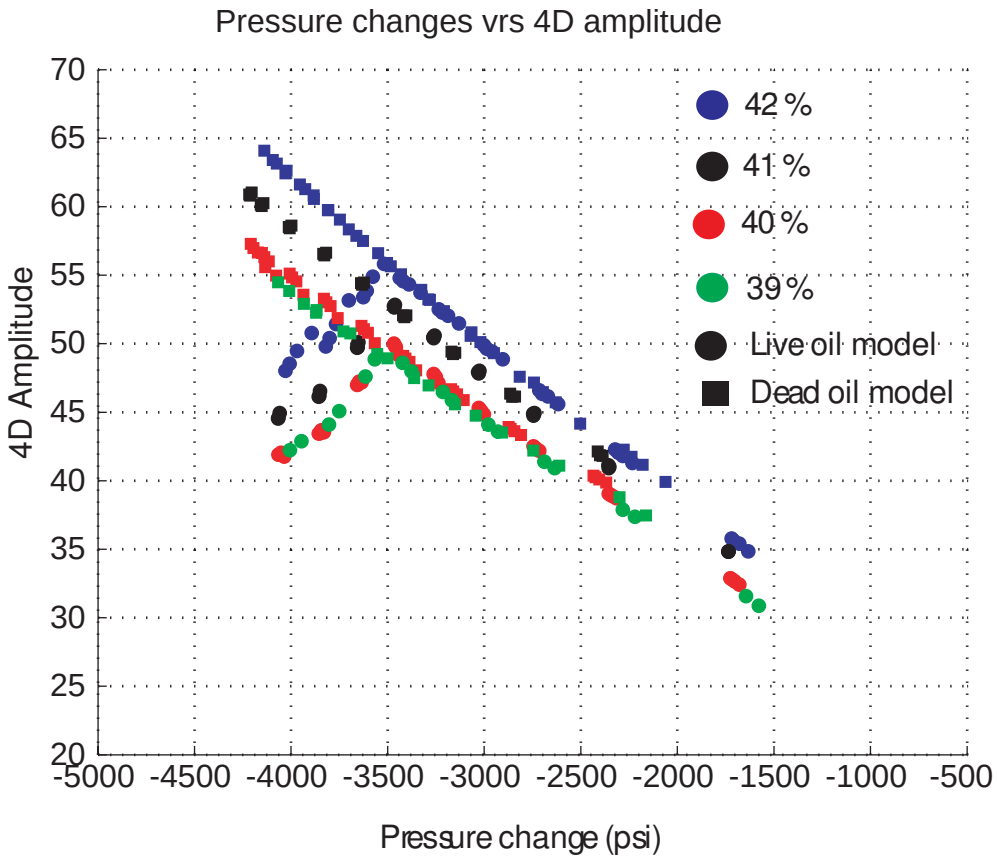

Figure 5.25: Initial porosity map. The data points used for cross-plotting 4D amplitude and pore pressure changes are shown in black. The well produces from the highest initial porosities (from 39% up to 42 %).

saturation changes. Furthermore, before reaching the BPP, the data have the same behavior as the dead oil case. Therefore the same trend equation used in the dead oil model can be used for the live oil model when the reservoir is above BPP.

According to the methodology proposed in chapter 3, after cross-plotting pressure changes against 4D amplitude, equation 5.9 is used to fit the data from each initial porosity (figure 5.27).

$$\Delta A = C_1 * (\Delta P^{C_2}) \tag{5.9}$$

The coefficients C_1, C_2 are expressed as a function of initial porosity (table 5.5). Figure 5.28 shows how the coefficients vary as a function of initial porosity. It is observed that for porosities larger than 39%, the coefficients show different trends. This is because some areas with initial porosities of 39%, 40%, 41% and 42% are below BPP. Therefore I ignored porosities higher than 39% to estimate the linear fits, which relate initial porosities and the coefficients:

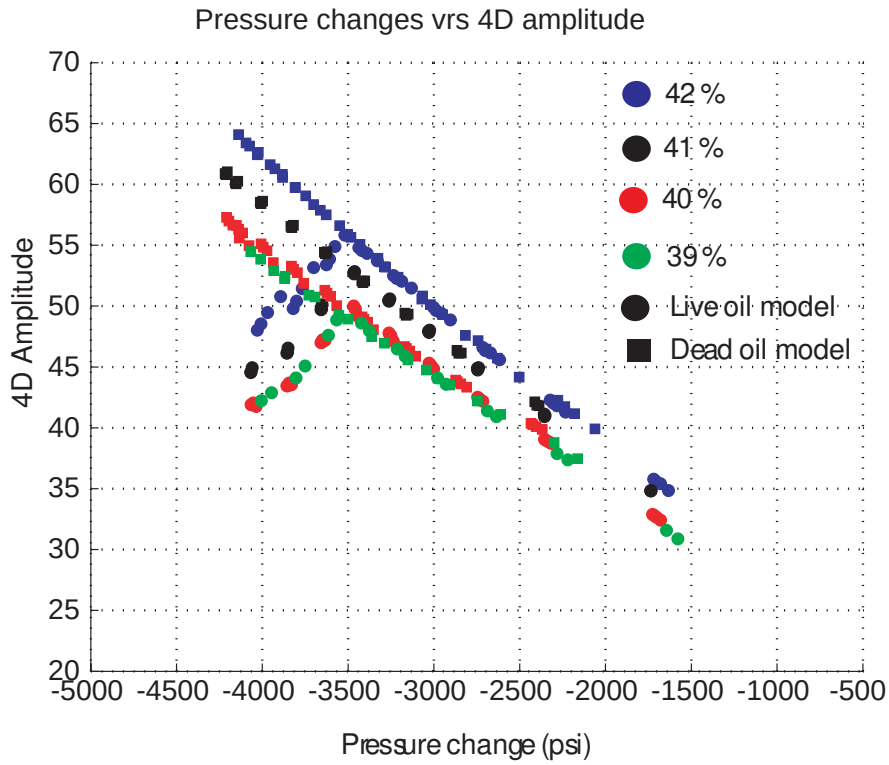

Figure 5.26: 4D amplitude vs pressure changes for dead and live oil models. The data points are extracted along the horizontal well.

$$C_1 = 3.46 * \phi_i - 1.024 \tag{5.10}$$

$$C_2 = -0.958 * \phi_i + 0.985 \tag{5.11}$$

Then, replacing C_1 and C_2 in equation 5.9

$$\Delta A = (3.46 * \phi_i - 1.024) * (\Delta P^{(-0.958*\phi_i + 0.985)}) \tag{5.12}$$

Equation 5.12 is used to estimate pressure changes in the areas where the reservoir is above BBP.

Figure 5.29 shows the cross-plot between pressure changes and 4D amplitude for areas where the reservoir pressure is BBP (i.e. along the producer and porosity families higher than 39%). Notice that linear fits can be used to correlate pressure changes and 4D amplitude. Equation 5.13 is used to predict pressure changes when gas has been released into the system.

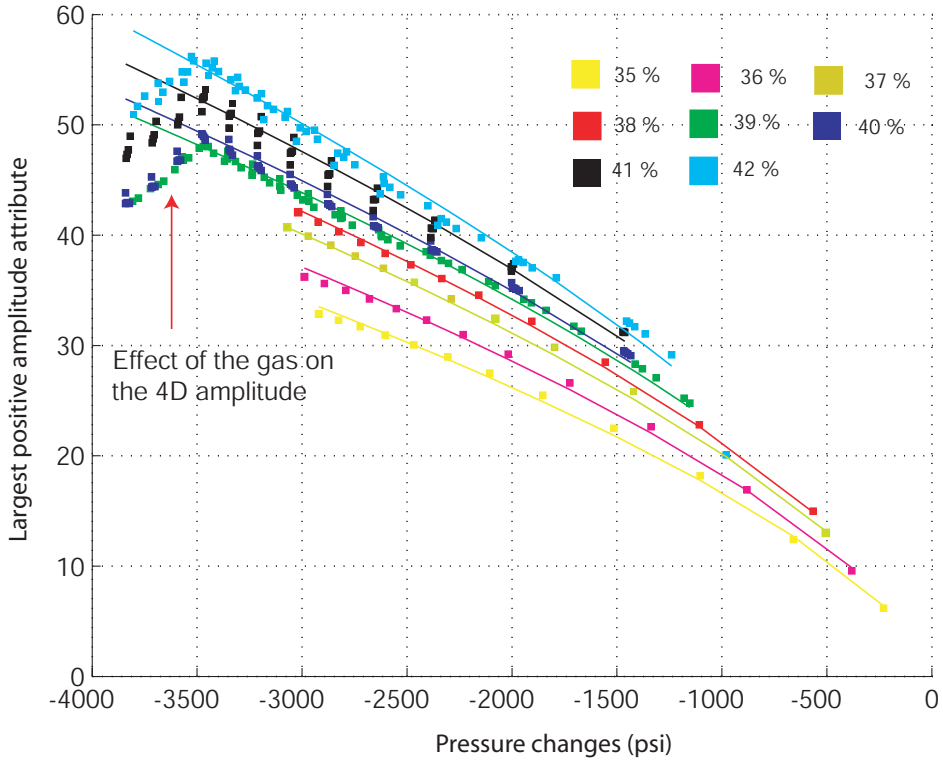

Figure 5.27: 4D amplitude vs pressure changes for the live oil model. The colored lines are the predicted values using equation 5.9 and the coefficients shown in table 5.5. The location of data points is shown in figure5.20B.

Initial Porosity	C1	C2
0.35	0.18474	0.65179
0.36	0.21579	0.64288
0.37	0.26928	0.62497
0.38	0.28672	0.6233
0.39	0.32228	0.61367
0.4	0.31734	0.61862
0.41	0.32001	0.62471
0.42	0.26925	0.6528

Table 5.5: Coefficients C_1, C_2 for equation 5.9

$$\Delta A = (C_3 * \Delta P) + C_4 \tag{5.13}$$

The coefficients C_3 and C_4 depend on the initial porosity (figure 5.30) and are listed in table 5.6. Linear fits are used to relate C_3 and C_4 with initial porosity:

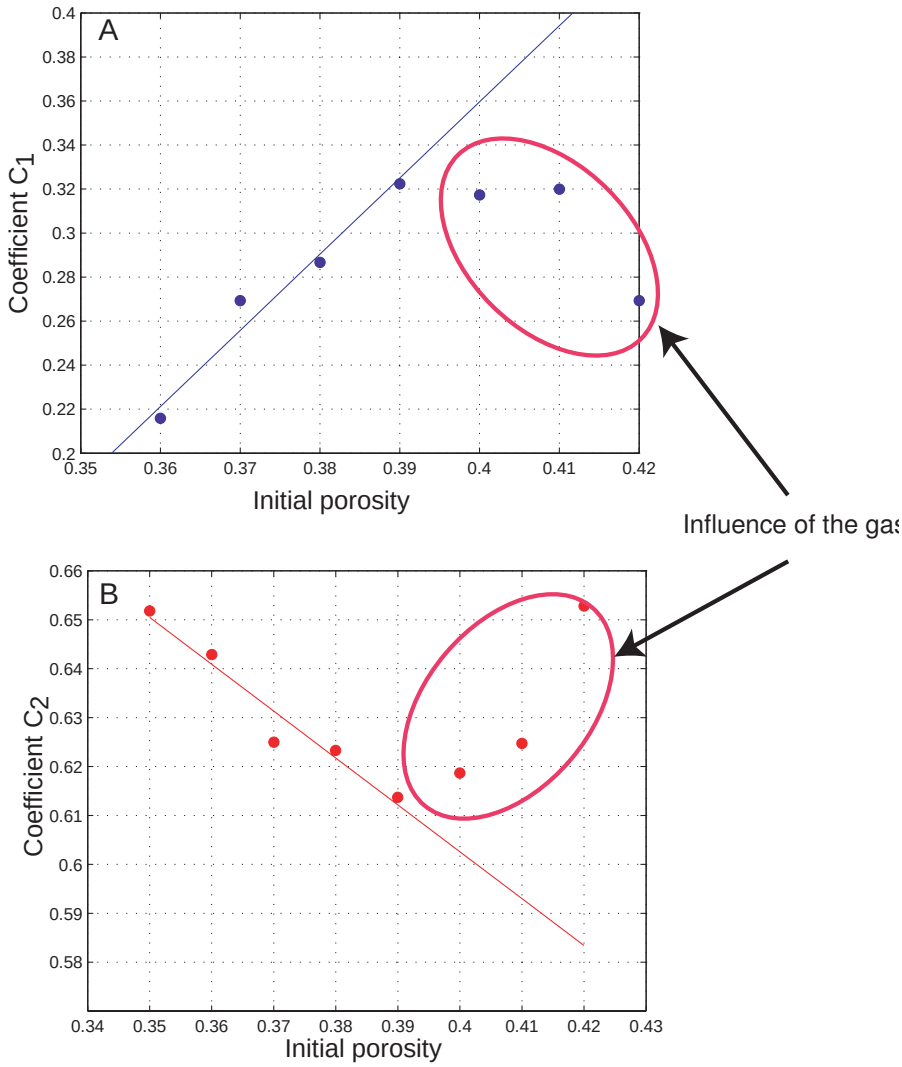

Figure 5.28: A. Coefficients C_1 against initial porosity. B. Coefficients C_2 against initial porosity. These coefficients are used in equation 5.9. The best linear fits (equations 5.10 and 5.11) were estimated using data from initial porosities of 35%, 36%, 37% and 38%.

$$C_3 = 0.1065 * \phi_i - 0.06132 \tag{5.14}$$

$$C_4 = 291.06 * \phi_i - 6.1538 \tag{5.15}$$

Then, replacing C_3 and C_4 in equation 5.13:

$$\Delta A = (0.1065 * \phi_i - 0.06132) * \Delta P) + (291.06 * \phi_i - 6.1538) \tag{5.16}$$

Equation 5.16 is used to estimate pressure changes in the areas where the reservoir is below BBP.

Initial Porosity	C3	C4
0.39	-0.01951	104.07
0.4	-0.01858	114.25
0.41	-0.01789	115.09
0.42	-0.01645	113.49

Table 5.6: Coefficients C_3, C_4 for equation 5.13

Comparison between the pore pressure changes predicted from 4D amplitude attributes and the outputs from the reservoir model.

Equations 5.12 and 5.16 are used to estimate the pressure changes after 20 years of production. Equation 5.16 is used when the gas saturation is different than zero; otherwise eq. 5.12 is used. This means that gas saturation is required to estimate pressure changes.

After 20 years of production, maximum pressure depletion occurs around the producer as shown in figure 5.31A. Furthermore, the pore pressure is below bubble point, therefore the gas saturation has increased in this area (figure 5.31B). If the 4D amplitude was merely responding to the pressure changes, it would be expected an 4D amplitude increases. However as 4D amplitude map (figure 5.31C) indicates, there is a decrease in the amplitude response due to presence of gas.

Figure 5.32A shows the pressure changes predicted from 4D amplitude after 20 years of production. There is a good agreement between this pressure map and the reservoir output (figure 5.32B). The absolute error histogram (figure 5.33) indicates that the mean error is 12.8 psi with a standard deviation of 49.6 psi.

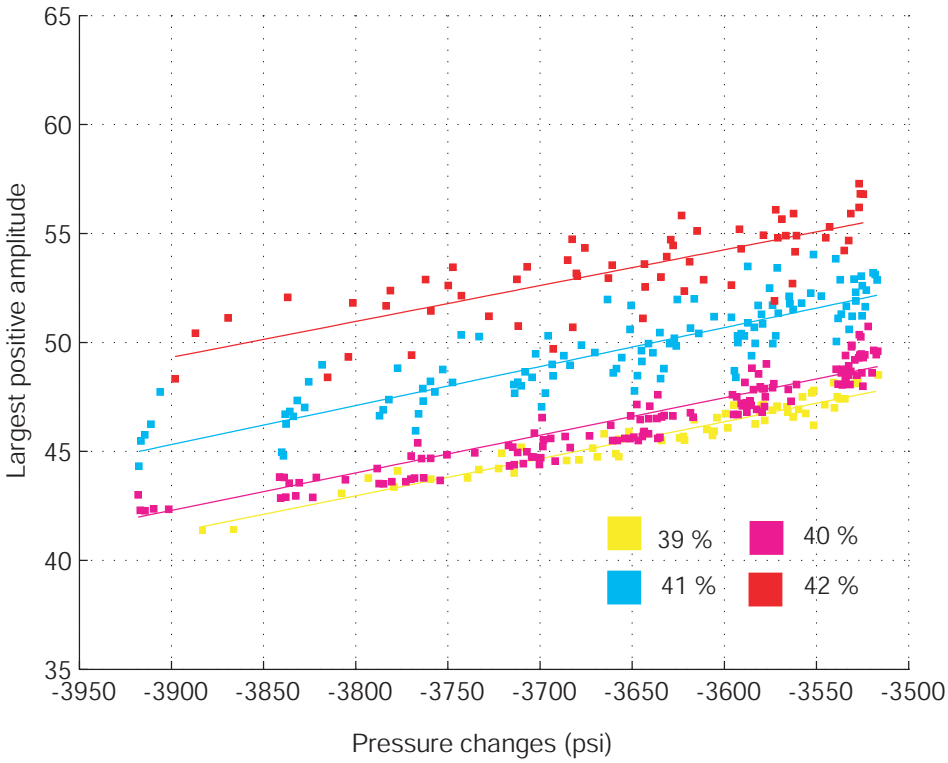

Figure 5.29: 4D amplitude vs pressure changes for data below BBP. The colored lines are the predicted values using equation 5.13 and the coefficients shown in table 5.5. The data points are along the well.

Predicting pressure changes using equations 5.12 and 5.16 for a specific time, requires the reservoir gas saturation changes for the same period of time. However, two attributes approach similar to the one proposed by Floricich et al. (2005) can be explored to predict pressure and saturation changes. The trend equation is defined for two seismic attributes that are sensitive to pressure and gas saturation changes. In compacting reservoir, a time attribute and an amplitude attribute could be combined. This was out of the scope of this thesis, however it should be considered in future analysis of the present research (chapter 7).

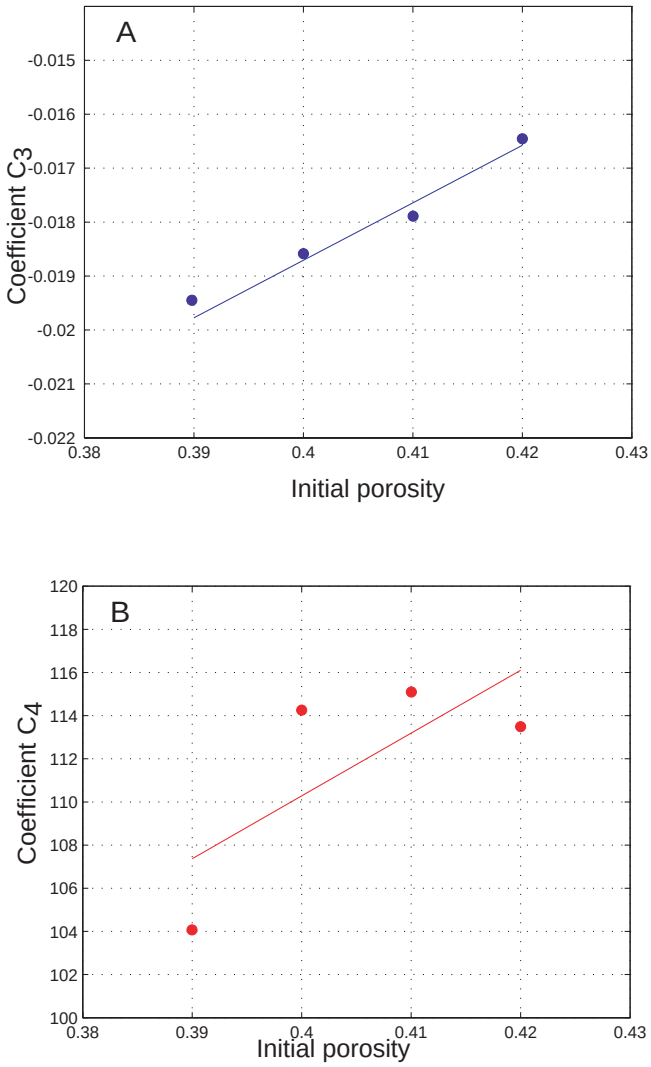

Figure 5.30: A. Coefficients C_3 against initial porosity. B. Coefficients C_4 against initial porosity. These coefficients are used in equation 5.13. The best linear fits (equations 5.14 and 5.15) were estimated using data from initial porosities of 39 %, 40%, 41% and 42%.

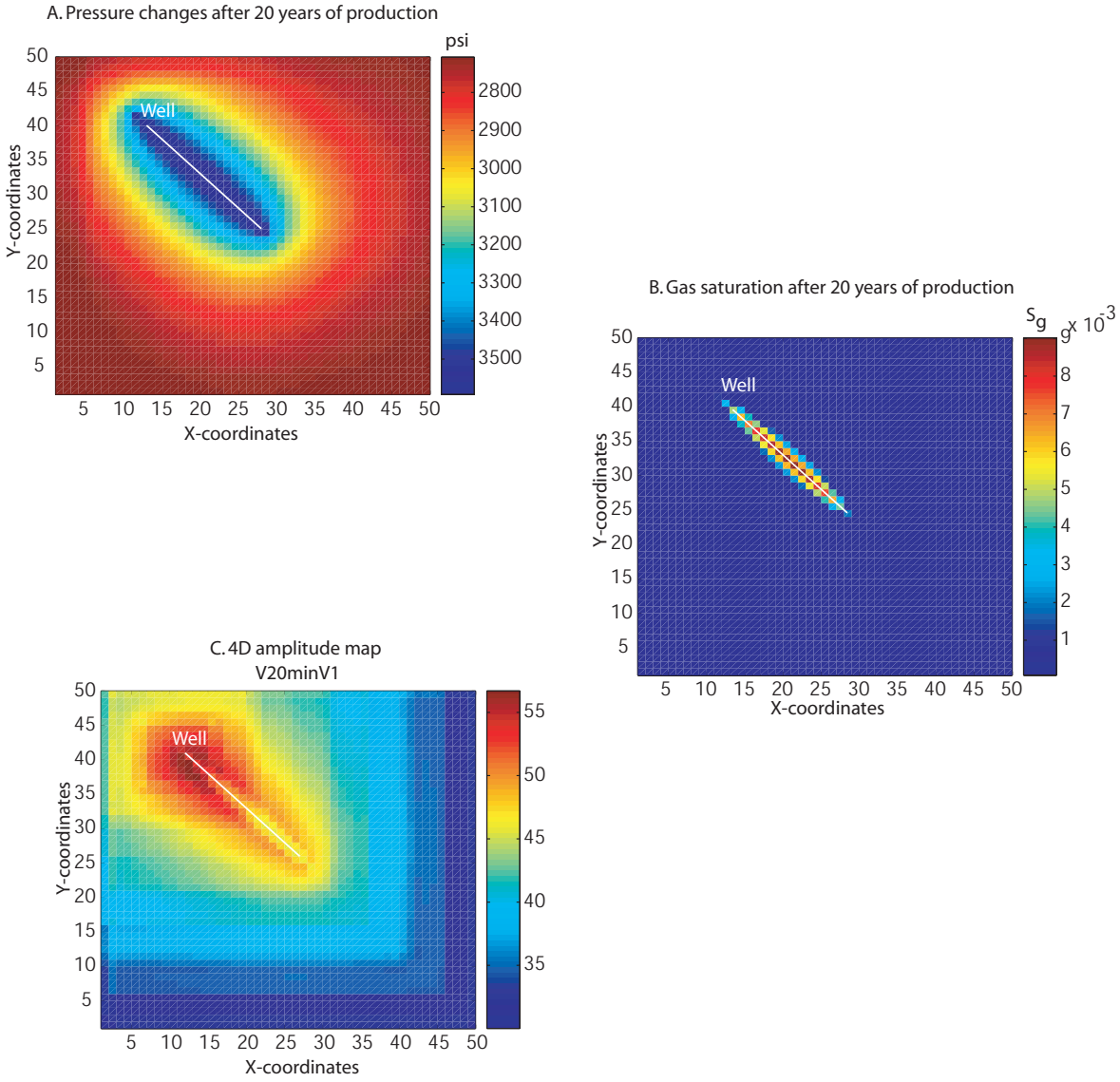

Figure 5.31: Pressure changes, gas saturation changes and 4D amplitude map at 20 years of production for a live oil case. A. Pressure changes estimated from the reservoir model. B. Gas saturation from the reservoir model. C. 4D amplitude response. Due to the gas effect along the producer well, the 4D amplitude response decreases even though the pore pressure has decreased and the rock has compacted.

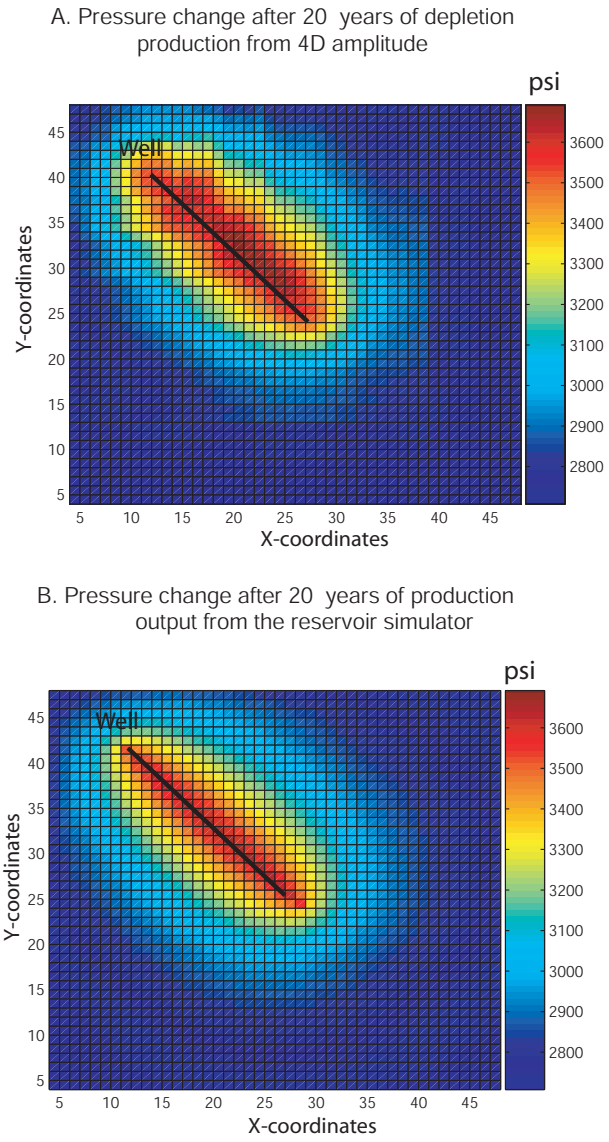

Figure 5.32: Pressure changes predicted from 4D amplitude for a live oil case. A. Pressure changes after 20 years predicted from 4D amplitude. B. Pressure changes after 20 years output from the reservoir model.

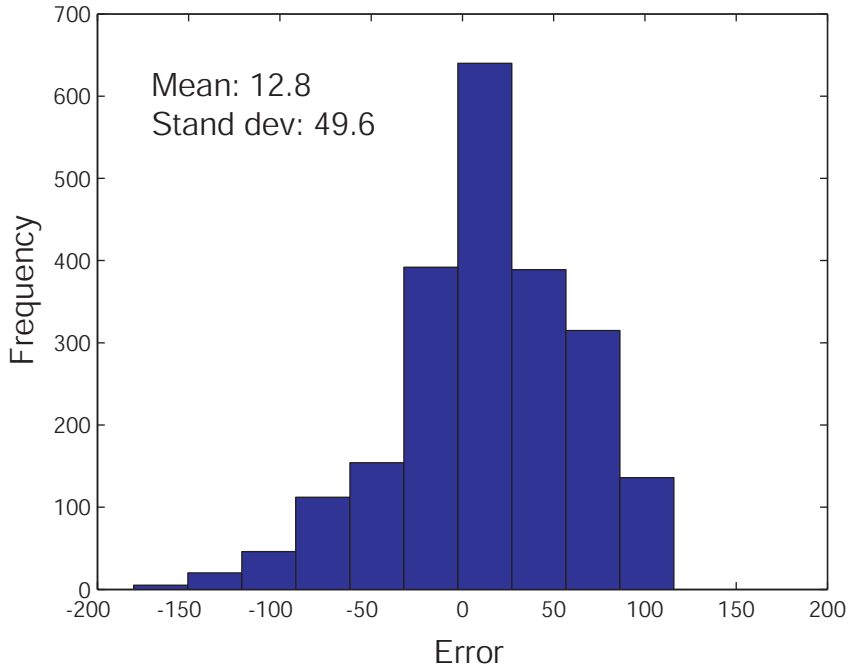

Figure 5.33: Histogram of the absolute error for the pressure prediction.

5.3 Summary

The main objective of this chapter was to investigate the influence of the structure and the free gas in the reservoir have on the pressure changes predicting from 4D seismic.

In order to evaluate the impact of the thickness on the pressure predictions, two synthetic examples were created. Model I is a layered horizontal model and model II is based on the structure of the south east flank of the Valhall Field. After, running the iterative coupling simulation and generated the synthetic seismic at different stages of production for both models, pressure changes and 4D amplitude are cross-plotted. From these cross-plots it was observed that there is more scatter on the data for model II than for model I. This is because the thickness variation influences the 4D amplitude response. However, the same trend equation (i.e. a power law equation) could be used to estimated pressure changes in both models. If I used equation 5.3 to determine the pressure changes for both models, the errors in the pressure predictions are higher for model II due to the thickness variation. Therefore, in order to compensate for that effect in model II, I decided to normalize the 4D amplitude and the pressure changes, dividing them by the amplitude and pressure at initial conditions (eq. 5.5). This procedure seems to remove the thickness footprints and allows the pressure changes predicted

from 4D amplitude to be closer to the reservoir model outputs.

The second part of this chapter concentrates on defining an equation that considers the free gas on the reservoir. Firstly, I created a live oil model where the reservoir has been depleted BBP and the gas saturation has increased. After analyzing the time-lapse seismic on this synthetic example, I found out that the gas released into the system, reduces the 4D amplitude response. Therefore, the methodology to predict pressure changes using 4D amplitude proposed in chapter 3 was modified to incorporate the effect of the gas as follows:

For $S_g < 0$

$$\Delta A = C_1 * (\Delta P^{C_2}) \tag{5.17}$$

For $S_g > 0$

$$\Delta A = (C_3 * \Delta P) + C_4 \tag{5.18}$$

Chapter 6

Investigating the impact of the overburden elastic parameters on the 4D seismic signal

The previous chapters have addressed the issue of estimating pressure changes in compacting reservoirs using 4D amplitudes. The amplitude of a reflected wave at an interface is a function of the reflection coefficient and is defined by the acoustic impedance contrast between the two mediums. In non-compacting reservoirs, the changes in the acoustic impedance are restricted to the reservoir interval itself, whereas for compacting producing reservoirs, the rock deformation impacts both the reservoir and the overburden. Therefore, the amplitude extracted at the top of the reservoir will carry with it information regarding the stress/strain changes occurring in the layer immediately above the reservoir. If this is not understood or accounted for, then 4D amplitude changes may be incorrectly attributed to reservoir compaction or pressure changes. In this chapter, I investigate the impact that the elastic parameters of the overburden (Young's modulus and Poisson's ratio) have on vertical strain, P-wave velocities and 4D amplitude.

I will consider seven synthetic models where the elastic parameters of the overburden, especially the layer immediately above the reservoir, vary. The geometry of the models, reservoir quality, fluid properties and depletion pattern are identical for the seven models in an attempt to isolate the impact of the overburden.

All the models are rectangular boxes with 60 grid cells in the x and y directions. In the vertical direction, there are 14 layers, arranged as follows: ten layers above the reservoir (overburden), one layer for the reservoir and three layers below the reservoir (underburden). The total number of grid cells is therefore 50400 (60X60X14). The x and y dimensions of each grid bock decrease towards the reservoir area. The reservoir grid is a subset of the finite element stress grid and its size is 50x50x1. The reservoir is located in layer 10; layer 9 is therefore the layer immediately above the reservoir and is the layer that most of the discussion of this chapter is based up on. For ease of explanation I will often use "layer 9" to refer to "the layer immediately above the reservoir". The reservoir is produced by a single well during 18 years. The initialization is identical in all the cases. At initial conditions the stress distribution is the same and the reservoir pore pressure starts at 45 MPa. The initial production rate is set to 6800 bbl/day.

6.1 Description of elastic parameters of the overburden in the different models

The overburden layers used in the models are based upon the geology of the overburden in the Valhall Field and their initial thicknesses of are based on the average thickness found in the south east flank of the Valhall Field. The models consist of 14 layers and they are distributed as shown in figure 6.1. From top to base, the first four layers correspond to the Nordland Group, the next two layers correspond to the Hordaland Group and the Rogaland Group (Balder, Sele and Lista) is represented by the last three layers. According to BP internal reports, when geomechanical models are used to predict the sea floor subsidence in the Valhall Field, special attention is paid of elastic parameters to the Rogaland Group in order to improve the results of the models. Given the apparent changes in the Rogaland Group, I am interested in understanding what occurs to the 4D seismic attributes when the elastic parameters of these formations are changed. For all models, the materials are assumed to have linear elasticity and therefore there are two parameters that control the stress/strain response: a) the Young's modulus (E) which is a measure of the stiffness of rock, i.e. the rock resistance against being compressed by a uniaxial stress, and b) the Poisson ratio (ν) which is a measure of lateral expansion relative to longitudinal contraction. The elastic parameters for the upper most 6 layers are kept identical for all the models and they are summarized in table 6.1. Layer 7 represents the Balder Formation and its thickness is 11 m, layer 8 represents the Sele Formation and has a thickness

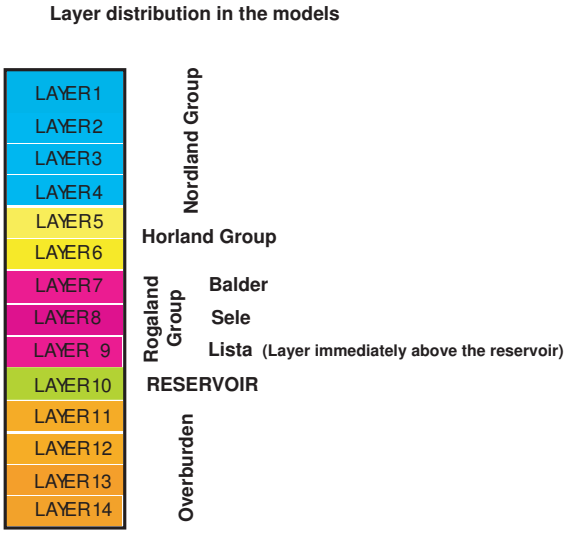

Figure 6.1: Layers distribution for the seven models.

of 9 m and layer 9 represents the Lista Formation and has a thickness of 22 m (figure 6.2). Through varying the elastic parameters of the three layers immediately above the reservoir (layers 7, 8, 9) and by keeping the same pressure depletion pattern I will attempt to understand the key elements that control the velocity changes in the overburden.

Table 6.2 summarizes the model parameters. The geomechanical parameters in model 1 are based on the results of several studies carried out in Valhall and Ekofisk Field (Kristiansen, 1998; Nagel, 1998b; Herwanger & Horne, 2005). In the other models, variations up to 13 % in the elastic parameters are considered. Extremely soft or weak overburden rocks have not been reported in the Valhall Field, therefore I considered that the models represent the type of rocks that can be present in the overburden of Valhall.

- Model 1 is considered the base case scenario. The three layers have the same elastic parameters ($\nu = 0.41$ and E =81000 KPa).
- Model 2: The three layers have different Young's modulus ($E_{layer_7} > E_{layer_8} > E_{layer_9}$) but the Poisson's ratios are the same as the ones used in model 1.
- Models 3 and 4: Investigate changing the Young's modulus for layer 9 only. In model 3, layer 9 is relatively weak ($E_{layer_7} = E_{layer_8} > E_{layer_9}$) and in model 4 layer 9 is relatively strong ($E_{layer_7} = E_{layer_8} < E_{layer_9}$).

- Models 5 and 6: Investigate the role of the Poisson's ratio but Young's modulus is kept the same as in model 1. In model 5, layer 9 has a relatively lower Poisson's ratio ($\nu_{layer_7} = \nu_{layer_8} > \nu_{layer_9}$). In model 6, layer 9 has a relatively larger Poisson's ratio ($\nu_{layer_7} = \nu_{layer_8} < \nu_{layer_9}$).
- Model 7: Layer 9 is described as a weaker material flanked on either side by a stronger material as shown in figure 6.4. The aim is to analyze the velocity response in layer 9, when E varies.

Layer 10 represents the reservoir and is identical for all the models. The reservoir characterization, including geomechanical and fluid properties, is the same as the model used in chapter 3. A detailed description of fluid properties is shown in table 3.2. The initial reservoir porosity varies from 35% up to 42% (figure 6.3) and to capture the rock compaction, I use two slope elastic behavior (section 3.1). Finally, layers 11 to 14 represent the underburden and for the purposes of the analysis, their geomechanical properties do not vary between models (table 6.1).

Layer	**Young Modulus (E)** 10^3 **Kpa**	**Poisson's ratio** (ν)
	Overburden	
Layer 1	80	0.4
Layer 2	80	0.4
Layer 3	80	0.4
Layer 4	60	0.4
Layer 5	92	0.43
Layer 6	60	0.4
	Under-burden	
Layer 11	60	0.18
Layer 12	60	0.18
Layer 13	200	0.3
Layer 14	200	0.3

Table 6.1: Linear elastic parameters for the upper 6 layers and the underburden used in the seven models.

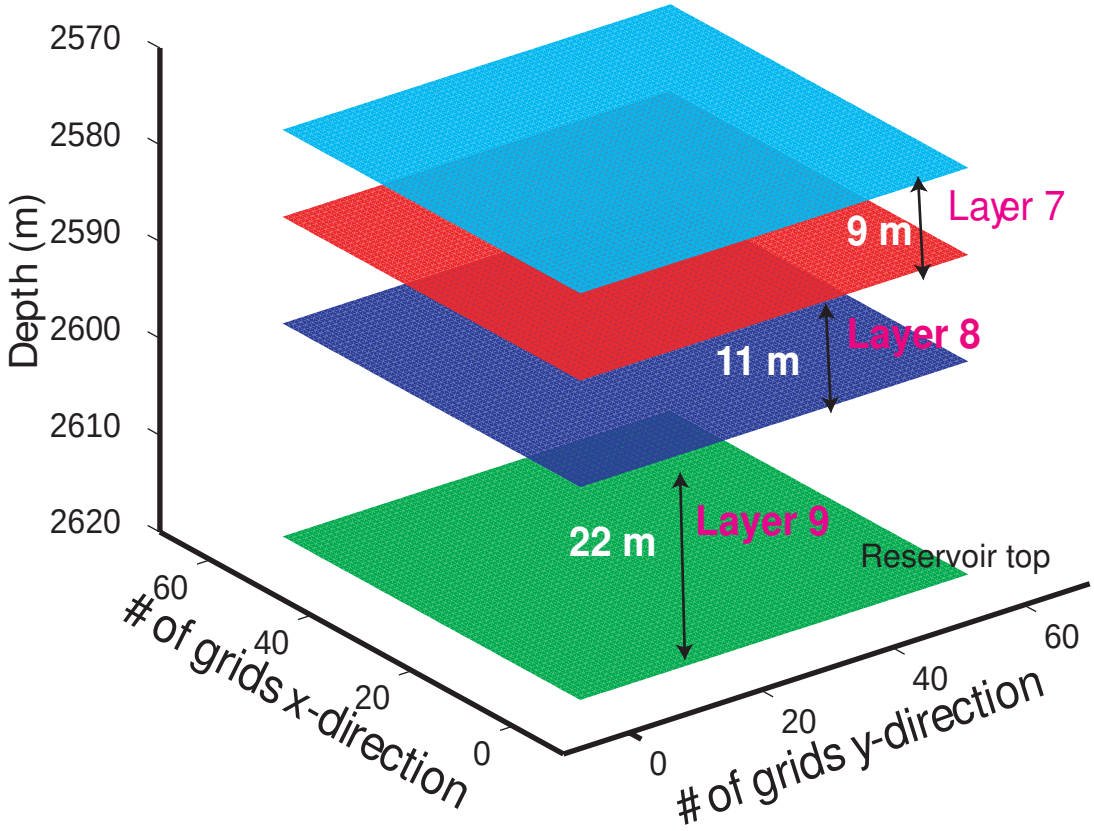

Figure 6.2: Thickness of layers 7, 8 and 9. The layers 7, 8 and 9 represent the Rogaland Group (Balder, Sele and Lista) in the Valhall Field.

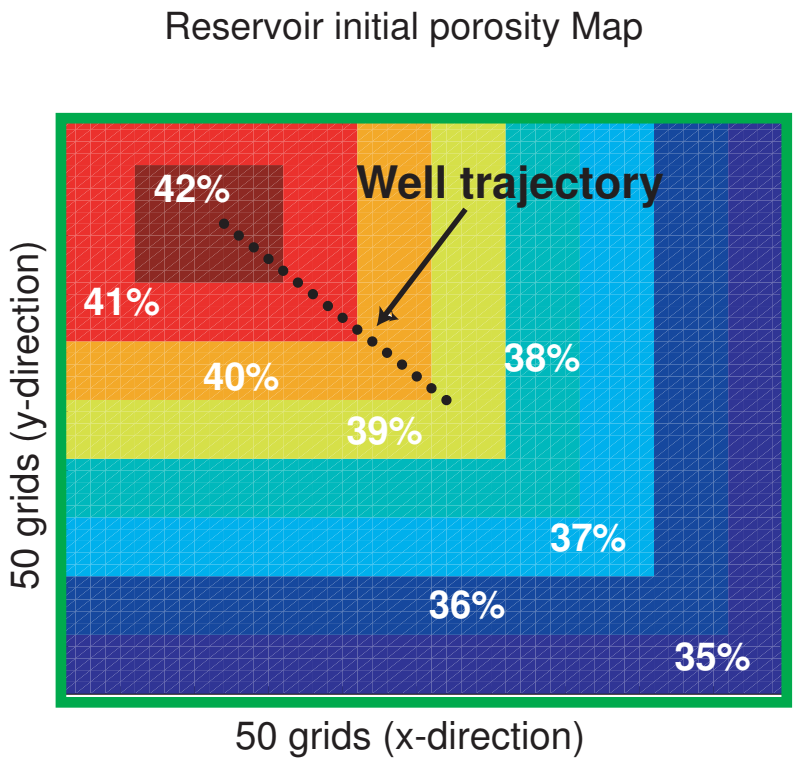

Figure 6.3: Initial reservoir porosity map used for the seven models.

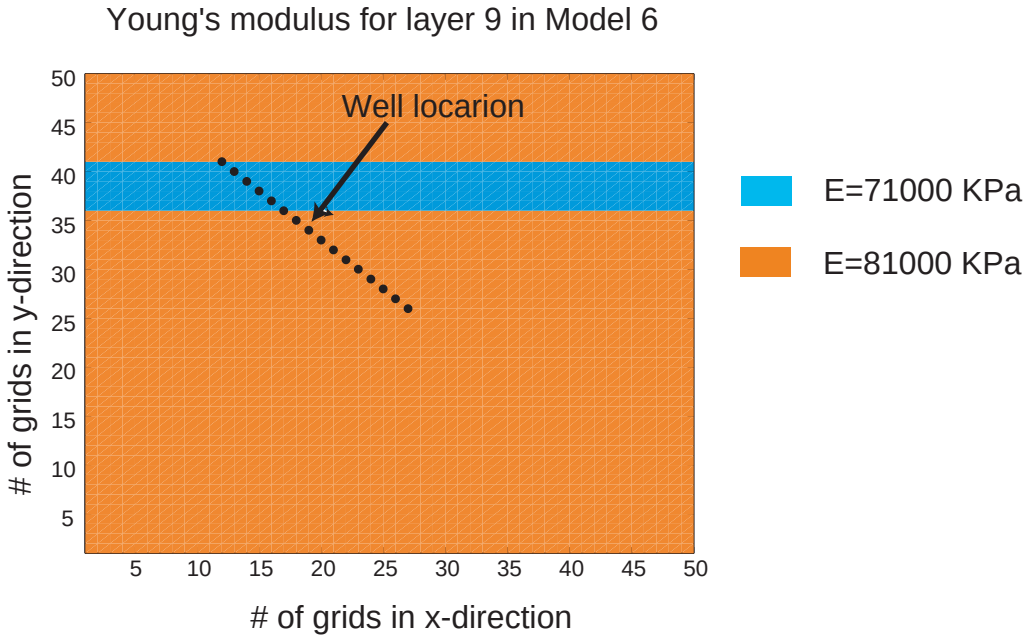

Figure 6.4: Young's modulus for Layer 9 in model 7 (map view). Layer 9 has one "strip" of lower strength material.

Model 1	**Young's modulus (E)** 10^3 **Kpa**	**Poisson's ratio** (ν)
Layer 7	81	0.46
Layer 8	81	0.46
Layer 9	81	0.46
Model 2	**Young's modulus (E)** 10^3 **Kpa**	**Poisson's ratio** (ν)
Layer 7	91	0.46
Layer 8	81	0.46
Layer 9	71	0.46
Model 3	**Young's modulus (E)** 10^3 **Kpa**	**Poisson's ratio** (ν)
Layer 7	81	0.46
Layer 8	81	0.46
Layer 9	71	0.46
Model 4	**Young's modulus (E)** 10^3 **Kpa**	**Poisson's ratio** (ν)
Layer 7	81	0.46
Layer 8	81	0.46
Layer 9	91	0.46
Model 5	**Young's modulus (E)** 10^3 **Kpa**	**Poisson's ratio** (ν)
Layer 7	81	0.46
Layer 8	81	0.46
Layer 9	81	0.41
Model 6	**Young's modulus (E)** 10^3 **Kpa**	**Poisson's ratio** (ν)
Layer 7	81	0.41
Layer 8	81	0.41
Layer 9	81	0.46
Model 7	**Young's modulus (E)** 10^3 **Kpa**	**Poisson's ratio** (ν)
Layer 7	81	0.46
Layer 8	81	0.46
Layer 9	E varies across the layer	0.46

Table 6.2: Linear elastic parameters for the models. Model 1 is considered the base case scenario. The elastic parameters in the other models vary up to 13 % respect to model 1.

6.2 Effect of the overburden elastic parameters on the reservoir pore-pressure, average normal stress and effective stress

Pore pressure depletion and the associated compaction produces a redistribution of stresses inside and outside of a reservoir. The response of the layers above the reservoir due to the changes in the stress field is controlled by the elastic parameters of these rocks. Also, the mechanical response that the surrounding rocks of a reservoir has due to hydrocarbon extraction, can have an impact on the

reservoir pressure depletion. Rothenburg et al. (1994) developed an analytical solution for coupling the well flow and the overburden deformation and showed that ignoring the mechanical properties of the surrounding rocks can lead to incorrect predictions regarding the reservoir production behavior. When a reservoir is depleted, the reservoir material tends to compact and the overburden reacts trying to reduce the reservoir compaction. The effectiveness of this reaction to prevent reservoir deformation depends on the relative stiffness of the reservoir in relation to the stiffness of the overburden. When an overburden is soft relative to reservoir, the constraining effect is negligible.

To compare the effect that the mechanical properties of the overburden has on the reservoir rock a series of profiles along the producer were generated for each one of the models. Changes in pore pressure, effective and normal average stresses together with vertical strain are shown in figure 6.5. The changes correspond to 18 years of production. Most of the profiles overlaid each other, indicating no major differences in the reservoir properties due to the variation in the geomechanical properties of the overburden layers. Model 2 is the only model with a different response. In model 2, the reservoir depletes more than the other models, producing changes in the pore pressure together with larger effective and normal average stresses (figures 6.5A, 6.5B, 6.5C). Each one of the layers representing the Rogaland Group in model 2 has a different Young's modulus. This is contrary to the other models which consider the Lista and Sele as one material and Balder is the only layer in which properties vary (table 6.2). In model 2, the paleocene section has a thickness of 42 m and the stiffness of the three layers decreases progressively towards the reservoir, while the Poisson's ratio is kept constant. This variation in the stiffness of the thick Rogaland Group (42 m) makes the cap rocks to "squeeze" the reservoir and increases the pressure depletion. For the other cases, the only layer whose elastic parameters changes, has a thickness of 22 m and it has low influence on the reservoir pressure depletion. Therefore, variations on the elastic parameters of the surrounding strata are influencing not only the land/sea floor subsidence but perhaps as well the pressure depletion mechanism in compacting reservoirs. It is important to have enough information to describe the overburden geomechanical response. This means not to confine the knowledge just about the formation immediately above the reservoir but include the whole surrounding rocks.

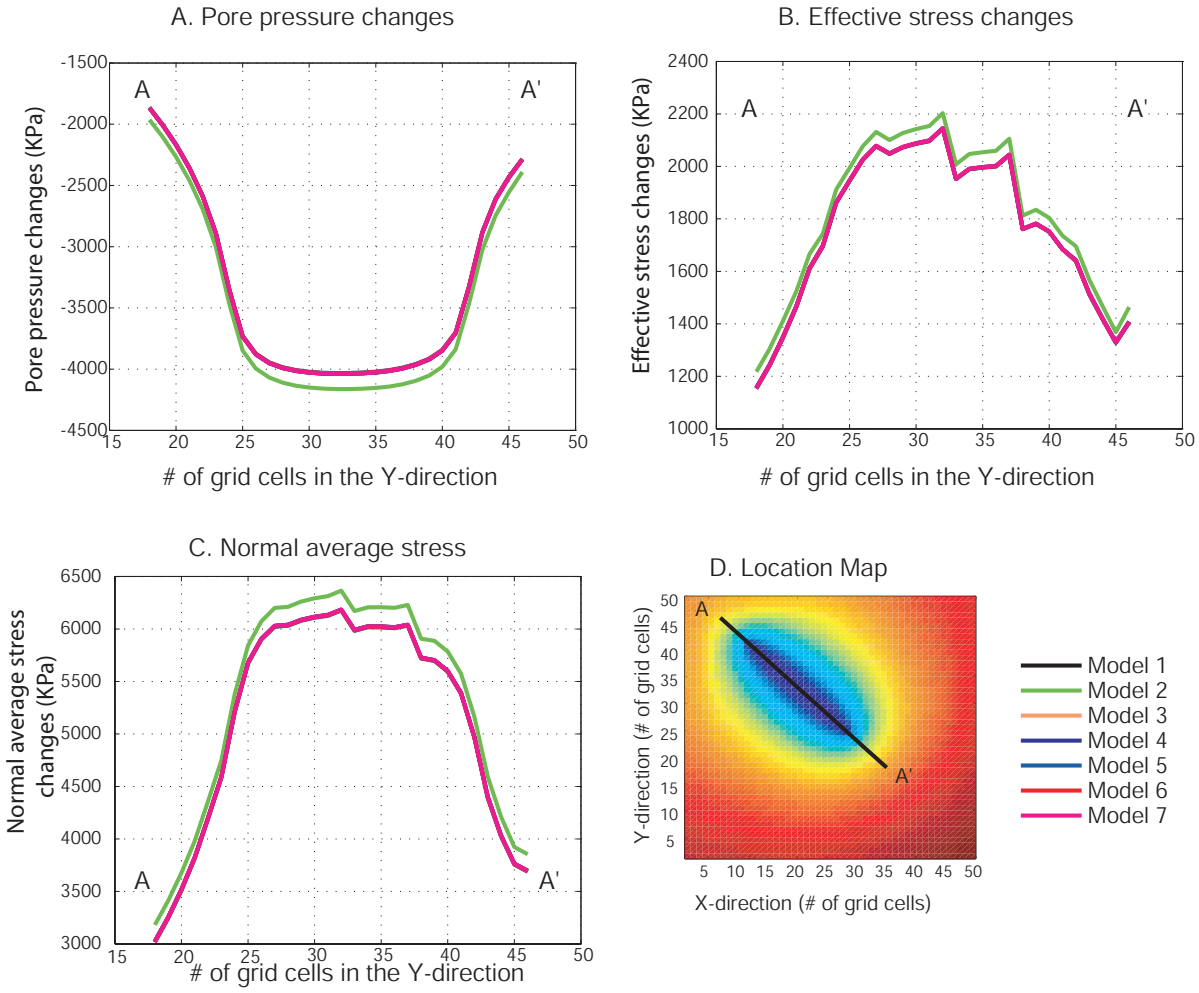

Figure 6.5: Variation of the pore-pressure, stress and strain after 18 years of production. A. Pore pressure changes along the producer well. B. Effective stress changes along the producer well. C. Normal Average stress along the producer well. D. Location of the producer well. Only model 2 is different, all the rest overlay each other.

6.3 Variations in vertical strain due to changes in Young's modulus of the layer immediately above of the reservoir

In this section, I compare the resultant vertical strain of four models where the Young's modulus in the layer immediately above the reservoir (layer 9) varies. Understanding the variations in the vertical strain is important because the changes in the P-wave velocity (υ) for the overburden have been defined as a function of the vertical strain (ε_z) as shown in equation 6.1 (Hatchell & Bourne, 2005).

$$\frac{\Delta\upsilon}{\upsilon} = -r * \varepsilon_z \tag{6.1}$$

Models 2 and 3 have the weakest materials (E=71 MPa) for layer 9; model 1 and 7 have intermediate strength material (E=81 MPa) and model 4 represents the strongest material (E=91 MPa). Figures 6.6A and 6.6B show two cross-sections taken from the models (figures 6.6C for location). Along each cross-section, the vertical strain after 18 years of production is plotted for each model. Both profiles show that the vertical strain increases as the Young's modulus decreases. Models 2 (red profiles) and 3 (blue profiles) undergo the largest deformation (i.e. largest vertical strain) in layer 9 since they have the lowest Young's modulus of all of the models. This implies that all else being equal, the largest P-wave velocity changes will occur in models 2 and 3. The profiles from models 1 (black profile) and 7 (orange profile) are similar. Layer 9 in model 1 has a Young's modulus is equal to 81 MPa while in model 7, the layer 9 is described as a weaker material (E=71 MPa) flanked on either side by stronger material (E=81 MPa) (figure 6.4). This explains why both models have very similar behavior but in some areas the layer 9 in model 7 deformed more than in model 1 (red circles in figure 6.6A). Finally, model 4 (green profile) has the largest Young's modulus of all of the models (E=91 MPa), and correspondingly has the smallest vertical strain and the minimum p-velocity change.

To further elucidate the difference between the models, I estimate the vertical strain change ($\Delta\varepsilon_{z_{modeln}}$) for layer 9 in models 2, 3, 4 and 7 relative to the vertical strain for layer 9 in model 1 ($\varepsilon_{z_{model1}}$) as shown by equation 6.2.

$$\Delta\varepsilon_{z_{modeln}} = \frac{\varepsilon_{z_{modeln}} - \varepsilon_{z_{model1}}}{\varepsilon_{z_{model1}}} \tag{6.2}$$

Model 1 is considered the base case scenario since the Rogaland Group (layers 7, 8 and 9) is rep-

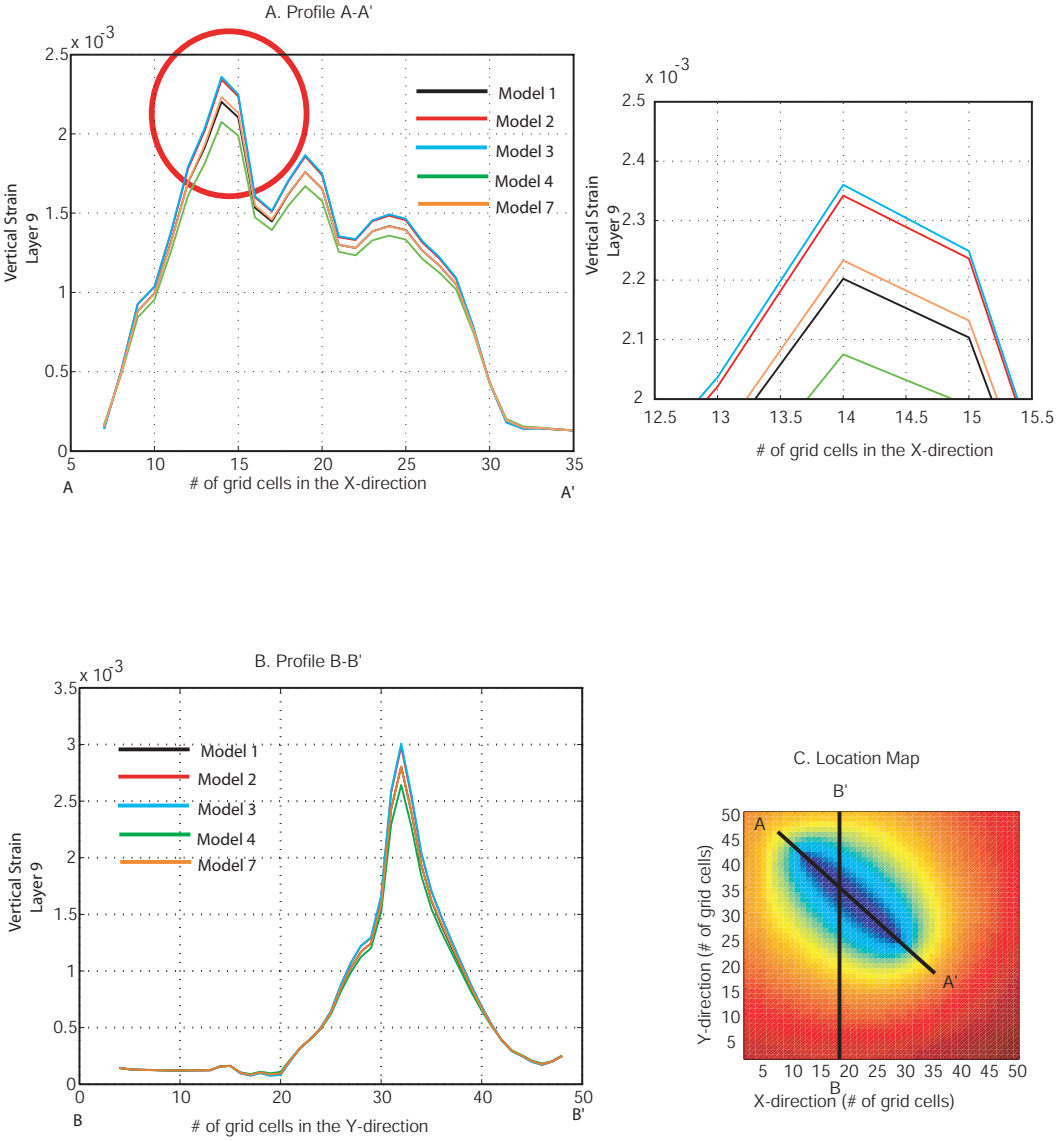

Figure 6.6: The effect of the Young's modulus in the vertical strain. A. Vertical strain along profile A-A'. B. Vertical strain along profile B-B'. C. Location of the profiles. The models with the weakest materials for layer 9 (models 2 and 3) undergo the greatest vertical strain.

resented by a single material (table 6.2). Figure 6.7 shows $\Delta\varepsilon_{z_{modeln}}$ after 18 years of production along the profile A-A'. This cross-section is parallel to the producer well (figure 6.6C) and the area between the head and the toe of the well is marked with red arrows in figure 6.7. The largest vertical strain changes occur in model 3 (blue line), where the layer 9 has the lowest E and the layers 8 and 7 are kept as the same as model 1. This means that decreasing the Young's modulus by 13% causes an increase in the vertical strain of 5%. Model 2 (red line) is characterized by the decrease of the stiffness of layers 7,8 and 9 with depth (i.e. $E_{layer_7} > E_{layer_8} > E_{layer_9}$). Even though model 2 and 3 have the same elastic parameters for layer 9, having a stronger layer 7 in model 2 generates a smaller $\Delta\varepsilon_{z_{model2}}$ than $\Delta\varepsilon_{z_{model3}}$. Model 7 shows very similar vertical strain to model 1, (i.e. $\Delta\varepsilon_{z_{model7}}$ is close to zero). For most of the parts along the profile the Young's modulus for layer 9 is the same in both models. However, there are areas where the material is weak in model 7 (red circle) causing the vertical strain changes.

For a linear elastic material, the vertical deformation not only depends on the elastic parameters but also on how the reservoir is been depleted. For all the models, there is a single producer that undergoes pure pressure depletion. From this is a simple scenario where there is no influence of other producers or the structure and where the only parameter varying is the Young's modulus, the following observations can be made:

- A lower Young's modulus results in a greater vertical strain and viceversa. The Young's modulus was decreased by 13% in model 3 and was increased by same amount in model 4. The changes in vertical strain for both models was of 5 % relative to model 1. Both profiles have similar shape but with oppositive sign. This shows that it is possible to have different vertical strain response (i.e. different P-wave velocity change) in the layer immediately above of a reservoir if the Young's modulus of that layer is different but the reservoir has the same porosity and undergoes the same pressure depletion pattern.

- Varying the Young's modulus of the layers above layer 9 has an effect on the vertical strain in layer 9. In other words, the vertical strain on the layer immediately above the reservoir is not only controlled by its own elastic parameters and the reservoir stress path but also by the elastic parameters of the surrounding layers.

- The vertical strain on a material is also controlled by the Young's modulus lateral variation on the material. Comparing models 3 and 7, it is observed that the vertical strain of a weak

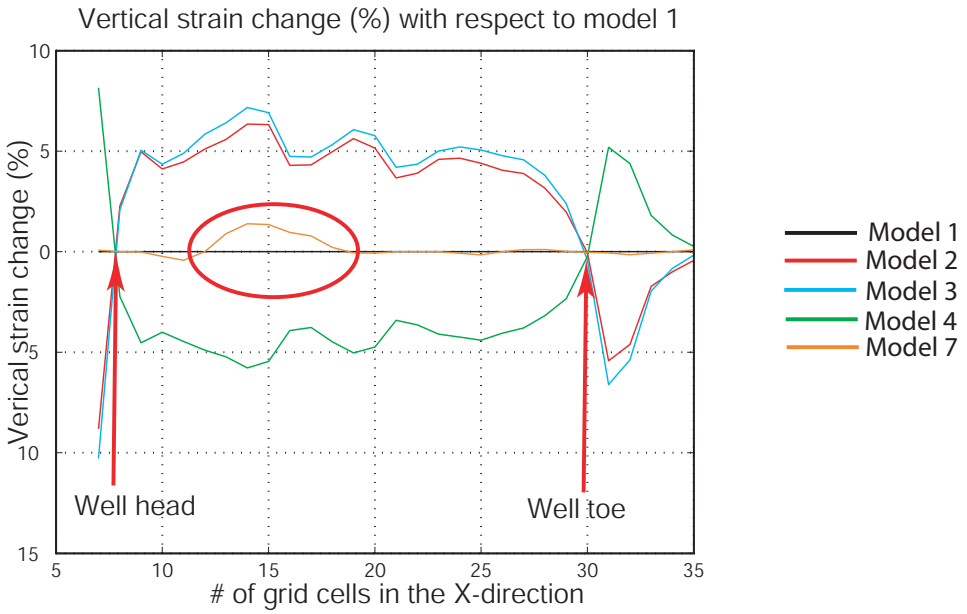

Figure 6.7: Vertical strain changes in the models relative to the vertical strain in model 1 for layer 9. The increase (model 4) or decrease (model 2) of the Young's modulus by 13% with respect to model 1 produce a change in vertical strain of 5 % relative to model 1.

material (model 2) is larger than the vertical strain of the same weak material embedded in a strong material (model 7).

6.4 Variations in the vertical strain due to changes in Poisson's ratio of the layer immediately above of the reservoir

Poisson's ratio (ν) is the ratio of the strain in the normal direction to the applied load, divided by strain in the direction of the applied load (axial strain). This means that when a material is compressed in one direction, it tends to expand (or rarely, contract) in the other two directions; Poisson's ratio measures this tendency. In this section, I quantify changes in the vertical strain of layer 9 due to either increase or decrease of the Poisson's ratio. I compare the vertical strain outputs of models 1, 5 and 6. Model 1 has the same Poisson's ratio for layers 7, 8 and 9; model 5 uses a lower Poisson's ratio for layer 9 and model 6 has a lower Poisson's ratio for layer 7 and 8. A series of profiles are shown in figure 6.8. They represent the vertical strain for layer 9 at different sections through the models. A comparison between figures 6.8A and 6.6A, shows that the largest vertical

strain corresponds to model 5 (red line) in figure 6.8A. This indicates that decreasing the Poisson's ratio by 10 % deforms more layer 9 more than decreasing or increasing Young's modulus by 13 % as in models 3 and 4. Examining the profiles from models 1 and 6 in figure 6.8, shows that the effect of having a lower Poisson's ratio for layers 7 and 8 (model 6) does not significantly influence the vertical strain in layer 9 (i.e. the vertical strain from both models is nearly identical).

As in section 6.3, I estimate the vertical strain change ($\Delta\varepsilon_{z_{modeln}}$) for layer 9 in models 5 and 6 relative to the vertical strain for layer 9 in model 1 ($\varepsilon_{z_{model1}}$) as shown by equation 6.2. Figure 6.9 shows $\Delta\varepsilon_{z_{modeln}}$ after 18 years of production along the profile A-A'. This cross-section is parallel to the producer well (figure 6.8E) and the area between the head and the toe of the well is marked with read arrows in figure 6.9). The largest vertical strain changes occur in model 5 (green line), where the layer 9 has the lowest Poisson's ratio. This means that decreasing the Poisson's ratio by 10% causes an increase in the vertical strain of 38%. Model 6 (orange line) is characterized by lower Poisson's ratio for layers 7 and 8 which decreases the vertical strain less by 5 %.

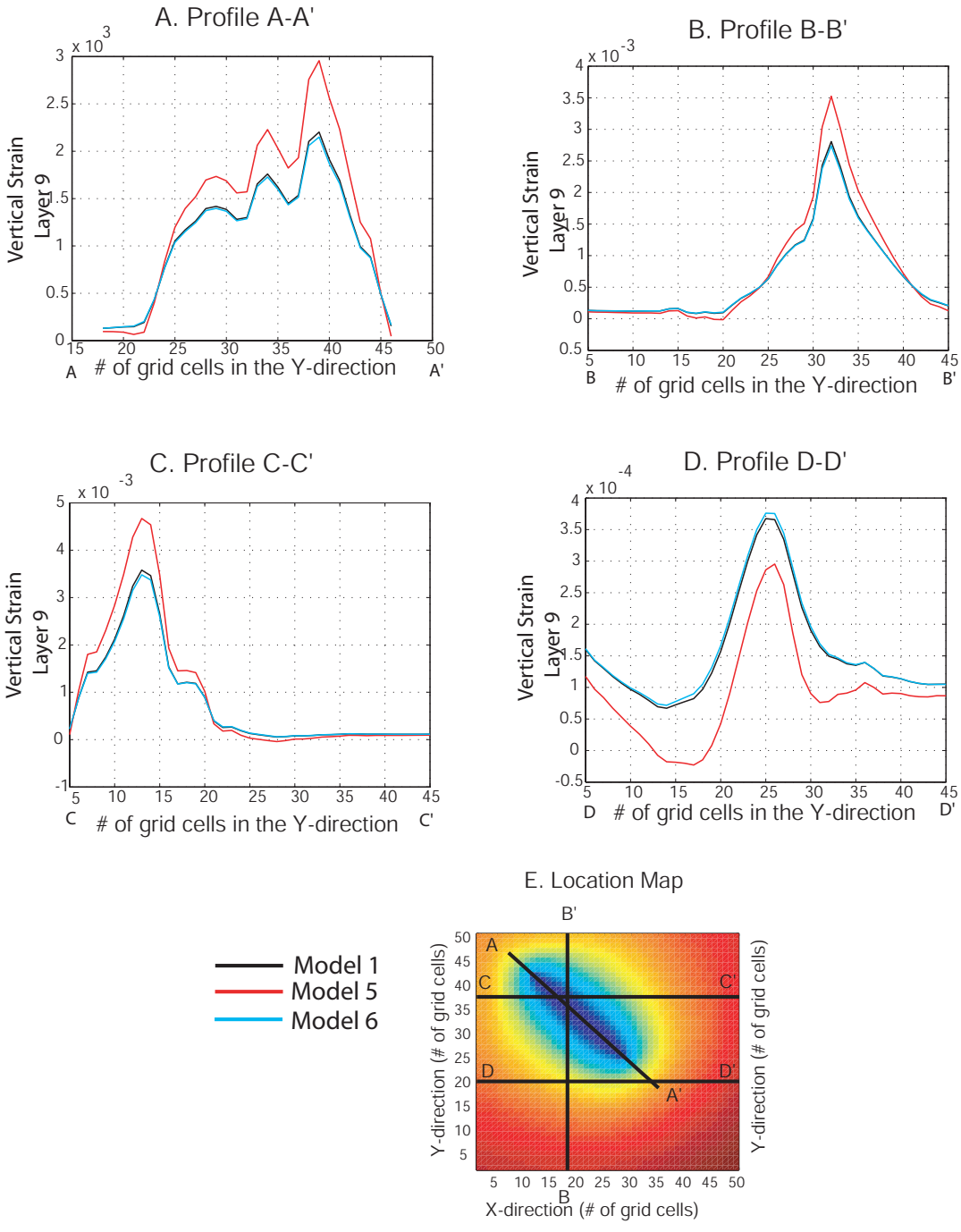

Figure 6.8: The effect of the Poisson's ratio in the vertical strain for layer 9. A. Vertical strain along profile A-A'. B. Vertical strain along profile B=B'. C. Vertical strain along profile C-C'. D. Vertical strain along profile D-D'. E. Location of the profiles. The largest changes in the vertical strain are observed in model 5.

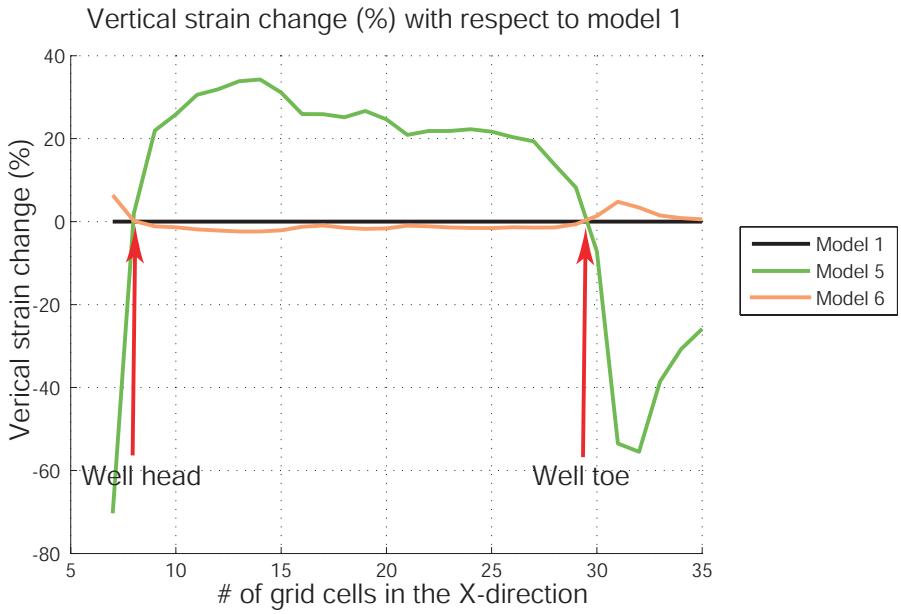

Figure 6.9: Vertical strain changes in the models relative to the vertical strain in model 1 for layer 9. The largest vertical strain changes occur in model 5.

6.5 4D seismic amplitudes and variations in the overburden elastic parameters

The previous sections have investigated the role of Young's modulus and Poisson's ratio in determining the vertical strain in the layer immediately above the reservoir. In this section I investigate the role that these two parameters have on the 4D amplitude response. In previous chapters I have calibrated the 4D amplitude to the pore pressure changes and initial porosity. Therefore if the 4D amplitude is highly influenced by the overburden response, the pore pressure predictions from such calibration will have an associated error.

6.5.1 Generation of the synthetic seismic for each of the models

The same methodology explained in chapter 3 was used to generate synthetic seismograms. After running the iterative coupled fluid flow and geomechanics simulation for each one of the 7 models, the outputs from the simulation (pressure changes, effective stress changes and strain) were used to determine the P-wave velocity and density for the reservoir and overburden rock.

The reservoir acoustic impedances were calculated by a conventional fluid substitution using the combination of Gassmann equation and fluid property correlations proposed by Batzle and Wang (1991).

The overburden P-wave velocities were calculated as a function of vertical strain as shown in eq. 6.1 (Hatchell & Bourne, 2005). The R-factor is a parameter that dictates how sensitive is the velocity changes to the vertical strain. A R-factor equal to 5 was used (Hatchell & Bourne, 2005). All of the models have the same acoustic impedance for overburden and reservoir at initial conditions.

Finally, synthetic seismic volumes for the different times were created using a convolutional model. The input wavelet used to convolve with the reflectivity series, was extracted from the LoFS data. Seismic data are generated for a pre-production state (baseline volume) and after 2, 4, 6, 8 and 10 years of production (monitor volumes).

Figures 6.10A and 6.10B show the percentage changes in P-wave velocity for the layer 9 and the reservoir after 18 years of production along the producer. In general, it is observed that the largest velocity changes occur at the reservoir due to the pore pressure depletion and porosity reduction. Therefore the resultant 4D amplitude is most strongly influence by reservoir pressure and initial porosity. In general for the seven models, the P-wave velocity changes in the reservoir are very similar indicating that the pressure and porosity changes are very close between the models. However the P-wave velocity changes in layer 9 vary from model to model because the vertical strain is different in each of the models. Furthermore, the greatest velocity changes in layer 9 occur in model 5. This model has the lowest Poisson's ratio for layer 9 and undergoes the largest vertical strain. However, the greatest velocity changes in the reservoir come from model 2. The P-wave velocity in the reservoir depends on the pore-pressure and the effective stress. In model 2 (red), these two parameters vary slightly in comparison with the rest of the models because layers 7 and 8 are stiffer. Figure 6.11 shows two seismic traces extracted at certain location along the well for model 2. The seismic trace prior production is in blue and the seismic trace after 14 years of production is red. As shown in the figure, the reflectivity response at the reservoir level is a trough-peak doublet for all the models. The trough is correlated with the top of the reservoir because the wavelet crosses from a high acoustic impedance media (layer 9) to a low acoustic impedance media. The base is identified by a strong peak, as a result of the acoustic impedance increase at layer immediately below the reservoir (layer 11). However the trough at the top of the reservoir decreases with time. This means that the contrast between the

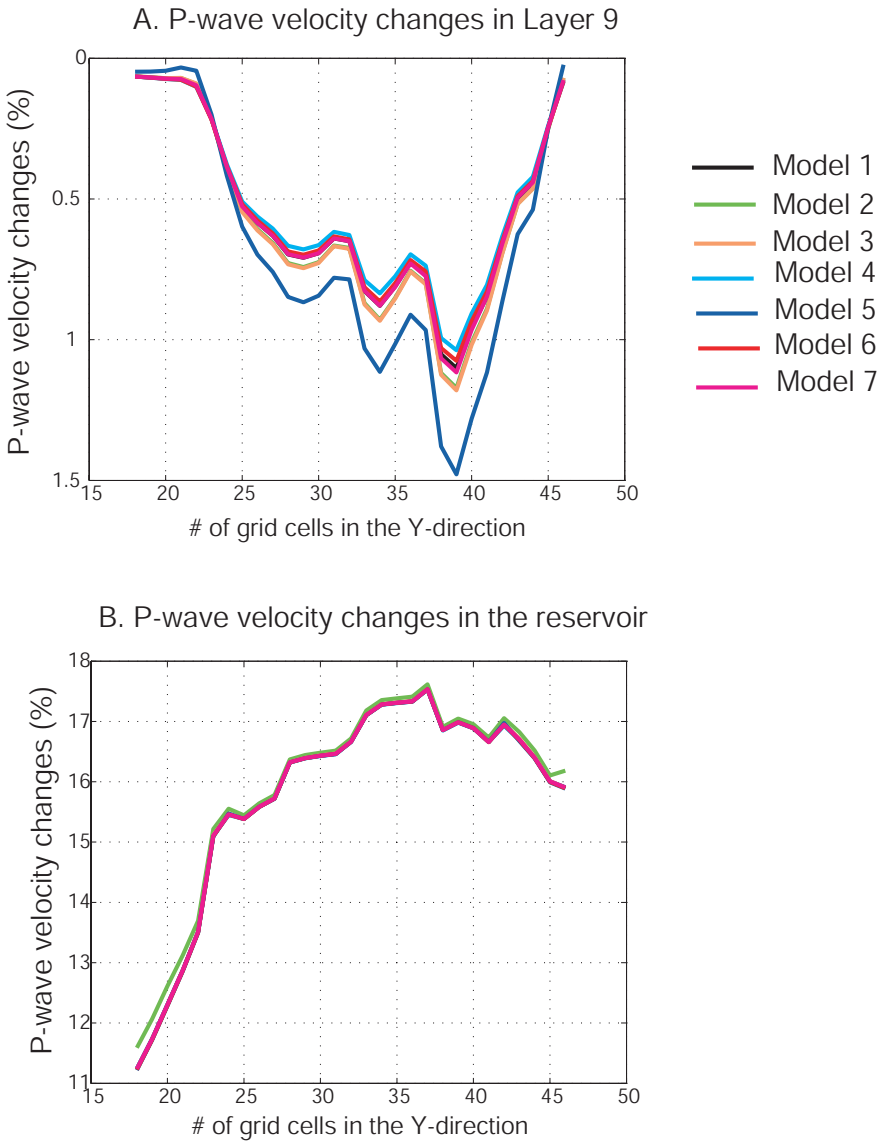

Figure 6.10: P-wave velocity changes in the reservoir and the layer immediately above the reservoir. A. P-wave velocity changes in the layer immediately above the reservoir (layer 9). B. P-wave velocity changes in the reservoir.

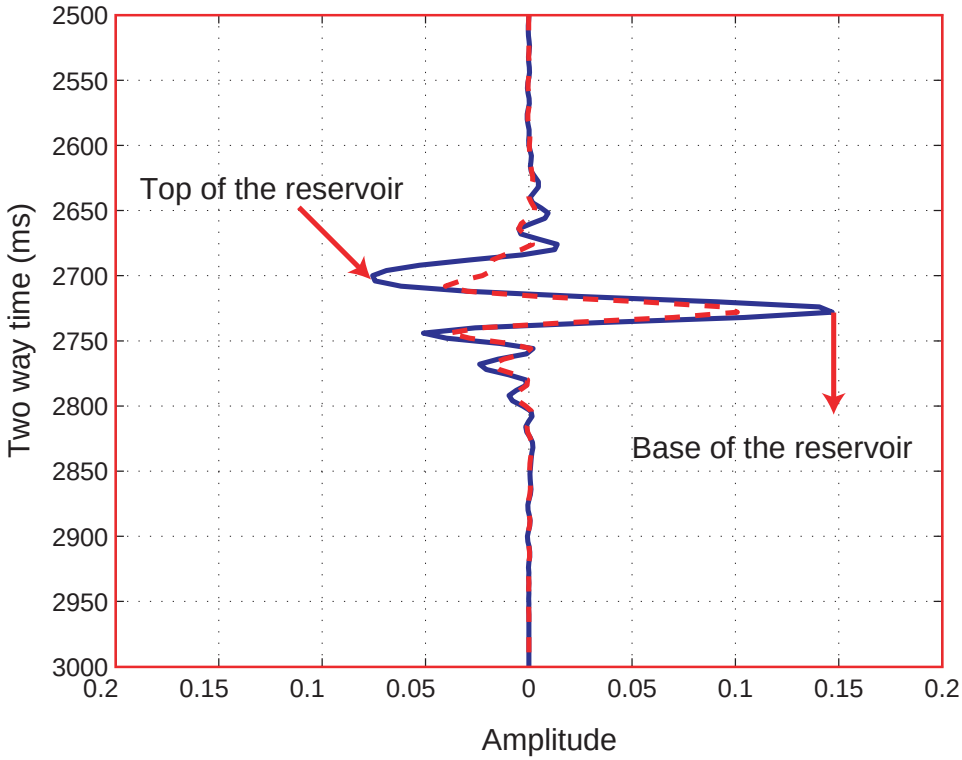

Figure 6.11: Example of the time-lapse response observed in the models. The reflectivity response is a trough at the top of the reservoir. This trough decreases through time due to the velocity decrease in layer 9 and the velocity increase in the reservoir. The same response is observed for all the models.

acoustic impedance of layer 9 and the reservoir decreases during production. After pressure depletion and rock compaction occurs, the layer 9 P-wave velocity decreases as a function of strain while the P-wave velocity and density in the reservoir increase. This makes the acoustic impedance in layer 9 decrease and the acoustic impedance in the reservoir increase, therefore the trough becomes more positive. When the difference volumes are created, the 4D signal at the reservoir level is a peak. Therefore, to map the time-lapse amplitude signature, a similar approach to the one adopted in chapter 3 to generate 4D amplitude attributes is used. The largest positive amplitude is extracted in a window of 35 ms.

6.5.2 Comparison of the 4D amplitude response between the models

Figure 6.12 shows the Largest Positive Value attribute along the producer for all of the models. The seismic volume at initial conditions is the baseline survey and the monitor one is the seismic

volume after 18 years of production. Since model 2 has the largest pressure drop of all of the models, its largest 4D amplitude response is not because the P-wave velocity changes in layer 9 but to the variations in the P-wave velocity and density in reservoir. Figure 6.13 shows the amplitude change (ΔA_{modeln}) at the top of the reservoir in all of the models relative to the amplitude changes in model 1 (ΔA_{model1}) as shown by equation 6.3. Except for model 2 (red), the variation in the 4D amplitude response in each model relative to model 1 is considered to be the result of the acoustic impedance changes layer 9. Model 5 (light blue) exhibits the second largest change in 4D amplitude after model 2. The main reason for having a different 4D amplitude response between models 5 and 1 is a lower Poisson's ratio for layer 9 in model 5. This means that decreasing the Poisson's ratio by 10% varies the 4D amplitude by less than 2 % around the producer. The amount of change in the 4D amplitude in models 3 (green) and 4 (orange) are correlated with the variations in the Young's modulus. Decreasing or increasing the Young's modulus by 10 % seems to have minimum impact of the 4D amplitude (less than 1 % changes) in these models.

$$\Delta A_{modeln} = \frac{A_{modeln} - A_{model1}}{A_{model1}} \tag{6.3}$$

6.5.3 Effect of the R-factor on the 4D amplitude response

One key parameter is the R-factor or the sensitivity of P-wave velocity changes to vertical strain. This parameter is relatively poorly constrained. For the overburden layers in the North Sea, the R-factor has been studied by several authors (Stables *et al.*, 2007; Hatchell & Bourne, 2005; Janssen *et al.*, 2006) and values from 1 up to 10 have been proposed for the fields in the North Sea (table 2.1). A R-factor equal to 5 was used for all of the seven models, however it is possible that the R-factor is higher or even varies depending on the overburden material across the field. If this is the case, greater 4D amplitude changes due to overburden properties could be expected. To investigate this uncertainty, I re-estimated the 4D amplitude changes for models 1 and 5 using R-factor equal to 15. Figure 6.14 compares these results between the 4D amplitudes. There are four profiles, model 1 with R-factor equals 5 (red), model 5 with R-factor equals 5 (green), model 1 with R-factor equals 15 (black) and model 5 with R-factor equals 15 (blue). Varying the R-factor from 5 to 15 significantly increases the 4D amplitude. The black arrows indicates a zone in the reservoir where the initial porosity and pressure depletion are the same for the four cases. However, the 4D amplitude response

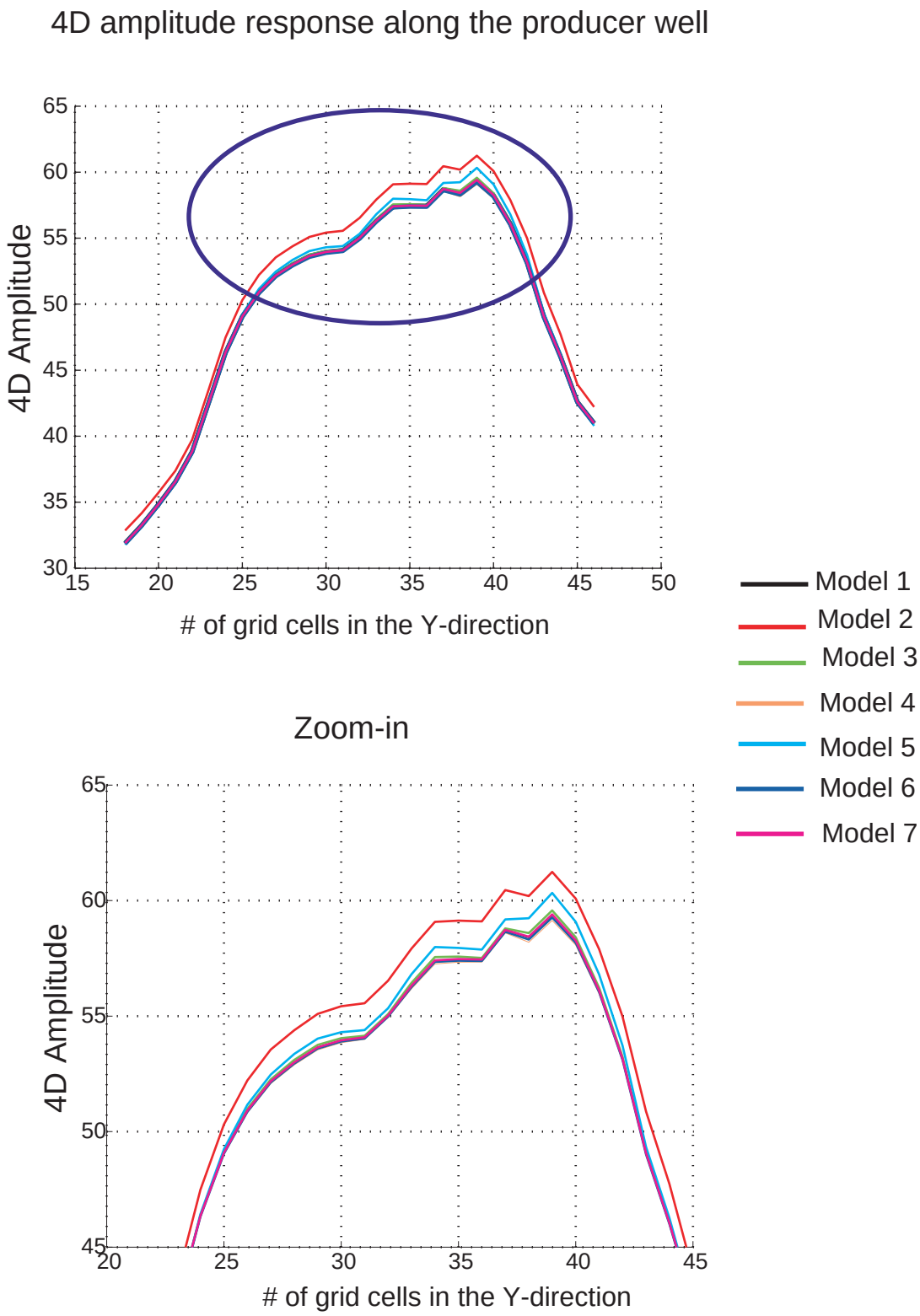

Figure 6.12: 4D amplitude response at the top of the reservoir. The amplitude changes correspond to 18 years of production.

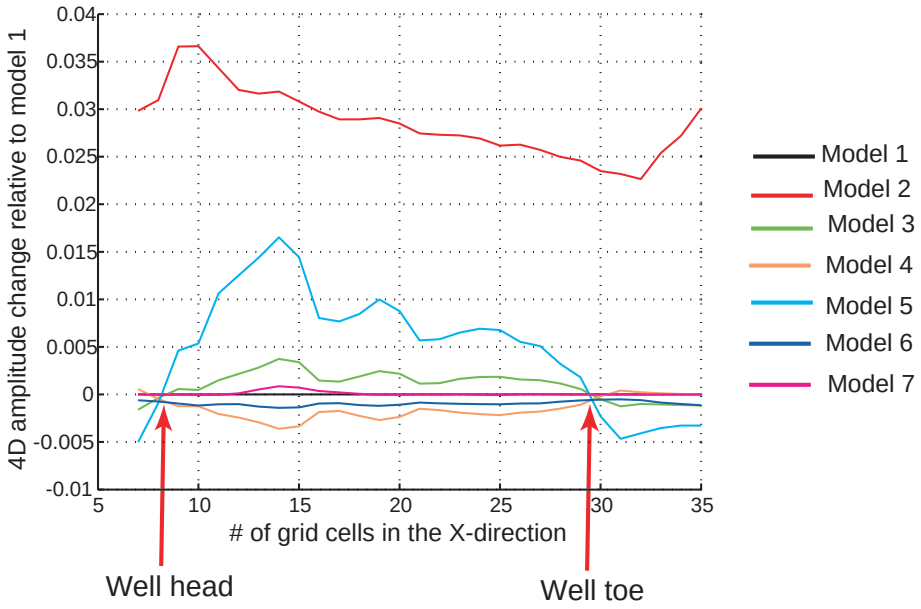

Figure 6.13: 4D amplitude changes in the models relative to the 4D amplitude in model 1.

is different; when the R-factor is 15, the amplitude changes are larger since the P-wave velocity in layer 9 are more sensitive to the vertical strain.

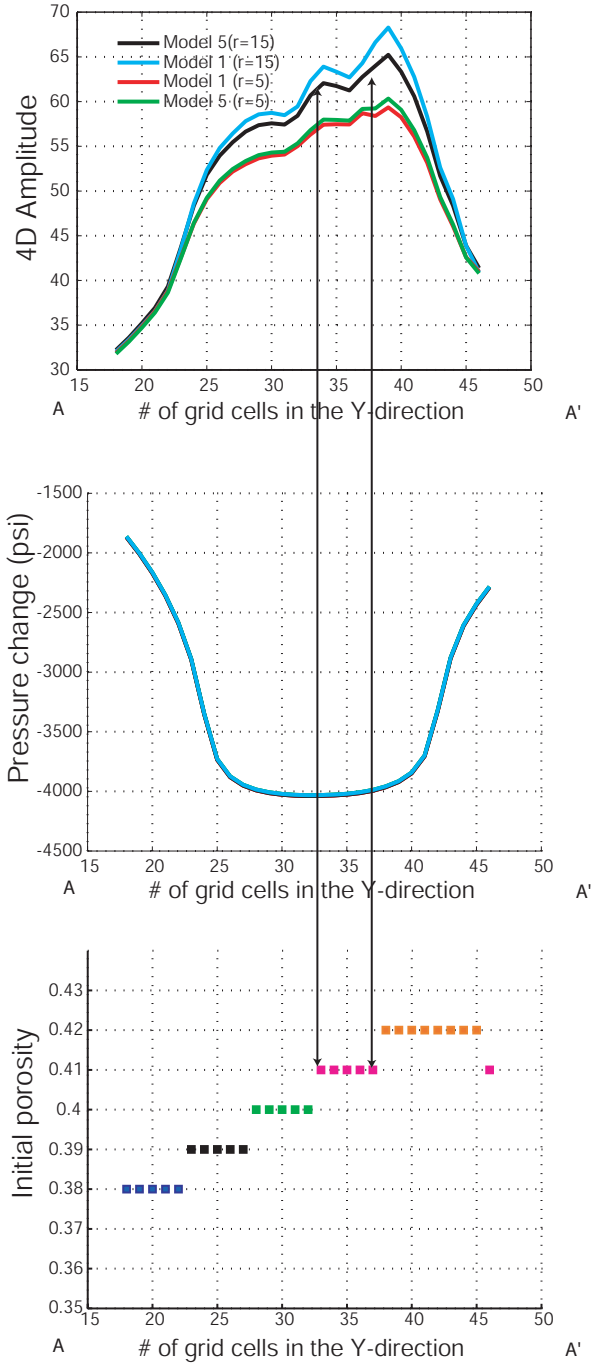

Figure 6.14: 4D amplitude response due to different R-factors. The section is along the producer well. The 4D amplitude response is different in zones where the initial porosity and pressure depletion are the same. When the R-factor is equal to 15, the amplitude changes are larger than the ones when the R-facto is equal to 2.

6.6 Effect of the overburden elastic parameters on the time-shift attribute

In this section, I first examine the effect of the Young's modulus and Poisson's ratio on the time-shift attribute, using the seven models previously described. Subsequently, I discuss the effect of using different R-factors (5 and 15) on the time-shift and finally I compare 4D amplitude and time-shift from the seven models. Time-shift occurs due to physical movement of the reflectors and the changes in p-velocities. Therefore, it will be affected by the velocity changes in the overburden. The time-shifts are an accumulative response of the changes occurring the overburden (velocity changes and subsidence) while the 4D amplitude response is only due to the changes in the reservoir and the layer immediately above.

Figure 6.15 shows the time-shifts calculated for all of the models along the producer well. For all of the cases, the time-shifts appear identical. The largest time-shift change observed is less than 1 ms. Therefore, varying the Young's modulus and the Poisson's ratio up to 10 % in the layer 9 has very little influence in the time-shift.

A comparison between figures 6.15 and 6.12 suggests that 4D amplitude is more influenced by the variation in the Young's modulus or Poisson ratio than the time-shifts. This observation is quantified by computing the relative changes in 4D amplitude and time-shift for two grid cells in the models using equations 6.3 and 6.4 respectively. The two grid cells are located along the well but the first data set of points correspond to the grid cell in the middle of the well where the maximum pressure depletion occurs and the second one is from a grid cell with initial porosity of 42% (points A and B in figure 6.16). The results are summarized in table 6.3.

$$\Delta TS_{modeln} = \frac{TS_{modeln} - TS_{model1}}{TS_{model1}} \tag{6.4}$$

If I ignore the changes in 4D amplitude and time-shift from model 2 since they are related with higher pressure depletion at the reservoir, the second largest changes are related to the 4D amplitude and associated with model 5. As has been discussed before, this model has a Poisson's ratio 10% smaller than the Poisson's ratio in model 1. This suggests that even though the time-shift attributes are entirely dependent on deformation of the overburden and its velocity changes, small variations on

Highest pore pressure depletion (Point A in figure 6.16)			
Model	Description	Max.4D Amp change (%)	Max. Time-shift (%)
2	E_{L7} is higher(26%), E_{L8} is equal(0%), E_{L9} is lower(13%)	2.74	-0.39
3	E_{L9} is higher (13%)	0.11	-0.31
4	E_{L9} is lower (13%)	-0.15	0.001
5	ν_{L9} is lower (10%)	0.56	-0.37
6	ν_{L7} & ν_{L8} is lower (10%)	-0.08	-0.222
Initial porosity = 42 % (Point B in figure 6.16)			
Model	Description	Max. 4D Amp change (%)	Max. Time-shift (%)
2	E_{L7} is higher(26%), E_{L8} is equal(0%), E_{L9} is lower(13%),	3.18	-0.31
3	E_{L9} is higher (13%)	0.37	-0.19
4	E_{L9} is lower (13%)	-0.36	0.083
5	ν_{L9} is lower (10%)	1.8	0.032
6	ν_{L7} & ν_{L8} is lower (10%)	-0.14	0.052

Table 6.3: Summary of the changes in 4D signal (amplitude and time-shift) for the different models relative to model 1. The data were extracted at the maximum pressure depletion and the largest initial porosity (figure 6.16)

the elastic parameters of the layer immediately above the reservoir have minimum or zero impact on the time-shifts.

Comparing the 4D amplitude and the time-shift when different R-factors are used, indicates that both attributes are considerably affected by this parameter. Figure 6.17 shows the time-shift (top graph) and the 4D amplitude (bottom graph) along the well for model 5 when R-factors are equal to 5 (red line) and 15 (black line) are used. Both attributes are affected by the R-factors and the variations in the time-lapse attributes are not homogenous along the well; for instance neither the two 4D amplitude profiles nor the two time-shift profiles are parallel to each other. However, the time-shift attribute is more influenced by increasing the R-factor. Figure 6.18 shows the percentage change in 4D amplitude (top graph) and time-shift (bottom graph) when R-factor is equal to 15 relative to the case when the R-factor is equal to 5. The largest changes are associated to the time-shift. For instance at grid cell 14 (red arrow on the graphs), if a R-factor of 15 is used instead of 5, the time-shift attribute increases by 172 % while the 4D amplitude only increases by 13 %.

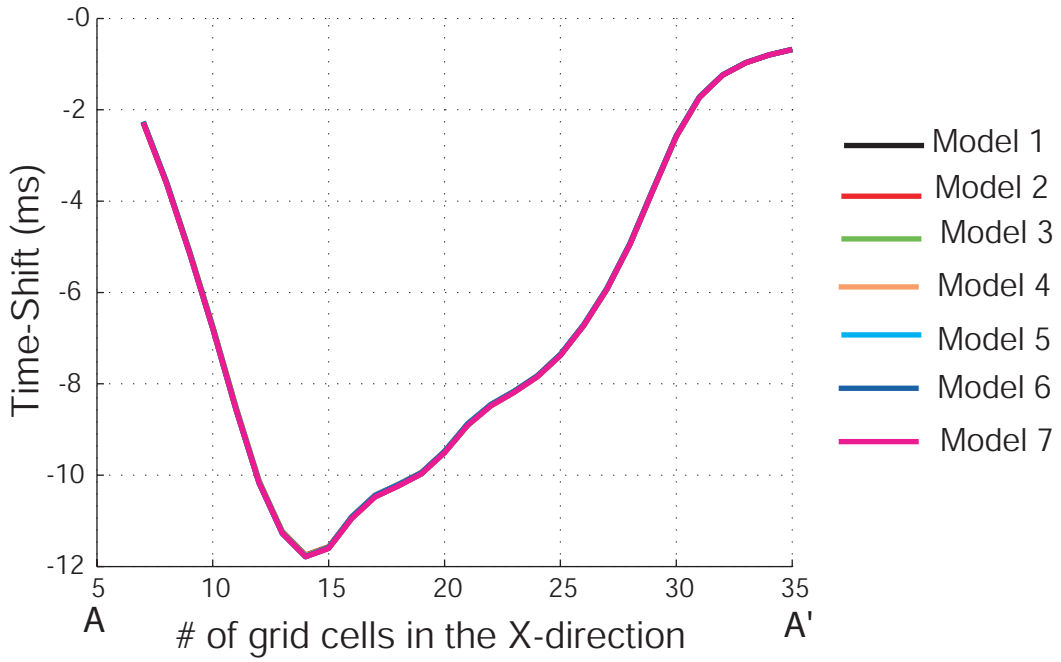

Figure 6.15: The time-shift attribute for the seven models. A. The time-shift attribute for the seven models. The profile is along the producer. The variations in the time-shift due to changes in either the Poisson's ratio or Young's modulus are undetectable (less than 1 ms).

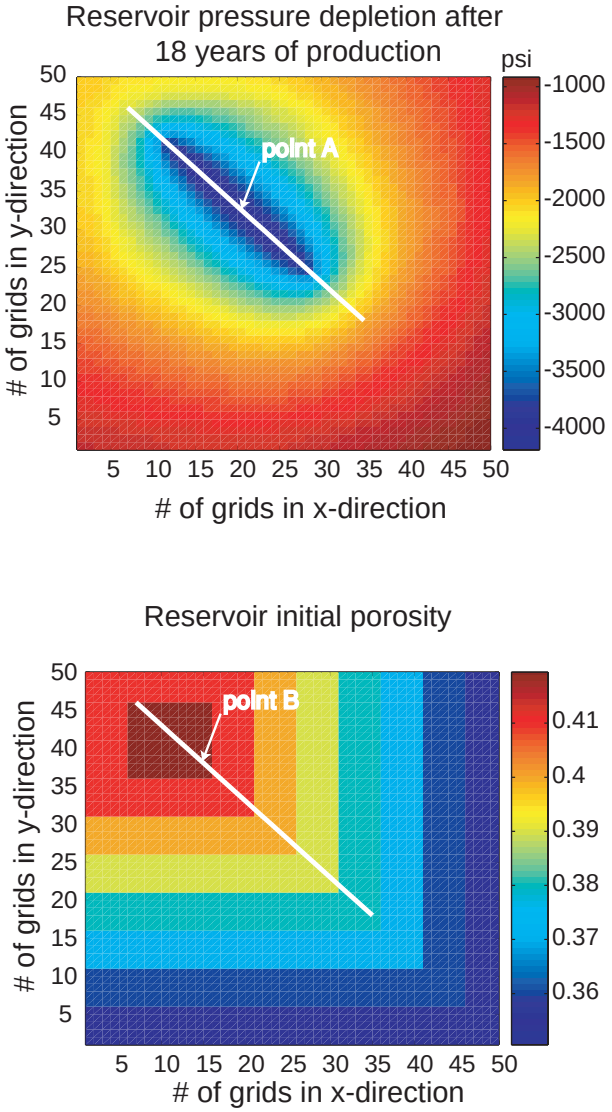

Figure 6.16: Location of the data points used in table 6.3. Point A is located in the middle of the well where the maximum depletion occurs and point B is located where the initial porosity is equals to 42%.

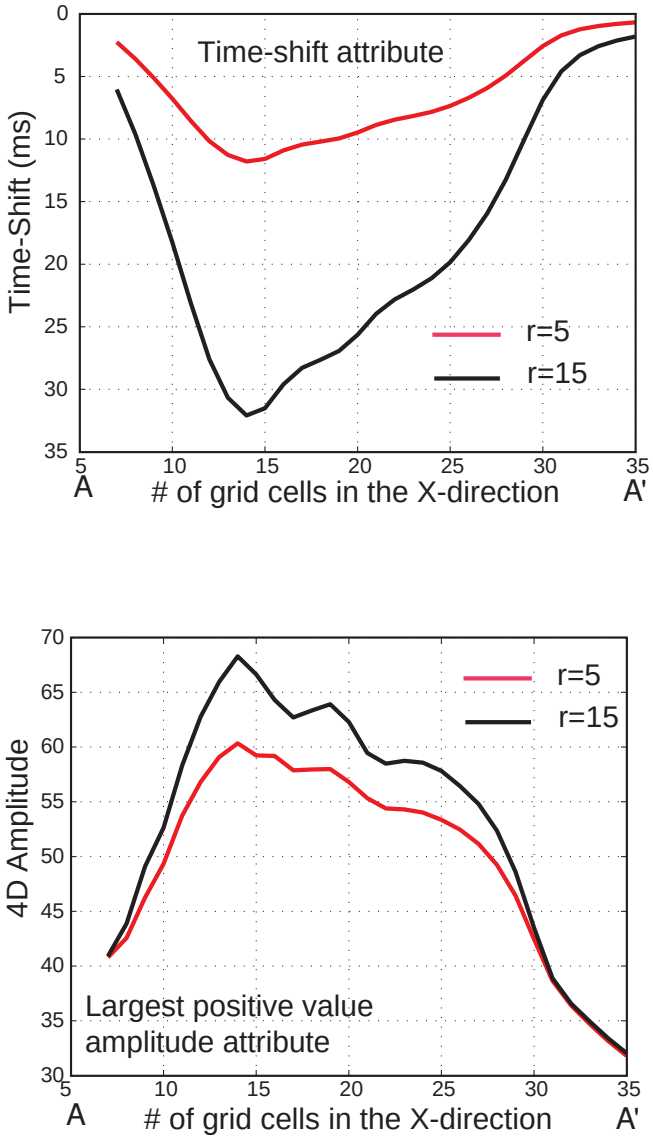

Figure 6.17: 4D attributes using different R-factors for model 5. A. Time-shift attribute for two R-factors. B. 4D amplitude for two R-factors. The profiles are along the producer.

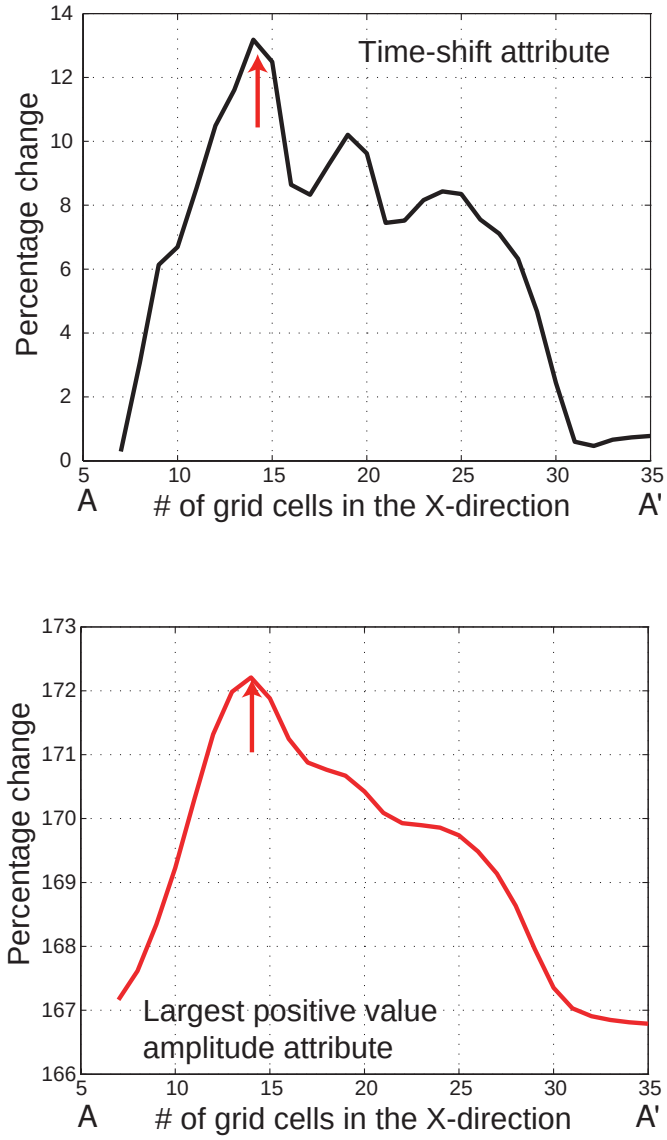

Figure 6.18: Percentage change in time-lapse attributes due to two different R-factors (5 and 15). A. Percentage change in 4D amplitude. B. Percentage change in time-shift. The profiles are along the producer.

6.7 Summary

The aim of this chapter was to understand the role that the elastic parameters of the overburden play on the 4D amplitude response and time-shift. In other words, I performed sensitivity tests of the 4D analysis to the overburden geology. The elastic parameters of the overburden are commonly neither measured or modeled in 4D studies. I created seven models where the Young's modulus and the Poisson ratio were changed by up to 13 %. The reference values for these parameters are based on the reported data for the overburden in the Valhall area. All models consisted a simplified rectangular grid with a single well producing for 18 years. The effect of increasing the R-factor was also investigated in the this chapter. The 4D attributes (amplitude and time-shift) were estimated using two R-factors (5 and 15) and the results were compared.

The simulation outputs show that there is a strong link between the reservoir depletion and the overburden deformation and this is controlled not only by the amount of depletion but also by the overburden elastic parameters. For instance, increasing the Young's modulus with depth for the Rogaland group (Balder, Sele, Lista) creates a larger pore pressure depletion than just increasing or decreasing the Young's modulus for the Lista formation (layer immediately above the reservoir). In terms of the 4D amplitude response at the top of the reservoir, variations up to 13% in the elastic parameters of the layer immediately above the reservoir do not influence significantly the 4D amplitude response. The maximum 4D amplitude variations were observed when the Poisson's ratio was decreased from 0.46 to 0.41. This causes a 4D amplitude increment of 1.8 % where the maximum depletion was occurring. Similarly, decreasing or increasing the Young's modulus of the layer above the reservoir by 13%, has a minimum impact on the 4D amplitude. The variations in the elastic parameters of the layer immediately above the reservoir impact more the 4D amplitude than the time-shift. All of the time-shift changes due to variations in the Young's modulus and Poisson's ratio were less than 1 ms.

The time-shift attribute is the most influenced by the R-factor. Increasing the R-factor from 5 to 15, causes the time-shift to increase up to 172 % while the 4D amplitude only increases by 13 %. This is because the time-shift is accumulative and respond to all the velocity changes, occurring from top of the reservoir to the sea floor. Therefore, it is crucial to avoid any misalignment between the monitor surveys and the baseline in order to extract a 4D amplitude response that is caused merely by the reservoir dynamic changes.

These models represents a simple scenario of pressure depletion and therefore extension of the results to more complex depletion patterns is likely not valid. Also, I analyzed the results for scenarios where the elastic parameters (Young's modulus and Poisson's ratio) vary up to 13 % for the layers immediately above the reservoir. If the uncertainty on these parameters or their changes across the field are within this range, it can be concluded that the 4D amplitude or the time-shift will not be significantly influenced by these variations. However, further analysis needs to be done (i.e. modelling) if larger variations on the elastic parameters of the overburden are expected.

Chapter 7

Conclusions and recommendations for future work

In this thesis a new approach has been presented for estimating pressure from time-lapse seismic data in compacting reservoirs. The methodology is based on the integration of time-lapse seismic with dynamic and static data from the reservoir. The approach has been successfully tested on synthetic and field data. The significant results and the main concluding remarks of the thesis are summarized in this chapter. Recommendations on how to extend the present work are also addressed.

7.1 Conclusions

I have performed a 4D seismic analysis for the case when fluid pressure and rock deformation are linked. Based on this analysis, I have developed a new method that provides a practical way to calibrate 4D amplitude attributes with pressure changes and initial reservoir porosity in compacting reservoirs. The new technique was tested on time-lapse seismic data from the south east flank of the Valhall Field. The Valhall Field is a Norwegian chalk reservoir (North Sea) that has undergone compaction when produced.

The origin, consequences and ways to measure rock compaction were explained in **chapter 1**. Rock compaction develops due to porosity reduction when fluids are extracted from a weak or over-pressured reservoir. The main parameter that controls the reservoir deformation is the effective

stress acting on the reservoir rock. The reduction in effective stress due to pore pressure depletion leads to the reduction in porosity and thickness and therefore compaction. The magnitude of this compaction effect depends on the overall mechanical stiffness of the rock. The examples of compacting fields presented in chapter 1, indicate that is not a new phenomenon and occurs worldwide. Furthermore, these types of reservoirs are excellent candidates for time-lapse studies because the time-lapse signal is relatively easy to observe. The changes in the elastic properties of the rocks are not just restricted to the reservoir zone but are also observed in the overburden and underburden rocks as an associated strain deformation. However the rock compaction makes predicting pressure and saturation from 4D seismic more challenging.

The literature review in **chapter 2**, indicates that the 4D seismic studies are moving towards a more quantitative approach. Nowadays, techniques such as EPASS-I and EPASS-II have been successfully used in non-compacting reservoir. These techniques use reservoir and production engineering data combined with time-lapse seismic to transform the 4D seismic signal directly into pressure and saturation maps. However, in order to produce reliable pressure change maps from 4D seismic attributes in compacting reservoirs, I needed not merely to integrate geophysics, reservoir engineering and geology, but also include geomechanics (i.e. the relation stress and strain or how the rock deform). Therefore, to understand and interpret 4D anomalies in compacting reservoirs, required firstly, predict the strain/stress response of the rocks due to particular pressure depletion at the reservoir. This was done by using a simulator that couples the fluid flow and rock deformation equations in a iterative manner. Subsequently, the outputs from the simulations (pressure, saturation, stress/strain) were used to estimate the seismic response for pre-production and produced cases by a conventional fluid substitution using the combination of the Gassmann equation (Gassmann, 1951) and fluid property correlations (Batzle & Wang, 1992). The P-wave velocities after compaction had occurred for the overburden and underburden were estimated assuming P-wave velocity changes as a function of vertical strain ($\frac{\Delta V_p}{V_p} = -r * \varepsilon_z$) (Hatchell *et al.*, 2005a). Finally, the synthetic seismograms were generated using the convolutional modelling.

In **chapter 3**, I explored a new approach to estimate reservoir pressure changes in compacting reservoirs using a synthetic model based on the south east flank of the Valhall Field. The first step was extracting the largest positive amplitude. This is the time-lapse seismic attribute that is most sensitive to pressure changes. The next step was to cross-plot pressure changes versus the largest

positive amplitude at well locations. Followed by the definition of a power equation that relates amplitude changes as a function of pressure changes ($\Delta A = C_1 * (\Delta P^{C_2})$). The coefficients ($C_1$ and C_2) are shown to depend on the initial reservoir porosity (i.e. higher porosity rocks are prone to compact more than rocks with lower porosity). This rock deformation is also recorded by the 4D seismic attribute. The pressure changes interpreted from synthetic seismograms showed a good agreement with the outputs from the reservoir flow simulator, and demonstrated the accuracy of this method. However, the error analysis indicated that the largest positive amplitude correlates better with effective stress changes ($\Delta\sigma^{'}$) than pore pressure changes (ΔP_f). This is because the pressure depletion and its associated rock compaction causes stress redistribution inside the reservoir and in the surroundings rocks which changes the normal average stress.

In **chapter 4**, the technique developed in chapter 3 was applied to the south east flank of the Valhall Field. A baseline and five repeat 3D surveys were selected. Two 4D attributes were used, the Largest Positive Value (amplitude attribute) and the speed up attribute (time attribute). The latter attribute captures the P-wave velocity increases in the reservoir due to pressure depletion and reservoir compaction. Initial porosity maps and pressure estimations from the reservoir model together with the two 4D seismic attributes were used to define a trend equation that correlates pressure changes with the time-lapse response. This equation was found to be linear ($\Delta A = (D_1 * \phi_i + D_2) * \Delta P$). Coefficients ($D_1$ and D_2) are controlled by the initial porosity. By applying this methodology, the understanding of the change in pressure and rock deformation across the flank is improved. The zones with the highest initial porosity have a strong 4D signal due to the rock compaction associated with the pressure depletion. Therefore in these areas, the pressure predictions from the 4D attributes shows a good correlation with the outputs from the reservoir model. However, there are some areas with non-observable 4D seismic. This can be mainly attributed to one of two factors. Firstly, zones where there has been not enough compaction to enhance the 4D response because the reservoir is thin and has low porosity and secondly, areas where the fluid flow is not occurring as a result of small faults or barriers. Furthermore, a comparison between the pressure maps predicted from 4D amplitude and the ones from the speed up attribute indicate that the some of the differences between both maps are due to the rock compaction at formations above the reservoir. This effect does not produce a 4D amplitude signature but it is captured by the time-shift attribute.

The impact that the structure and gas saturation have on the technique was evaluated in **chapter**

5. Strong thickness variations are shown to increase the errors on the pressure prediction. This is mitigated if relative values instead of absolute values are used to estimate pressure changes ($\frac{\Delta A}{A_1} = C_1 * (\frac{\Delta P}{P_1})^{C_2}$). Furthermore, the presence of gas on the reservoir requires a modification of the trend equation in order to accurately predict the pressure changes and account for the presence of free gas on the reservoir

$$\Delta A = (C_3 * \Delta P) + C_4 \tag{7.1}$$

Sensitivity analysis was performed to evaluate the effect that the overburden velocity changes have on the 4D attributes in **chapter 6**. Small changes in the elastic properties of the overburden have no impact in the reservoir 4D amplitude response. Synthetic models show that variations between 10% to 15% in the Poisson's ratio and Young's modulus of the layer immediately above the reservoir causes negligible changes (less than 4 %) in the 4D amplitude response. However, variations in the R factor considerably influences the 4D attributes and in particular the time-shift attributes. Increasing the R-factor from 5 to 15, causes the time-shift to increase up to 172% while the 4D amplitude only increases by 13%

7.2 Recommendations for future work

The methodology presented in this thesis is a new approach which has been developed and applied on synthetic and real field data. However, further research is required in order to refine and make this technique more robust and applicable to a wider range of reservoirs. This further research is addressed under the following categories:

7.2.1 Separation of pressure and gas saturation

The effect of gas saturation on the 4D amplitude was discussed on chapter 5. However, the methodology proposed in this thesis should be extended to predict simultaneously gas saturation and pressure changes from 4D attributes. This could be done by using a multi-attribute approach for example:

- Select two 4D seismic attributes, for example the largest positive amplitude and the speed-up attribute.

- Calibrate each 4D attribute with pressure and gas saturation changes at the well location in order to estimate an equation that relates pressure changes (ΔP) and gas saturation (ΔS) with the 4D attribute.
- Determine the relationship between each of the coefficients of the equation with the initial porosity. This produces two mathematical expressions, one for each attribute.
- Then, there is a system of two equations, one for each attribute, and two unknowns (ΔP and ΔS) which can be resolved.

7.2.2 Investigation of the effect of water injection on the 4D seismic for compacting reservoirs

Predicting pressure and saturation changes due to fluid injection from 4D attributes in compacting reservoirs has not been analyzed in this thesis. In chalk reservoirs, the water flooding decreases the pore collapse strength, which means that the rock compaction might accelerate. This effect is known as the water weakening. For instance, the rock compaction and its associated sea floor subsidence was first noticed at Ekofisk Field in 1984. The reduction in reservoir pressure was the main cause behind the reservoir compaction at this point. In the early nineties, an aggressive water injection programme was started with the purpose of pressure maintenance and enhanced recovery. Furthermore it was expected to slow and eventually stop subsidence at the producing platforms. However, as the pressures began to stabilize, there was no impact on the subsidence rate. The subsidence rate remained essentially constant and nowadays, it is believe that the water weakening phenomenon had become the primary mechanism for compaction in the field (Sylte *et al.*, 1999). Therefore, in the case of water flooding in chalk reservoirs, a further line of research will need to investigate the impact that water injection, pressure increase and porosity reduction have on the 4D seismic. This will require: a) lab data that describe how the elastic properties of chalk vary as a function of initial porosity and water saturation, b) data that provide reliable information about the changes in pressure and water saturation at well locations, and c) time-lapse seismic data that are designed to continuously monitors the water and pressure front movement.

7.2.3 Strain from 4D amplitude maps

As discussed in chapter 3, the effective stress shows a better correlation with 4D seismic than pore pressure changes. If the materials are linear elastic, there is a direct relationship between stress and strain ($\varepsilon = \frac{1}{E} * \sigma$), therefore the possibility that 4D amplitude seismic could be used to predict strain at the reservoir should be explored (i.e. rock compaction). Further work is needed in order to determine an equation that correlates a 4D amplitude attribute as a function of initial porosity and strain. This will require data that provide information about the rock deformation at the well locations. Then, these data could be cross plotted against a 4D amplitude attribute to define a trend equation. One possible source of these type data can be the Radioactive Marker Technique (RMT). RMT is an in-situ method to measure reservoir rock compaction and it normally has been used to evaluate uniaxial compressibility coefficients and to calibrate geomechanical models (Macini & Mesini, 2002). Predicting reservoir strain from 4D amplitude will be a very valuable information for reservoir management since it will help to know the amount of porosity reduction that has occurred.

7.2.4 Use of geomechanical models to calibrate the results from 4D seismic analysis

As discussed throughout this thesis, coupled fluid flow geomechanical modelling is an important ingredient to understand the relations between 4D seismic attributes and dynamic changes in compacting reservoirs. Therefore models that coupled fluid flow and rock deformation should always be used in further work in geomechanically active reservoirs. For instance, geomechanical simulation may help to define under which circumstances the normal average stress does not change in a way that 4D amplitude attributes will be only correlated with pore pressure changes. Also, in the case of using time-lapse seismic to predict water saturation, a well calibrated geomechanical model can help to answer the following question: a) what is the stress/strain redistribution above/below the reservoir due to water flooding? and b) how much is the porosity reduction due to the water weakening effect? In similar way, if reservoir strain is to be predicted from 4D attributes, the strain as an output from a geomechanical model can be directly compared with 4D amplitude attribute map in order to determine the degree of correlation between both parameters.

7.2.5 Impact of the 4D noise

Future work could concentrate on understanding the nature of the 4D noise in compacting reservoir and the impact of the compaction on seismic acquisition repeatability and geometry. Questions that could be addressed are: a) how much the rock compaction and sea floor subsidence (i.e. the physical movement of the reflectors) will influence the repeatability and geometry of subsequent monitor surveys? and b) how much 4D noise will be created by the changes in overburden velocities? Part of this work is currently a PhD work by the ETLP Group at Heriot-Watt University.

References

Askim, O.J. 2003. *Seismic Forward Modeling in a Chalk Reservoir with Permanent Monitoring.* Eur. Assn. Geosci. Eng. Page A16.

Barkved, O., K. Buer K. B. Halleland R. Kjelstadli T. Kleppan, & Kristiansen, T. 2003. *4D Seismic Response of Primary Production and Waste Injection at the Valhall Field.* Eur. Assn. Geosci. Eng. Page A22.

Barkved, O., Heavey, P., Kjelstadli, R., Kleppan, T., & Kristiansen, T. 2003. Valhall fieldStill on plateau after 20 years of production: Society of Petroleum Engineers. *SPE Paper*, **83957**, 16.

Barkved, O.I., & Kristiansen, T. 2005. Seismic time-lapse effects and stress changes: Examples from a compacting reservoir. *The Leading Edge*, **24**, 1244.

Barkved, OI, Kommedal, JH, & Thomsen, L. 2004. The role of multi-component seismic data in developing the Valhall Field (Norway): 66th Annual Conference and Exhibition, EAGE. *Extended Abstracts,*, **15**.

Batzle, M., & Wang, Z. 1992. Seismic properties of pore fluids. *Geophysics*, **57**, 1396.

Byerley, G., Pedersen, J., Roervik, K., Ranaweera, K., & Janssen, A. 2006. Reducing risk and monitoring water injection using time-lapse (4D) seismic at the Ekofisk field.

Calvert, R. 2005. *Insights and methods for 4D reservoir monitoring and characterization: 2005 Distinguished Instructor Short Course.* Society of Exploration Geophysicists.

Chin, LY, Thomas, LK, Sylte, JE, & Pierson, RG. 2002. Iterative coupled analysis of geomechanics and fluid flow for rock compaction in reservoir simulation. *Oil & Gas Science and Technology*, **57**(5), 485–497.

Clark, V.A. 1992. The effect of oil under in-situ conditions on the seismic properties of rocks. *Geophysics*, **57**, 894.

Cole, S., Lumley, D., Meadows, M., & Tura, A. 2005. Pressure and saturation inversion of 4D seismic data by rock physics forward modeling.

Corzo, M., & MacBeth, C. 2006. Towards accurate quantitative monitoring of compacting reservoirs using time-lapse seismic.

Davis, E., Wright, C., Demetrius, S., Choi, J., & Craley, G. 2000. Precise Tiltmeter Subsidence Monitoring Enhances Reservoir Management. *Soc. Petrol. Eng. Paper*, **62577**, 19–23.

Eason, G., Noble, B., & Sneddon, IN. 1955. On Certain Integrals of Lipschitz-Hankel Type Involving Products of Bessel Functions. *Philosophical Transactions of the Royal Society of London. Series A, Mathematical and Physical Sciences*, **247**(935), 529–551.

Eason, G., Noble, B., & Sneddon, IN. 1976. Subsidence in the Boliva Coast. *Proceedings of the Anaheim Symposium*, **121**, 257–265.

Farmer, CL., & Barkved, OI. 1999. Influence of syn-depositional faulting on thickness variations in chalk reservoirs–Valhall and Hod fields. *Petroleum Geology of Northwest Europe: Proceedings of the 5th Conference. Geological Society, London*, 949–957.

Ferronato, M., Gambolati, G., Teatini, P., & Bau, D. 2006. Interpretation of Radioactive Marker Measurements To Evaluate Compaction in the Northern Adriatic Gas Fields. *Soc. Petrol. Eng. Paper*, **97752**, 401–411.

Fjær, E., Holt, R, Horsrud, P., Raaen, A, & Risnes, R. 1992. Petroleum related rock mechanics. *Developments in petroleum science*, **33**, 1–325.

Floricich, M., MacBeth, C., & Staples, R. 2005. *An engineering-driven approach for separating pressure and saturation using 4D seismic: Application to a Jurassic reservoir in the UK North Sea.* Soc. of Expl. Geophys. Pages 2464–2467.

Floricich, M., MacBeth, C., Staples, R., Evans, A., & Dijksman, N. 2006a. *Determination of a seismic and engineering consistent petroelastic model for time-lapse seismic studies: Application to the Schiehallion Field.* Soc. of Expl. Geophys. Pages 3205–3209.

Floricich, M., MacBeth, C., Stammeijer, J., Staples, R., Evans, A., & Dijksman, C. 2006b. *A New Technique for Pressure - Saturation Separation from Time-Lapse Seismic - Schiehallion Case Study.* Eur. Assn. Geosci. Eng. Page E017.

Gassmann, F. 1951. Uber die elastizitat poroser medien. *Vierteljahrsschrift der Naturforschenden Gesellschaft in Zurich*, **96**, 1–23.

Geertsma, J. 1957. The effect of fluid pressure decline on volumetric changes of porous rocks. *Trans. AIME*, **210**(1), 331–340.

Geertsma, J. 1973. Land subsidence above compacting oil and gas reservoirs. *J. Pet. Technol*, **25**, 734–744.

Goto, R., Lowden, D., Smith, P., & Paulsen, J.O. 2005. Steered-streamer 4D case study over the Norne field.

Gouveia, W.P., Johnston, D.H., Solberg, A., & Lauritzen, M. 2004. Jotun 4D Characterization of fluid contact movement from time-lapse seismic and production logging tool data. *The Leading Edge*, **23**(11), 1187–1194.

Guilbot, J., & Smith, B. 2002. 4-D constrained depth conversion for reservoir compaction estimation Application to Ekofisk Field. *The Leading Edge*, **21**(3), 302–308.

Gutierrez, M., Lewis, RW, & Masters, I. 2001. Petroleum reservoir simulation coupling fluid flow and geomechanics. *SPE Reservoir Evaluation & Engineering*, 164–172.

Hall, S.A., MacBeth, C., Barkved, O.I., & Wild, P. 2005. Cross-matching with interpreted warping of 3 D streamer and 3 D ocean-bottom-cable data at Valhall for time-lapse assessment. *Geophysical Prospecting*, **53**(2), 283–297.

Hatchell, P., & Bourne, S. 2005. Rocks under strain: Strain-induced time-lapse time shifts are observed for depleting reservoirs. *The Leading Edge*, **24**, 1222.

Hatchell, P, van den Beukel, A., Molenaar, M, Maron, K, Kenter, C, Stammeijer, J, van der Velde, J, & Sayers, C. 2005a. Whole earth 4D: Reservoir monitoring geomechanics.

Hatchell, PJ, Kawar, RS, & Savitski, AA. 2005b. Integrating 4D seismic, geomechanics and reservoir simulation in the Valhall oil field. *67th Meeting, EAGE, Expanded Abstracts, C*, **12**.

Hawkins, K., Howe, S., Hollingworth, S., Conroy, G., Ben-Brahim, L., Tindle, C., Taylor, N., Joffroy, G., & Onaisi, A. 2007. Production-induced stresses from timne-lapse shifts: A geomechanics case study from Franklin and Elgin fields. *The Leading Edge*, **26**(5), 655–662.

Herwanger, J., & Horne, S. 2005. Predicting time-lapse stress effects in seismic data. *The Leading Edge*, **24**, 1234.

Hodgson, N., MacBeth, C., Duranti, L., Rickett, J., & Nihei, K. 2007. Inverting for reservoir pressure change using time-lapse time strain: Application to Genesis Field, Gulf of Mexico. *The Leading Edge*, **26**, 649.

Hwang, L.F., & Lellis, P.J. 1988. Bright spots related to high GOR oil reservoir in green canyon.

Janssen, A.L., Smith, B.A., Byerley, C.P.G.W., & Norway, C.P. 2006. Measuring velocity sensitivity to production-induced strain at the Ekofisk Field using time-lapse time-shifts and compaction logs.

Jones, M., Leddra, M., & Addis, M. 1987. *Reservoir Compaction ans surface subsidence due to hydrocarbon extraction.* Tech. rept. Offshore Technology Report HMSO, London.

Kenter, C, Blanton, T, & Schreppers, G. 1998. Compaction study for Shearwater field. *Soc. Petrol. Eng. Paper*, **47280**.

Kjelstadli, R., Johnson, D., Barkved, O., Buer, T., & Kristiansen, T. 2005. Quantitative history match of 4D seismic response and production data in the Valhall Field: Society of Petroleum Engineers. *SPE Paper*, **96317**.

Kommedal, JH, Barkved, OI, & Howe, DJ. 2004. Initial experience operating a permanent 4C seabed array for reservoir monitoring at Valhall: 74th Annual International Meeting, SEG. *Expanded Abstracts*, 2239–2242.

Kommedal, JH, Barkved, OI, & Henneberg, K. 2005. Repeatability using a permanently installed seismic array: 67th Annual Conference and Exhibition, EAGE. *Extended Abstracts,*, **16**.

Kommedal, J.H., Barkved, O.I., van Gestel, J.P., & Pettersen, R.S.H. 2007. Processing strategies for multiple repeat 4D seismic.

Kristiansen, T. 1998. Geomechanical Characterization of the Overburden above the Compacting Chalk Reservoir at Valhall. *Eurock*, **98**, 193–202.

Lancaster, S., & Whitcombe, D. 2000. Fast-track 'coloured'inversion.

Landrø, M. 1999. *Discrimination between pressure and fluid saturation changes from time-lapse seismic data*. Soc. of Expl. Geophys. Pages 1651–1654.

Landrø, M. 2001. Discrimination between pressure and fluid saturation changes from time-lapse seismic data. *Geophysics*, **66**, 836.

Landrø, M., & Stammeijer, J. 2004. Quantitative estimation of compaction and velocity changes. *Geophysics*, **69**, 949–957.

Lumley, D., Meadows, M., Cole, S., & Adams, D. 2005. Estimation of reservoir pressure and saturations by crossplot inversion of 4D seismic attributes.

MacBeth, C. 2004. A classification for the pressure-sensitivity properties of a sandstone rock frame. *Geophysics*, **69**, 497.

MacBeth, C., Soldo, J., & Floricich, M. 2004. *Going quantitative with 4D seismic analysis*. Soc. of Expl. Geophys. Pages 2283–2286.

Macini, P., & Mesini, E. 2002. Measuring Reservoir Compaction Through Radioactive Marker Technique. *Journal of Energy Resources Technology*, **124**, 269.

Minkoff, S.E., Stone, C.M., Bryant, S., & Peszynska, M. 2004. Coupled geomechanics and flow simulation for time-lapse seismic modeling. *Geophysics*, **69**(1), 200–211.

Nagel, NB. 1998a. Ekofisk field overburden modelling. **47345**, 177–186.

Nagel, NB. 1998b. Ekofisk Field Overburden Modelling. *Proc. Eurock Rock Mechanics in Petroleum Engineering, SPE/ISRM*, **47345**(2), 177–186.

Parker, JR. 1993. Petroleum Geology of Northwest Europe: Proceedings of the 4th Conference. *Geological Society, London*.

Patzek, T., Silin D., & Barenblatt, G. 2001. Impact of rock micro and macrostructures on the behaviour of two-pahse fluid flow. *22nd International Energy Agency Workshop, Viena*.

Pedersen, S., & Rhett, D. 1998. A parametric study of Compressional and Shear wave velocities in Ekofisk reservoir chalk: Society of Petroleum Engineers. *SPE Paper*, **47295**, 7.

Pettersen, Ruth. 2006. *Can amplitude and travel time information to be combine to improve model based 4D inversion?* M.Phil. thesis, Department of Petroleum Engineering and Applied Geophysics, Norwegian University of Technology and Science.

Poland, J., & Davis, G. 1969. Land subsidence due to withdrawal of fluids. *Reviews in Engineering Geology*, 187–269.

Pourciau, R, Fisk, J, Descant, F, & Waltman, R. 2004. Completion and well-performance results: Genesis field. *Journal of petroleum technology*, **56**(4), 50–51.

Rickett, J., Duranti, L., Hudson, T., Regel, B., & Hodgson, N. 2007. 4D time strain and the seismic signature of geomechanical compaction at Genesis. *The Leading Edge*, **26**, 644.

Rothenburg, L., Bratli, RK, & Dusseault, MB. 1994. A poro-elastic solution for transient fluid flow into a well.

Schutjens, P.M.T.M., Burrell, R., Fehmers, G., Hindriks, K., Collins, C., & van der Horst, J. 2007. On the stress change in overburden resulting from reservoir compaction: Observations from two computer models and implications for 4D seismic. *The Leading Edge*, **26**, 628.

Settari, A., & Mourits, FM. 1998. A Coupled Reservoir and Geomechanical Simulation System. *SPE Journal*, **3**(2), 219–226.

Settari, A., & Walters, DA. 1999. Advances in coupled geomechanical and reservoir modeling with applications to reservoir compaction.

Skempton, AW. 1960. *Effective Stress in Solid Concrete and Rock Pore Pressure and Suction in Soils.*

Stables, R., Ita, J., Burrell, R., & Nash, R. 2007. Monitoring pressure depletion and improving geomechanical models for the Shearwater Field using 4D seismic. *The Leading Edge*, **26**(5), 636–642.

Stenvold, T., Elken, O., Zumberge, M., Sasagawa, G., & Nooner, S. 2006. High-precision relative depth and subsidence mapping from seafloor water pressure measurements. *SPE Reservoir Evaluation Engineering*, **6**(6), 380–389.

Stronen, L. K., & Digranes, P. 2000. *The Gullfaks field - 4D seismic enhances oil recovery and improves the reservoir description.* Eur. Assn. Geosci. Eng. Page Session:X0033.

Sylte, JE, Thomas, LK, Rhett, DW, Bruning, DD, & Nagel, NB. 1999. Water induced compaction in the Ekofisk field.

Terzaghi, K. 1936. The shearing resistance of saturated soils and the angle between the planes of shear. *Proc. 1st Int. Conf. Soil Mech*, **1**, 54–56.

Tran, D., Settari, A., & Nghiem, L. 2004. New iterative coupling between a reservoir simulator and a geomechanics module. *SPE/ISRM Rock Mechanics Conference.*

van Gestel, J.P., Barkved, O.I., & Kommedal, J.H. 2007. Valhall life-of-field seismic automated workflow.

Vidal, S., Huguet, F., & Mechler, P. 2002. Characterizing reservoir parameters by integrating seismic monitoring and geomechanics. *The Leading Edge*, **21**(3), 295–301.

Wiborg, R., & Jewhurst, J. 1986. Ekofisk Subsidence Detailed and Solutions Assessed. *Technology, Oil & Gas Journal*, 47–51.

Xu, H., & Nur, A. 2001. Integrating reservoir engineering and satellite remote sensing for (true) continuous time-lapse reservoir monitoring. *The Leading Edge*, **20**(10), 1176–1179.

Zoeppritz, K. 1919. Erdbebenwellen VIIIB, On the reflection and propagation of seismic waves. *Gottinger Nachrichten*, **1**, 66–84.

Appendix A

Derivation of the compaction equation

This appendix shows the full derivation of the compaction equation (Eq. 1.19) discussed in chapter 1. This equation is used to estimate the compaction under uniaxial strain conditions.

When pore pressure (ΔP_f) is present and the material is considered linear elastic, the equations 2.20, 2.21 and 2.22 become:

$$E\Delta\varepsilon_x = \Delta\sigma_x - \nu(\Delta\sigma_y + \Delta\sigma_z) - (1-2\nu)\alpha\Delta P_f \tag{A.1}$$

$$E\Delta\varepsilon_y = \Delta\sigma_y - \nu(\Delta\sigma_x + \Delta\sigma_z) - (1-2\nu)\alpha\Delta P_f \tag{A.2}$$

$$E\Delta\varepsilon_z = \Delta\sigma_z - \nu(\Delta\sigma_x + \Delta\sigma_y) - (1-2\nu)\alpha\Delta P_f \tag{A.3}$$

Assuming that the Biot's constant (α) is equal to the unit and uniaxial compaction ($\Delta\varepsilon_y = \Delta\varepsilon_z$ and $\Delta\sigma_y = \Delta\sigma_z$), the Eq. A.4 is obtained.

$$(\Delta\sigma_y + \Delta\sigma_z) = \frac{2\nu\Delta\sigma_x + 2(1-2\nu)\alpha\Delta P_f}{1-\nu} \tag{A.4}$$

Replacing Eq. A.4 into Eq. A.3,

$$E\Delta\varepsilon_z = [\frac{1-\nu-2\nu^2}{1-\nu}](\Delta\sigma_z - \Delta P_f) \tag{A.5}$$

Since the overburden stress remains constant ($\Delta\sigma_z$=0) and $\Delta\varepsilon_z = \frac{\Delta H}{H}$, the compaction formula can be written as:

$$\frac{\Delta H}{H} = \frac{1-\nu-2*\nu^2}{(1-\nu)*E} * \Delta P_f \tag{A.6}$$

Appendix B

Biot's equations for deformation in a 3D porous media and Darcy's flow equations

In the The traditional (uncoupled) reservoir simulation solves the pore pressure distribution in the reservoir from the Darcy equation:

$$\nabla^T \frac{k}{\phi\eta} \nabla p = C_t \frac{\delta}{P_f} \delta t \tag{B.1}$$

where P_f is the pore fluid pressure, k is the permeability matrix, η is the viscosity of the fluid, ϕ is the porosity, and C_t is the total compressibility of the fluid and reservoir rock system. In iterative and fully coupled simulations solve the Biots formulation of fluid flow and deformation in porous media. Biots law consists of the following five equations for incompressible fluid (Gutierrez *et al.*, 2001): Effective stress law:

$$\sigma^{'} = \sigma_T - \alpha P_f \tag{B.2}$$

2. Constitutive relation:

$$\delta\sigma^{'} = D\delta\varepsilon \tag{B.3}$$

3. The static equilibrium equation

$$\nabla^T \sigma + F = 0 \tag{B.4}$$

4. Darcy's law

$$v = -\frac{k}{\eta}\nabla^T P_f \tag{B.5}$$

5. The mass balance equation

$$\nabla^T v + \varepsilon_v + \frac{\alpha\phi P_f}{\kappa_{fr}} = 0 \tag{B.6}$$

where:

σ = Total stress

$\sigma^{'}$ = Effective stress

ε = Strain

ε_v = Volumetric strain

D = Constitutive matrix

F = Body forces

v = Fluid Darcy's velocity

κ_{fr} = Bulk modulus of the rock frame